Dealing with unpredictability and heterogeneity: contributions to modelling and control of renewable and multi-source energy conversion systems

Antoneta Iuliana Bratcu

Université Grenoble Alpes

HABILITATION À DIRIGER LA RECHERCHE

Pour obtenir le diplôme

DE L'UNIVERSITÉ GRENOBLE ALPES

Spécialité : **Automatique–Productique**

Arrêté ministériel : 25 mai 2016

Présentée par

Antoneta Iuliana BRATCU

préparée au sein de **Grenoble Image Parole Signal Automatique Laboratoire (GIPSA-lab)**
dans l'École Doctorale **Électronique, Électrotechnique, Automatique et Traitement du Signal (EEATS)**

Dealing with unpredictability and heterogeneity: contributions to modelling and control of renewable and multi-source energy conversion systems

Thèse soutenue publiquement le **18 novembre 2022**,
devant le jury composé de :

Mme. Mara TANELLI
Professeure, Politecnico di Milano, Milan, Italie, Présidente

Mme. Jing SUN
Professeure, Université de Michigan, Ann Arbor, Michigan, États Unis, Rapporteur

M. Leopoldo GARCIÁ FRANQUELO
Professeur, Université de Séville, Séville, Espagne, Rapporteur

M. Guillaume SANDOU
Professeur, CentraleSupélec, Université Paris-Saclay, Gif-sur-Yvette, France, Rapporteur

M. Gilney DAMM
Directeur de recherche, Université Gustave Eiffel, Marne-la-Vallée, France, Examinateur

M. Malek GHANES
Professeur, Centrale Nantes, Nantes, France, Examinateur

M. Daniel HISSEL
Professeur, Université de Franche-Comté, Belfort, France, Examinateur

M. Seddik BACHA
Professeur, Université Grenoble Alpes, Grenoble, France, Examinateur

M. Olivier SENAME
Professeur, Grenoble INP, Grenoble, France, Examinateur

Acknowledgments

The following lines aim at simply saying "*Thank you!*" to all the wonderful people I have had the chance to meet and learn from.

My amazing teachers, my inspiring mentors... my brilliant colleagues... my sparkling, warm and devoted friends... here, in France, and there, in Romania. Together with my either constant companions, or episodic or hazardous, yet meaningful meetings, we are all in a great adventure of knowledge... and I am grateful for that.

I wish I could thank Professor Emil CEANGĂ in person, but this is no longer possible. Professor CEANGĂ was the first one having taught me about signals and systems, some thirty years ago now, at "Dunărea de Jos" University of Galaţi, in Romania. Later, I was lucky to work with him. I have done my best to write this memoir in respectful memory of his teachings.

I cannot finish without loving and grateful thoughts for my parents, who have always supported me through the endeavours of my life. My wonderful mother has recently passed away. She would have been happy to learn that I am now able to defend my habilitation thesis. I guess that these lines help me to somehow accept my guilt and payback for a cruel disobedience and stupid incomprehension... because, after all, I was such a normal child.

Contents

Chapter 1

Introduction

1.1 Why this memoir?

The exercise of writing this HDR (*Habilitation à Diriger des Recherches*) memoir has some quite "prosaic" original motivations: indeed, it is required in the French system, in order to be authorized to conduct research activities, that is, to supervise Ph.D. theses. Therefore, it is *a priori* about a rather "administrative" reporting.

However, as personal perceptions are subjective by definition, each researcher can take the liberty of performing this "have to" her/his way. This is why I decided to use this task as an opportunity to look back at my research career with some questions in mind: here is what I have done because it was interesting and motivating to me – but *was it significant and useful in a larger sense*? *Are the contributions reported here really meaningful*?

In other words, an exercise of delivering an honest, objective, self-critical and relativized analysis of one's past research activity, subsequently accompanied by a projection into the future, to answer a legitimate question: and now what? *What comes next*?

While in my case it was not quite obvious to summarize roughly the last twenty years of my career, I have done my best to write this memoir such that it contains at least some partial answers to the above questions. The reported activity mainly concerns ***optimal and robust control approaches for electrical energy conversion systems – characterized by a large penetration of renewables and presence of storage units*** – with strong emphasis of the associated ***application*** aspects: ***real-time preliminary validation, processor-unit embedding and real-world testing***. Focus is on different types of renewables – wind, photovoltaic and micro-hydro – and then on (hybrid) storage power management within multi-source systems and microgrids.

Apart from their steady societal and ecological interest – which have lastly rendered them "*en vogue*" from both scientific and research funding opportunity viewpoints – these dynamical systems are challenging in view of at least two of their features: *unpredictability* and *heterogeneity*. A constant idea was adopted throughout the approaches summarized here: to transform these *challenges*, as much as possible, in *opportunities* for control design.

This memoir is organized as follows. In the remainder of this first chapter a description of my career evolution is given, before introducing in a rather informal manner the necessity and motivation of the proposed scientific approach (Chapter 2). The following two chapters summarize the core of my contributions, with focus on the optimal control of renewable energy conversion systems (Chapter 3) and then on Power Management System robust design for multi-source electrical energy systems and microgrids (Chapter 4). Once the summarizing effort accomplished, the concluding Chapter 5 aims at identifying some research directions worthy to pursue.

1.2 Curriculum Vitae

General information

- Last name: BRATCU
- Given names: Antoneta Iuliana
- Birth date and place: January 13th 1972 at Galaţi (Romania)
- E-mails: antoneta.bratcu@{gipsa-lab.fr, gipsa-lab.grenoble-inp.fr, grenoble-inp.fr}

University degrees

- 2001: **Ph.D. degree** in *Control Systems and Informatics* (*Automatique et Informatique*), University of Franche-Comté, Besançon, France – ***with honours*** (*mention* « ***très honorable*** »)
  - Title: *Systematic determination of precedence graphs and assembly line balancing* (in French: *Détermination systématique des graphes de précédence et équilibrage des lignes d'assemblage*)
  - Assessment Committee:
    Guy JUANOLE (Professor at University of Toulouse), president
    Jean-Paul BOURRIÈRES (Professor at University of Bordeaux 1), rapporteur
    Bernard DESCOTES-GENON (Professor at "Joseph Fourier" University, Grenoble), rapporteur
    Alain BOURJAULT (Professor at Ecole Nationale Supérieure de Mécanique et Microtechniques – ENSMM, Besançon), examiner
    Abdellah EL MOUDNI (Professor at University of Technology of Belfort-Montbéliard – UTBM, Belfort), examiner
    Gérard VALLET (Engineer at ADEPA), examiner
    Jean-Michel HENRIOUD (Professor at University of Franche-Comté, Besançon), thesis supervisor
    Viorel MÎNZU (Professor at "Dunărea de Jos" University of Galaţi, Romania), thesis supervisor
- 1998: **Bachelor Economist**, *International Transactions*, "Dunărea de Jos" University of Galaţi (Romania), Faculty of Economical and Administration Sciences
- 1996: **Master in Engineering**, *Power Electronics and Advanced Control Systems for Energy Conversion*, "Dunărea de Jos" University of Galaţi (Romania), Faculty of Electrical Engineering
- 1995: **Bachelor Engineer**, *Control Systems and Industrial Informatics*, "Dunărea de Jos" University of Galaţi (Romania), Faculty of Electrical Engineering

Functions

Since September 2011: Associate Professor, CNU (*Conseil National des Universités*) 61 Section (*Control systems, informatics and signal processing*).

- 2011 – 2016: Tenured position on **CNRS – Grenoble INP Chair** "*Modelling and control of dynamical systems with applications to smart grids*"
- Establishment (**teaching** affiliation): École Nationale Supérieure de l'Eau, l'Énergie et l'Environnement (ENSE^3 – Grenoble INP), Grenoble (France)
- Laboratory (**research** affiliation): Grenoble Image Speech Signal Automatic Control Laboratory (GIPSA-lab), UMR (*Unité Mixte de Recherche*) CNRS 5216

Teaching service and responsabilities

- Teaching service
  - 2011 – 2016: **64 hours ETD / year** while on **CNRS – Grenoble INP Chair**
    - Control systems for electrical energy (lectures, computer sessions – 2nd year of *Engineering of electrical energy* specialty (*Ingénierie de l'Energie Electrique* – IEE), ENSE^3 / Grenoble INP)
    - Modelling and control of power electronic converters (computer sessions – 2nd year IEE ENSE^3)
    - Design and control of electrical grids (project – 1st year ENSE^3)

  - since 2016 to date : **192 hours ETD / year**
    - Control systems for electrical energy (lectures, computer sessions, practical sessions – 2nd year IEE ENSE^3)
    - Modelling and control of power electronic converters (computer sessions – 2nd year IEE ENSE^3)
    - Design and control of electrical grids (project – 1st year ENSE^3)
    - Control and regulation (practical sessions – 1st year *Electrical and power engineering* (*Génie électrique et énergétique* – GEE) apprenticeship specialty ENSE^3)
    - Control and numerical regulation (lectures, computer sessions – 2nd year apprenticeship GEE ENSE^3)
    - Optimization in electrical power systems (computer sessions – 3rd year IEE, 3rd year *Energy systems and markets* (*Systèmes énergétiques et marchés* – SEM) specialty and international master *Smart grids and buildings*, ENSE^3)
  - **tutoring** of 2 students in final diploma project and 1 student in apprenticeship (in average per year)
  - since 2015 **coordination of the teaching unit** "Control systems for electrical engineering", 2nd year IEE ENSE^3
  - since 2019 **coordination of the integrating project unit**, 3rd year of *Control Engineering and Intelligent Systems* (*Automatique et Systèmes Intelligents* – ASI), ENSE^3

- Administrative responsibility at GIPSA-lab
  - 2012 – 2018: **Coordinator of local organization of *Grenoble Summer School of Automatic Control*** – annual scientific event hosted by GIPSA-lab, having Ph.D. students as main audience, on a different topic each year

- 1995 – 2011: teaching and research staff at "Dunărea de Jos" University of Galaţi (Romania), Faculty of Electrical Engineering
  - 1995 – 2000: Teaching Assistant (308 hours/year, practical sessions only)
    - Basics of control systems
    - Numerical methods
    - Modelling and simulation of dynamical systems
  - 2000 – 2005: Lecturer (308 hours/year, lectures and practical sessions)
    - Basics of control systems
    - Numerical methods
    - Modelling and simulation of dynamical systems
  - 2005 – 2011: Associate Professor (224 hours/year, lectures and practical sessions)
    - Real-time models for electromechanical conversion
    - Microprocessors
    - Theory of dynamical systems

- Administrative responsibility at "Dunărea de Jos" University of Galaţi
  - 2003 – 2011: Secretary of Galaţi Territorial Section of *Romanian Society of Automatic Control and Technical Informatics* (SRAIT)

Research

- December 2007 – December 2009: **post-doctoral fellowship** with Grenoble Electrical Engineering Laboratory (G2ELab) / Grenoble Institute of Technology (Grenoble INP), while Associate Professor at "Dunărea de Jos" University of Galaţi (Romania), Faculty of Electrical Engineering
- October 2004 – May 2005: **post-doctoral fellowship** granted by the Agence Universitaire de la Francophonie (A.U.F.) with École Nationale Supérieure des Mines de Saint Étienne (ENSM.SE), Industrial Engineering and Informatics Center (G2I)

- December 2001 – December 2002: **post-doctoral fellowship** granted by Regional Council of Champagne-Ardenne Region with University of Technology of Troyes (UTT), Optimization of Industrial Systems Laboratory (LOSI)
- November 1996 – July 2001: **Ph.D. student** at Laboratoire d'Automatique de Besançon (LAB), while Teaching Assistant and then Lecturer at "Dunărea de Jos" University of Galaţi (Romania), Faculty of Electrical Engineering

National (Romanian) distinction

- 2007 IN HOC SIGNO VINCES PRIZE, *Engineering Sciences* Section, of National Academic Scientific Research Council (C.N.C.S.I.S.), granted to Ph.D. holders younger than 35 years, for outstanding research activity

1.3 Research activity overview

Overview of my research activity is presented below as decomposed into **two chronologically-successive parts**, in coherence with the evolution of my carreer.

1.3.1 Before having joined GIPSA-lab (1995 – 2011, in Romania and during post-doctoral fellowships in France)

My research activity during this period can globally be described as developping and applying **dynamic optimization techniques**, both **continuous** and **discrete**, for industrial systems control. To this end, systematic procedures aiming at extremizing objectives expressed by functions or functionals defined over either continuous or discrete spaces, are employed as mathematical tools. Numerical implementation of such procedures is achieved by means of dedicated software tools.

There are two main classes of industrial systems targeted as applications, namely:

– systems requring use of *discrete* (combinatorial) *optimization methods*: design, optimization and reconfiguration of production systems, such as assembly lines and transfer lines;

– systems requiring application of *continuous optimization methods*, namely ***multi-criteria optimal control of renewable energy conversion systems*** – such as *wind*, *photovoltaic*, *micro-hydro* – going towards implementation of supervision and energy/power optimal management strategies, possibly supposing coupling with combinatorial optimization methods.

Modelling and solving of problems of the first class of systems rely on either exact or heuristic methods such as dynamical programming, branch-and-bound algorithms (*e.g.*, in C++ implementations), constrained linear-integer programming (*e.g.*, with C++ and ILOG as software tools), logical programming with constraints (*e.g.*, with PROLOG as software tool).

As regards problems of the second class, their developpment supposes extensive use of software environments dedicated to analysis and design of continuous dynamical systems, such as MATLAB® /Simulink® .

In the case of *renewable energy conversion systems*, mathematical statement of the multi-criteria optimization is specific to each conversion technology, but in all cases *maximization of conversion efficiency* is aimed at. As it is in general about nonlinear dynamical systems, design methods may include some *linear* ones (*e.g.*, deterministic and stochastic LQ design), but most of them are specifically *nonlinear* (*e.g.*, sliding mode, feedback linearization, Extremum Seeking Control, *etc.*).

It is the second class of systems my research interest has been focused on during following years; therefore, this is detailed below.

Implementation and exploitation of **renewable energy conversion systems** challenges control engineering practitioners first of all because of the discontinuity, unpredictability and randomness of the primary resource, but also because of the nonlinearity of their static power curves.

For ***grid integration*** of such systems, the control approach is indispensable in order to solve the generally ***Maximum Power Point Tracking (MPPT)*** problem – taking account of a strongly variable, *a priori* unknown

or at least either difficult-, or expensive-to-measure(estimate) resource – as well as the "smooth" integration into the grid, which must allow disturbance rejection coming from both sides and also weakly-distorted, good-quality sinusoidal current injection into the grid.

In the case of ***autonomous*** (stand-alone, islanded) ***AC systems*** or ***microgrids***, as these are not connected to the strong (infinite-power) grid, control objectives mainly deal with ensuring voltage and frequency regulation despite of load variations, which always requires advanced, generally nonlinear, control methods and tools.

My research experience in this domain concerns the **wind, photovoltaic and micro-hydro energy conversion systems**.

Design of ***minimal-knowledge-based MPPT optimal control laws*** was one of the main goals, while envisaging an as easy as possible real-world implementation, robust at both parameter and modelling uncertainties. This goal naturally supposes design of appropriate pulse-width-modulation (PWM)-based modelling and control of the ubiquitous DC/AC and AC/AC power electronic converters, acting as actuators in this context.

I also have experience with ***real-time validation*** of such control laws, namely on dedicated test benches implementing the whole conversion chain, including the grid connection. To this end, ***Hardware-in-the-loop simulation (HILS)*** techniques were extensively used and an original systematic design of a HILS system in a general case was proposed.

As regards effective applications, wind and micro-hydro systems were here concerned, whose operation is based on three-phase rotating electrical machines coupled with the primary energy sources, in this case, the turbines. From a control viewpoint, the role of machines is to impose the steady-state operating point to the turbines, which further enables the possibility of controlling them according to the goal. To this end, a suitable modelling and identification approach is obviously necessary.

1.3.2 After having joined GIPSA-lab (2011 to date)

At Grenoble Images Speech Signal and Control Laboratory (GIPSA-lab, UMR CNRS 5216), I joined the *Linear Systems and Robustness* (*Systèmes Linéaires et Robustesse* – **SLR**) team, within the *Control Systems Department*. This team was carrying out theoretical, methodological and applied research, towards novel structural, algebraic, robust, optimization-based approaches of analysis, observation, identification and control of dynamical systems. Having solid skills in modelling, identification, observation and control of linear systems, SLR team was focusing on taking into account the modelling uncertainties and various disturbances into the control or estimation design.

My arrival in 2011 as an **Associate Professor** on a tenured position on **CNRS – Grenoble INP Chair** "*Modelling and control of dynamical systems with applications to smart grids*" had the role of enhancing SLR potential on the electrical energy topic, thus giving me the opportunity of diversifying my research topics.

Evolution of my research topics has continued after GIPSA-lab restructuring at the beginning of 2020, when I joined the newly created **MODUS** (*Modelling and Optimal Decision for Uncertain Systems*) team, within the *Control Systems and Diagnostic Pole*. MODUS team is committed to bring its skills and know-how at bridging the gap between advanced control and its real-world application in a broad regard. To this end, the employed methods will aim at complementing *classical* approaches – such as *Lyapunov-based* or *optimal control* – by *data-driven* and *learning-based* methods to take account of uncertainties and big data issues, very frequently occurring in nowadays real-world systems.

Since my arrival at GIPSA-lab, my research work has been developed along with several directions.

One of these directions is the ***design of robust and linear parameter-varying (LPV) optimal control methods*** for ***coordination*** inside of ***multi-source electrical systems*** supplying irregular loads, for both *embedded* applications – such as supply systems on board of electric vehicles – or *stationary* applications – such as different microgrid use cases, requiring formulation of different control objectives, respectively. The ***dynamic specialization*** of sources – within identifiable frequency ranges placed around the so-called ***characteristic frequency*** – is here taken into account in order to minimize their exploitation stress and prolong their lifetimes. In this case, the control problem can be cast into a ***robust disturbance rejection formalism***, such as the $\mathcal{H}_\infty$ ***framework***.

This was the topic of the 2012–2015 Ph.D. thesis of Waleed NWESATY (defended in 2015) – where a three-source

system has been considered – as well as of a technology pre-transfer project funded by Institut Carnot *Logiciels et Systèmes Intelligents* (LSI) and of its continuation towards effective transfer with Linksium Grenoble Alpes Technology Transfer Office (TTO). A ***rapid-prototyping demonstrator*** was conceived and built at GIPSA-lab for test and validation purpose, in order to advance the technology readiness level (TRL) of the proposed solution. In the context of the technology transfer, ***two software licenses*** and a ***know-how procedure*** are in progress to protect the intellectual rights.

In the same framework is also placed the design of a ***multi-variable robust control of microgrids with strong penetration of renewable energy sources and storage units***. This was the core topic of the Ph.D. thesis of Quang-Linh LAM, run in collaboration with Grenoble Electrical Engineering Laboratory (G2ELab) during 2014–2017, defended in 2018. Both ***frequency*** and ***voltage control and stability*** of stand-alone microgrids were addressed. Use of $\mathcal{H}_\infty$ framework allowed a ***comprehensive control design methodology*** being proposed, as well as a thorough robustness analysis – in relation with some strongly varying parameters, such as the storage unit state of charge – both of which were validated on a real-time ***Power Hardware-in-the-Loop (PHIL)*** dedicated test bench at G2ELab.

Another research direction is represented by the ***control of renewable energy conversion systems***, which I continued to work on, also continuing to develop my well-established collaboration with G2ELab. Namely, topics related to ***operation optimization*** of *wind*, *photovoltaic* and *micro-hydro* systems, but also to their ***grid integration***, were approached in this context, which largely rely upon ***power electronic converter control***. In the framework of this collaboration, validations were primarily achieved on PHIL real-time benches. In addition, in the specific case of ***micro-hydro*** energy conversion systems, the effective assessment was advanced by tests on a ***real-world prototype***, involving complementary skills and control implementation know-how. This topic issued several journal articles durig this period.

In relation with control approaches, optimization approaches were also developed, aiming at ***optimizing the decision making process for smart grids evolving under uncertainties***. Energy-cluster-based modelling at different aggregation levels – *e.g.* of a building, a quarter or a region – as well as ***agent-based optimization*** were used to this end. Integration of electric vehicles into the grid (***V2G***) for ancillary service purposes was formulated and solved as an optimization problem. These issues were the core topic of **Smart Energy** research project granted by Grenoble Institute of Technology (Grenoble INP)) during 2012–2014, in which I co-supervised two six-month post-doctoral fellows, Salam HAJJAR and Julian FERNANDEZ, respectively.

A recent research interest is focused on the ***modelling of smart grids as cyber-physical systems***, for control purposes. In smart grids co-existence of the energy grid and the communication network is fundamental. Hence, ***modelling of interactions between the energy layer and the communication one*** is here a challenging issue, specific to smart grids, because of the need to conciliate in a certain manner – and ideally within a single model, if at all possible – two systems of different natures: the *continuous-time-driven* dynamics of the energy grid and the *discrete-event-driven* dynamics of the superposed communication network.

This has recently been identified as a challenging research topic in the academic Grenoble area and made the object of the 2016–2019 Ph.D. thesis of Ronak FEIZIMIRKHANI (defended in March 2020), co-supervised in collaboration with G2ELab, funded in the context of **CY-PHY-GRID** research project granted by **AGIR** (*Alpes Grenoble Innovation et Recherche*) funding scheme of Grenoble Alpes University. In this thesis ***ARMA models of GOOSE*** (Generic Object-Oriented Substation Event) ***traffic*** of the standard ***IEC 61850*** are developed. Also, ***estimation of maximum delay in smart grids with proprietary (known) architecture*** was validated on an intelligent substation test bench available at G2ELab. Results are useful for smart grid supervision operators.

1.3.3 Short overview of most significant five publications

- *Journal articles*

  1. A.I. Bratcu, I. Munteanu, S. Bacha, D. Picault, B. Raison (2011). Cascaded DC-DC converter photovoltaic systems: power optimization issues. *IEEE Transactions on Industrial Electronics*, 58(2), 403–411. – article in top 1% most highly cited between 2011 and 2015 in ISI Thomson Web of Science

This article is one of the first having proposed application of *Extremum Seeking Control* (ESC) to *photovoltaic* (PV) conversion systems. A novel energy conversion configuration is here also proposed, together with specific methods of harvesting the maximum power.

2. I. Munteanu, A.I. Bratcu (2015). MPPT for grid-connected photovoltaic systems using ripple-based extremum seeking control: analysis and control design issues. *Solar Energy*, 111, 30–42.

   This article presents a detailed systemic analysis of implementing the *Maximum Power Point Tracking* (MPPT) for PV systems by means of Extremum Seeking Control (ESC). This is an on-line optimum tracking, when this optimum moves in an *a priori* unknown manner as a consequence of solar irradiance variation. A *systematic ESC control design procedure* is proposed.

3. W. Nwesaty, A.I. Bratcu, O. Sename (2016). Power sources coordination through multivariable LPV/Hinf control with application to multi-source electric vehicles. *IET Control Theory and Applications*, 10(16), 2049–2059.

   In this article the problem of *coordinating several storage units, of different technologies*, which compose a multi-source system – *e.g.*, a microgrid containing batteries, supercapacitors and fuel cells – in a way such that to respect their *dynamic specialization* and thus to preserve at most their reliability and lifetime. This problem of dynamic (frequency) separation of sources' operation is approached in a well-posed formal framework, namely, that of *robust control for linear parameter-varying (LPV) systems*.

- *Books*

1. I. Munteanu, A.I. Bratcu, N.A. Cutululis, E. Ceangă (2008). *Optimal control of wind energy systems – Towards a global approach*. Advances in Industrial Control Series, Springer, London, U.K. ISBN 978-1-84800-079-7, 283 pages.

   In this monograph one of the most promising advanced control methods of wind energy conversion systems are detailed: optimal LQ control, sliding mode control, feedback linearizing control. Hardware-in-the-loop simulation (HILS) results obtained on dedicated test benches are discussed, which enhance the opportunity and pertinence of applying the proposed methods.

2. S. Bacha, I. Munteanu, A.I. Bratcu (2013). *Power Electronic Converters Modelling and Control – With Case Studies*. Advanced Textbooks in Control and Signal Processing Series, Springer, London, U.K. ISBN 978-1-4471-5478-5, 454 pages.

   This book is an *advanced textbook* targeting mainly a Ph.D.-student audience working with electrical energy conversion systems, where power electronic converters are indispensable. These converters exhibit strongly nonlinear dynamic behaviour, very fast and also hybrid dynamics, as well as parameter variance. Hence, they propose multiple challenges to control designers.

   This book is composed of *two parts* covering *twelve chapters* in total: a first part (first five chapters) dedicated to *analysis* (*modelling*) methods and a second part (next seven chapters) focused on the *synthesis* (*control design*), detailing both classical and advanced control methods for power converters. Representative case studies are presented from a pedagogical perspective. Problems with solution, as well as problems proposed for solving are provided at the end of each chapter.

   Some chapters of this book serve as support for the teaching unit "Power Electronics II – Modelling and control of power electronic converters" of the *Engineering of electrical energy* specialty at *École Nationale Supérieure de l'Eau, l'Énergie et l'Environnement* (ENSE^3 – Grenoble INP).

1.4 Supervision of doctoral and post-doctoral works

Publications issued within different supervised Ph.D. theses and post-doctoral works can be found in the list of scientific publications (Section 1.11). Names of the different supervised Ph.D. students and post-doctoral fellows appear in magenta in that list.

Table 1.1: Ph.D. students co-supervised at GIPSA-lab and the corresponding supervision shares.

	Ph.D. student	Time interval	Supervision share
1	Ronak FEIZIMIRKHANI	2016–2020	65%
2	Quang-Linh LAM	2014–2018	50%
3	Waleed NWESATY	2012–2015	75%
4	Adrian FLORESCU	2009–2012	25%

Table 1.1 offers an inverse-chronological-order synthetic view of the four Ph.D. theses I co-supervised since I have joined GIPSA-lab in 2011, at 215% aggregated supervision share. Next, the supervised doctoral and post-doctoral works are enumerated.

Defended Ph.D. theses

1. **Ronak FEIZIMIRKHANI** (Doctoral School in Electronics, Electrotechnics, Automatic Control and Signal Processing (*École Doctorale en Electronique, Electrotechnique, Automatique et Traitement du Signal* – EEATS); funding in the context of CY-PHY-GRID research project granted by AGIR (*Alpes Grenoble Innovation et Recherche*) funding scheme of Grenoble Alpes University, November 2016 – October 2019; **defended on March 4th 2020**), supervison share **65%**; supervisor Professor Yvon BÉSANGER (G2Elab)
   Modelling and analysis of smart grids as cyber-physical systems
   https://tel.archives-ouvertes.fr/tel-03285450/

   R. Feizimirkhani has had a two-year postdoctoral position (2020 – 2022) with the project *Analysis of delays in interoperable smart grids* (*Analyse des retarDs dans les smArt Grids InterOpérables* – ADAGIO), funded by Institut Carnot *Énergies du futur*. At the present, she is an R&D engineer with Atos in Grenoble, France.

2. **Quang-Linh LAM** (EEATS Doctoral School; funding by French Ministry, October 2014 – September 2017; **defended on January 17th 2018**), supervision share **50 %**; supervisor Professor Delphine RIU (G2ELab)
   Advanced control of microgrids for frequency and voltage stability: robust control co-design and real-time validation
   https://tel.archives-ouvertes.fr/tel-01836292/document

   At the present Q.-L. Lam works as an Assistant Lecturer – Researcher with Polytechnic School of Danang in Vietnam.

3. **Waleed NWESATY** (EEATS Doctoral School; funding by French Ministry, October 2012 – September 2015; **defended on October 22nd 2015**), supervision share **75%**; supervisor Professor Olivier SENAME (GIPSA-lab)
   LPV/$\mathcal{H}_\infty$ control design of on-board energy management systems for electric vehicles
   https://hal.archives-ouvertes.fr/tel-01237735/
   At the present, W. Nwesaty is a project leader of hardware/software electronic systems with Cémios, Rhône-Alpes Region, France.

4. **Adrian FLORESCU** (EEATS Doctoral School; funding by French Ministry, October 2009 – September 2012; **defended on November 19th 2012**), supervision share **25%**; supervisor Professor Seddik BACHA (G2ELab)
   Optimized energy flow management on board of electric vehicles
   https://tel.archives-ouvertes.fr/tel-00798937v1/document
   At the present, A. Florescu is an R&D engineer with Safran Electrical & Power, Ile-de-France, France.

Ph.D. theses co-supervised at "Dunărea de Jos" University of Galaţi (Romania)

Until 2013 in Romania only Full Professors could oficially supervise Ph.D. thesis. Co-supervision activity below is reported based on letters provided by the official supervisor.

1. **Iulian MUNTEANU** (2002 – 2006, funding by doctoral contract), supervision share **50%**; supervisor Prof. Emil CEANGĂ
   Contributions to the optimal control of wind energy conversion systems
   www.etc.ugal.ro/imunteanu/phd_disertation.pdf

I. Munteanu was an R&D engineer with GIPSA-lab, having worked between 2017 and 2020 on K-INF technology transfer project funded by the Technology Transfer Office (*Société d'Accélération du Transfert Technologique* – SATT) Linksium Grenoble Alpes.

2. **Adriana SCARLAT** (2009 – 2012, funding by doctoral contract), supervision share **30%**, namely between 2010 and 2011; supervisor Prof. Emil CEANGĂ
Advanced control of wind energy conversion systems
(in Romanian: *Sisteme avansate de conducere a proceselor de conversie a energiei eoliene*)
http://www.gup.ugal.ro/guppress/index.php/test/catalog/book/402
At the present, A. Scarlat Burlibaşa is an Associate Professor with the Department of Control Systems and Electrical Engineering at the Faculty of Control Systems, Computers, Electrical and Electronic Engineering of "Dunărea de Jos" University of Galaţi (Romania).

Post-doctoral fellows

1. **Ronak FEIZIMIRKHANI** (September 2020 – August 2022, funding in the context of *Analyse des retarDs dans des smArt Grids InterOpérables – ADAGIO* research project granted by Institut Carnot *Énergies du Futur*), supervision share **25 %**
Communication delay estimation in interoperable smart grids

   At the present, R. Feizimirkhani is an R&D engineer with Atos in Grenoble, France.

2. **Julian Alberto FERNANDEZ** (June – November 2014, funding in the context of *Smart Energy* research project granted by Grenoble Institute of Technology (Grenoble INP)), supervision share **50 %**
Decision optimization under uncertainty in smart grids – optimal grid integration of electric vehicles

   After having passed the period from 2016 until 2021 in the British Columbia region in Canada, while employed as a post-doctoral fellow with the University of Victoria, then as a research scientist with the Clean Energy Research Center and as a project manager with the University of British Columbia, J.A. Fernandez is now working as a senior consultant with WSP in Vancouver, Canada.

3. **Salam HAJJAR** (July – December 2014, funding in the context of *Smart Energy* research project granted by Grenoble INP), supervision share **50 %**
Decision optimization under uncertainty in smart grids by means of collaborative multi-agent stategies

   After having passed four years as an Assistant Professor at Marshall University / College of Electrical and Computer Engineering in Huntington, West Virginia, S. Hajjar is presently an Assistant Professor at West Virginia University, Beckley, West Virginia, U.S.A.

1.5 Technology transfer projects and industrial collaborations

1. **July – October 2020**: **Expertise report** for *Faiveley Transport (Wabtec Group)* (**12 000 Euros**), dealing with the design and implementation of a control solution for a Katium-power-converter-based Li-ion battery charger for railway applications.

2. **April 2017 – April 2018**: **Leader of technology pre-transfer project *K-INF***: *Embedded real-time PMS for multi-source electrical energy systems* (*Système embarqué de gestion temps réel des systèmes d'énergie multi-sources*) funded by Institut Carnot *Logiciels et Systèmes Intelligents* (LSI)
   – objective: technology readiness level (TRL) advancement of a robust coordination Power Management System (PMS) solution for multi-source electrical systems with application to electrical vehicles' on-board supply systems
   – technology transfer of the results obtained during W. Nwesaty's Ph.D. thesis (*LPV/$\mathcal{H}_\infty$ control design of on-board energy management systems for electric vehicles*), targeting a possible further funding by Linksium Grenoble Alpes Technology Transfer Office (TTO) (Société d'Accélération du Transfert Technologique – SATT)
   – duration: 12 months
   – budget: **72 000 Euros** (out of which one Senior R&D engineer)

3. **October 2018 – March 2020**: **Leader of technology transfer project *K-INF**: *Robust PMS for multi-source electrical energy systems* (*Gestionnaire d'énergie robuste embarqué des systèmes multi-sources*) funded by Linksium Grenoble Alpes TTO (pursuing the above-listed K-INF **technology pre-transfer project** in the use case of frequency regulation in microgrids with renewable energy sources and hybrid storage units)
   – technology transfer objective: either **licensing** to an existing enterprise, or **start-up** creation
   – duration: 18 months
   – budget: **183 561 Euros** (out of which one Senior R&D engineer)
   https://www.k-inf.fr
4. **October – December 2014**: **Expertise report** for *Schneider Electric* (**10 000 Euros**), dealing with an improved control solution of a kVA-rated three-phase generation system containing a storage unit (battery).

Participations at international technology exhibitions and fairs
Goal: showcasing K-INF technology and demonstrator.

1. 2018 *Global Industrie / Smart Industrie*, March 27–30 2018, Paris Nord Villepinte, France;
2. 2018 *European Utility Week*, November 6–8 2018, Vienna, Austria;
3. 2019 *European Utility Week / Initiate! Hub*, November 12–14 2019, Paris Expo Porte de Versailles, France;
4. 2020 *Forum 5i* (*I*nnovation – *I*ndustrie – *I*nclusion – *I*nvestissement – *I*nternational) / *Technological showcase*, September 29 2020, World Trade Center Grenoble, France
   https://www.pocmedia.fr/forum-5i-une-vitrine-pour-les-chercheurs-entrepreneurs/

1.6 Research management and related activities

Research projects

1. **2022 – 2023**: **Leader** of the exploratory research project
   Partial-derivative-model-based estimation of battery state of health parameters (**PaDeSoH**)
   funded by the national **IDEX** (*Investissements d'avenir*) programme (ANR-15-IDEX-02) through local **IRGA** (*Initiatives de Recherche à Grenoble Alpes*) funding scheme
   – comprising twelve-month post-doctoral fellow funding (**75 000 Euros**)
2. **2016 – 2019**: **Leader** of *Alpes Grenoble Innovation et Recherche* (**AGIR**) 2016 project, funded by Grenoble INP
   Modelling and analysis of smart grids as cyber-physical systems (**CY-PHY-GRID**)
   – comprising three-year Ph.D. thesis funding (Ronak FEIZIMIRKHANI) + 3 500 Euros accompanying funding
3. **June – November 2015**: **Leader of CNRS Exploratory Project**
   Modelling and analysis of smart grids as cyber-physical systems for decentralized control purpose (**CYBERGRID**)
   – partners: 2 research laboratories from Grenoble area: GIPSA-lab and G2ELab
   – budget: **11 000 Euros** (travel, master internships and small equipment)
   – results of this project allowed further collaboration funding within the framework of the above-listed 2016 AGIR project
   http://www.celluleenergie.cnrs.fr/2015-Appel-a-Projets-Exploratoires-de-la-Cellule-Energie-du-CNRS
4. **2013 – 2017**: **Member of ANR Progelec project** (42 months)
   Photovoltaic units integrated into electrical grids with distributed storage (*PhotovoltAïques integRés aux réseAux électriques avec stockages DIStribuEs* – **PARADISE**)
   – partners: 5 research laboratories and 3 SMEs as industrial partners
   – budget: **1 900 565 Euros** in total (out of which 758 480 Euros funded by ANR), out of which **167 725 Euros** for GIPSA-lab
   https://anr.fr/fr/projets-finances-et-impact/projets-finances/projet/funded/project/anr-13-prge-0007/?tx_anrprojects_funded%5Bcontroller%5D=Funded&cHash=21f68bca02f63561937f882bc23f4574
   http://www.gipsa-lab.fr/projet/PARADISE/accueil.html

5. **2012 – 2014**: **GIPSA-lab responsible** in the structuring project ***Smart Energy*** funded by Grenoble INP in the framework of *Support of Excellence and Innovation* (*Soutien à l'Excellence et à l'Innovation* – SEI) scheme
   – partners: 4 research laboratories from Grenoble area: Grenoble Electrical Engineering Laboratory (G2ELab), Sciences for Design, Optimization and Production Laboratory (Laboratoire des Sciences pour la Conception, l'Optimisation et la Production de Grenoble – G-SCOP), Grenoble Informatics Laboratory (Laboratoire d'Informatique de Grenoble – LIG), GIPSA-lab
   – funding of 2 six-month post-doctoral fellowships at GIPSA-lab (J.A. Fernandez and S. Hajjar)
   http://www.grenoble-inp.fr/grenoble-in-press/pour-une-gestion-intelligente-de-l-energie-567122.kjsp

Submitted applications

- **2022**: Participation to proposal writing of **Horizon Europe European Innovation Council (EIC) PathFinder Challenge project application**
  Supercapacitor and Battery Hybrid Energy Storage System for Improved Energy Storage – **SuperBESS**
  – topic HORIZON-EIC-2022-PATHFINDERCHALLENGES-01-02 (*Mid to long term and systems integrated energy storage*
  – call identifier HORIZON-EIC-2022-PATHFINDERCHALLENGES-01
  – project coordinators: Vasco da Gama Colab Energy Storage Associaçao (Portugal)
  – three-partner consortium: Vasco da Gama Colab / Portugal, Grenoble INP / France, SINTEF Energi AS / Norway

Participation to research projects applications

1. **2020**: Participation to proposal writing of **H2020 RIA (Research and Innovation Actions) European project application**
   STadium storAGE: Multi-use hybrid battery storage for application in nearly net zero energy football stadium – **STAGE**
   – topic LC-BAT-9-2020
   – call identifier H2020-LC-BAT-2019-2020 (*Building a Low-Carbon Climate-Resilient Future Next-Generation Batteries*)
   – project coordinators: Badenova Warmeplus GMBH & Co. KG, Franhofer Institute for Solar Energy Systems (Germany)
   – nine-partner consortium: 1 academic institution (Grenoble INP / France), 2 research institutes (Fraunhofer Institute / Germany, Austrian Institute of Technology / Austria), 2 large industrial groups (Badenova Warmeplus / Germany, ABB Power Grids S.p.a. / Italy), 4 SMEs (Skeleton Technologies / Estonia, Visblue Aps / Denmark, Fundacion Tekniker / Spain, R2M Solution / Spain)
   which was favourably evaluated (total score **13 out of 15** for three criteria: "Excellence" 4.5/5, "Impact" 3.5/5, "Quality and efficiency of the implementation" 5/5), but not funded within the given budgetary limits;
2. **2014**: Participation to proposal writing of **H2020 RIA European project application**
   Energy Optimal Design of 3-wheels Pedelec – **EO3BIKE**
   – topic GV-5-2014
   – call identifier H2020-GV-2014
   – project coordinator: Grenoble INP / GIPSA-lab (Prof. Olivier SENAME)
   – eleven-partner consortium: 3 academic institutions (Grenoble INP / France, Politecnico di Milano / Italy, Technische Universiteit Delft / The Netherlands), 2 local authorities (Isère County / France, Authority for Transport / Malta), 2 centers (European Center for Information and Communication Technologies / Germany, Centre de Ressources et d'Innovation Mobilité Handicap (CEREMH) / France), 4 SMEs (Soben / France, Zehus S.R.L. / Italy, EBL Gmbh / Germany, Klaxon Mobility S.R.L. / Italy)
   which was favourably evaluated (total score **12 out of 15** for three criteria: "Excellence", "Impact", "Quality and efficiency of the implementation"), but not funded within the given budgetary limits (first-ranked not funded application).

1.7 Initiated academic collaborations

1. September **2016**: Kick-off of a collaboration on control of modular multi-level power electronic converters (MMCs) with Prof. Remus TEODORESCU of Department of Energy Technology / Aalborg University / Denmark
   – article co-authoring
2. October **2015**: One-week visit at Department of Sustainable Electrical Energy / Delft University / The Netherlands, in the group of smart grids led by Prof. Peter PALENSKY, in the context of CYBERGRID Exploratory Project funded by the Energy Cell of CNRS
   – presentation of on-going work on modelling of energy–communication interactions in the smart grids
3. **2014 – 2015**: Kick-off of collaboration with Systems and Transportation Laboratory (Laboratoire Systèmes et Transports – SET) of University of Technology of Belfort-Montbéliard (UTBM) / France
   – coordinated control of multi-source electrical energy systems, with application to microgrids – in particular, on-board supply systems of electric vehicles
   – first goal: real-time validation of the at-that-time-on-going Ph.D. work of W. Nwesaty (*LPV/Hinf control design of on-board energy management systems for electric vehicles*) during April 2015
   – collaboration pursued with publication of an article in *IEEE Transactions on Control Systems Technology*

1.8 Evaluation activities

Ph.D. assessment committees

1. **2023** (date to be established): Quentin HILPERT – *Modélisation et détermination des stratégies de conditionnement de puissance pour des réseaux de puissance répartis pour des applications embarquées aéronautiques et spatiales* – supervised by Prof. Stéphane CAUX, Plasma and Energy Conversion Laboratory (LAPLACE – Laboratoire Plasma et Conversion d'Énergie) / Toulouse Institute of Technology (INPT), Toulouse, France. EDSYS (Systems) Doctoral School
   – member
2. December 15 **2022**: Lucas MOLINA BARROS – *Supervisory Control of Reconfigurable HVDC grids* – supervised by Prof. Laurent PIÉTRAC, SIGMA Clermont, and Assoc. Prof. Emil DUMITRESCU, Ampère Laboratory / INSA Lyon, France. ED160 (Electronics, Electrotechnics and Control) Doctoral School
   – member
3. November 25 **2022**: Grégoire LE GOFF – *Scalable Control Allocation Methods for the Modular Multilevel Converter from Modelling to Real Time Implementation* – supervised by Prof. Maurice FADEL, Plasma and Energy Conversion Laboratory (LAPLACE – Laboratoire Plasma et Conversion d'Énergie) / Toulouse Institute of Technology (INPT), Toulouse, France. GEETS (Electrical Engineering, Electronics, Telecommunications and Health) Doctoral School
   – member
4. January 29 **2021**: Yankai XING – *Control of direct current connections (HVDC) for the damping of inter-area oscillations* – supervised by Prof. Bogdan MARINESCU, Laboratory of Digital Sciences of Nantes (LS2N – Laboratoire des Sciences du Numérique de Nantes) / École Centrale Nantes, France. MATHSTIC (Mathematics and Information and Communications Science and Technology) Doctoral School
   – member
   https://www.ls2n.fr/event/soutenance-de-these-de-xing-yankai-equipe-dsg/
5. September 27 **2019**: Saber LAAMIRI – *Commande des systèmes électriques : machines synchrones et convertisseurs multi-niveaux* – supervised by Prof. Malek GHANES, Laboratory of Digital Sciences of Nantes (LS2N – Laboratoire des Sciences du Numérique de Nantes) / École Centrale Nantes, France. MATHSTIC Doctoral School (Mathematics and Information and Communications Science and Technology)
   – member
   https://www.ls2n.fr/event/soutenance-de-these-de-saber-laarimi-equipe-commande/

6. November 28 **2016**: Rasmus PEDERSEN – *Power Management and Voltage Control using Distributed Resources* – supervised by Prof. Rafael WISNIEWSKI and Assoc. Prof. Christoffer SLOTH, Aalborg University (Denmark) / Department of Electronic Systems
   – rapporteur
   http://www.aau.dk/arrangementer/vis/phd-defence-by-rasmus-pedersen---power-management-and-voltage-control-using-distributed-resources-.cid293919
7. August 23 **2016**: Lóránd BEDE – *Advanced and Robust Control of Grid Connected Converters* – supervised by Assoc. Prof. Tamas KEREKES and Prof. Remus TEODORESCU, Aalborg University (Denmark) / Department of Energy Technology
   – rapporteur
   http://www.en.tek-nat.aau.dk/news-events/show-event/phd-defence-by-lorand-bede-on-advanced-and-robust-grid-control-of-power-converters.cid260286

Peer-to-peer evaluation of research projects

1. **2019**: Scientific evaluation of a *Strategic Research Initiatives* (*Initiatives de Recherche Stratégique* – IRS) project, in the framework of *Excellence Initiatives* (IDEX) national funding schemes
2. **2014**: Scientific evaluation of an *ANR Young Researcher* (*Jeunes Chercheuses Jeunes Chercheurs* – JCJC), in the framework of 2014 ANR Call for Generic Proposals
3. **2014**: Scientific evaluation of an *Individual Research Grant*, The Israel Science Foundation (ISF)
4. **2012**: Member of the *European Working Group on Electricity Grids*: Exercise Defining a SET-Plan European Energy Education and Training Initiative
   – objective: drafting recommandations in order to improve the European educational offer in electrical grids

Peer-to-peer review

Reviewer of:
– approx. 4–5 journal submissions per year: *IEEE Transactions on Control Systems Technology*, *IEEE Transactions on Industrial Electronics*, *IEEE Transactions on Vehicular Technology*, *IET Renewable Power Generation*, *ISA Transactions*, *etc.*;
– approx. 2–3 conference submissions per year: *American Control Conference* (ACC), *Mediterranean Conference on Control and Automation* (MED), *IFAC World Congresses* and *IFAC Symposiums/Conferences/Workshops*, *etc.*

1.9 Impact and recognition

On a **national** level, I am member of:

- CNU (*Conseil National des Universités*): substitute member starting from 2020, Section 61 (*Control systems, informatics and signal processing*);
- *Modelling and Control of Dynamic Systems* (GdR MACS) – more specifically, *Electrical Systems Control* (CSE) and *Intelligent Grids and Electrical Systems* (RSEI) workgroups
  http://gdr-macs.cnrs.fr/membres/antoneta-iuliana-bratcu;
- *Club of Teachers and Researchers in Electronics, Electrotechnics and Control Systems* (Club des Enseignants et des Chercheurs en Electronique, Electrotechnique et Automatique – Club EEA).

Table 1.2: Citations' number and Hirsch indices in mostly used scientometric databases (December 2022).

	Web of Science	**Scopus**	**Google Scholar**
Total citations	1267	1601	4024
Self-citations excluded	1201	1505	
h-index	14	17	24
(without self-citations)	(14)	(16)	

In terms of **international** recognition, I can mention:

- membership of IFAC Technical Committee 6.3 Power and Energy Systems (since 2017)
  https://tc.ifac-control.org/6/3/members;
- IPC member of *11th IFAC Symposium on Control of Power and Energy Systems* – CPES 2022
  https://cpes2021.com/en/commitees;
- member of *Control Systems* Technical Track Program Committee at the 32nd *IEEE International Symposium on Industrial Electronics* – ISIE 2023

https://2023.ieee-isie.org/technical-technical_tracks/tt-06-control-systems/;

- Technical Associate Editor at *2023 IFAC World Congress*
  https://www.ifac2023.org/about/pc/
- elevation to the IEEE Senior Member grade in 2018;
- IPC member of *International Conference on System Theory, Control and Computing* – ICSTCC
  https://icstcc.ugal.ro/2022/index.php/committees/international-program-committee

Table 1.2 gives a synthetic view of my publications' impact in terms of number of citations and scientometric Hirsch indices. Other information about my scientific performance can be found at:
https://exaly.com/author/5703917/antoneta-iuliana-bratcu/rankings

1.10 Scientific publications 1996–2001

- *During the Ph.D. thesis*

  My Ph.D. thesis, ***Systematic determination of precedence graphs and assembly line balancing*** (in French: *Détermination systématique des graphes de précédence et équilibrage des lignes d'assemblage*), defended in July 2001 at Université de Franche-Comté, Besançon, France, is a contribution to a global approach of rational design of assembly systems, organized into two main parts.

  https://tel.archives-ouvertes.fr/tel-00258992

  More precisely, its first part is dedicated to the generation of precedence graphs to be used in assembly line balancing. The existence of a *structural property* – called property Π – is proved to be *necessary and sufficient to ensure the equivalence between a set of assembly sequences and a single precedence graph*. Based upon this property, two algorithms are proposed for systematic generation of precedence graphs.

  The second part is dedicated to the analysis of *self-balancing assembly systems*, whose design avoids solving an assembly line balancing classical problem. It is sufficient that such systems satisfy a simple technological constraint of placing the (human) operators on the line – from slowest to fastest – for spontaneously obtaining the optimal balancing. The sufficient condition for self-balancing – the "well-ordering" – is proved using stability criteria of discrete-time dynamical systems.

  This thesis issued the publications listed below.

  Book chapters

  1. J.M. Henrioud, A. Bratcu (1999). Algorithm for generating the precedence graphs in assembly systems. In: *Software and Hardware Engineering for the 21st Century* (Ed. Nikos E. Mastorakis), pp. 44–49. World Scientific Engineering Society Press. ISBN 960-8052-06-8.
  2. V. Mînzu, A. Bratcu (1999). Precedence graphs generation using assembly sequences. In: *Software and Hardware Engineering for the 21st Century* (Ed. Nikos E. Mastorakis), pp. 122–127. World Scientific Engineering Society Press. ISBN 960-8052-06-8.

  Articles in international journals without impact factor

  1. A. Bratcu, V. Mînzu (2001). Self-balancing manufacturing systems regarded as hybrid dynamical systems. *Control Engineering and Applied Informatics* – Romanian Society of Control Engineering and Technical Informatics (SRAIT), 3(3), 11–16.
  2. V. Mînzu, A. Bratcu (2000). Some results on the modelling of TSS manufacturing lines. *Annals of "Dunărea de Jos" University of Galaţi*, III (*Electrotechnics, Electronics, Automatic Control, Informatics*), 40–47. http://www.ann.ugal.ro/eeai/index.html.
  3. V. Mînzu, D. Cernega, A. Bratcu (1998). A stochastic algorithm for treating the precedence constraints in discrete optimization problems. *Annals of "Dunărea de Jos" University of Galaţi*, III, 46–51. http://www.ann.ugal.ro/eeai/index.html.

  Articles in proceedings of IFAC and IEEE conferences

  1. A. Bratcu, V. Mînzu (2001). Modelling and analysis of self-balancing manufacturing lines as hybrid dynamic systems. In: *Procs. of the 9th IFAC Symposium on Large Scale Systems: Theory & Applications – LSS 2001*, Bucharest, Romania, July 18–20 2001, pp. 37–42.

2. A. Bratcu, J.-M. Henrioud, V. Mînzu (2001). A look at self-balancing manufacturing lines through theory of hybrid dynamical systems. In: *Procs. of the 2001 IEEE International Symposium on Assembly and Task Planning – ISATP 2001*, Fukuoka, Japan, May 28–29 2001, pp. 375–380.
3. A. Bratcu, V. Mînzu (1999). A simulation study of self-balancing production lines. In: *Procs. of the 1999 IEEE International Conference on Intelligent Engineering Systems – INES 1999*, Stará Lesná, Slovakia, November 1–3 1999, pp. 165–170.
4. V. Mînzu, A. Bratcu, J.-M. Henrioud (1999). Construction of the precedence graphs equivalent to a given set of assembly sequences. In: *Procs. of the IEEE International Symposium on Assembly and Task Planning – ISATP 1999*, Porto, Portugal, July 21–24 1999, pp. 14–19.

Articles in proceedings of other international conferences

1. A. Bratcu (1999). Nonlinear modelling of a self-balancing production line. In: *Procs. of the 11th European Simulation Symposium – ESS 1999*, Erlangen, Germany, October 26–28 1999, pp. 481–483.
2. A. Bratcu, V. Mînzu, J.-M. Henrioud (1999). Equivalence between a given set of assembly sequences and a set of precedence graphs. In: *Procs. of the 12th International Conference on Control Systems and Computer Science – CSCS 12*, Bucharest, Romania, May 26–28 1999, pp. 295–300.

- *Other collaborations* during the same period issued the following publications:

Articles in international journals without impact factor

1. A. Bratcu, I. Bivol (1996). A control algorithm for an asynchronous machine imposing speed evolution. *Annals of "Dunărea de Jos" University of Galaţi*, III, 23–27. http://www.ann.ugal.ro/eeai/index.html.

Articles in proceedings of IFAC conferences

1. D. Cernega, A. Bratcu (1998). Design of a discrete event based supervisor for continuous processes. In: *Procs. of the 8th IFAC/IFORS/IMACS/IFIP Symposium on Large Scale Systems: Theory & Applications – LSS 1998*, Patras, Greece, July 15–17 1998, pp. 59–64.
2. C. Tudorie, V. Ariton, A. Bratcu (1998). Knowledge-based decision and conversation in a hybrid diagnosis system. In: *Procs. of the 8th IFAC/IFORS/IMACS/IFIP Symposium on Large Scale Systems: Theory & Applications – LSS 1998*, Patras, Greece, July 15–17 1998, pp. 51–54.

1.11 Scientific publications 2002–2022

Names of the different supervised Ph.D. students and post-doctoral fellows, as well as Master students, appear in magenta in the list below.

Books

1. S. Bacha, I. Munteanu, A.I. Bratcu (2013). *Power Electronic Converters Modelling and Control – With Case Studies*. Advanced Textbooks in Control and Signal Processing Series, Springer, London,U.K. ISBN 978-1-4471-5478-5, 454 pages.
2. I. Munteanu, A.I. Bratcu, N.A. Cutululis, E. Ceangă (2008). *Optimal control of wind energy systems – Towards a global approach*. Advances in Industrial Control Series, Springer, London, U.K. ISBN 978-1-84800-079-7, 283 pages.
3. A.I. Bratcu, A. Filipescu (2004). *Numerical methods used in analysis of dynamical systems* (in Romanian: *Metode numerice utilizate în analiza sistemelor – aplicaţii*). MatrixRom, Bucharest, Romania. ISBN 973-685-828-6, 142 pages.
4. E. Ceangă, I. Munteanu, A. Bratcu, M. Culea (2001). *Signals, circuits and systems. 1st Part: Signal analysis* (in Romanian: *Semnale, circuite şi sisteme. Partea I: Analiza semnalelor*). Academica, Galaţi, Romania. ISBN 973-8316-16-2, 201 pages.

Book chapters

1. I. Munteanu, A.I. Bratcu, E. Ceangă (2013). Low-power wind energy conversion systems: generation configurations and control objectives. In: *Handbook of Wind Power Systems* (Eds. P. Pardalos *et al.*), pp. 773–803. Springer, London, U.K. ISBN 978-3-642-41080-2.

2. I. Munteanu, A.I. Bratcu, S. Bacha, D. Roye (2010). Real-time physical simulation of wind energy conversion systems. In: *Wind Power* (Ed. S.M. Muyeen), pp. 233–258. IN-TECH. ISBN 978-953-7619-81-7.
3. S. Belmokhtar, A.I. Bratcu, A. Dolgui (2006). Modular machining line design and reconfiguration: some optimization methods. In: *Manufacturing the Future: Concepts-Technologies-Visions* (Eds. V. Kordic, A. Lazinica, M. Merdan), ch. 5 (pp. 125–152). pro literatur Verlag, Mammendorf, Germany. ISBN 3-86611-198-3.
4. D.C. Cernega, A.I. Bratcu, A. Şerbencu (2005). Discrete event supervision for communication protocol conversion. In: *Intelligent Systems at the Service of Mankind II* (Eds. W. Elmenreich, J. Tenreiro Machado, I. J. Rudas), pp. 227–238. UBooks Verlag, Augsburg, Germany. ISBN 3-86608-052-2.

International patents

1. A.M. Andreica, S. Bacha, A.I. Bratcu, J. Guiraud, I. Munteanu, D. Roye (Grenoble Institute of Technology, Electricité de France) (2009). *Hydraulic turbomachine for recovering and converting kinetic energy of water currents into electricity, has regulation units electrically regulating power from generator to ensure that shaft rotates at same speed relative to another shaft.* Patent WO2010020735-A1, FR2935159-A1.

APP (Agence pour la Protection des Programmes – Software Protection Agency) software and know-how patent applications – ***alphabetical order*** of authors

1. A.I. Bratcu, I. Munteanu, J.-M.W. Nwesaty, O. Sename (2018). *K-INF Multi-source management system robust design.* Grenoble Institute of Technology, Grenoble Alpes University. *APP software application*, RT2018013, version 1.1 May 2018.
2. A.I. Bratcu, I. Munteanu (2019). *K-INF Multi-storage energy management system robust design for frequency regulation in AC microgrids.* Grenoble Institute of Technology, CNRS, Grenoble Alpes University. *APP software application.*
3. A.I. Bratcu, I. Munteanu (2020). *Design procedure of a robust multi-storage energy management for frequency regulation in AC microgrids.* Grenoble Institute of Technology, CNRS, Grenoble Alpes University. *Know-how patent application.*

Articles in international journals with impact factor

1. Q-L. Lam, D. Riu, A.I. Bratcu, A. Labonne, C. Boudinet (2022). Power hardware-in-the-loop validation of primary frequency robust control in stand-alone microgrids with storage units. *Electrical Engineering* (Springer). To appear, DOI: 10.1007/s00202-022-01666-6.
2. R. Feizimirkhani, A.I. Bratcu, Y. Bésanger, A. Labonne, T. Braconnier (2021). A methodology for the evaluation of the message transmission delay over IEC 61850 communication network – a real-time HV/MV substation case study. *Sustainable Energy, Grids and Networks*, 28, art. no. 100555.
3. Q-L. Lam, A.I. Bratcu, D. Riu (2021). Multi-variable $\mathcal{H}_\infty$ control approach for voltage ancillary service in autonomous microgrids : design and sensitivity analysis. *IEEE Access*, 9, 140212–140234.
4. J.-M.W. Nwesaty, A.I. Bratcu, A. Ravey, D. Bouquain, O. Sename (2020). Robust energy management system for multi-source DC energy systems – real-time setup and validation. *IEEE Transactions on Control Systems Technology*, 28(6), 2591–2599.
5. Q.L. Lam, A.I. Bratcu, C. Boudinet, M. Thomas, A. Labonne, D. Riu (2020). Primary frequency $\mathcal{H}_\infty$ control in stand-alone microgrids with storage units: a robustness analysis confirmed by real-time experiments. *International Journal of Electrical Power and Energy Systems*, 115, art. no. 105507.
6. M. Hauck, A. Rumeau, A.I. Bratcu, S. Bacha, I. Munteanu, D. Roye (2018). Identification and control of a river-current-turbine generator – application to a full-scale prototype. *IEEE Transactions on Sustainable Energy*, 9(3), 1365–1374.
7. W. Nwesaty, A.I. Bratcu, O. Sename (2016). Power sources coordination through multivariable LPV/$\mathcal{H}_\infty$ control with application to multi-source electric vehicles. *IET Control Theory and Applications*, 10(16), 2049–2059.

8. A. Florescu, A.I. Bratcu, I. Munteanu, A. Rumeau, S. Bacha (2015). LQG optimal control applied to on-board energy management system of all-electric vehicles. *IEEE Transactions on Control Systems Technology*, 23(4), 1427–1439.
9. A. Florescu, S. Bacha, I. Munteanu, A.I. Bratcu, A. Rumeau (2015). Adaptive frequency-separation-based energy management system for electric vehicles. *Journal of Power Sources*, 280, 410–421.
10. I. Munteanu, A.I. Bratcu (2015). MPPT for grid-connected photovoltaic systems using ripple-based extremum seeking control: analysis and control design issues. *Solar Energy*, 111, 30–42.
11. A. Burlibaşa, I. Munteanu, A.I. Bratcu (2014). Unitary power control strategy for low-power wind energy conversion system using active speed stall control for full-load regime. *IET Renewable Power Generation*, 8(6), 696–706.
12. C. Vlad, A.I. Bratcu, I. Munteanu, S. Epure (2014). Real-time replication of a stand-alone wind energy conversion system: error analysis. *International Journal of Electrical Power and Energy Systems*, 55, 562–571.
13. O. Crăciun, A. Florescu, I. Munteanu, A.I. Bratcu, S. Bacha, D. Radu (2014). Hardware-in-the-loop simulation applied to protection devices testing. *International Journal of Electrical Power and Energy Systems*, 54, 55–64.
14. A. Burlibaşa, I. Munteanu, A.I. Bratcu (2012). Control law design of a low-power wind energy system using active speed stall techniques. *Control Engineering and Applied Informatics* – Romanian Society of Control Engineering and Technical Informatics (SRAIT), 14(3), 15–24.
15. M. Vallet, I. Munteanu, A.I. Bratcu, S. Bacha, D. Roye (2012). Synchronized control of cross-flow-water-turbine-based twin towers. *Renewable Energy*, 48, 382–391.
16. M. Andreica Vallet, S. Bacha, I. Munteanu, A.I. Bratcu, D. Roye (2011). Management and control of operating regimes of cross-flow water turbines. *IEEE Transactions on Industrial Electronics*, 58(5), 1866–1876.
17. M. Hauck, I. Munteanu, A.I. Bratcu, S. Bacha, D. Roye (2011). Operation of grid-connected cross-flow water turbines in the stall region by direct power control. *IEEE Transactions on Industrial Electronics*, 58(4), 1132–1140.
18. A.I. Bratcu, I. Munteanu, S. Bacha, D. Picault, B. Raison (2011). Cascaded DC-DC converter photovoltaic systems: power optimization issues. *IEEE Transactions on Industrial Electronics*, 58(2), 403–411.
19. I. Munteanu, A.I. Bratcu, M. Andreica, S. Bacha, D. Roye, J. Guiraud (2010). A new method of real-time physical simulation of prime movers used in energy conversion chain. *Simulation Modelling Practice and Theory*, 18(9), 1342–1354.
20. I. Munteanu, A.I. Bratcu, S. Bacha, D. Roye, J. Guiraud (2010). Hardware-in-the-loop-based simulator for a class of variable-speed wind energy conversion systems: design and performance assessment. *IEEE Transactions on Energy Conversion*, 25(2), 564–576.
21. C. Vlad, I. Munteanu, A.I. Bratcu, E. Ceangă (2010). Output power maximization of low-power wind energy conversion systems revisited: possible control solutions. *Energy Conversion and Management*, 51(2), 305–310.
22. C. Vlad, I. Munteanu, A.I. Bratcu, E. Ceangă (2009). Anticipative control of low-power wind energy conversion systems for optimal power regime. *Control Engineering and Applied Informatics* – Romanian Society of Control Engineering and Technical Informatics (SRAIT), 11(4), 26–35.
23. I. Munteanu, A.I. Bratcu, E. Ceangă (2009). Wind turbulence used as searching signal for MPPT in variable-speed wind energy conversion systems. *Renewable Energy*, 34(1), 322–327.
24. A.I. Bratcu, A. Dolgui (2009). Some new perspectives in the analysis and simulation of bucket brigades (self-balancing production lines). *International Journal of Production Research*, Special Issue *Cutting Edge of French Community of Production Research*, 47(2), 369–387.
25. A.I. Bratcu, I. Munteanu, S. Bacha, B. Raison (2008). Maximum power point tracking of grid-connected photovoltaic arrays by using extremum seeking control. *Control Engineering and Applied Informatics* – Romanian Society of Control Engineering and Technical Informatics (SRAIT), 10(4), 3–12.

26. I. Munteanu, S. Bacha, A.I. Bratcu, J. Guiraud, D. Roye (2008). Energy-reliability optimization of wind energy conversion systems by sliding mode control. *IEEE Transactions on Energy Conversion*, 23(3), 975–985.
27. I. Munteanu, N.A. Cutululis, A.I. Bratcu, E. Ceangă (2005). Optimization of variable speed wind power systems based on a LQG approach. *Control Engineering Practice*, 13(7), 903–912.
28. A.I. Bratcu, A. Dolgui (2005). A survey of the self-balancing production lines ("bucket brigades"). *Journal of Intelligent Manufacturing*, 16(2), 139–158.
29. B. Rekiek, A. Dolgui, A. Delchambre, A. Bratcu (2002). State of art of optimization methods for assembly line design. *Annual Reviews in Control*, 26(2), 163–174.

Under-review submissions

- Q-L. Lam, D. Riu, A.I. Bratcu (2022). Frequency Robust Control Application in Islanded Microgrids Considering Parametric Uncertainties and Distinct Photovoltaic Penetration Rate Scenarios. Submitted to *Iranian Journal of Science and Technology – Transactions of Electrical Engineering* (Springer).

Articles in international journals without impact factor

1. S. Hajjar, A.I. Bratcu, A. Hably (2015). A day-ahead centralized unit commitment algorithm for a multi-agent smart grid. *Annals of Computer Science and Information Systems* – Polish Information Processing Society, 6, 265–271, on-line: http://dx.doi.org/10.15439/2015F227.
2. A. Scarlat, I. Munteanu, A.I. Bratcu, E. Ceangă (2010). Use of a configurable torque-speed dependence for power maximization of squirrel-cage-induction-generator-based wind energy conversion system. *Bulletin of the Polytechnic Institute of Iaşi – Automatic Control and Computer Science Section*, LVI(LX)(4), 41–60.
3. C. Vlad, I. Munteanu, A.I. Bratcu, E. Ceangă (2008). Optimal control in energy conversion of small wind power systems with permanent-magnet synchronous generators. *WSEAS Transactions on Systems and Control*, 3(7), 644–653.
4. I. Munteanu, S. Bacha, A.I. Bratcu, J. Guiraud, D. Roye (2007). Conception systématique des simulateurs temps réel hardware-in-the-loop – Application aux systèmes de conversion éolienne. *Journal Européen des Systèmes Automatisés* – Hermès-Lavoisier, 41(9-10), 1139–1164.
5. A.I. Bratcu, A. Dolgui (2007). Une généralisation du Modèle Normatif des lignes auto-équilibrées (« bucket brigades »). *Journal Européen des Systèmes Automatisés* – Hermès-Lavoisier, 41(3-4), 287–309.
6. I. Munteanu, N.A. Cutululis, A. Bratcu, E. Ceangă (2006). Using a nonlinear controller to optimize a variable speed wind power system. *Journal of Electrical Engineering*, 6(4), on-line: http://www.jee.ro/index.php/jee/article/view/WW1151314467W449faa23f2738.

Articles in proceedings of IFAC and IEEE conferences
IFAC

1. R. Ghassani, A.I. Bratcu, R. Teodorescu (2022). Genetic algorithm applied to state-feedback control design of grid and circulating current in modular multilevel converters. In: *Procs. of the 11th IFAC Symposium on Control of Power and Energy Systems – CPES 2022*, virtual, June 21–23 2022.
2. A.I. Bratcu, R. Teodorescu (2020). State-feedback control of grid and circulating current in modular multilevel converters. In: *Procs. of the 21st IFAC World Congress*, Berlin, Germany, July 12–17 2020. IFAC-PapersOnLine, 53(2), 12396–12401.
3. R. Feizimirkhani, A.I. Bratcu, Y. Bésanger (2018). Time-series modelling of IEC 61850 GOOSE communication traffic between IEDs in smart grids – a parametric analysis. In: *Procs. of the 10th IFAC Symposium on Control of Power and Energy Systems – CPES 2018*, Tokyo, Japan, September 4–6 2018. IFAC-PapersOnLine, 51(28), 444–449.

4. Q.L. Lam, A.I. Bratcu, D. Riu (2016). Robustness analysis of primary frequency H-inf control in standalone microgrids with storage units. In: *Procs. of the 2016 IFAC Workshop on Control of Transmission and Distribution Smart Grids – CTDSG 2016*, Prague, Czech Republic, October 11–13 2016. IFAC-PapersOnLine, 49(27), 123–128.
5. W. Nwesaty, A.I. Bratcu, O. Sename (2015). Reduced-order LPV controller for coordination of power sources within multi-source energy systems. In: *Procs. of the 8th IFAC Symposium on Robust Control Design – ROCOND 2015*, Bratislava, Slovakia, July 8–11 2015. IFAC-PapersOnLine, 48(14), 132–137.
6. W. Nwesaty, A.I. Bratcu, O. Sename (2014). MIMO Hinf control for power source coordination – application to energy management systems of electric vehicles. In: *Procs. of 19th IFAC World Congress 2014*, Cape Town, South Africa, August 2014, pp. 3905–3911.
7. A. Florescu, A.I. Bratcu, I. Munteanu, S. Bacha (2012). Energy management system within electric vehicles using ultracapacitors: an LQG-optimal-control-based solution. In: *Procs. of the 15th IFAC Workshop on Control Applications of Optimization – CAO 2012*, Rimini, Italy, September 2012, pp. 229–234.
8. A.I. Bratcu, D.C. Cernega, I. Munteanu (2006). Supervisory control of grid connected wind power systems to guarantee safe operation. In: *Procs. of the 3rd IFAC Workshop on Discrete-Event System Design – DESDes 2006*, Rydzyna, Poland, September 26-28 2006, pp. 117–122.
9. I. Munteanu, A.I. Bratcu, N.A. Cutululis, E. Ceangă (2005). A two loop optimal control of flexible drive train variable speed wind power systems. In: *IFAC Proceedings Volumes – Procs. of the 16th Triennial IFAC World Congress*, 38(1), 344–349.
10. A.I. Bratcu, D. Dulman, I. Munteanu, A. Dolgui (2004). Optimal motion planning of cooperative mobile robots in 2D environments. In: *Procs. of the 3rd IFAC Conference on Management and Control of Production and Logistics – MCPL 2004*, Santiago, Chile, November 3–5 2004, pp. 223–228.
11. I. Munteanu, A.I. Bratcu, L. Frangu (2004). Nonlinear control for stationary optimization of wind power systems. In: *Procs. of the IFAC Workshop on Automatic Systems for Building the Infrastructure in the Developing Countries – DECOM-TT 2004*, Bansko, Bulgaria, October 3–5 2004, pp. 195–200.
12. A.I. Bratcu, A. Dolgui (2003). Synergy, Collaboration and Self-Balancing in Production Systems – The Bucket Brigades. In: *Procs. of the IFAC Workshop Intelligent Assembly and Disassembly – IAD 2003*, Bucharest, Romania, October 9–11 2003, pp. 78–83.
13. I. Munteanu, E. Ceangă, N.A. Cutululis, A. Bratcu (2003). Linear quadratic optimization of variable speed wind power systems. In: *Procs. of the IFAC Workshop on Control Application of Optimisation – CAO 2003*, Visegrad, Hungary, June 30 – July 2 2003, pp. 162–167.
14. B. Rekiek, A. Delchambre, A. Dolgui, A. Bratcu (2002). Assembly line design: a survey. In: *Plenary Papers, Survey Papers and Milestones of the 15th Triennial IFAC World Congress*, Barcelona, Spain, July 21–26 2002, pp. 131–142.
15. A. Bratcu (2002). On the modelling of bucket brigades. In: *IFAC Proceedings Volumes – Procs. of the 15th Triennial IFAC World Congress*, 35, 97–102.

Under-review submissions

- I. Munteanu, A.I. Bratcu (2022). HILS-based demonstrator for real-time validation of robust control strategies: an electric vehicle application case. Submitted to *2023 IFAC World Congress*, Yokohama, Japan.

IEEE

1. R. Feizimirkhani, V.H. Nguyen, Y. Bésanger, Q.T. Tran, A.I. Bratcu, A. Labonne, T. Braconnier (2021). Application of Long Short-Term Memory (LSTM) neural network for the estimation of communication network delay in smart grid applications. In: *Procs. of 2021 IEEE International Conference on Environment and Electrical Engineering and 2021 IEEE Industrial and Commercial Power Systems Europe – EEEIC/I&CPS Europe 2021*, Bari, Italy, September 7–10 2021, pp. 1–6.

2. A.I. Bratcu, F. Ihuel, A. Contrepois (2021). Two-level state-space-based control strategy of Katium-power-converter-based Li-ion battery charger for railway applications. In: *Procs. of the 23rd European Conference on Power Electronics and Applications – EPE ECCE 2021*, Ghent, Belgium, September 6–10 2021, pp. 1–9.
3. A.I. Bratcu, F. Ihuel, A. Contrepois (2021). Katium-power-converter-based Li-ion battery charger for railway applications: control-oriented modelling. In: *Procs. of the 2021 IEEE Conference on Control Technology and Applications – IEEE CCTA 2021*, San Diego, California, U.S.A., August 9–11 2021, pp. 583–588.
4. M. Almeida Barbosa, K. Gül, A.I. Bratcu, I. Munteanu (2019). Management of a photovoltaic-battery-based microgrid in a prosumer context. In: *Procs. of the 6th International Symposium on Electrical and Electronics Engineering – ISEEE 2019*, Galaţi, Romania, October 18–20 2019, pp. 1–6.
5. R. Feizimirkhani, A.I. Bratcu, Y. Bésanger, A. Labonne, T. Braconnier (2019). Modeling of IEC 61850 GOOSE substation communication traffic using ARMA model. In: *Procs. of the 2019 IEEE PES Innovative Smart Grid Technologies – ISGT-Europe 2019*, Bucharest, Romania, September 29 – October 2 2019, pp. 1–5.
6. R. Rezvani, A.I. Bratcu. Robust control of a single-ended primary-inductor converter (SEPIC) (2017). In: *Procs. of the 5th International Symposium on Electrical and Electronics Engineering – ISEEE 2017*, Galaţi, Romania, October 20–22 2017, pp. 1–6.
7. T. Peirelinck, A.I. Bratcu, Y. Bésanger (2016). Impact of IEC 61850 GOOSE communication quality on decentralized reactive power control in smart distribution grids – a co-simulation study. In: *Procs. of the 2016 IEEE Electrical Power and Energy Conference – EPEC 2016*, Ottawa, Canada, October 12–14 2016, pp. 1–6.
8. Q.L. Lam, A.I. Bratcu, D. Riu (2016). Systematic multi-variable H-infinity control design for primary frequency regulation in stand-alone microgrids with high penetration of renewable energy sources. In: *Procs. of the 15th European Control Conference – ECC 2016*, Aalborg, Denmark, June 29 – July 1st 2016, pp. 1794–1799.
9. E. Sharma, A.I. Bratcu, C. Chiculiţă, Y. Bésanger (2015). Co-simulation of a low-voltage utility grid controlled over IEC 61850 protocol. In: *Procs. of the IEEE 5th International Conference on Electric Utility Deregulation and Restructuring and Power Technologies – DRPT 2015*, Changsha, China, November 26–29 2015, pp. 2365–2372.
10. A.I. Bratcu, V. Aulagnier (2015). Control of energy storage systems for three-phase applications. In: *Procs. of the 19th International Conference on System Theory, Control and Computing – ICSTCC 2015*, Cheile Grădiştei – Fundata Resort, Romania, October 14–16 2015, pp. 666–672.
11. J.A. Fernandez, A. Hably, A.I. Bratcu (2015). Assessing the economic profit of a vehicle-to-grid strategy for current unbalance minimization. In: *Procs. of 2015 IEEE International Conference on Industrial Technology – ICIT 2015*, Seville, Spain, March 17–19 2015, pp. 2628–2635.
12. Q.-L. Lam, D. Riu, A.I. Bratcu, J. Mongkoltanatas (2015). Multi-variable H-infinity robust control applied to primary frequency regulation in micro-grids with large integration of photovoltaic energy source. In: *Procs. of the 2015 IEEE International Conference on Industrial Technology – ICIT 2015*, Seville, Spain, March 17–19 2015, pp. 2921–2928.
13. W. Nwesaty, A.I. Bratcu, O. Sename (2014). Optimal frequency separation of power sources by multivariable LPV/$\mathcal{H}_\infty$ control: application to on-board energy management systems of electric vehicles. In: *Procs. of 2014 IEEE 53rd Annual Conference on Decision and Control – CDC 2014*, Los Angeles, California, U.S.A., December 15–17 2014, pp. 5636–5641.
14. W. Nwesaty, A.I. Bratcu, O. Sename (2014). LPV control for power source coordination – application to electric vehicles energy management systems. In: *Procs. of the 13th European Control Conference – ECC 2014*, Strasbourg, France, June 25–27 2014, pp. 2649–2654.

15. A. Florescu, S. Bacha, A. Rumeau, I. Munteanu, A.I. Bratcu (2013). PHIL simulation for validating power management strategies in all-electric vehicles. In: *Procs. of the 15th European Conference on Power Electronics and Applications – EPE 2013-ECCE Europe*, Lille, France, September 2–6 2013, pp. 1–6.
16. W. Nwesaty, A.I. Bratcu, A. Hably (2013). Extremum seeking control techniques applied to photovoltaic systems with multimodal power curves. In: *Procs. of International Conference on Renewable Energy Research and Applications – ICRERA 2013*, Madrid, Spain, October 20–23 2013, pp. 85–90.
17. M. Hauck, A. Rumeau, I. Munteanu, A.I. Bratcu, S. Bacha, D. Roye, A. Hably (2012). A 1:1 prototype of power generation system based upon cross-flow water turbines. In: *Procs. of the IEEE International Symposium on Industrial Electronics 2012 – ISIE 2012*, Hangzhou, China, May 28–31 2012, pp. 1414–1418.
18. A. Florescu, S. Bacha, I. Munteanu, A.I. Bratcu, A. Rumeau (2012). Results concerning ultracapacitor-based energy management strategy within electric vehicle. In: *Procs. of the 16th International Conference on System Theory, Control and Computing – ICSTCC 2012*, Sinaia, Romania, October 12–14 2012, pp. 1–7.
19. A. Florescu, S. Bacha, I. Munteanu, A.I. Bratcu (2012). Frequency-separation-based energy management control strategy of power flows within electric vehicles using ultracapacitors. In: *Procs. of the 38th Annual Conference of IEEE Industrial Electronics Society – IECON 2012*, Montreal, Canada, October 25–28 2012, pp. 2957–2964.
20. O. Crăciun, A. Florescu, I. Munteanu, S. Bacha, A.I. Bratcu, D. Radu (2011). Protection devices testing based on power-hardware-in-the-loop simulation. In: *Procs. of the 37th Annual Conference of IEEE Industrial Electronics Society – IECON 2011*, Melbourne, Australia, November 7–10 2011, pp. 3736–3741.
21. A. Scarlat, I. Munteanu, A.I. Bratcu, E. Ceangă (2010). Stability analysis for an improved power optimization method applied to a wind energy conversion system. In: *Procs. of the 3rd International Symposium on Electrical and Electronics Engineering – ISEEE 2010*, Galaţi, Romania, September 16–18 2010, pp. 187–192.
22. O. Crăciun, A. Florescu, S. Bacha, I. Munteanu, A. I. Bratcu (2010). Hardware-in-the-loop testing of PV control systems using RT-Lab simulator. In: *Procs. of 14th International Power Electronics and Motion Control Conference – EPE-PEMC 2010*, Ohrid, Macedonia, September 6–8 2010, pp. S2-1–S2-6.
23. M. Andreica, S. Bacha, D. Roye, I. Munteanu, A.I. Bratcu, J. Guiraud (2009). Cross-flow water turbines control under grid disturbances. In: *Procs. of IEEE PowerTech 2009*, Bucharest, Romania, June 28 – July 2 2009, pp. 1–6.
24. A.I. Bratcu, I. Munteanu, S. Bacha, D. Picault, B. Raison (2009). Power optimization strategy for cascaded DC-DC converter architectures of photovoltaic modules. In: *Procs. of the IEEE International Conference on Industrial Technology – ICIT 2009*, Churchill, Victoria, Australia, February 10–13 2009, pp. 1–8.
25. M. Andreica, S. Bacha, D. Roye, I. Munteanu, A.I. Bratcu, J. Guiraud (2009). Stand-alone operation of cross-flow water turbines. In: *Procs. of the IEEE International Conference on Industrial Technology – ICIT 2009*, Churchill, Victoria, Australia, February 10–13 2009, pp. 1–6.
26. A.I. Bratcu, I. Munteanu, E. Ceangă (2008). Optimal control of wind energy conversion systems: from energy optimization to multi-purpose criteria – a short survey. In: *Procs. of the 16th IEEE Mediterranean Conference on Control and Automation – MED 2008*, Ajaccio, France, June 25–27 2008, pp. 759–766.
27. A.I. Bratcu, I. Munteanu, E. Ceangă, S. Epure (2007). Energetic optimization of variable speed wind energy conversion systems by extremum seeking control. In: *Procs. of the IEEE Region 8 EUROCON 2007 International Conference on Computer as a Tool*, Warsaw, Poland, September 9–12 2007, pp. 2536–2541.
28. A.I. Bratcu, I. Munteanu, D.C. Cernega, M. Culea (2007). Safe and optimal operation of grid connected wind power systems by supervisory control. In: *Procs. of the IEEE Region 8 EUROCON 2007 International Conference on Computer as a Tool*, Warsaw, Poland, September 9–12 2007, pp. 2542–2549.
29. I. Munteanu, J. Guiraud, D. Roye, S. Bacha, A.I. Bratcu (2006). Sliding mode energy-reliability optimization of a variable speed wind power system. In: *Procs. of the 9th IEEE Workshop on Variable Structure Systems – VSS 2006*, Alghero Italy, June 5–7 2006, pp. 92–97.

30. A.I. Bratcu, A. Dolgui, S. Belmokhtar (2005). Reconfigurable transfer lines cost optimization – a linear programming approach. In: *Procs. of the 10th IEEE International Conference on Emerging Technologies and Factory Automation – ETFA 2005*, Catania, Italy, September 19–22 2005, pp. 625–632.
31. A.I. Bratcu (2004). A heuristic to minimize the equipment cost for large transfer lines with operations parallelization. In: *Procs. of the IEEE Conference on Intelligent Engineering Systems – INES 2004*, Cluj-Napoca, Romania, September 19–21 2004, pp. 579–583.
32. D.C. Cernega, A.I. Bratcu (2004). Communication protocol conversion solved by discrete event supervision. In: *Procs. of the IEEE Conference on Intelligent Engineering Systems – INES 2004*, Cluj-Napoca, Romania, September 19–21 2004, pp. 339–343.
33. A.I. Bratcu, L. Makdessian, A. Dolgui (2003). Minimisation of equipment cost for transfer lines with blocks of parallel tasks. In: *Procs. of the 5th IEEE International Symposium on Assembly and Task Planning – ISATP 2003*, Besançon, France, July 9–11 2003, pp. 109–114.

Articles in proceedings of other international conferences

1. Q.-L. Lam, A.I. Bratcu, D. Riu (2018). Voltage regulation in stand-alone microgrids with storage units: a multi-variable H-infinity control approach. In: *Procs. of CIRED Workshop 2018 on Microgrids and local energy communities*, Ljubljana, Slovenia, June 7–8 2018, paper 0511 (4 pages).
2. A. Scarlat, I. Munteanu, A.I. Bratcu, E. Ceangă (2011). Control and management of high-power wind energy conversion system operating regimes: towards aerodynamic-compliant energy performance. In: *Procs. of the 18th International Conference on Control Systems and Computer Science – CSCS 2011*, Bucharest, Romania, May 24–27 2011, 8 pages.
3. A. Scarlat, I. Munteanu, A.I. Bratcu, E. Ceangă (2010). Improved power optimization method for squirrel-cage-induction-generator-based wind energy conversion systems. In: *Procs. of the 14th International Conference on System Theory and Control – ICSTCC 2010*, Sinaia, Romania, October 17–19 2010, pp. 491–496.
4. C. Vlad, I. Munteanu, A.I. Bratcu, E. Ceangă (2008). A peak power tracker for low-power permanent-magnet-synchronous-generator-based wind energy conversion systems. In: *Procs. of the 12th WSEAS International Conference on Systems*, Heraklion, Greece, July 22–24 2008, pp. 407–412.
5. N.A. Cutululis, H. Bindner, I. Munteanu, A. Bratcu, E. Ceangă, P. Soerensen (2006). LQ optimal control of wind turbines in hybrid power systems. In: *Procs. of the European Wind Energy Conference – EWEC 2006*, Athens, Greece, February 27 – March 2 2006.
6. A.I. Bratcu, D. Dulman, I. Munteanu (2005). A two level optimal control structure for cooperative robot systems. In: *Procs. of the 14th International Workshop on Robotics in Alpe-Adria-Danube Region – RAAD 2005*, Bucharest, Romania, May 26–28 2005, pp. 268–273.
7. A.I. Bratcu, I. Munteanu, D. Dulman (2005). Maximum power point tracking for wind power systems: a minimal knowledge approach. In: *Procs. of the 15th International Conference on Control Systems and Computer Science – CSCS 2005*, Bucharest, Romania, May 25–27 2005.
8. I. Munteanu, N.A. Cutululis, A. Bratcu, E. Ceangă (2004). Using a nonlinear controller to optimize a variable speed wind power system. In: *Procs. of the 9th International Conference on Optimization of Electrical and Electronic Equipments (IEEE sponsored) – OPTIM 2004*, Braşov, Romania, May 20–23 2004, pp. 303–311.
9. A. Bratcu, A. Dolgui, L. Makdessian, F. Yalaoui (2002). Balancing and optimal cost resource planning of production lines with blocks of parallel tasks. In: *Procs. of the 1st CIRP (U.K.) International Seminar on Digital Enterprise Technology – DET 2002*, Durham, U.K., September 16–17 2002, pp. 159–162.

Francophone conferences

1. A.I. Bratcu, I. Munteanu, D.C. Cernega (2006). Modélisation à évènements discrets d'un système éolien à vitesse variable en vue de la commande supervisée. In: *Actes de la 6-ième Conférence Francophone de Modélisation et Simulation – MOSIM 2006*, Rabat, Maroc, April 3–5 2006. Lavoisier, CD-ROM, ISBN 2-7430-0893-8.

2. I. Munteanu, J. Guiraud, S. Bacha, D. Roye, A.I. Bratcu (2006). Méthodologie de simulation temps reel hardware-in-the-loop – application aux systèmes éoliens. In: *Actes de la 6-ième Conférence Francophone de Modélisation et Simulation – MOSIM 2006*, Rabat, Maroc, April 3–5 2006. Lavoisier, CD-ROM, ISBN 2-7430-0893-8.
3. A.I. Bratcu, A. Dolgui (2003). Lignes auto-equilibrées : nouveau concept, analyse et modélisation. In: *Revue des Systèmes* (Lavoisier), hors série/*4-ième Colloque Francophone sur la Modélisation des Systèmes Réactifs – MSR 2003*, pp. 195–209.
4. A.I. Bratcu, A. Dolgui (2003). Une relaxation du Modèle Normatif des lignes de production auto-équilibrées (« bucket brigades »). *Actes de la 4-ième Conférence Francophone de Modélisation et Simulation – MOSIM 2003*, Toulouse, France, April 23–25 2003, SCS European Publishing House, pp. 262–269.

Articles in proceedings of national conferences (France)

1. Q.L. Lam, A.I. Bratcu, D. Riu (2016). Frequency robust control in stand-alone microgrids with PV sources: design and sensitivity analysis. In: *Actes du 2-ième Symposium de Génie Électrique – SGE 2016*, Grenoble, France, June 7–9 2016, 8 pages.

Chapter 2

Necessity and motivation of the proposed scientific approach

2.1 Control-oriented characterization of renewable energy conversion systems (RECS)

In order to fix ideas and for justifying necessity of our approach and well positionning our contributions related to control of renewable energy conversion systems (RECS), we will start in a ***system*** context, namely by considering a generic global block diagram of a ***microgrid*** built around a RECS based on a generic primary energy converter, as presented in Fig. 2.1. The microgrid concept dates back to some twenty years ago (for a comprehensive presentation, see, for example [1]); its interest from both research and economical viewpoints has constantly increased since then. The microgrid in Fig. 2.1 is equipped with a generic storage and power electronic interfaces playing the role of actuators for control.

The ***primary energy converter*** is led by the uncontrollable, random and intermittent variations of the natural resource involved, whose *non electrical* energy is converted into *electrical* energy to be further conveyed to what is generically identified in Fig. 2.1 as the "Electrical AC grid". This converter can, for example, be either a rotating prime mover coupled with a rotating electrical machine in the case of wind energy or micro-hydro conversion systems, or photovoltaic (PV) pannels obeying the photoelectric effect principle.

The two power electronic interfaces – grid-side and primary-converter-side, respectively – are coupled in a way such as to materialize an intermediary DC bus, thus enabling what is commonly called a ***back-to-back structure***. Existence of this DC bus allows a generic storage being inserted – but also a more complex DC microgrid in the general case – with the role of compensating for the renewable source intermittency. The ***primary-converter-side power electronic interface*** is typically a converter with voltage-boost function, allowing to obtain an output DC-bus voltage at a higher level than the input one; it is by means of controlling this interface that one imposes the operating point of the primary energy converter. As regards the ***grid-side power electronic interface***, this is typically an inverter, in charge with grid variables control (*e.g.*, injection of sinusoidal currents into the grid).

Different operation modes of such energy conversion system may be defined, essentially depending of the connection nature to the AC grid [2]–[4]. Thus, two main operating modes exist, namely ***grid forming*** – when the generation part of the system is connected to a small-power microgrid (experienced as a load) – and ***grid***

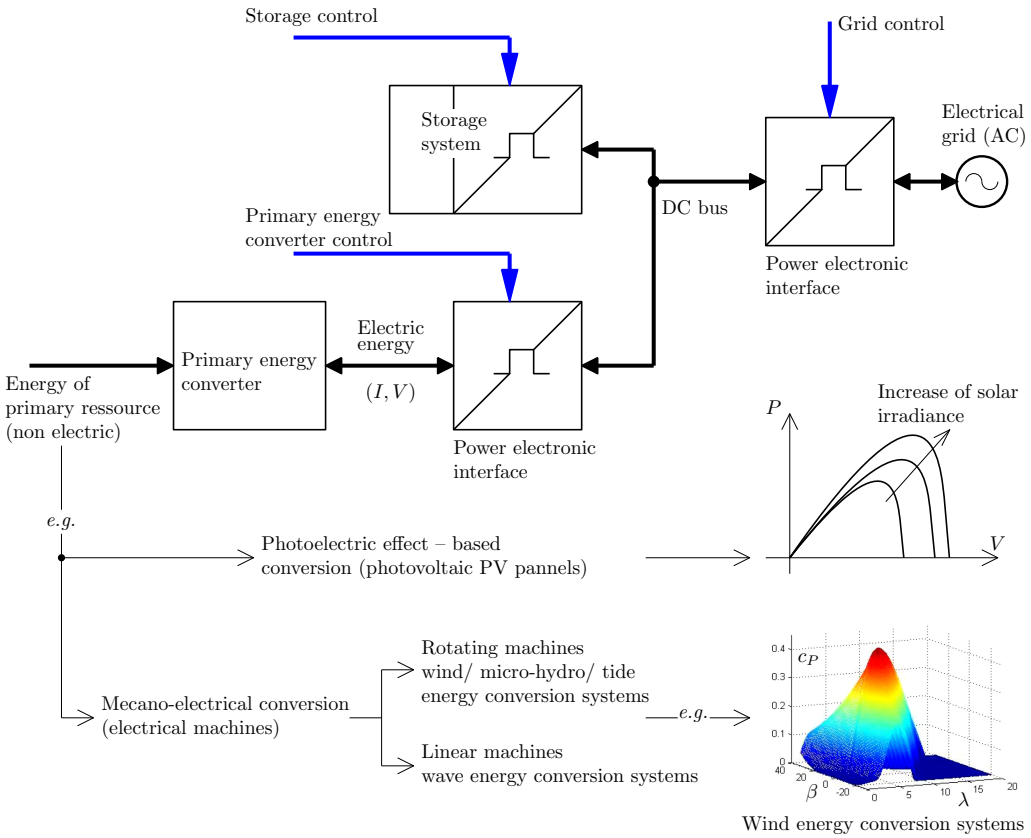

Figure 2.1: Generic global block diagram of a renewable-energy-based microgrid as generation system with generic storage, featuring back-to-back connection of power electronic converters by means of a common DC bus.

following – when the generation system is connected to the strong utility (infinite-power) grid. The two modes are directly translated in terms of control objectives of the ***grid power electronic interface*** – generically and globally indicated on the figure as "Grid control" – thus:

- in the grid-***forming*** mode the main objective is to maintain the output (***load***) voltage (V) and frequency (f) constant – this is why this mode is also called the ***Vf*** mode. The resulted microgrid operates in the so-called ***off-grid*** mode because it is not connected to the main, strong grid – this is also called ***autonomous*** or ***stand-alone*** operation [5], [6]. In this mode the role of the "Primary energy converter control" is:
  - either ***to maintain the DC-bus voltage as constant***, if the storage system is absent,
  - or ***to impose the operating point of the renewable source (primary energy converter)*** if the storage system is present and equipped of some local energy/power management system able to ensure a constant DC-bus voltage – a battery management system (BMS) is a typical example;
- in the grid-***following*** (***grid-connected*** or ***on-grid***) mode the main objective consists in controlling levels of output (***grid***) active and reactive power (P and Q, respectively), thus allowing participation of the renewable-energy-based system to ***ancillary services*** – this is why this mode is also called the ***PQ*** mode [7], [8]. In this mode two cases may appear:
  - either the demanded power, P^*, is less than the renewable source's maximum power, $P_{RENEmax}$: $P^* < P_{RENEmax}$.
    The required power level, P^*, can only be guaranteed if a storage system is present. In this case the renewable source becomes ***dispatchable*** due to presence of storage, which ensures that DC-bus voltage to be constant. Therefore, the role of the "Primary energy converter control" is ***to impose the operating point of the renewable source***;

– or the renewable source is ***not dispatchable*** because there is no storage system, and then it is required to provide the maximum power available in the resource: $P^* = P_{RENEmax}$.
In this case the DC-bus voltage is maintained constant by the "Grid control", that is, at inverter level, whereas the "Primary energy converter control" ***imposes the* maximum *operating point of the renewable source***. A ***Maximum Power Point Tracking*** (***MPPT***) control must then be put in place, in order to track *a priori* unknown renewable resource variations, whom available maximum power, $P_{RENEmax}$, actually depends on – see, for example, [9], [10], for MPPT statement and basic implementation in the case of wind turbines.

Therefore, MPPT is a focal control problem, intriguingly challenging mainly because the maximum power point changes with the resource in a generally unknown and unpredictible manner. Indeed, primary renewable energy converters are characterized by ***unimodal power curves*** for a given renewable resource level. Two examples are suggested in Fig. 2.1:

- of a ***PV*** system: the PV pannel power, P, ***unimodal*** dependence on PV pannel voltage, V, plotted for different ***solar irradiance*** levels;
- of a ***wind energy conversion system*** (WECS): the power coefficient, C_p, ***unimodal*** dependence on wind turbine's blade pitch angle, β, and on tip speed ratio, λ, which in turn depends on the ***wind speed*** and also on the turbine rotational speed. The power harvested from wind depends on C_p, which expresses the wind turbine efficiency.

  The power coefficient is defined for any rotating prime mover (another example are water turbines). In the case of rotating prime movers the ***variable-speed operation*** [11] is a concept enabling MPPT implementation.

The locus of all maximum power points is called the ***Optimal Regimes Characteristic*** (ORC). Irrespective of the primary energy converter nature, MPPT strategies may in a first place be based on *a priori* sufficient knowledge of maximum power points (and the ORC), namely obtained from an as complete as possible *off-line* identification of static power characteristics. However, it may be necessary that such identification to be resumed after some time, because of parameters' deviations over time in relation with their nominal (rated) values.

But, in most of cases, ORC exact description is not known. ***Control challenge is then formulated as being able to track the renewable energy variations in real time, based on minimal knowledge about the system, in particular, about the ORC***. Contributions having come as a possible response to this control challenge of ***MPPT for RECS*** are summarized in Chapter 3 of this memoir and concern:

- both ***ORC-good-knowledge-case***, namely state-of-the-art, conventional MPPT implementations – in Section 3.3 for water-turbine-based (micro-hydro) systems,
- and also ***ORC-minimal-knowledge-case***, namely by using ***Extremum Seeking Control*** (***ESC***) techniques [12], [13] in two versions:
  - by ***inducing* exogenous *periodic disturbances*** into the system in order to identify direction towards the maximum power point, therefore, its position – in Section 3.4 for PV systems;
  - by ***using disturbances* already existing in the system**:
    - in Section 3.2 in the case of WECS, where wind speed turbulence component (modelled as a coloured noise) is used as excitation signal in ESC,
    - and in Section 3.4 for some particular – meanwhile largely used – grid-connected PV system configurations, where the sinusoidal ripple of some variables is used as excitation signal in ESC.

Implementation of ***an energy-reliability trade-off by optimal control techniques for WECS*** is another topic summarized in Chapter 3, which is dedicated to control of all types of RECS. It is about configuring the best trade-off between two antagonistic demands: ***maximizing the power*** harvested from wind by tracking the ORC irrespective of the wind speed variations, meanwhile ***minimizing efforts*** for doing that, which leads in turn at mechanical fatigue reduction, thus preserving reliability. Contributions reported in Section 3.2 concern two control methods used to this end:

- a ***frequency-separation-based formulation of mixed-criteria dynamic optimization***, further allowing to cast the high-frequency-related subproblem into the ***Linear Quadratic Gaussian*** (***LQG***) control formalism,
- and ***Sliding Mode*** (***SM***) control, based upon defining a *wind-speed-varying* switching surface,

with the remark that the same general formal approaches can be applied (possibly with adaptations) to ***any rotating-prime-mover-based RECS***.

Finally, some of the contributions in Chapter 3, namely in Section 3.3, concern a larger viewpoint, with application to ***water-turbine-based (micro-hydro) energy conversion systems***, such as:

- ***direct active power control***, referring to *grid-connected* (otherwise said, ***PQ***) operation, where possibility of operating a RECS as a ***dispatchable*** power generation system ***despite absence of a storage unit*** is investigated;
- designing some ***proper management of "smooth" switching between the two modes*** – ***Vf*** and ***PQ*** – as a renewable generation system like the one in Fig. 2.1 may be required to switch between the grid-forming (*stand-alone*) and the grid-following (*grid-connected*) modes;
- and also ***synchronization of two rotating-prime-mover-based RECS*** for some global purpose, *e.g.*, alleviating mechanical efforts inside of a master-slave configuration.

2.2 Control approach to exploit complementarity within multi-source/hybrid electrical energy systems (MSES)

Decision of integrating energy sources of different types and technologies must obviously be based on the conclusion that theses sources behave better together than each alone. Thus, existence of the ***complementarity between the sources*** is here exploited as a first good premise, whereas their ***coordinated*** – possibly ***optimal*** with regard to some well-defined criterion – ***behaviour can only be guaranteed by control action*** [14]–[16].

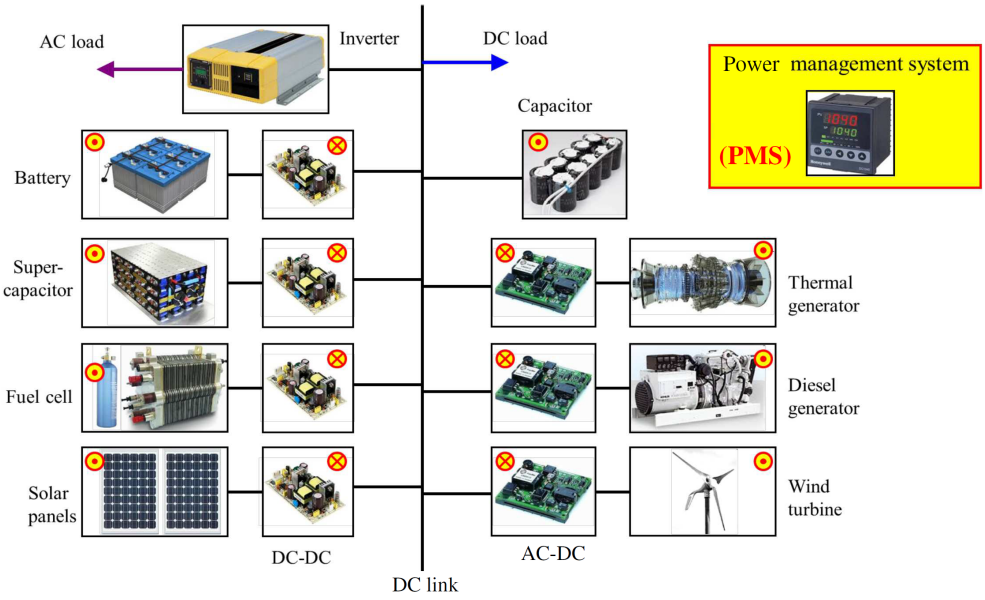

Figure 2.2: General configuration of a microgrid with classical and renewable sources and different types of storage, coupled in parallel on a common DC link, supplying both AC and DC loads.

Configuration of a generic multi-source-based microgrid as in Fig. 2.2 is considered; partial configurations of this one are also illustrative. It is equipped of *classical* – Diesel generator, thermal generator – as well as *renewable* sources – solar pannels, wind turbine – of *storage units* of diverse technologies – batteries, supercapacitors (ultracapacitors), fuel cells – and also of (possibly both) AC and DC loads.

Such a microgrid can operate in either grid-forming (stand-alone) or grid-connected mode, as previously explained in Section 2.1. In either case, sources' power flows are managed by a ***Power Management System*** (***PMS***), which embeds the control algorithm ensuring proper coordination of sources in view of a

common goal. Power flow management exhibits faster dynamics than those controlled at the level of an ***Energy Management System*** (***EMS***), thus PMS are placed nearer to the plant and lower in a possible multiple-layer control hierarchy. In particular, the PMS is the one implementing the effective coordination between sources in the sense of taking profit of their complementarity.

In this context notion of complementarity between two power source technologies refers specifically to their respective dynamic abilities in providing energy in a longer or a shorter term. Hence, complementarity supposes different variation speeds of the provided energy, thus different response times. It is therefore its ***dynamic*** substrate that enables complementarity to justify and meanwhile be exploited for control and coordination purposes.

Dynamic specialization of sources is best represented by Ragone plot [17], whose a quite complete version is resumed here in Fig. 2.3, where ***dynamic specialization range*** of each storage source can be identified through the relation between its ***energy density*** (*specific energy*) and its ***power density*** (*specific power*). A large span of storage technologies is illustrated:

- from ***high***-specific-***energy*** storage sources, such as fuel cells – able to provide energy in a long term, otherwise called "***energy*** sources" for this reason, so specialized in the ***low-frequency*** range when talking about energy variations –
- to the ***high***-specific-***power*** sources, such as ultracapacitors (supercapacitors) – able to provide energy very quickly, otherwise called "***power*** sources", so specialized in the ***high-frequency*** range,

with different electrochemical storage (*e.g.*, batteries) or mechanical storage (*e.g.*, flywheels) technologies being placed in between.

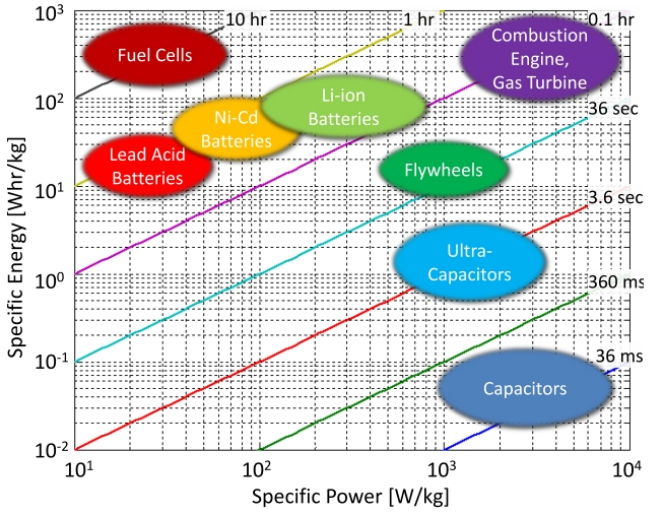

Figure 2.3: Ragone plot: dynamic specialization of different source/storage technologies.

Notion of ***characteristic (own) frequency of a source*** was introduced to quantify more precisely its dynamic specialization range:

$$f_p = \frac{\rho_p}{\rho_e}, \tag{2.1}$$

where ρ_p is the power density, measured in W/kg and read on the abscissa of Ragone plot, and ρ_e is the energy density, measured in J/kg and represented on the ordinate. Fig. 2.4 presents characteristic frequency values for some of the main storage technologies.

It is thus clear that a given source behaves best when exploited in its specialization range – *i.e.*, when variation spectrum of the power demand is placed ***around its characteristic frequency*** – because its ***reliability*** and ***lifetime*** are best ensured this way. Reliability requirements may impose the decision to suitably complement – otherwise said, to ***hybridize*** – a high-energy-density source, also identified as ***main source***, by a high-power-density one, identified as ***auxiliary source***, in order to protect the first from possible damages due to unappropriate exploitation outside its specialization range. Two classes of indicators for hybridization are important in a first place for initial sizing and rating the hybrid source/storage system:

- *power potential of hybridization* (*PPH*): based on the possibility of reducing the main source's size – in terms of rated power, weight, cost, *etc.* – due to the presence of the auxiliary one
- and *energy potential of hybridization* (*EEH*): based on taking into account variation spectrum of load power and also regularity of charging/discharging cycles of the main source if this is a storage one.

In such a hybrid tandem the auxiliary source will supply the high-magnitude fast variations of power demand, which the main source is not specialized to supply. Note that the simple decision to put together these two types

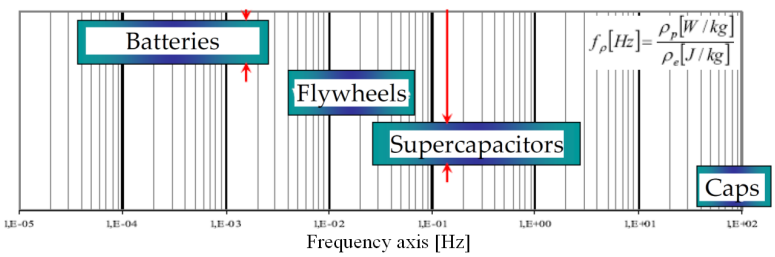

Figure 2.4: Characterization of main storage technologies by their characteristic frequencies.

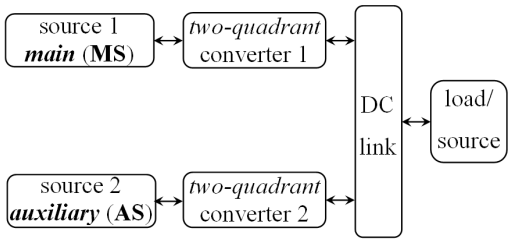

Figure 2.5: Simplified block diagram of a hybrid two-storage-unit supply system in a stand-alone microgrid.

of sources is not sufficient to guarantee their ***realiability-aware operation***, a ***multi-source PMS*** must also be designed to appropriately coordinate them – this action supposes, irrespective of the method employed, that sources be ***dynamically separated***. We will then talk about dynamic separation or, equivalently, ***frequency separation*** of sources. Moreover, in order to exhaust all optimization possibilities, ***PMS design may already be considered in the phase of initial system sizing*** – this kind of approach is called ***system-control co-design***.

To further fix ideas, a partial version of the generic microgrid in Fig. 2.2 is considered, namely in the form of a *hybrid two-storage-unit* supply system, materializing a stand-alone microgrid. Simplified block diagram in Fig. 2.5 shows both sources, the main one and the auxiliary one, coupled in parallel to a common DC link by means of two-quandrant converters ensuring their bidirectionality (charging/discharging) and further interacting with a load/source. Roles of the two-quadrant converters can, for example, be ensured by synchronous buck converters.

A *battery-ultracapacitor* supply system on board of an electric vehicle (EV) is a typical instance in this regard, which originally motivated the approach detailed here. This motivation – based on collaboration with Ph.D. student Adrian FLORESCU, co-supervised by Professor Seddik BACHA and myself, and post-doctoral fellow Iulian MUNTEANU, with the help of R&D engineer Axel RUMEAU – is developed next and issued the two main journal publications below:

- A. Florescu, S. Bacha, I. Munteanu, A.I. Bratcu, A. Rumeau (2015). Adaptive frequency-separation-based energy management system for electric vehicles. *Journal of Power Sources*, 280, 410–421.
- A. Florescu, A.I. Bratcu, I. Munteanu, A. Rumeau, S. Bacha (2015). LQG optimal control applied to on-board energy management system of all-electric vehicles. *IEEE Transactions on Control Systems Technology*, 23(4), 1427–1439.

The most intuitive implementation of a frequency-separation PMS for the hybrid system in Fig. 2.5 is by means of a ***frequency splitter*** – composed of a low-pass filter and a high-pass filter having the same folding frequency, $1/T$ – which dispatches the low-frequency and high-frequency components of power demand towards the main and auxiliary sources, respectively. Having initially been presented in our conference paper [18], this idea subsequently evolved towards an ***adaptive*** version of this control strategy, implemented in a classical, widely-used two-level structure, resumed here in Fig. 2.6 [19]:

- the upper-level control mainly implements the DC-link voltage regulation, but also a control loop in charge with maintaining auxiliary source (AS)'s state of charge (SoC) – otherwise said, its voltage – within admissible limits; the frequency splitter, whose folding frequency is rendered adjustable by means of an adaptive strategy, is also embedded here;
- the lower-level control concerns control loops of the two sources' currents.

The idea of rendering variable the separation frequency allows adapting solicitation of the two sources while taking into account additional constraints related to AS SoC and load requirements (charge/discharge) at a given moment. Thus, flexibility is added by allowing the main source (MS) taking over the role of AS if ever the AS SoC does not any longer allow its operation as a peak-power source.

The obtained results suggested to go beyond empirical-rule-based adaptive dynamic-separation PMS for hybrid systems based on differently, complementarily specialized sources. Idea of using an ***optimal control framework*** thus appeared, having initially been proposed in our conference paper [20].

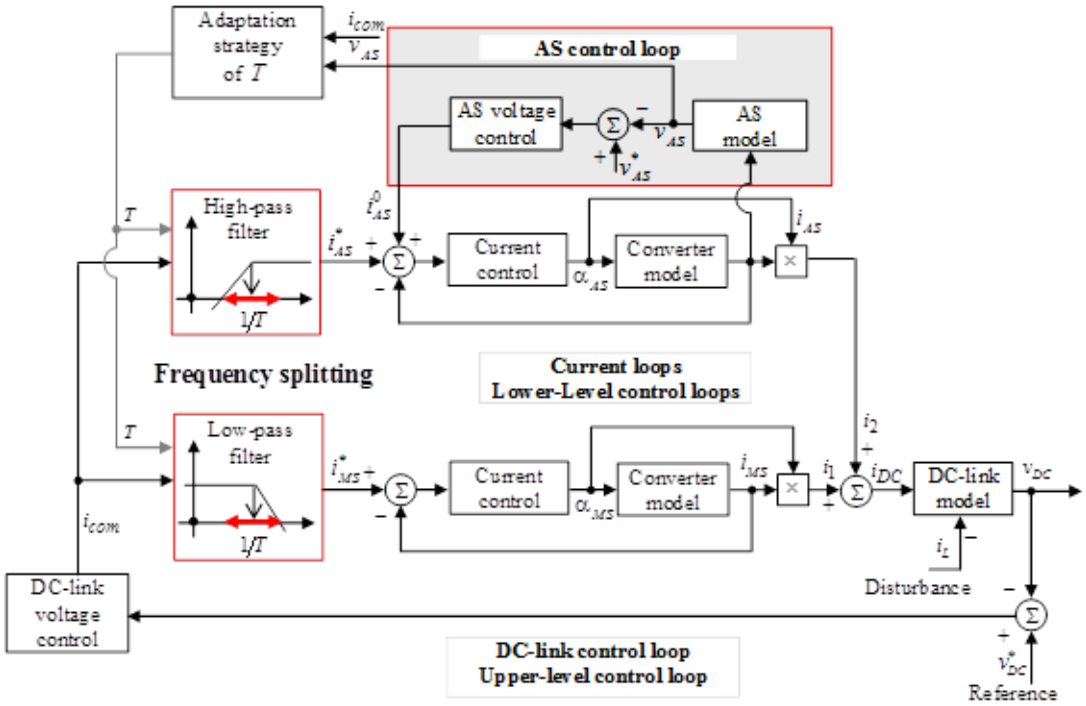

Figure 2.6: Adaptive-frequency-splitting-based two-level PMS: the lower-level control concerns both the main source (MS) and the auxiliary source (AS) current loops, whereas the upper-level control consists of the DC-link voltage control [19].

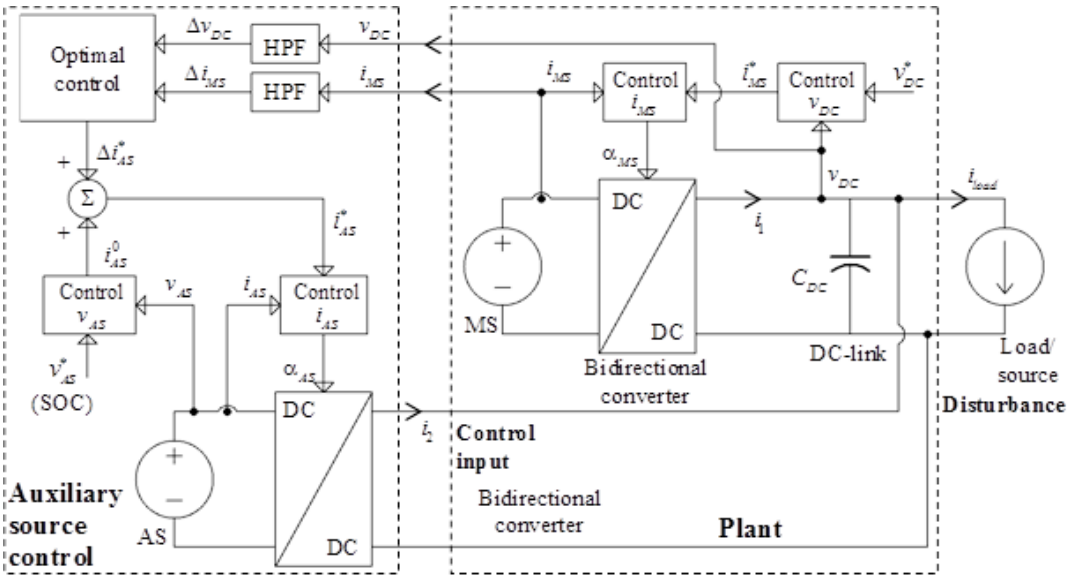

Figure 2.7: General power flow configuration and optimal-control-based PMS for the class of two-DC-DC-source power system supply described in Fig. 2.5, used for off-grid applications [21].

Fig. 2.7 details the principle of an optimal-control-based PMS for the same class of two-storage-unit multi-source system like the one in Fig. 2.5. It is assumed that MS current is controlled in order to ensure DC link voltage regulation, despite stochastic and *a priori* unknown variations of reversible load's power (current), by means of a two-loop control structure whose outer closed loop represents the plant – identified by the block "Plant" in Fig. 2.7 – for the subsequent control design approach. The aim is to cast the problem into an ***optimal stochastic-disturbance-rejection formalism***, as presented in our journal paper [21].

To this end, the block "Plant" is modeled as a family of linearized (linear parameter varying) systems in

variations – obtained by high-pass filtering (HPF) – around operating points corresponding to different mean values of load current. Further formalization is based on the idea that ***the AS together with its converter plays the role of an actuator for the "Plant"***, able to reject high-frequency disturbances represented by load current variations. In this way, designing an adjustable trade-off between MS's current variations and AS's current variations can be straightforwardly expressed as a trade-off between performance and control effort.

To conclude, the block "Optimal control" in Fig. 2.7 contains the result of an ***LQG optimal control problem*** coupled with a ***gain scheduling strategy*** to cover the whole range of load variations. Thus, the two power sources are controlled to share the stochastically-variable reversible load according to their respective dynamic specialization ranges.

Note that the relation between the "Plant" (MS and DC link) closed-loop bandwidth and the HPF folding frequency is the most important degree of freedom in the dynamic-separation-based PMS design, as it should practically follow the relation between the respective characteristic frequencies of the two sources.

The idea of associating an optimization index to the dynamic separation of sources depending on their dynamic specializations, *i.e.*, their respective characteristic frequencies, leads naturally to the possibility of ***generalizing the optimal approach for an arbitrary number of sources, n***. Note that stating an LQG problem in the above-mentioned form for an n-source hybrid system is not any longer effective; introduction of more degrees of freedom in the design is necessary. In this context, approaching PMS design by using *weighting functions* within an $\mathcal{H}_\infty$ ***robust control design*** allows sufficient flexibility in suitably conditionning the sources' dynamic closed-loop behaviour, in addition to ***guaranteeing robustness in stability and performance***. Further combination with ***Linear Parameter Varying*** (***LPV***) techniques – *e.g.*, in a *polytopic approach*, thus generalizing gain scheduling methods – ensures extending domain of well performance.

Following these ideas, contributions summarized in Chapter 4 concern developments around $\mathcal{H}_\infty$ and LPV methods, exploited for well-performing multi-source PMS design with guaranteed performance. Two class of applications are illustrated for purpose of effectiveness validation, namely:

- in Section 4.2 ***generalization of PMS design guidelines for n-source generation systems*** is detailed, then validated in the case of *three-source* (n=3) *DC microgrids on board of all-electric multi-storage vehicles*;
- ***design of robust PMS for frequency and voltage regulation in stand-alone AC microgrids*** is presented and validated in Section 4.3 in the context of *using ultracapacitors as fast storage units*.

2.3 *Hardware-in-the-loop simulation* (HILS) as systematic method of experimental validation

Scientific results and developments around this topic originate in the exposure I had benefited from to work that Professor Emil CEANGĂ carried out in the mid-1990s at "Dunărea de Jos" University of Galaţi in Romania. Indeed, articles [22]–[24], issued from his collaboration with a team from Université du Havre in France, are among the first ones dealing with replicability of renewable-energy-conversion governing phenomena under controlled conditions.

Unpredictability of operating conditions of different renewable-energy sources and the associated significant risks render very difficult *in situ* preliminary experimental validation of control laws. The ***hardware-in-the-loop simulation (HILS)*** principle is nowadays widely employed for rapid prototyping, as recognized of full effectiveness. In this way, replicable experiments can repetitively be carried out in laboratory conditions on dedicated test rigs.

Generally speaking, the HILS concept consists in the closed-loop connection of both physical and software parts, in order to replicate in laboratory (controlled, customizable) conditions the dynamic behaviour of an industrial process or system. The software part results from modelling those parts of the real system which will be *simulated* – because it is to expensive and/or dangerous to use the *real* parts – whereas the physical part is taken as it is from that system.

Since its definition and introduction at the beginning of the 1990s for developing and testing control structures for mechanical equipments [25] – HILS applications in the automotive industry using the MATLAB®/Simulink®

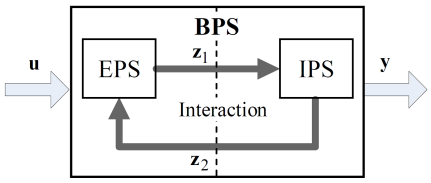

Figure 2.8: Representation of the interaction between the investigated physical system (IPS) and the emulated physical system (EPS) within the basic physical system (BPS) [29].

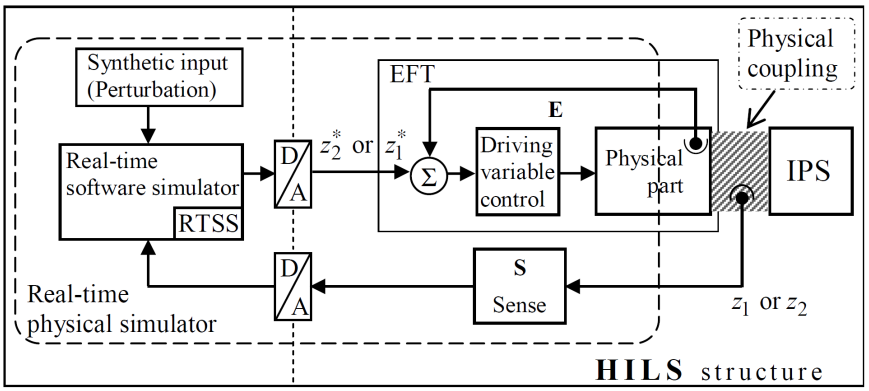

Figure 2.9: Real-time physical simulator (RTPS) within a general HILS structure [29].

software on a dSPACE^{TM} development kit date back to 1996 [26], [27] – HILS concept has increasingly been used – in particular, for control law rapid prototyping – being now involved in other modern concepts such as, for example, the *digital twin*.

Based on concepts, terminology and methodological aspects first introduced in [23], then partially used in [24] and [28], a ***systematic design method of HIL simulators*** resulted when I was with the group led by Professor Emil CEANGĂ at "Dunărea de Jos" University of Galaţi, namely within the collaboration with Ph.D. students Iulian MUNTEANU and Nicolaos Antonio CUTULULIS, as the seventh chapter of our 2008 Springer monograph:

- I. Munteanu, A.I. Bratcu, N.A. Cutululis, E. Ceangă (2008). *Optimal control of wind energy systems – Towards a global approach*. Advances in Industrial Control Series. Springer, London. ISBN 978-1-84800-079-7, 283 pages.

Let a *basic physical system* (BPS) be considered, for which a generic control problem is formulated. A HIL simulator is aimed at cost-effectively and safely replicating the BPS dynamic behaviour, for as realistic as possible closed-loop deterministic experiments under customizable conditions.

HILS structures basic idea relies upon assuming that the BPS can be naturally divided into two interacting subsystems, namely a first subsystem – for which closed-loop experiments are very expensive and deterministic experiments are almost impossible – and a second subsystem, undertaking the control action. Thus, it is the first subsystem whose behaviour must be replaced by a physical simulator; it is called an *emulated physical system* (EPS), whereas the second subsystem exists in the HIL simulator exactly as it is in the BPS. Being the object of study, the second subsystem is called an *investigated physical system* (IPS).

The interaction EP–IPS supposes a power transfer between them and is characterized by a pair of *interaction variables*, further denoted as $\mathbf{z}_1$ and $\mathbf{z}_2$. Having assumed that the "active" participant – *i.e.*, able of providing energy – is the EPS, with the IPS being the energy absorber, the interaction, as experienced by the EPS, is depicted in Fig. 2.8. The physical nature of the interaction variables depends on BPS in a biunique manner. Being the cause variable, $\mathbf{z}_1$'s variation initiates the energy imbalance; $\mathbf{z}_2$ is the response variable. Product of thusly defined interaction variables has always power dimension.

The EPS is replaced by a *real-time physical simulator* (RTPS), which must offer the "natural" environment for IPS and must replicate the models of the EPS and of the interaction EPS–IPS, in order for the resulted HIL simulator to approximate the BPS dynamics. Basically, the RTPS must *physically* provide one of the interaction variables based on the *measure* of the other one and on the EPS model. A tracking loop at the output of the RTPS – called the *effector* (EFT) – is in charge with this task; the controlled variable is called *driving variable* and the other one, *response variable*. The EFT reference is established by the *real-time software simulator* (RTSS), according to a model of the EPS, referred to as EPSM. Fig. 2.9 details the RTPS structure for the simplified case when the interaction variables are scalars.

There are two main ways of choosing the generic driving and response variables, namely:

1. if the variable chosen as driving variable is an output/state of the BPS, then it is an effect variable ($\mathbf{z}_2$), so the model implemented in the RTSS is strictly causal and is obtained directly from the EPS model;
2. if the variable chosen as driving variable is a cause variable ($\mathbf{z}_1$), then the model implemented in the RTSS is non-causal and is fed by a measure of the effect, $\mathbf{z}_2$.

Both cases have drawbacks: quite slow dynamic in the first case, need of computing time derivatives – thus noise increasing – in the second case. Some other remarks can also be made. First, as the IPS is generally "active", it induces in BPS variations of potential energy, so its influence on the RTPS should not be neglected. Also, Fig. 2.9 shows that the response variable is affected by the transducer dynamic (described by vector field **S**) and the driving variable by the effector dynamic (described by vector field **E**). Therefore, these variables have actually slightly modified instantaneous values, thus affecting the HILS emulation accuracy.

The above remarks lead to formulating the ***basic reproducibility conditions***, which must be met for the EPS to be successfully replaced by the RTPS:

- computation inside the RTSS must be sufficiently faster than the dynamic of the EPS (real-time condition);
- the EFT dynamic must be faster than that of the EPS (the tracking loop is sufficiently fast);
- the passband of the transducers must be sufficiently large.

As a conclusion to the above conceptualization approach, a ***seven-step systematic design procedure of HIL systems*** is provided in [29] as an operational tool. A comprehensive application of this procedure for designing a PMSG-based WECS real-time physical simulator is reported in our book chapter [30].

Effectiveness of a real-time simulator is judged upon its performance against the mathematical model to replicate – in other words, what is *mathematically* modeled is compared to what is *physically* obtained on the simulator. In particular, the ***simulator's capability of replicating the desired time and frequency response***, for an as large as possible frequency domain, is of crucial importance.

With respect to this issue, two main publications can be cited, whose results are synthetically discussed next. In both works the considered configuration is that of a ***permanent-magnet-synchronous-generator (PMSG)-based wind energy conversion system (WECS)***, in a ***grid-connected*** case in the first work, while in the second work a ***stand-alone (off-grid)*** operation is studied.

As regards how the HIL simulator is built in each of the two cases, another difference exists between the two case studies, namely regarding the choice of the driving variable: it is about a ***torque-driven*** simulator in the first case and about a ***rotational-speed-driven*** one in the second case. Both time- and frequency-domain performance of the respective real-time simulator are thoroughly assessed in both works. Analysis of real-time replication errors finally allows some remarks when the two cases are compared one against the other, as it can be concluded next.

1. I. Munteanu, A.I. Bratcu, S. Bacha, D. Roye, J. Guiraud (2010). Hardware-in-the-loop-based simulator for a class of variable-speed wind energy conversion systems: design and performance assessment. *IEEE Transactions on Energy Conversion*, 25(2), 564–576,

   which discusses the results obtained by experimenting on the multi-functional test rig at Grenoble Electrical Engineering Laboratory (G2ELab), during my post-doctoral 2008–2009 internship, within collaboration with post-doctoral fellow Iulian MUNTEANU, Professors Daniel ROYE and Seddik BACHA, with the precious help of R&D engineer Joël GUIRAUD.

   In this work, a complete grid-connected generation chain employing a horizontal-axis fixed-pitch three-bladed rotor PMSG-based WECS is chosen as example for the step-by-step illustration of the HIL simulator design procedure.

   Fig. 2.10 offers an overall synthetic view of how the HIL simulator is built, starting from the WECS configuration as a basic physical system (**BPS**) in Fig. 2.10a). Identification of both emulated and investigated physical systems (**EPS** and **IPS**, respectively), as well as interaction between the two, is also suggested in this first part of the figure.

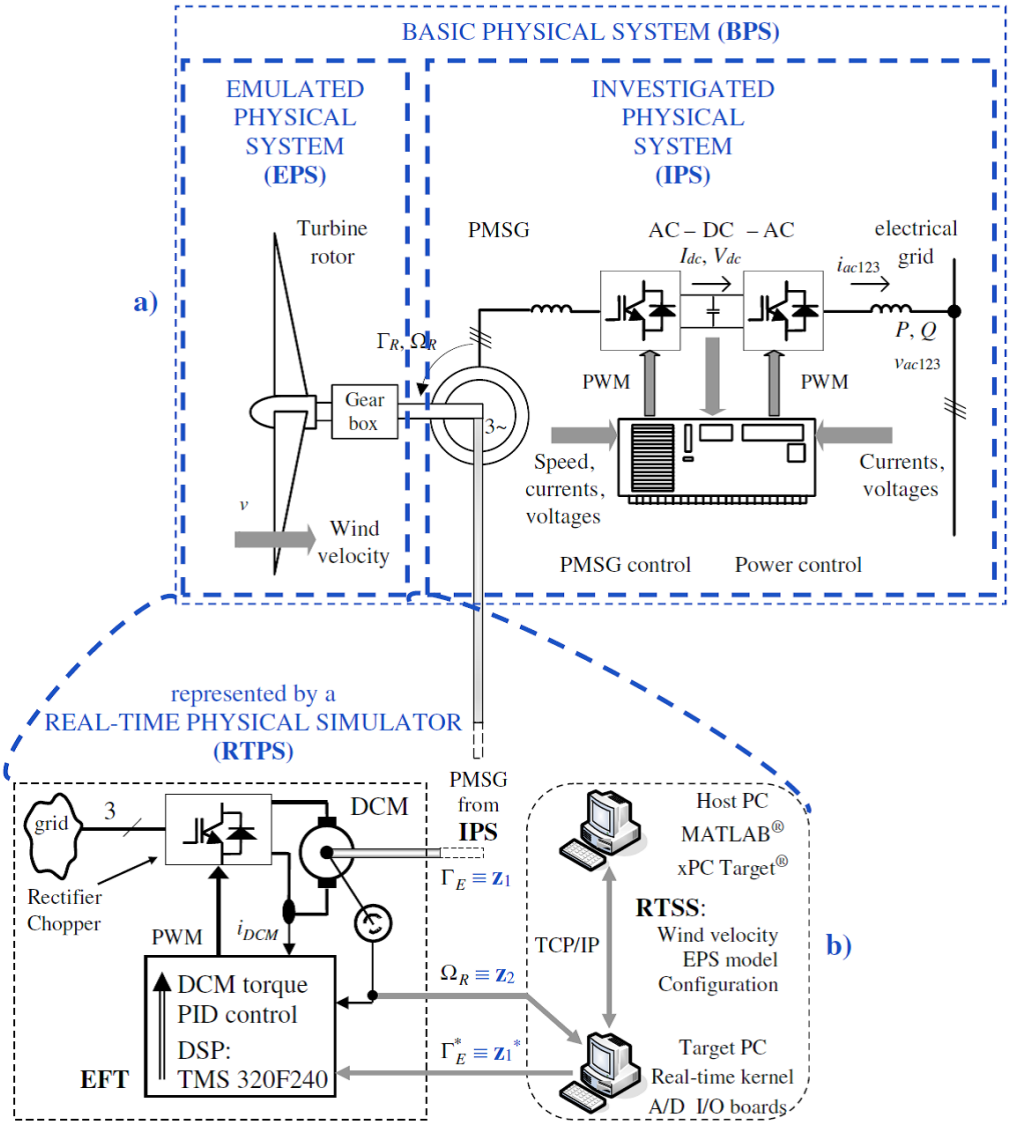

Figure 2.10: Structure of a grid-connected PMSG-based WECS from the viewpoint of the HIL simulator design procedure [31]: a) emphasizing interaction between EPS and IPS within the BPS; b) emphasizing interaction between EFT and RTSS within the RTPS that replaces the EPS.

Fig. 2.10b) further shows how the EPS is replaced by a real-time physical simulator (**RTPS**) and presents details about structures of both effector (**EFT**) and real-time software simulator (**RTSS**) within the RTPS. As also indicated in this second part of the figure, interaction between EFT and RTSS is here based on having chosen the *rotational speed*, Ω_R – an *effect* variable – as *driving variable*; therefore, the model implemented in the RTSS is *strictly causal*. The *response variable* is then the *electromagnetic torque*, Γ_E, a *cause* variable. The imposed torque value, Γ_E^*, serves as a reference to the EFT; therefore, the EFT is in this case *torque driven* within the RTPS.

Fig. 2.11 offers a glimpse of ***HIL simulator frequency-domain accuracy***. Thus, the simulator's frequency response was measured by applying variable-frequency exogenous sinusoidal variations around a typical steady-state point – here, an operating point close to the maximum power point was established, which is characterized by an average wind speed – here, about 8 m/s.

The two parts of Fig. 2.11 are dedicated to results on the two input-to-output transfer channels, respectively – that is, from the *wind speed* (*disturbance* input) to rotational speed (Fig. 2.11a)), and from *electromagnetic torque* (*control* input) to rotational speed (Fig. 2.11b)), respectively.

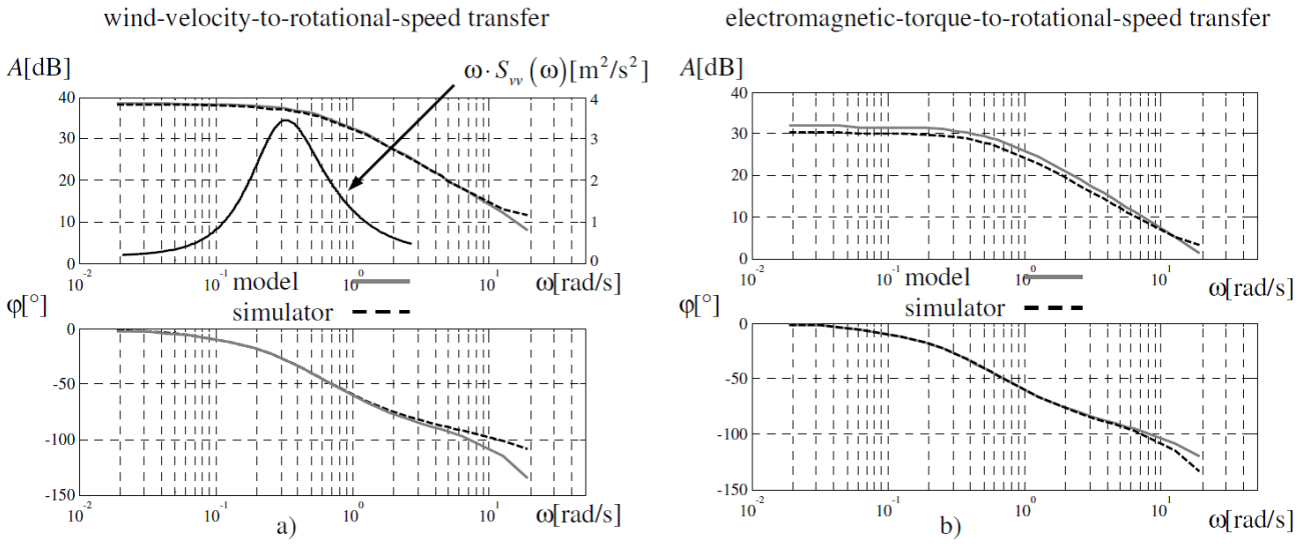

Figure 2.11: Bode plots allowing to evaluate the errors associated to real-time replication in the frequency domain [31]: a) disturbance-to-output transfer channel; b) control-input-to-output transfer channel.

Bode plots in Fig. 2.11a) are shown along with a typical spectral density of the wind turbulence, with most of energy located between 0.1 and 1 rad/s [44]. Simulation errors are negligible for almost the whole frequency range considered, which totally includes the wind speed spectrum, thus suggesting that the simulator fully succeeds in replicating the real system in response to the wind speed variations.

Fig. 2.11b) indicates that replication errors with respect to the electromagnetic torque are slightly larger than those on the disturbance-to-output channel, especially the gain errors. This fact is however not critical, since the error is almost constant (3 dB) over the whole frequency range of interest, so easy to compensate by control action. The electromagnetic torque dynamic is controllable and it must essentially follow the dynamic of the main disturbance, *i.e.*, of the wind turbulence, where the high-frequency variations are usually not present, for reasons of minimizing the fatigue loads [44]. The replication error is thus relevant in the same frequency range as in the case of wind turbulence.

2. C. Vlad, A.I. Bratcu, I. Munteanu, S. Epure (2014). Real-time replication of a stand-alone wind energy conversion system: error analysis. *International Journal of Electrical Power and Energy Systems*, 55, 562–571,

   which presents the results issued from experiments on the dedicated test rig at "Dunărea de Jos" University of Galaţi in Romania, within collaboration with Romanian colleagues Ciprian VLAD and Silviu EPURE.

   In this case, the investigated physical system (IPS) consists of a variable-speed PMSG-based stand-alone WECS supplying a wide range DC load by means of a diode bridge rectifier and a DC–DC step-down converter. Unlike in the first above-discussed case, the second choice of the driving variable was made here – thus, a *speed-driven* real-time physical simulator (*RTPS*) is built, with the *a priori* drawback of a reduced bandwidth [29]. This drawback was significantly alleviated by embedding into the real-time software simulator (RTSS) a feed-forward compensation of the inherent physical disturbance produced by the generator torque variations.

   The block diagram of the HIL structure is presented in Fig. 2.12, where the different parts and the interaction between them can directly be identified. This time, it is the *electromagnetic torque*, T_G – a cause variable – that is chosen as *driving variable*; its estimation based on sensing the current value, I_R, is here preferred to a more expensive solution employing a torque transducer. It results further that the rotational speed, Ω – an effect variable – plays here the role of response variable, so the effector within the RTPS is driven by the rotational speed imposed value, Ω^* (it is said that it is *speed driven*). RTSS is implemented on a dSPACE$^{\text{TM}}$ rapid prototyping system identified as DS1103 in Fig. 2.12.

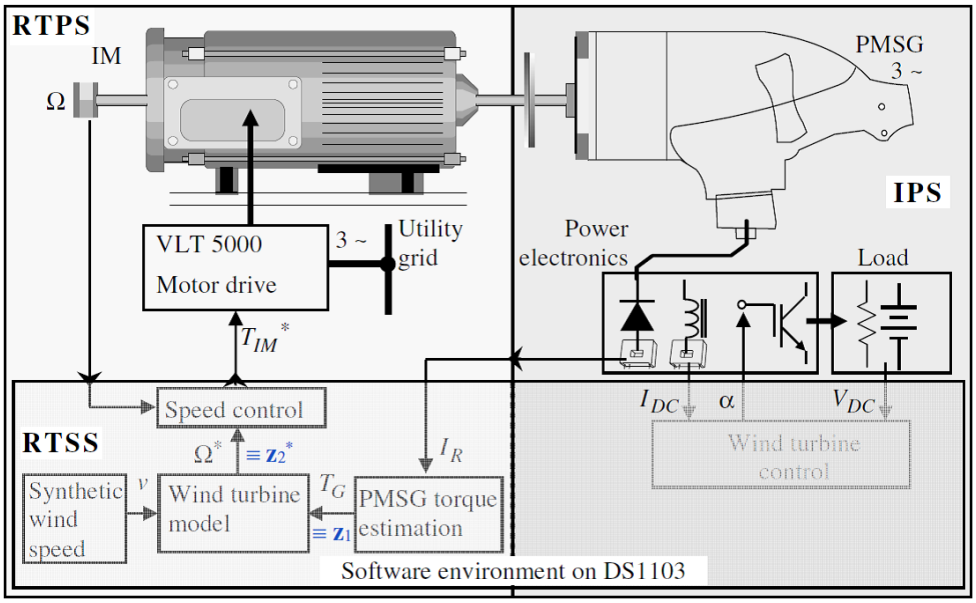

Figure 2.12: HIL simulator design applied to a stand-alone PMSG-based WECS: emphasizing interaction between IPS and RTPS [32].

Like in the first HIL simulation case presented before, the ***simulator frequency-domain accuracy*** was analyzed for a frequency range larger than two decades. To this end, small-amplitude variable-frequency sinusoidal variations of its exogenous signals, the wind speed and the load current reference, were applied around a typical operating point. Fig. 2.13 exhibits the Bode plots for both input–to-output channels.

The replication accuracy on each transfer channel is assessed in relation to the frequency spectrum of its respective exogenous signal. For the *first* channel – corresponding to *disturbance* influence on output – very good simulation quality is revealed in the frequency range of interest (Fig. 2.13 (a) and (b)): the maximum gain error is below 1 dB and is placed within the bandwidth, whereas phase lag errors are negligible. Both gain error and phase lag error increase with the frequency. Very good simulation quality can also be concluded on the *second* channel – corresponding to *control input* influence on output – in the frequency range of the load current reference variations (Fig. 2.13 (c) and (d)), with replication errors being here slightly more visible than on the first transfer channel. Gain errors of around 1 dB can be viewed along the whole frequency range of interest and phase lag errors are placed around 2°.

Having now a ***concluding look*** at the two above-presented HIL simulation case studies, one can note that the theoretically-predicted worse dynamic replication accuracy of a speed-driven simulator *vs.* that of a torque-driven one [29] can be outperformed by ***appropriately enhancing the software part*** to accomodate compensation strategies of different negative influences. Indeed, Figs. 2.11 and 2.13 sustain the idea that ***quite similar performance*** of the two is possible to obtain.

2.4 Heterogeneity and stochasticity of energy–communication interaction in smart grids

Always within the topic of grid and microgrid technology, we now put the focus on what renders them "*smart*". Information and Communication Technologies (ICT) are key concepts having enabled in the last years the digitalization revolution. In particular, what is today called as the *energy transition* – roughly described by the transition from fossil-based and centralized to renewable-based and decentralized energy production, but also by new manners of consuming this energy – is largely due to the growing intelligence of the nowadays power distribution grids.

One of the definitory features of the emerging concept of "***smart grid***" suposses that different entities – production units, loads, circuit breakers, power stations, *etc.* – can communicate with each other and exchange information

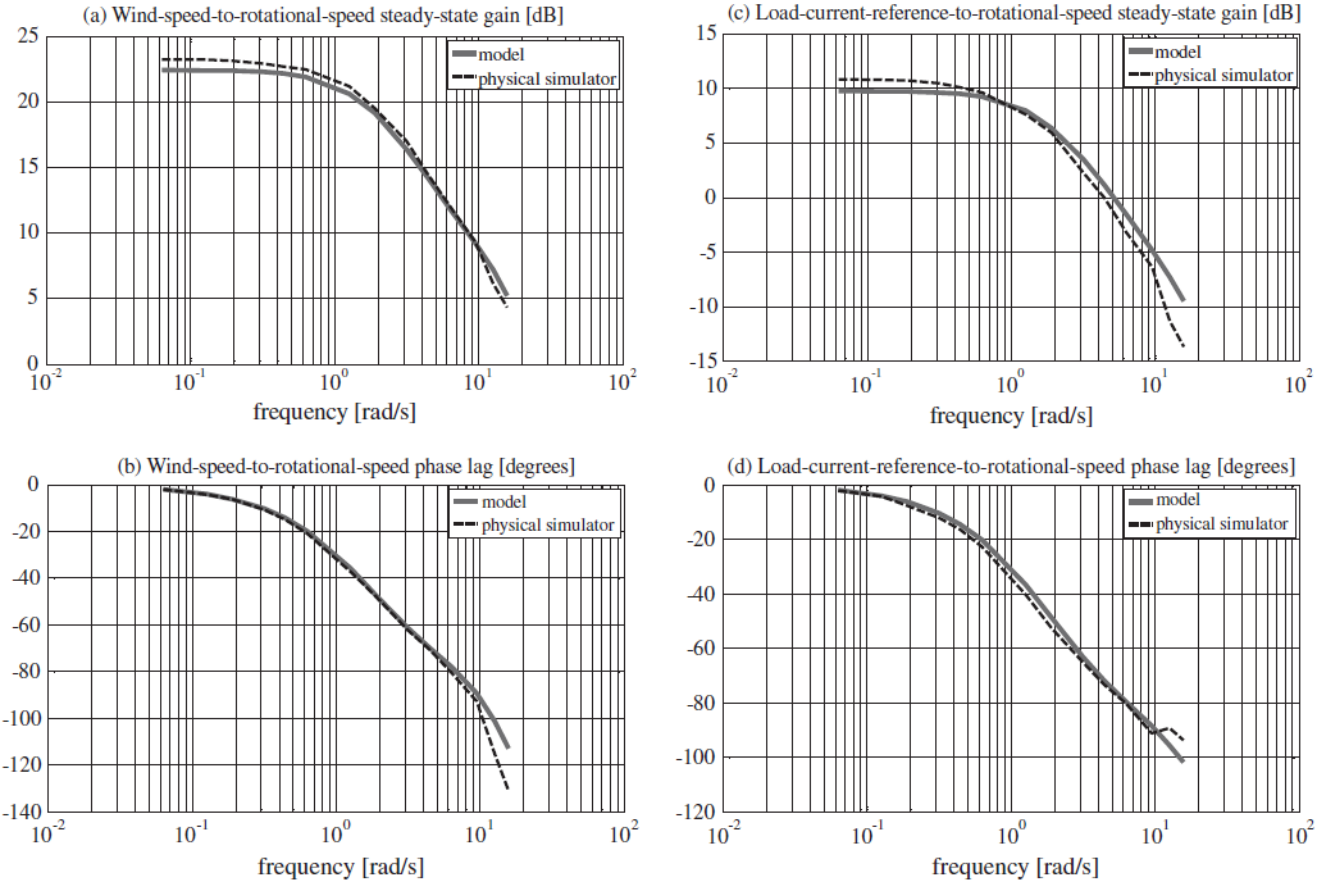

Figure 2.13: Real-time simulation performance in the frequency domain – simulator *vs.* linearized model Bode plots obtained around average wind speed of about 7 m/s chosen as typical operating point [32]: (a) and (b) wind-speed-to-rotational-speed transfer channel; (c) and (d) load-current-reference-to-rotational-speed channel.

by means of a communication network that overlays – or it is integrated into – the energy network. Imbrication between these two networks becomes increasingly important, leading to concepts such as *critical infrastructures*. Governing phenomena have non-unitary character – multi-domain, multi-physics – and take place at different time scales (multi-scale); this is a real challenge for stating a unitary modelling and control paradigm.

New communication protocol standards have especially been defined for the smart grids [33]–[35]; among them, the ***IEC-61850 standard*** is nowadays one of the most used. Irrespective of the protocol used, the information flow through a communication network generally exhibits ***variable delays*** potentially responsible for unstable – or at least degraded – behaviour of the power system. Moreover, certain asynchronous events – erroneous transmissions, collisions, loss of data packets, *etc.* – may also take place. Thus, a smart grid in interaction with its communication network exhibits *hybrid dynamics*. The energy grids have already been analyzed as complex interconnected systems and modelled as hybrid dynamic systems in a systematic context allowing to study their structural properties such as the stability [36]. Recent works have envisaged more general methods for modelling the communication protocols for large-scale systems [37].

Modelling of smart grids as cyber-physical systems has become quite recently a topic of interest within our research. The smart grids considered here rely upon distributed Intelligent Electronic Devices (IEDs) equipped, among others, with sophisticated communication functions to perform supervision, protection and control. As the performance of the underlying communication network can affect power grid operation, focus was put on obtaining a modeling method for its Quality of Service (QoS) analysis.

In this context, a ***methodology of evaluation of the maximum message transmission delay*** using an analytical model based on *Network Calculus Theorem* can be cited here as main result. This methodology is proposed and validated on a smart-grid communication network implemented on a real reduced-scale HV/MV smart

substation test bench equipped with a real-time IEC-61850-traffic generator within a *cooperative load-shedding* scenario. Thus, to fix ideas, but without losing generality, the chosen substation real-time scenario – whose schematics is depicted in Figure 2.14 – includes three communicating IEDs participating in a common task of load shedding, while two other IEDs are added to generate background, perturbation traffic, for generalization purposes.

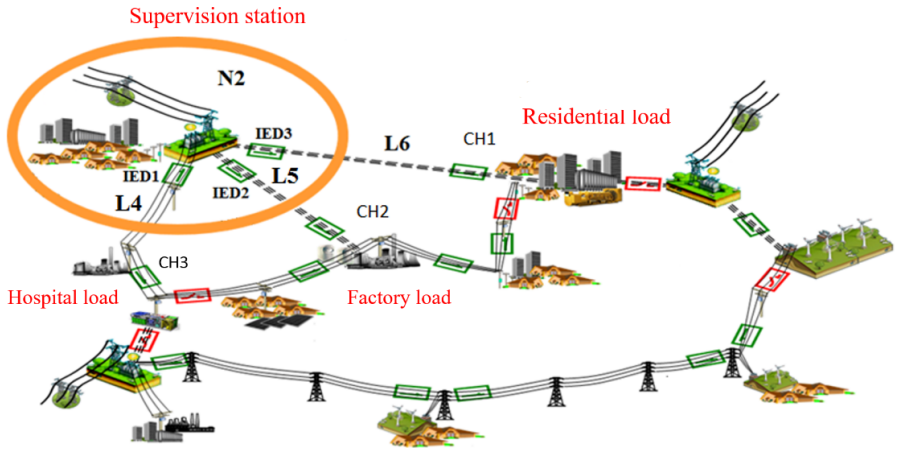

Figure 2.14: Reduced-scale laboratory distribution grid with smart substation implementing a three-IED-based load shedding scenario – residential load is the less prioritary [38].

In the Network Calculus, characteristics of a *cumulative function* $F(t)$ describing the data traffic flow by *the number of flow bits observed in the time interval* $[0, t]$ must be identified. The communication network consists mainly of a set of switches (or routers) which represent the service stations (or ports) for the data flows passing through the network; connection configuration of these ports is supposed perfectly known. Any arriving data flow needs a guaranty to be served at each port, so it is upper-bounded by an ***arrival curve*** and lower-bounded by a ***service curve*** [39].

The *arrival curve* defines constraints on the traffic flow arriving at a port; thus, variations of function $F(t)$ are supposed to be upper-bounded by an increasing function $\alpha(t)$, named arrival curve [40]:

$$F(t) - F(s) \leq \alpha(t-s), \forall s \leq t. \tag{2.2}$$

One of the most used arrival curves is the so-called (σ, ρ)-model proposed in [41], which is a simple linear model:

$$\alpha(t) = \sigma + \rho t, \tag{2.3}$$

where σ signifies the burstiness of the flow in bits and ρ represents an upper bound on the long-term average rate of the traffic flow in bits/s.

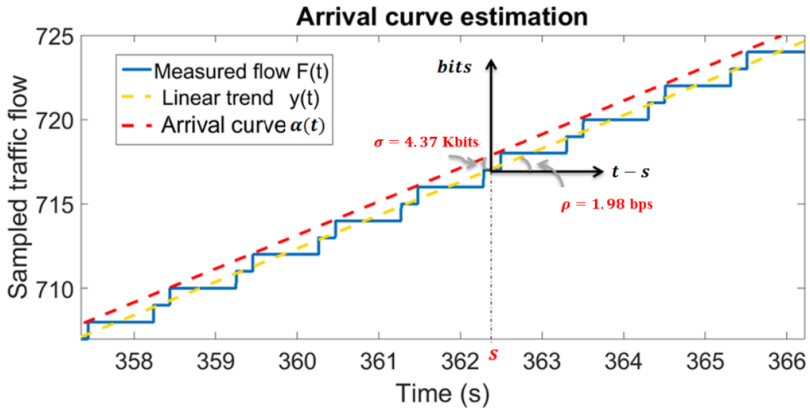

Figure 2.15: Determining arrival curve parameters by identifying the upper-bound linear curve of cumulative function $F(t)$ – illustration for first flow at first port, corresponding to scenario in Fig. 2.14 [38].

Effective determination of these two parameters results from linear curve fitting of the upper bound of measured cumulative function $F(t)$ for each flow, as shown in Fig. 2.15 as an example for the first flow passing through the first port in the considered load-shedding scenario.

The *service curve* is a function of time defining lower bounds on the services provided by ports during a defined time interval. The rate-latency $\beta(t)$ model is a widely used service curve model represented by a linear function as

$$\beta(t) = R[t-T]^+, \tag{2.4}$$

where $[x]^+$ denotes the $max\{x, 0\}$, R signifies the transmission rate in bits/s and T represents the latency in seconds [40]. It is said that a flow receives $\beta_{R,T}$ as a service curve when that flow is served by the rate of R in T time after its arrival at the service system. If there is only one flow passing through a port, R and T are taken from the port (switch or router) datasheet. If there is more than one flow, then datasheet values are penalized to reflect influence of the other flows – exact penalizing formulae depend on the adopted queue-scheduling policy, that is, either First Input First Output (FIFO) or Priority Queuing (PQ) [42].

Network calculus is developed in the *min-plus* algebra, according to which the message transmission delay for each flow j passing through each port i is upper-bounded by a quantity depending on the characteristics of its arrival curve, *i.e.*, σ_j, and the received service from that port, *i.e.*, T_i and R_i:

$$D_{i,j} \leq h(\alpha_j, \beta_i) = T_i + \frac{\sigma_j}{R_i} \tag{2.5}$$

Further, estimation of maximum transmission delay relies upon building several matrix-form models – physical connection model, logical connection model, source model and service model [43] – in relation with the *digraph* representation of the network, supposed completely known, then by using these models to obtain the *message distribution matrix* for each flow j, S_j. Information within S_j matrix is then used for maximum delay estimation of each traffic flow, based on corroborating estimations of form (2.5).

The proposed methodology – synthesized in Figure 2.16 – is therefore essentially an ***identification-based*** one, *i.e.*, consisting in fitting objectively measured data on models with known structure. Here D is the number of data flows passing through a number P of service stations (switches or routers). First, the arrival curve is fitted over the measured flows by means of an identification process resulting in the (ρ,σ)-model, as illustrated in Fig. 2.15. Then, message distribution is modeled and the maximum delay is estimated for each flow receiving services at each port. To evaluate the estimation effectiveness, estimated values are compared against delays measured objectively by a network analyzer – in this case, Wireshark. Comparison shows very satisfactory estimation errors (within 10%).

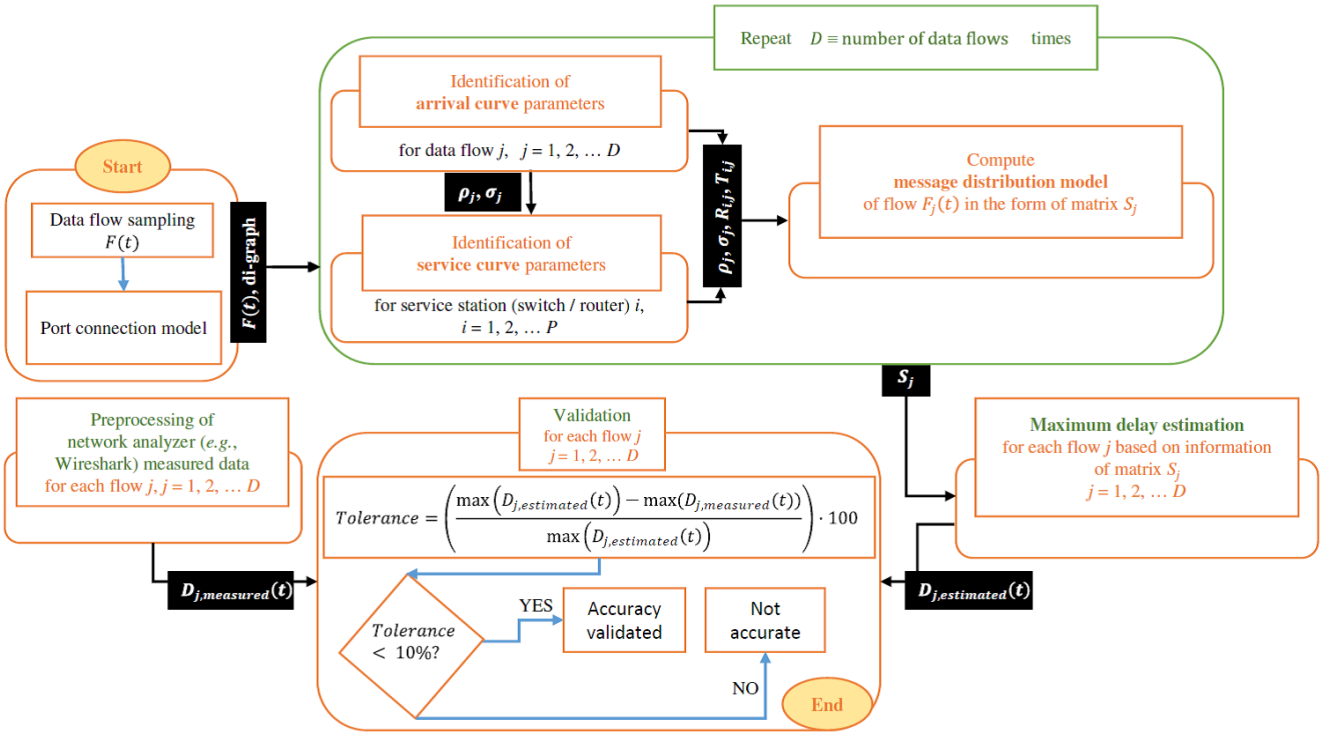

Figure 2.16: Major-step flowchart of the proposed identification-based methodology of maximum communication delay estimation for networks with completely known configuration [38].

The analytical-method-based maximum delay estimation proves reliable; however, it is limited to the cases with a completely known network structure, which is the case of the proprietary networks. If *a priori* knowledge about

the communication network is not available, some other estimation approach should be envisaged.

These results were obtained within the collaboration with Ph.D. student Ronak FEIZIMIRKHANI, working under the co-supervision of Professor Yvon BÉSANGER and myself, with the help of R&D engineers Antoine LABONNE and Thierry BRACONNIER, and are presented in the journal article below, as main concluding publication result:

- R. Feizimirkhani, A.I. Bratcu, Y. Bésanger, A. Labonne, T. Braconnier (2021). A methodology for the evaluation of the message transmission delay over IEC 61850 communication network – a real-time HV/MV substation case study. *Sustainable Energy, Grids and Networks*, 28, art. no. 100555.

While this method is independent of the communication protocol, the IEC 61850 protocol serves to illustrate its effectiveness. The method is applied on a pre-sampled traffic data, *i.e.*, off-line. On-line application of this method on a sliding T-width time window on an *a-priori*-not-known, possibly evolving network, would give a time evolution of the maximum delay. Such information may further be used with machine-learning algorithms to predict delay upper bounds. In addition, more complex scenarios such as inter-substation communication with faults, modern QoS strategies (*e.g.*, Priority Queuing) and dynamic networks (*e.g.*, delay optimal routing) or some message characteristics such as variable-length data, on-line flow studies while they are generated by different sources with different flow rates are interesting to be analyzed.

This topic is presently under ***ongoing exploration***, in particular during the post-doctoral internship of Ronak FEIZIMIRKHANI. Its average-term further development makes the object of prospective research directions, as detailed in Chapter 5, Section 5.3.

Chapter 3

Mitigating unpredictability of renewable energy conversion systems (RECS) by optimal control methods

This chapter attempts offering an overall view of our main research contributions in solving control problems for renewable energy conversion systems (RECS), usually involving ***multi-criteria dynamic optimization***, expressed in terms of sometimes sophisticated ***trade-offs*** to take account of ***antagonistic objectives*** and complex constraints. The different mathematical formulations and solving approaches employed to this end are overviewed in the introductory Section 3.1.

The reporting made here roughly covers a ten-year time span (**2003–2013**), with some publications slightly exceeding this period. Most of the results had been obtained before having joined GIPSA-lab in Grenoble, namely during a part (2003–2011) of my time at "Dunărea de Jos" University of Galaţi in Romania and my postdoctoral fellowship at G2ELab in Grenoble (2008–2009). Sections 3.2, 3.3 and 3.4 are each dedicated to an instance of RECS, namely, to wind energy conversion systems, micro-hydro – *i.e.*, water-turbine-based – energy conversion systems and photovoltaic systems, respectively.

Some useful insights are aimed at in the concluding Section 3.5.

3.1 From control objectives to formal control approaches

This section aims at pointing out the main steps to take on the way from formulation of control objectives – in terms specific to each RECS technology – to mathematical modelling and then identification of most appropriate formal control approaches to employ. Two classes of RECS are here considered, which are distinguished by the presence – and absence, respectively – of moving mechanical parts. Thus, the first class is based on a mechanical-to-electrical conversion, involving *rotating turbines as prime movers* – more precisely, wind energy conversion systems (***WECS***) and micro-hydro energy conversion systems (***miHECS***) are those which our contributions are focused on. The other RECS class consists of the photovoltaic (***PV***) systems.

In order to fix ideas and further justify our global vision, some basic definitions and concepts characterizing the ***wind***-turbine-based RECS (WECS) are briefly introduced, that also apply to ***water***-turbine-based RECS (miHECS). Indeed, the analogy between these two types of RECS is very pertinent, being originated in the analogy

between the two primary *flowing* resources, the wind and the water, respectively.

Performance of a wind turbine is generally characterized by means of its non-dimensional characteristic performance curves [44]. Thus, the tip speed ratio, λ, and the power coefficient, C_p – already qualitatively recalled in Section 2.1 of this memoir – are essential notions for expressing the ***aerodynamic performance of a wind turbine***.

The ***tip speed ratio*** is the ratio between the peripheral blade speed and the wind speed:

$$\lambda = \frac{R \cdot \Omega_l}{v}, \tag{3.1}$$

with R being the blade length, Ω_l being the low-speed shaft rotational speed and v being the wind speed.

The non-dimensional ***power coefficient***, C_p, describes the power extraction efficiency of a wind turbine. Theoretical maximum of $C_p(\lambda)$, obtained by assuming perfect blade design, equals 0.59 and is called the *Betz limit*. For control purposes, an useful remark is that curve $C_p(\lambda)$ is ***unimodal*** – Fig. 3.1 presents an instance of this curve, namely for a typical two-bladed wind turbine – meaning that the power conversion efficiency has a well determined maximum for a specific tip speed ratio, denoted by λ_{opt}. The *torque coefficient*, denoted by C_Γ and defined as:

$$C_\Gamma(\lambda) = \frac{C_p(\lambda)}{\lambda}, \tag{3.2}$$

is an additional variable that characterizes the wind torque, Γ_{wt}.

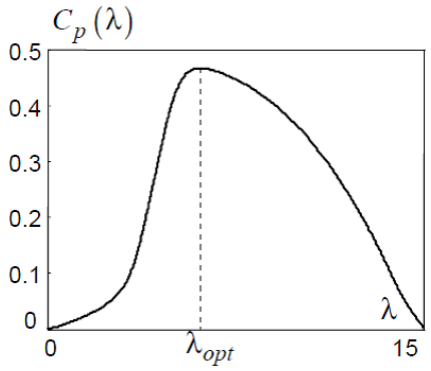

Figure 3.1: Unimodal allure of a wind turbine's power coefficient, C_p, as function of its tip speed ratio, λ [44].

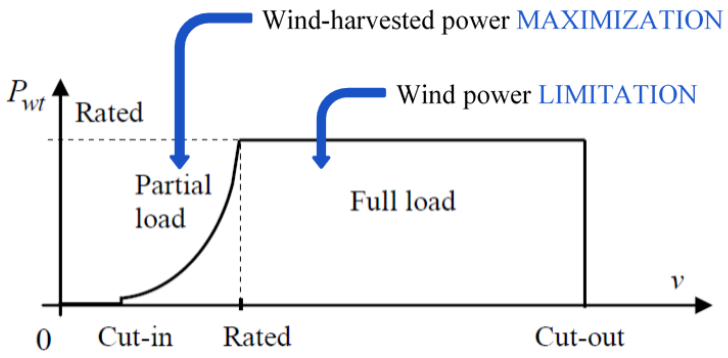

Figure 3.2: Wind power *versus* wind speed characteristic, with identification of main control objectives for each operating region.

The ***wind-harvested power*** by a wind turbine rotating in air of density ρ is expressed as [44]:

$$P_{wt} = \frac{1}{2} \cdot \rho \cdot \pi R^2 \cdot v^3 \cdot C_p(\lambda), \tag{3.3}$$

that allows concluding that the captured power characteristic, $P_{wt}(\Omega_l)$, at constant wind velocity, has the same unimodal allure as the power coefficient in Fig. 3.1. Therefore, the turbine rotor outputs non-negligible mechanical power if rotating in an intermediary speed range, which depends on the wind speed.

Fig. 3.2 presents the different operating regions of a wind turbine, in relation with the wind speed. A wind turbine operates, with different dynamics, from the cut-in wind speed (usually 3–4 m/s, for modern wind turbines) to the cut-out wind speed (around 25 m/s). The wind power varies proportionally with the wind speed cubed – according to (3.3) – until it reaches the wind turbine rated power corresponding to the rated wind velocity. The wind turbine operation range is thus splitted in two: below the rated (also called ***partial-load region***) and ***full-load region*** (between the rated and the cut-out wind speed). As also indicated in Fig. 3.2, while in partial load the control objective is ***wind power maximization***, in full load the captured power must be ***limited to the rated*** by control action to avoid mechanical damage.

Our contributions focus on the *optimal control of WECS in partial-load region* – more generally, on the ***optimal control of rotating-turbine-based RECS*** – so it is this topic that will be detailed next. Roughly speaking, the aim is the ***Maximum Power Point Tracking*** (MPPT) – as anticipated in Section 2.1 – possibly included either in a more complex optimization objective to suitably express some desired trade-off, or in a multi-level control/supervising structure to take account of additional constraints.

To further fix ideas, the turbines considered here have *fixed pitch*, therefore, the MPPT is enabled by the concept of ***variable-speed operation*** [11]. It is mainly about ***hill-climbing*** methods, ***perturb-and-observe*** (PO)-based methods – among which ***extremum seeking control*** (ESC) – ***linear quandratic gaussian*** (LQG) and ***sliding mode*** control. Some of the control approaches employed for WECS were also applied for miHECS, as presented next within this chapter. Note also that, while application of LQG and sliding mode control was particularly adapted to the first class of RECS (*i.e.*, with moving parts), hill-climbing and ESC are examples of application to both classes of RECS considered here – in particular, for implementing the MPPT for PV systems, whose unimodal allure of curves of output-power-*vs.*-voltage has already been recalled in Fig. 2.1 in Section 2.1.

As regards WECS power limitation in full-load region (*i.e.*, for high winds), a comprehensive overview – including both passive and active control – is given in the fourth chapter of our monograph [29].

The above introduction of maximizing the wind-harvested power in WECS serves as an illustrative case able to suggest generalizations for formulating the MPPT under a more general form. Such an MPPT formalization would be applicable – with adaptations – to practically any class of RECS, as they are all characterized by unimodal power conversion efficiency curves. Under some conditions, these curves can be multimodal – such as for PV system configurations under partially-shaded conditions – and in this case further extensions and adaptations may apply [45]–[47].

Next, presentation of **MPPT under a form generally applicable to all RECS** is aimed at.

MPPT is difficult to put in place when ***precise information about RECS unimodal efficiency curves is not available***, which is almost always the case in practice. That is, neither the abscissa, nor the ordinate of the maximum efficiency curve is known – moreover, both of them vary with the primary resource – *i.e.*, with either the wind/water speed for WECS/miHECS, or the solar irradiance level for the PV systems – which, in addition, is usually difficult and/or expensive to measure. Thus, a method of "primary resource tracking" should be implemented, able to ensure operation at maximum power irrespective of resource variations. It is about tracking the ***Optimal Regimes Characteristic*** (ORC), defined as the locus of all maximum power points. Figs. 3.3 a) and b) present the ORC allure of a fixed-pitch WECS in the wind-power-*versus*-rotational-speed plane, and of a PV system in the PV-power-*versus*-voltage plane, respectively. In particular, Fig. 3.3b) illustrates a case where the peak power locus does not correspond to a function, but to a curve.

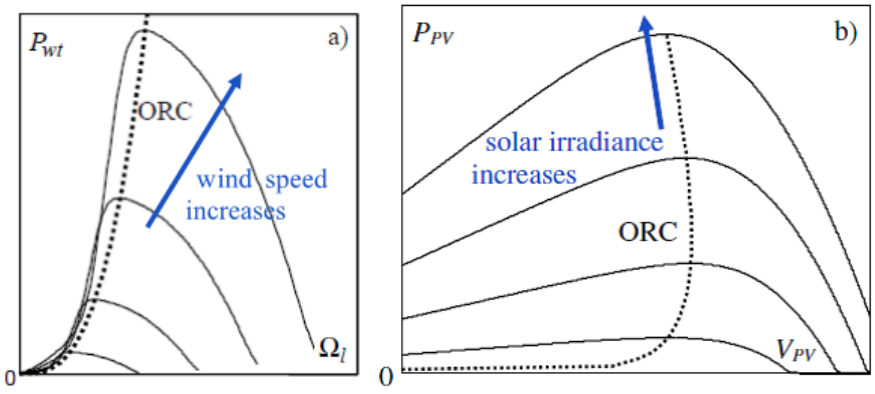

Figure 3.3: Example of locus of maximum power points on the power curve of a RECS, materializing the ORC when the primary resource varies: a) case of a fixed-pitch WECS; b) case of a PV system.

The basic idea of MPPT is that, given a certain value of the primary resource, to adjust the reference of the independent variable – *i.e.*, the abscissa – such that to maximize the dependent variable, *i.e.*, the power. Next, let the abscissa be generically denoted as x. In order to establish whether its reference must be either increased or decreased, it is necessary to estimate the current position of the operating point in relation to the maximum of the power curve. This can be done in two main ways, as follows.

- The abscissa reference is modified by a variation Δx, the corresponding change in the captured power, $\Delta P_{harvested}$, being determined in order to estimate the value $\partial P_{harvested}/\partial x$. The sign of this value indicates the position of the operating point in relation to the maximum of characteristic $P_{harvested}(x)$. If the abscissa reference is adjusted in ramp with a slope proportional to this derivative, then the system evolves to the optimum, where $\partial P_{harvested}/\partial x = 0$.

  This MPPT principle is illustrated in Fig. 3.4, where four decision cases are identified, depending on the actual operating point position in relation to the maximum on the power curve, under a form suggesting the action of climbing a hill. Then, based on the relation $\dfrac{\partial P_{harvested}}{\partial x} = \dfrac{\mathrm{d}P_{harvested}}{\mathrm{d}t} \Big/ \dfrac{\mathrm{d}x}{\mathrm{d}t}$, the decision rules can be inferred as shown in Table 3.1.

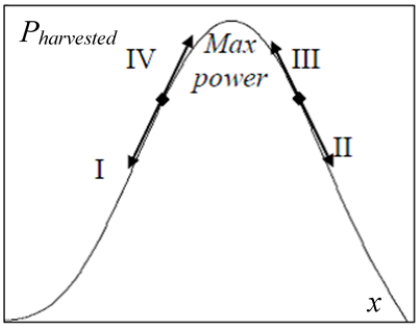

Figure 3.4: Illustration of the hill-climbing decision process in MPPT.

Table 3.1: Basic logic decision rules of MPPT, inferred from Fig. 3.4.

$\frac{\mathrm{d}x}{\mathrm{d}t}$ \ $\frac{\mathrm{d}P_{harvested}}{\mathrm{d}t}$	< 0	> 0
< 0	$x \nearrow$ – case I	$x \searrow$ – case II
> 0	$x \searrow$ – case III	$x \nearrow$ – case IV

- A ***probing signal is added*** to the current x reference; this signal is a slowly variable sinusoid, whose amplitude does not significantly affect the system operation, but still produces a detectable response in the harvested power evolution. The operating point position in relation to the maximum is then obtained by comparing the phase lag of the probing sinusoid and that of the sinusoidal component of active power. If the phase lag is zero/π, then the current operating point is placed on the ascending/descending part of $P_{harvested}(x)$; therefore, the slope of the x reference must increase/decrease in order for the operating point to approach the maximum. Around the maximum, the probing signal does not produce any detectable response, hence the abscissa reference does not any longer have to change.

The above simplified presentation of MPPT techniques assumes negligible influence of factors like the high-frequency variations of the primary resource or some system unmodelled or parasitic dynamics.

The second version of MPPT led to formalising the ***Extremum Seeking Control*** (ESC) approach, which relies upon finding the extremum of some unimodal hard-to-model dynamics based on the plant's response to some sinusoidal probing signals [48], [12], [13].

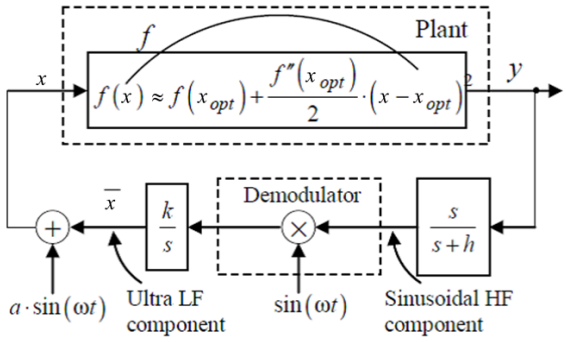

Figure 3.5: Explanation of the ESC principle [12].

Fig. 3.5 [12] explains the ESC principle by means of a closed-loop block diagram. The ESC controller performs a modulation/demodulation operation and its output has a harmonic component called the probing signal. The role of the washout filter is to separate the high-frequency components of the plant output. After demodulation and integration, the average component of the control input is obtained, which is further summed up with the probing signal and fed back to the plant. Fig. 3.5 depicts the case of a plant containing a dynamic described by a generic unimodal function denoted by $f(x)$, which has a maximum at x_{opt}. It is assumed that the argument of function f has two components: an average one, $\overline{x}$, and a harmonic probing component, of amplitude a.

Consider then the Taylor series of this function around its maximum, $f(x_{opt})$, with $\widetilde{x} = x_{opt} - \overline{x}$ denoting the optimum searching error. As the integrator constant, k, and the excitation amplitude, a, are positive and the function f is concave in its extremum – *i.e.*, $f''(x_{opt})$ is negative – based on the diagram shown above, it results that the search error gradient is negative [13]:

$$\frac{\mathrm{d}\widetilde{x}}{\mathrm{d}t} = \frac{k \cdot a^2 \cdot f''(x_{opt})}{4} \cdot \widetilde{x}, \tag{3.4}$$

thus corresponding to a convergent searching process. The excitation frequency, ω, must be sufficiently large to ensure closed-loop stability; the washout filter parameter, h, depends on this frequency [13].

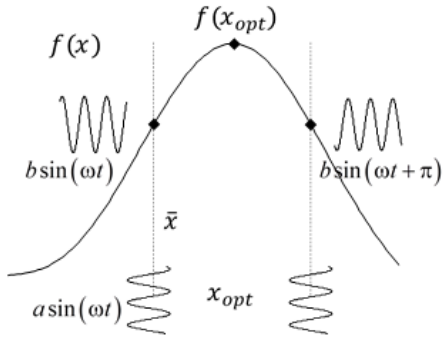

Figure 3.6: Application of ESC principle illustrated on the unimodal power conversion efficiency curve of a generic RECS.

Further insights can be formulated if considering the unimodal power conversion efficieny curve of a RECS, as in Fig. 3.6 – *e.g.*, power coefficient in the case of rotating turbines, power-*versus*-voltage curve in the case of PV systems, *etc.* The same generic notations $f(x)$ are preserved next for this curve. Consider a hypothetic ω-frequency sinusoidal variation of the variable x with a sufficiently small amplitude a. Depending on the position of the operating point on the slope of the efficiency curve, the $f(x)$ variation will be sinusoidal, in phase with the x variation for the ascending part and out of phase (with a phase lag of π) for the descending part (the intermodulation components for small a being neglected). It follows that the integrator input, $\mathrm{d}\widetilde{x}/\mathrm{d}t$, will toggle its sign as the operating point moves from a side to the other of the f optimum, and, assuming equal slopes of the $f(x)$ curve, its value – and consequently the search direction – varies as in:

$$\frac{\mathrm{d}\widetilde{x}}{\mathrm{d}t} = \pm k \cdot b \cdot sin^2(\omega t) \tag{3.5}$$

Equation (3.5) guarantees that the operating point will move to the optimal position with a speed of convergence depending proportionally on k and a and inverse proportionally on ω [13].

Applicaton of ESC in its above-described standard form appears to be almost naturally suited for RECS, especially when there are no moving parts. Indeed, while ESC techniques prove to be easily applicable, without great inconvenients, for example, to PV systems, injection of an artificial sinusoidal probing signal has some drawbacks when rotating turbines are involved. For example, in the case of WECS, given that the plant is naturally excited by a random signal, namely the wind, it would be difficult to separate the response to the probing sinusoid from the total output signal, which appears as random too. The solution would be to increase the signal magnitude and/or to use filters. However, large signals may induce supplementary mechanical loads, whereas filters provide delayed feedback information.

The idea of avoiding adding supplementary excitation led to formulate ***a new form of ESC, that of using the already existing perturbation, which is present as a result of the stochastic nature of the primary resource***. For example, in the case of WECS, this already-in disturbance is the wind speed turbulence. In this case, the modulation process is naturally achieved by means of (nonharmonic) high-frequency wind variations.

As detailed in Section 3.2, ***the wind speed turbulence used as searching signal within ESC*** ensures good performance, provided that information about system state is poor.

The same idea – of using already-in disturbances as probing (searching) signals – can be generally applied to RECS. For example, for ***some particular classes of grid-connected PV systems*** it is possible to put into evidence that certain signals contain ***sinusoidal components***, which can be used as ***already existing searching signals in ESC algorithms***. Contributions on application of this new ESC version, as well as of ***standard ESC*** for maximizing the power captured by PV systems, are detailed in Section 3.4.

Remark: ***Direct imposing of the optimal operating point position*** is a specific MPPT method for ***rotating prime movers*** – such as wind and water turbines – widely used in practice, especially for medium- and high-power turbines.

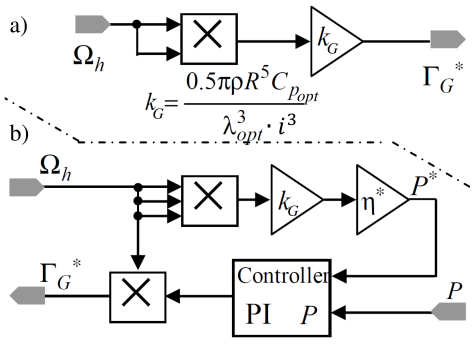

Figure 3.7: Two manners of implementing MPPT for rotating prime movers by directly imposing the optimal operating point position [29].

This method represents a rather *static* viewpoint, based on forcing the turbine rotor to operate in partial load at maximum power, corresponding to the instantaneous primary resource flow speed. Equivalently, this means imposing to the electrical generator the electromagnetic torque corresponding to the maximum power available in the resource. The turbine works at maximum efficiency when turning at optimal tip speed ratio, λ_{opt}, so the maximum power, $P_{harvested_{max}}$, is proportional to the generator rotational speed cubed, denoted by Ω_h in Fig. 3.7, where the index "h" stands for *high*-speed shaft:

$$P_{harvested_{max}} = \underbrace{\frac{0.5\pi\rho R^5 C_{p_{opt}}}{\lambda_{opt}^3 \cdot i^3}}_{k_G} \cdot \Omega_h^3 = k_G \cdot \Omega_h^3 \tag{3.6}$$

In (3.6) $C_{p_{opt}} = C_p(\lambda_{opt})$ and "i" denotes the ratio of the drive train multiplier between the low-speed shaft – the one driven by the resource flow – and the high-speed shaft, that of the generator; ρ is the resource (air/water) mass density and R is the turbine radius, *i.e.*, the length of its blades. Fig. 3.7 makes appear proportionality coefficient k_G and indicates two manners of implementing this kind of MPPT: a) by imposing the generator torque reference, Γ_G^*, computed based on the generator rotational speed measure, Ω_h:

$$\Gamma_G^* = \frac{P_{harvested_{max}}}{\Omega_h} = \frac{0.5\pi\rho R^5 C_{p_{opt}}}{\lambda_{opt}^3 \cdot i^3} \cdot \Omega_h^2 = k_G \cdot \Omega_h^2, \tag{3.7}$$

and b) by imposing a power reference, P^*, and using a PI controller to modify the generator mechanical characteristic and further obtain the torque reference, Γ_G^*. Conversion efficiency, η^*, may also be present in P^* computation.

As the control structure allows tracking the primary resource flow speed within admissible limits of mechanical loads, this method can only be used under slow variations of the resource, thus achieving a static optimization. For turbulent conditions, filtering is necessary, along with using compliant PI parameters, to ensure sufficiently slow closed-loop dynamics. This method is strongly sensitive to parameter variations.

While remaining focused on **rotating-prime-mover-based RECS**, the necessity of achieving power maximization along with reasonable mechanical loads – in a reliability-aware context, of fatigue loads reduction for prolonging the RECS service time – led to idea of properly sizing a so-called **energy-reliability trade-off**, expressed as an optimality criterion. Next section is dedicated to some of the contributions we proposed by following this idea, for the specific case of *wind* energy conversion systems (WECS).

3.2 Optimal control of wind energy conversion systems (WECS)

Placing the ***harvested power maximization*** within a ***sustainable*** approach renders mandatory to also take into account reliability issues related to the WECS mechanical structure, that is, ***minimizing intensity of loads***, responsible on a long term of fatigue phenomena. A ***multi-purpose optimization*** is achieved in this way.

To fix ideas and introduce main concepts, symbols and notations, the general configuration of a horizontal-axis-turbine-based WECS is depicted in Fig. 3.8 in two versions, fundamentally differentiated from the point of view of power flow control, enabled by means of the AC/DC/AC – also called *back-to-back* – power electronic topology.

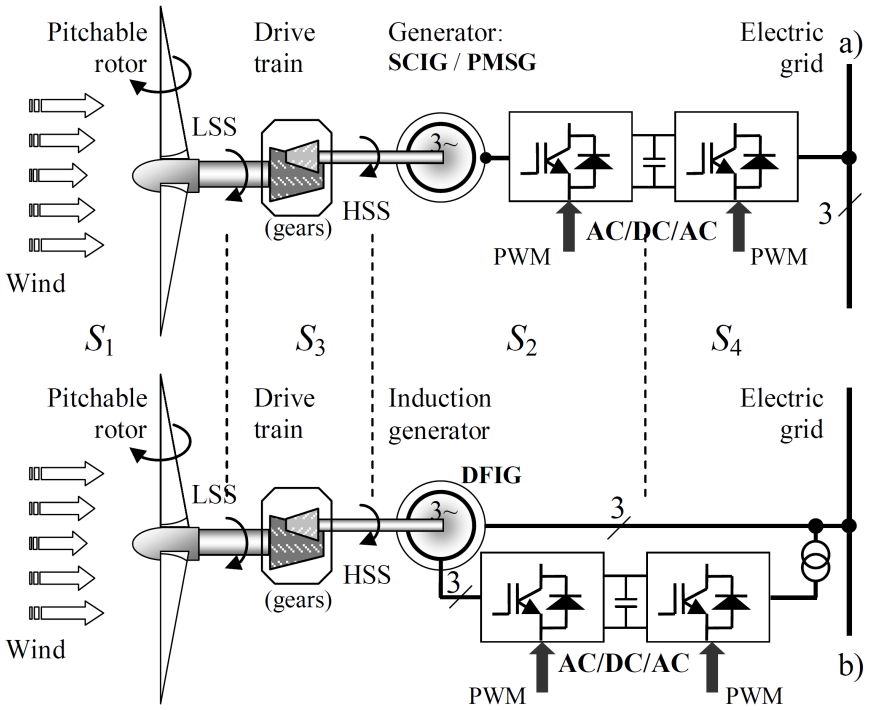

Figure 3.8: General configuration of a WECS based on a horizontal-axis turbine and different generators: a) SCIG/PMSG; b) DFIG [29].

Thus, Fig. 3.8a) presents the case based on either a squirrel-cage induction generator (SCIG) or a permanent-magnet synchronous generator (PMSG) – in this case the AC–AC converter is stator grid-connected and rated at the generator's power level. In Fig. 3.8b) a doubly-fed induction generator (DFIG) is employed – in this case, it is the rotor that is interfaced with the grid by means of the power electronic converter, so only part of the generated power is transferred to the grid. From a system viewpoint, the conversion chain consists into four interacting main components : the *aerodynamic subsystem* (AS) – S_1 and the *electromagnetic subsystem* (EMS) – S_2, interacting by means of the *drive train* (mechanical transmission) – S_3, whereas S_4 denotes the *grid interface*.

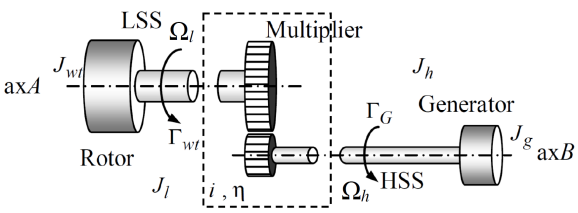

Figure 3.9: Schematics of a WECS *rigid* drive train [29].

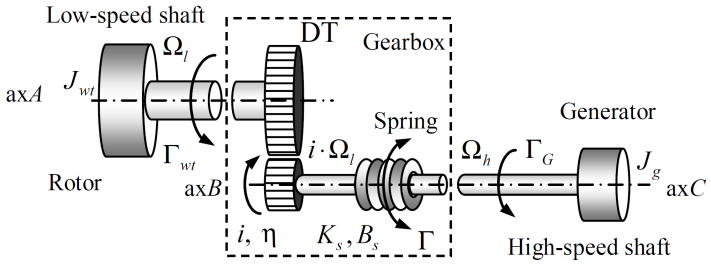

Figure 3.10: Schematics of a WECS *flexible* drive train [29].

The drive train is single (fixed) multiplying ratio, denoted by i, of efficiency η, either *rigid* (Fig. 3.9) or *flexible* (Fig. 3.10). Within the drive train, LSS and HSS denote low- and high-speed shafts, respectively, with Ω_l and Ω_h being the rotational speed of the LSS and HSS, respectively. Figs. 3.9 and 3.10 make appear equivalent inertias J_l and J_h, which depend on wind turbine axis inertia, J_{wt}, and generator inertia, J_g, as well as wind turbine torque, Γ_{wt}, and generator torque, Γ_G. For the flexible case – where LSS and HSS are elastically coupled by means of a spring of stifness K_s and damping B_s – a new internal torque Γ is rendered visible.

The action of two control subsystems is suggested on Fig. 3.8: ensuring the variable-speed operation (exerted on S_1, S_2 and S_3) and respectively controlling the power transfer at grid imposed parameters (exerted on S_4).

Contributions briefed within this section were obtained within the collaboration with Ph.D. student Iulian MUNTEANU, working under the supervision of Professor Emil CEANGĂ at "Dunărea de Jos" University of Galaţi, Romania, and under the supervision of Professors Daniel ROYE and Seddik BACHA during his 2005 doctoral internship at G2ELab in Grenoble, France. They are as follows.

- A first control approach starts from formulating an optimal control problem with ***mixed criteria***, whose central idea consists in applying the ***frequency separation principle*** – widely used in control systems –

in an original manner, adapted to WECS particularities and needs. Thus, it is shown that the two above-mentioned antagonistic requirements can be expressed within two distinct dynamic (frequency) domains; hence, a two-time-scale WECS dynamic is identified, driven by the ***seasonal*** (in ***low*** frequency) and the ***turbulence*** (in ***high*** frequency) component of the wind speed, respectively.

In the ***high-frequency domain***, the two antagonistic objectives are cast into an ***LQG problem***. The resulting ***control structure*** has the merit of being ***desensitized to WECS parameter variations***, thus rendering unnecessary adaptive structures. Main results are resumed in Subsection 3.2.1; they were published in:

I. Munteanu, N.A. Cutululis, A.I. Bratcu, E. Ceangă (2005). Optimization of variable speed wind power systems based on a LQG approach. *Control Engineering Practice*, 13(7), 903–912.

Moreover, this vision can be generalized to ***all the main WECS control objectives*** – such as, for example, those related to electric power conditioning – as they ***can be treated as pairs of antagonistic goals taking place into two separable frequency domains, respectively*** – this idea is detailed as a global conclusion of our monograph [29].

- A second solution employs ***sliding mode control*** techniques: captured power maximization is guaranteed by operating the wind turbine on an ***adaptive sliding surface***, whose position in relation to the *Optimal Regimes Characteristic* (ORC) defines the sought-for energy-reliability trade-off. Main results are synthesized in Subsection 3.2.2; they were reported in:

  I. Munteanu, S. Bacha, A.I. Bratcu, J. Guiraud, D. Roye (2008). Energy-reliability optimization of wind energy conversion systems by sliding mode control. *IEEE Transactions on Energy Conversion*, 23(3), 975–985.

- A third, ***ESC-based***, solution takes profit of the fact that the ***searching signal*** is already present in the system excitation: it is about the ***turbulence component of the wind speed***, modelled as a psedo-random signal. The information about the actual operating point position in relation to the maximum power point is decided upon the phase lag between the captured power signal and turbine rotational speed signal. This approach is resumed in Subsection 3.2.3 – details can be found in:

  I. Munteanu, A.I. Bratcu, E. Ceangă (2009). Wind turbulence used as searching signal for MPPT in variable-speed wind energy conversion systems. *Renewable Energy*, 34(1), 322–327.

3.2.1 Frequency-separation-based optimal control of WECS

Fig. 3.11 gives a glimpse of how WECS dynamics can be split into two distinct frequency domains, respectively corresponding to the two spectral ranges identified in the wind speed dynamics: a low-frequency dynamic due to the ***seasonal*** (long-term, ***low-frequency***) component of the wind velocity, v_s, and a fast, ***high-frequency*** dynamic in response to the action of the ***turbulent*** wind velocity, v_t. In Fig. 3.11 $S(f)$ is the wind speed power spectral density in Van der Hoven's large-band (six-decade) wind speed model [44].

The low-frequency component, v_s , determines the average position of the operating point on the wind turbine characteristic – this position is subject to slow, low-frequency dynamics, considering that their spectrum is entirely placed inside the turbine bandwidth – and the turbulence component, $\Delta v = v - v_s \equiv v_t$, excites the high-frequency dynamics by generating high-frequency variations around this point. Hence, the evolution of WECS measurable variables (*i.e.*, generator rotational speed, Ω_h), is the superposition of some slow dynamics (SD) and some turbulent dynamics (TD), as suggested in Fig. 3.11. Thus, the idea of separately compensating the two dynamics [49], by designing a two-loop control structure, naturally resulted. Based on using the measured system output, Ω_h, and measured total wind speed, v, as feedback information, the two loops use estimated values of v_s and v_t, respectively.

The electromagnetic subsystem (EMS, identified as S_2 in Fig. 3.8) is torque controlled, so it can be treated as a first-order element providing electromagnetic torque much faster than the drive train's dynamic.

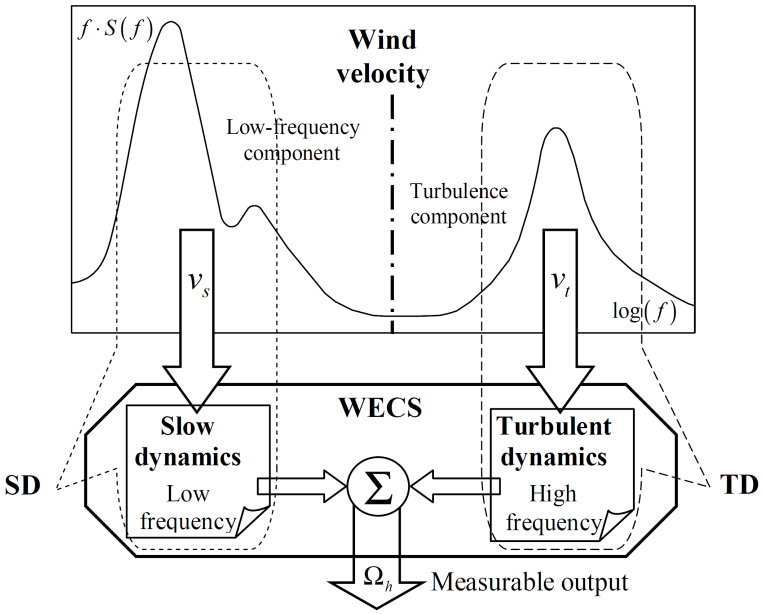

Figure 3.11: Intuitive illustration of the frequency separation of WECS dynamics [29].

Because the torque variations induced by the seasonal wind component, v_s, are negligible, the SD-related optimization problem may be reduced to λ_{opt} tracking. In contrast, the mechanical fatigue due to the turbulence wind component, v_t, is significant, so the TD-related optimization problem may be cast into an LQG dynamic optimization. Two control loops result in this way: a low-frequency loop (***LFL***), using v_s within a steady-state optimal controller (***tip speed controller*** – TSC) to ensure steady-state operation on the ORC and a high-frequency loop (***HFL***), using v_t within an ***LQG controller***, for dynamic optimization of the linearized system's behaviour around this point.

Therefore, choice of the ***frequency limit between what is considered SD and TD****, respectively, is crucial in ultimately trading off the power optimization against the mechanical stress alleviation.*

Note also that, as the initial, global optimization problem was split into two sub-problems, each of which is intended to be solved to optimality, then the solution obtained by aggregating the two separate solutions is in general ***sub-optimal***. Its closeness to the ideal, optimal solution depends again upon ***how sharply the two wind dynamics can be separated***.

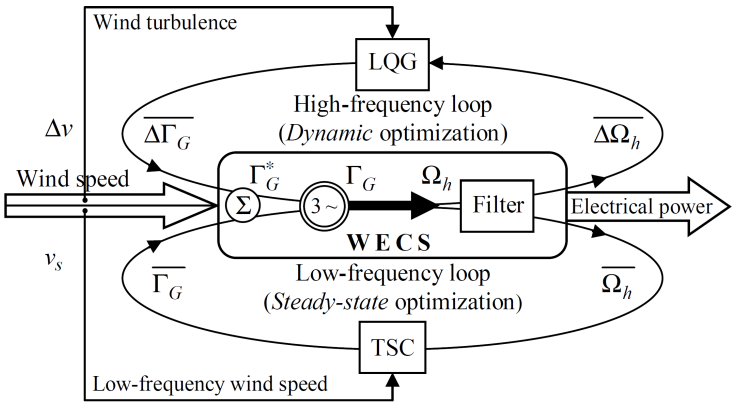

Figure 3.12: Block diagram suggesting implementation of frequency separation principle by means of a two-loop control structure [49].

Next, any variable x from the system is decomposed into two components: a steady-state one, denoted by $\overline{x}$, and a high-frequency one, representing variations around the steady-state value, $\Delta x = x - \overline{x}$, with $\overline{\Delta x} = \Delta x/\overline{x}$ being the normalized variations.

The steady-state value, $\overline{x}$, belongs to the LFL and the normalized variation, $\overline{\Delta x}$, is treated within the HFL. The block diagram of the frequency-separation-based two-loop optimal control structure – referred to in the following by its acronym, **2LFSP** [49], [29] – is shown in Fig. 3.12. $\overline{\Omega_h}$ and $\overline{\Delta\Omega_h}$ are fed back into the LFL and the HFL, respectively, to further provide each a torque reference component, $\overline{\Gamma_G}$ and $\overline{\Delta\Gamma_G}$ respectively. The total torque reference to be fed into the electromagnetic subsystem is the sum $\Gamma_G^* = \overline{\Gamma_G} + \Delta\Gamma_G$, with $\Delta\Gamma_G = \overline{\Delta\Gamma_G} \cdot \overline{\Gamma_G}$. The slow dynamics also embeds the dynamic of the associated exogenous signal, v_s, while $\Delta v = v - v_s \equiv v_t$ is embedded in the turbulent dynamics.

The steady-state optimization aimed at in the **LFL** can be ensured by tracking the low rotational speed corresponding to λ_{opt}, $\Omega_{l_{opt}} = v_s \cdot \lambda_{opt}/R$, enabled by variable-speed operation. A tip speed controller (**TSC** in Fig. 3.12) is used for this purpose, whose reference is computed based upon v_s. A classical PI and an on-off controller are two possible versions of such a controller.

The *PI control* loop can be either a torque, speed or active power loop, with an action equivalent to imposing a

generator torque reference given by (3.7), which is often called the **$\mathbf{K}\cdot\boldsymbol{\Omega}^{\mathbf{2}}$ law** [11], [44], [50], [51]. As regards the *on-off controller*, this consists in zeroing the difference $\sigma(t)=\lambda_{opt}-\overline{\lambda(t)}$, where $\overline{\lambda(t)}$ is computed with the seasonal, low-frequency wind speed component, v_s, and a measure of low-speed shaft rotational speed, Ω_l [52], [53]:

$$\overline{\lambda(t)}=\frac{R\cdot\Omega_l}{v_s} \tag{3.8}$$

As mentioned before, the role of the **HFL** is to alleviate the mechanical stress induced by exclusively aiming at maximizing the harvested power within the LFL. To this end, the HFL control problem is cast into an LQ Gaussian optimization problem defined on the linearized model around the maximum-power steady-state operating point – as ensured by the LFL – with an energy-reliability trade-off performance index of the form [54]:

$$I=\underbrace{E\left\{\alpha\cdot\left[\lambda(t)-\lambda_{opt}\right]^2\right\}}_{I_1\text{ – power maximization}}+\underbrace{E\left\{\Delta\Gamma_G^2(t)\right\}}_{I_2\text{ – mechanical effort minimization}}\rightarrow\min, \tag{3.9}$$

where $E\{\cdot\}$ is the statistical average symbol. Parameters of the linearized model depend on the operating point, that is, on the low-frequency wind speed, v_s. It is especially the case of the ***torque parameter***, γ, which depends significantly on v_s through the tip speed ratio $\overline{\lambda(t)}$ given by (3.8) [54]:

$$\gamma=\gamma\left(\overline{\lambda(t)}\right)=\frac{C_p'(\overline{\lambda(t)})\cdot\overline{\lambda(t)}}{C_p(\overline{\lambda(t)})}-1, \tag{3.10}$$

where $C_p'(\lambda)=\mathrm{d}C_p(\lambda)/\mathrm{d}\lambda$. The gain-scheduling control solution proposed in [54] was supposing the exact knowledge on how parameters, especially γ, depend on the operating point. Or, this is practically never the case, as the information about $C_p(\lambda)$ is often poor or difficult to obtain. ***The combined action of the two control loops inside the 2LFSP practically desensitizes the system in relation to the static operating point, by cancelling the variation of the torque parameter, γ, vs. the tip speed,*** λ. Indeed, if the system is maintained by the LFL around the maximum-power steady-state point, irrespective of the wind speed, then $C_p'(\lambda_{opt})\approx 0$; therefore, according to (3.10), γ is maintained around:

$$\gamma(\lambda_{opt})\approx -1 \tag{3.11}$$

To fix ideas, the case of a ***rigidly-coupled induction-generator-based low-power WECS*** is chosen next to particularize application of 2LFSP control strategy [49]; in [55] application of 2LFSP to *flexibly*-coupled WECS is presented. Based on slow and turbulent WECS dynamics modelling, the control design methods of LFL and HFL are briefed, respectively. Effectiveness of the combined action of the two control loops is illustrated by some real-time (on-line) simulations carried out on an electromechanical WECS simulator.

WECS slow (low-frequency) dynamics model is obtained by tangent linearization of the mechanical interaction around an operating point. Thus, using notations introduced in Fig. 3.9, the first-order transfer function from the generator torque, $\overline{\Gamma_G}$, to $\overline{\Omega_h}$, the HSS rotational speed, results as:

$$H_{\overline{\Gamma_G}\rightarrow\overline{\Omega_h}}=-\frac{i^2/K_{wt}}{(i\cdot J_h)/K_{wt}\cdot s+1}, \tag{3.12}$$

where J_h is the HSS inertia, i is the speed multiplier ratio and K_{wt} is the absolute value of the slope of the wind-turbine-torque-*vs.*-LSS-speed curve, $\Gamma_{wt}(\Omega_l)$, in the chosen operating point. As *stable* operating points are placed on the descending part of the $\Gamma_{wt}(\Omega_l)$ curve, then K_{wt} is defined by: $K_{wt}=\left|\overline{\frac{\partial\Gamma_{wt}}{\partial\Omega_l}}\right|=-\overline{\frac{\partial\Gamma_{wt}}{\partial\Omega_l}}$.

Based on (3.12) – which indicates a linear system variant with the operating point, so ultimately with v_s – the ***LFL tip speed controller*** – TSC in Fig. 3.12 – can result as a PI controller, tuned, for example, according to the empirical Ziegler–Nichols procedure [56]. In any case, tuning of TSC parameters is not critical, because the low-frequency wind speed, v_s, varies much more slowly comparatively to the WECS dynamics.

WECS turbulent (high-frequency) dynamics model results as a linearized-in-*normalized*-variations model, namely obtained by considering as state variables the normalized variation of the low rotational speed around its steady-state value, $\overline{\Delta\Omega_l}$, and the normalized variation of the wind torque around its average value, $\overline{\Delta\Gamma_{wt}}$. The normalized wind speed variation, $\overline{\Delta v(t)}$, is here modelled as a pseudorandom process yielded by passing a white noise, $e(t)$, through a first-order shaping filter:

$$\dot{\overline{\Delta v(t)}} = \frac{1}{T_w} \cdot \left(e(t) - \overline{\Delta v(t)} \right), \tag{3.13}$$

where $T_w = L_t / v_s$ is the filter time constant, with L_t being the turbulence length, which is usually found empirically for a given wind site. Equation (3.13) results as a simplified adaptation of the non-integer-shaping-filter-based wind turbulence model in [57].

WECS high-frequency model can thus be put into the form of a linear system, having $\mathbf{x}(t) = \begin{bmatrix} \overline{\Delta\Omega_l(t)} & \overline{\Delta\Gamma_{wt}(t)} \end{bmatrix}^T$ as ***state*** vector, $u(t) = \overline{\Delta\Gamma_G(t)}$ as ***control*** input, $e(t)$ as ***disturbance*** input and $z(t) = \overline{\Delta\lambda(t)}$ as ***output***:

$$\begin{cases} \dot{\mathbf{x}} = \underbrace{\begin{bmatrix} 0 & 1 \\ \frac{\gamma}{T_w} & \frac{\gamma}{J_T} - \frac{1}{T_w} \end{bmatrix}}_{\mathbf{A}} \cdot \mathbf{x} + \underbrace{\begin{bmatrix} -\frac{1}{J_T} \\ -\frac{\gamma}{J_T} \end{bmatrix}}_{\mathbf{B}} \cdot u + \underbrace{\begin{bmatrix} 0 \\ \frac{2-\gamma}{T_w} \end{bmatrix}}_{\mathbf{L}} \cdot e \\ z = \underbrace{\begin{bmatrix} \frac{2}{(2-\gamma)} & -\frac{1}{(2-\gamma)} \end{bmatrix}}_{\mathbf{C}} \cdot \mathbf{x}, \end{cases} \tag{3.14}$$

where $J_T = \dfrac{\overline{\Omega_l} \cdot J_l}{\overline{\Gamma_{wt}}} = \dfrac{\overline{\Omega_h} \cdot J_h}{\overline{\Gamma_{wt}}}$ has dimensions of time constant and the different matrices can be identified: the state matrix $\mathbf{A}$, the input matrix $\mathbf{B}$, the exogenous disturbance matrix $\mathbf{L}$ and the output matrix $\mathbf{C}$.

Performance index in (3.9) is adapted to model (3.14) such as to express an LQG problem. Thus, the first component, I_1, corresponding to ***captured power maximization*** or, otherwise said, to ***maintaining the system around*** λ_{opt}, results as a quadratic form of the state vector:

$$I_1 = E\left\{ \overline{\Delta\lambda}^2(t) \right\} = E\left\{ \mathbf{x}^T(t) \cdot \mathbf{C}_\alpha^T \mathbf{C}_\alpha \cdot \mathbf{x}(t) \right\} \to \min, \tag{3.15}$$

with matrix $\mathbf{C}$ defined in (3.14) and matrix $\mathbf{C}_\alpha = \sqrt{\alpha} \cdot \mathbf{C}$. The second component, I_2, corresponding to ***mechanical (control) effort minimization***, results as:

$$I_2 = E\left\{ \overline{\Delta\Gamma_G}^2(t) \right\} = E\left\{ u^T(t) \cdot \mathbf{R} \cdot u(t) \right\} \to \min, \tag{3.16}$$

with matrix $\mathbf{R} = 1$. By summing up (3.15) and (3.16) the global index I is obtained:

$$I = E\left\{ \mathbf{x}^T(t) \cdot \underbrace{\mathbf{C}_\alpha^T \mathbf{C}_\alpha}_{\mathbf{Q}} \cdot \mathbf{x}(t) + u^T(t) \cdot \mathbf{R} \cdot u(t) \right\} \to \min, \tag{3.17}$$

Provided that the LFL is working properly, the parameters of the turbulent dynamic are time invariant; hence, the stated LQG dynamic optimization problem is also time invariant. LQG controller existence and uniqueness are guaranteed if the open-loop system meets a well-known set of structural properties, among which the controlability of ($\mathbf{A}$,$\mathbf{B}$) matrix pair [58]. The solution of this problem is the generator torque control input normalized variation obtained as full-state feedback:

$$u(t) \equiv \overline{\Delta\Gamma_G(t)} = -\mathbf{K} \cdot \mathbf{x}(t), \tag{3.18}$$

where the feedback vector gain $\mathbf{K} = \mathbf{R}^{-1} \cdot \mathbf{B}^T \cdot \mathbf{S}$ is computed based on the unique, symmetric and positive semi-definite matrix solution $\mathbf{S}$ of the Riccati algebraic matrix equation:

$$\mathbf{S}\cdot\mathbf{A}+\mathbf{A}^T\cdot\mathbf{S}+\mathbf{C}_\alpha^T\cdot\mathbf{C}_\alpha-\mathbf{S}\cdot\mathbf{B}\cdot\mathbf{R}^{-1}\cdot\mathbf{B}^T\cdot\mathbf{S}=0 \tag{3.19}$$

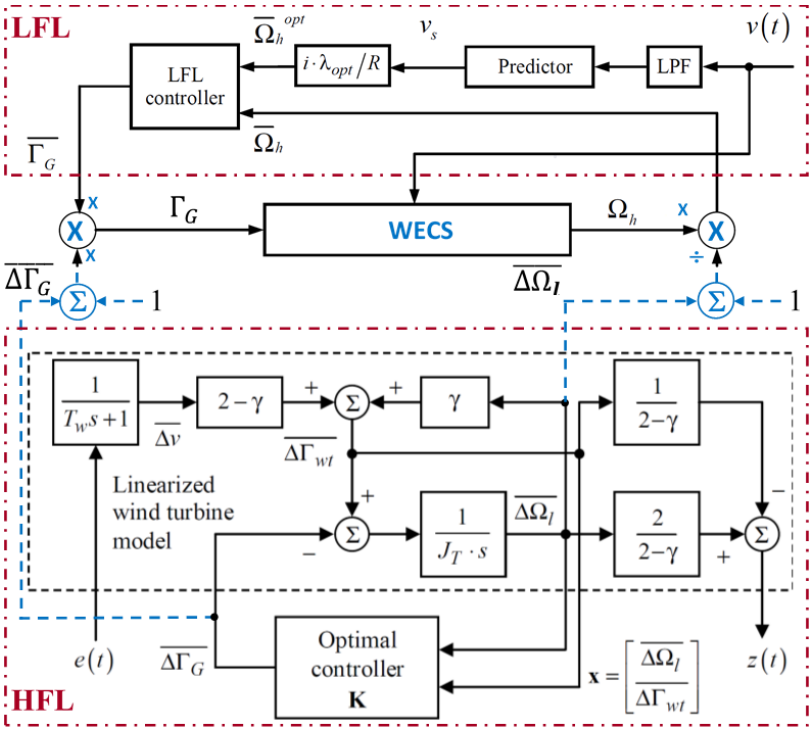

Figure 3.13: 2LFSP applied to a rigidly-coupled WECS: implementation of LFL and HFL and their combined action [49], [29].

Implementation details of both LFL and HFL, as well as the interaction between them, can be viewed in the block diagram in Fig. 3.13. The low-frequency component, v_s, is usually obtained by low-pass filtering the signal $v(t)$ provided by the anemometer; *e.g.*, a fourth-order Butterworth low-pass filter having the cut-off frequency at most equal with the WECS bandwidth may be used for this goal [49]. Estimation of the low-frequency wind speed may be improved by prediction [59], [29].

Some representative ***real-time simulation results*** – resumed from [49] – are next presented to illustrate **the inter-conditioned operation of the LFL and HFL** into the same optimal control structure for a ***low-power*** (6 kW) ***variable-speed fixed-pitch rigid-drive-train induction-generator-based WECS***. To this end, a small-scale WECS electromechanical simulator, conceived based upon the HILS concept (see Section 2.3 in Chapter 2), having the generator rotational speed, Ω_h, as driving variable [24], was employed. Both PI-controller-based and on-off-controller-based LFL implementations were tested, but only results with the PI-controller-based one are summarized here.

Time evolutions of some relevant variables are presented, which suggest ***the role of tuning parameter*** α in the HFL (the weighting coefficient of index (3.9)) in trading-off the closeness of the operating point to the optimal one and the mechanical load intensity induced by the torque variations, with LFL PI controller parameters being constant.

The **LFL** is excited by the low-frequency component of the wind speed, v_s (Fig. 3.14a)), taking values in the usual range, from 4 to 10 m/s; here, v_s results as the output of a fourth-order Butterworth low-pass filter – the LPF in Fig. 3.13 – with 0.1 Hz as cut-off frequency. Fig. 3.14b) shows that the LFL ensures operation on the ORC, corresponding to the tip speed of λ_{opt}; indeed, ***torque parameter*** γ – which is strongly dependent of λ, according to (3.10) – ***exhibits*** in this figure ***reasonably small variations around the value*** $\gamma(\lambda_{opt})=-1$. The amplitude of these variations depends on v_s, which is the output of the separating filter.

Concerning the **HFL**, the variables of interest are normalized variations around the optimal operating point ensured by the LFL, *i.e.*, that of the tip speed ratio, $z(t)=\overline{\Delta\lambda(t)}$, and that of the generator torque, which is the control input, $u(t)=\overline{\Delta\Gamma_G(t)}$. Maximum variations of the operating point can reasonably be considered within $\pm20\%$ around the optimal values. For each value of α among the several tested, the state feedback vector gain, $\mathbf{K}$, was computed based upon the model's parameters obtained for v_s in the middle of its variation range.

The suggested qualitative interpretation of results in Fig. 3.15 confirms expectations, that is, ***the amplitude of the tip speed ratio normalized variation***, $\overline{\Delta\lambda}$, ***decreases with the value of*** α, ***while that of the electromagnetic torque***, $\overline{\Delta\Gamma_G}$, ***increases***. Indeed, large α values correspond to interest placed on maximizing control performance, to the detriment of control effort.

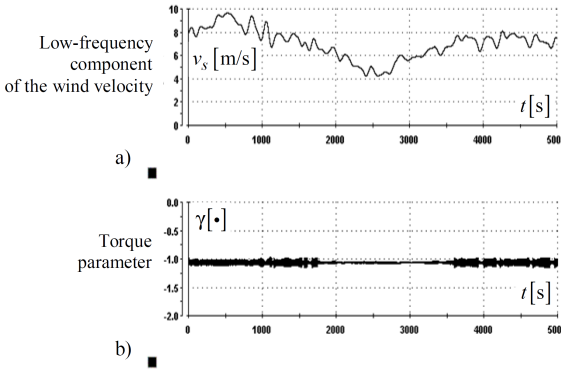

Figure 3.14: 2LFSP real-time simulation results [49]: effectiveness of the PI-controller-based LFL.

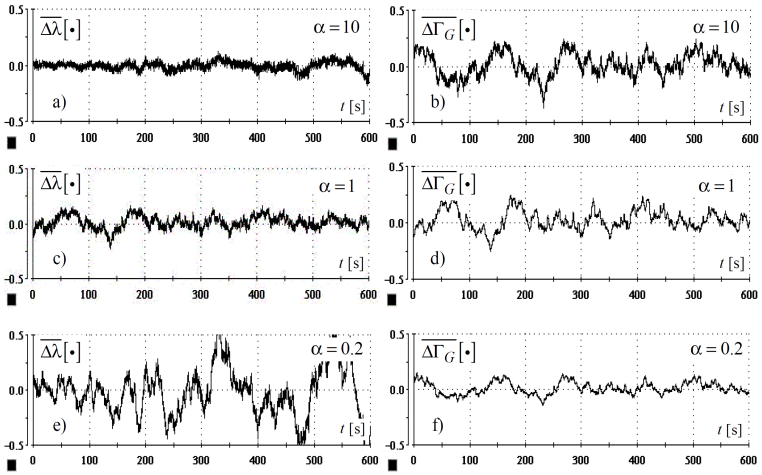

Figure 3.15: 2LFSP real-time simulation results [49]: evolution of the tip speed ratio [a), c), e)] and of the generator torque [b), d), f)] normalized variations for three values of the weighting coefficient, α, inside the HFL.

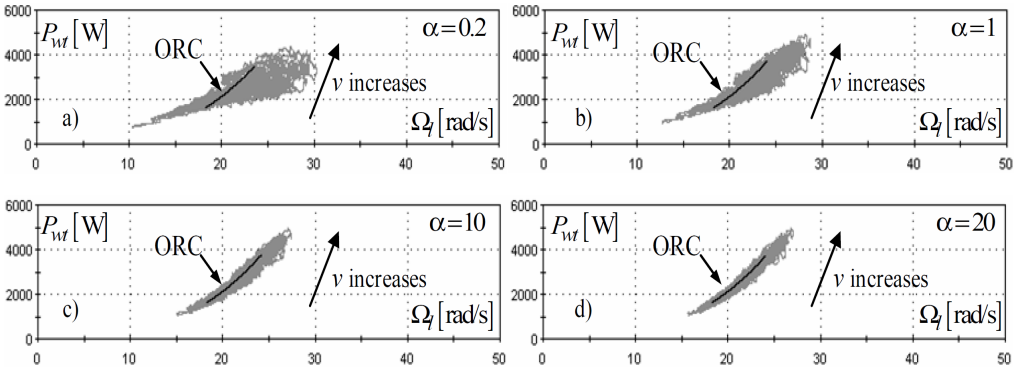

Figure 3.16: 2LFSP real-time simulation results [49]: tracking of the ORC thanks to the combined action of LFL and HFL.

These variations are both placed within the band of ±20% around zero, meaning that the unnormalized values are oscillating around the operating point with the same amplitude.

Fig. 3.16 shows the combined functioning of the two loops, the operating point variations around the ORC for four values of α. As expected, for small α (Figs. 3.16a) and c)), these variations are significantly larger than those for large α (Figs. 3.16b and d)) and increase as the wind speed increases.

3.2.2 Sliding-mode control of WECS for multi-purpose optimization

Variable structure control (VSC) is particularly effective for variable-speed WECS control, being naturally suited for implementation by the already existing high-frequency-switching power electronics and intrinsically robust to disturbances and parametric uncertainties, thus making unnecessary a precise knowledge of the system [60]–[62]. The increased mechanical stress due to chattering is here the main drawback; however, various methods are available to alleviate it.

The main general difficulty about the VSC design concerns the definition of a sliding surface with guaranteed properties of attractiveness and stability [63], [64]. Flexibility of the sliding-mode approach can be raised by adopting ***combined switching surfaces***, with multiple degrees of freedom, in order to allow ***multi-criteria optimization*** – in our case, the focus remains on captured power maximization along with minimization of the electromagnetic torque variations, responsible of inducing fatigue phenomena.

In this context, the contribution briefed here is resumed from [65] and deals with a sliding-mode approach for tracking the power optimum of a WECS. The design is based on ***systematic computation of the sliding surface***

from imposing a desired reduced-order dynamics, which further allows the turbine operation being adjusted to be more or less close to the ORC, according to a desired trade-off between the generator torque (control input) ripple and the optimum tracking. A ***multipurpose (energy-reliability) optimization*** is achieved in this way.

To fix ideas, a ***variable-speed rigid-drive-train doubly-fed-induction-generator (DFIG)-based WECS*** is here the chosen configuration – see Fig. 3.8b) and Fig. 3.9. The variable-speed regime is achieved by *generator torque vector control* ensuring a first-order closed-loop dynamic – from torque reference, Γ_G^*, to effective torque, Γ_G – of T_G time constant [66]–[68]. The same Van der Hoven's limited-frequency wind speed model – with a low-frequency component and a turbulence component – is adopted. The power coefficient curve, C_p, is considered known, the structural dynamics are negligible and a constant conversion global efficiency for the whole wind speed domain is assumed.

By coupling the single-mass model of the high-speed shaft (HSS) [69] (see notations in Fig. 3.9) with that of the controlled generator torque, a second-order nonlinear state model is obtained, which is already in the *regular form* required by the VSC design [63]:

$$\underbrace{\begin{bmatrix} \dot{\Omega}_h \\ \dot{\Gamma}_G \end{bmatrix}}_{\dot{\mathbf{x}}} = \underbrace{\begin{bmatrix} \dfrac{\Gamma_{wt}(\Omega_h \cdot i, v)}{i \cdot J_t} - \dfrac{\Gamma_G}{J_t} \\ -\dfrac{\Gamma_G}{T_G} \end{bmatrix}}_{f(\mathbf{x},t)} + \underbrace{\begin{bmatrix} 0 \\ \dfrac{1}{T_G} \end{bmatrix}}_{\mathbf{B}(\mathbf{x},t)} \cdot \underbrace{\Gamma_G^*}_{u}, \tag{3.20}$$

where $J_t = J_{wt}/i^2$. Based upon (3.20), the goal is to find a sliding surface allowing operation more or less close to the ORC, implicitly requiring an antagonistic sizing of the control effort. Thus, a ***wind-speed-dependent sliding surface*** is sought for, whose image in the (Ω_l, P_{wt}) plane must have a nonempty intersection with the ORC for each value of the wind speed and also an adjustable slope for tuning the sliding-mode dynamics – see also Fig. 3.17b), further presented, which is illustrative in this regard.

The sliding-mode dynamic may be imposed as equivalent to a linear one:

$$\dot{\Omega}_h = \frac{\Gamma_{wt}(\Omega_h \cdot i, v)}{i \cdot J_t} - \frac{\Gamma_G}{J_t} = \begin{bmatrix} a_1 & a_2 \end{bmatrix} \cdot \begin{bmatrix} \Omega_h \\ \Gamma_G \end{bmatrix}, \tag{3.21}$$

where a_1 and a_2 correspond to the adjustable first-order dynamic on the sliding surface. After some algebra, the ***sliding surface*** results as a function of the state vector variable:

$$\sigma\left(\mathbf{x} = \begin{bmatrix} \Omega_h & \Gamma_G \end{bmatrix}^T\right) = a_1 \cdot J_t \cdot \Omega_h + a_2 \cdot J_t \cdot \Gamma_G - J_t \cdot \dot{\Omega}_h, \tag{3.22}$$

thus also depending on the derivative of a state variable, $\dot{\Omega}_h$, which is particularly embarassing for the real-time implementation, as it increases high-frequency noises. Instead, this derivative can be estimated in practice by using a suitably chosen first-order high-pass filter.

Parameter a_1 represents the time constant of the sliding-mode dynamics – resulted from imposing the convergence speed to the sliding-mode regime – whereas choice of a_2 imposes the steady-state regime; in this way, the equilibrium on the sliding surface may be fully described. In our case, provided that power maximization is of interest, the equilibrium point is set to the optimal one, that is, on the ORC.

The two components of the ***sliding-mode control law***: the ***equivalent control input***, u_{eq}, and the ***on-off*** component, u_N, must now be computed. The ***equivalent control input*** has torque dimensions (N·m) and is obtained as:

$$u_{eq} = \Gamma_G - \frac{T_G}{(1 + a_2 J_t)} \cdot (a_1 J_t \Omega_h + a_2 J_t \Gamma_G) \cdot (a_1 - A(\lambda, v)), \tag{3.23}$$

where $A(\lambda, v) = \dfrac{K \cdot v \cdot R^2}{i^2} \cdot \dfrac{C_p'(\lambda)\lambda - C_p(\lambda)}{\lambda^2}$, with $K = 0.5\pi\rho R^2$ considered as invariant and $C_p'(\lambda)$ being the derivative of the power coefficient in relation to λ.

As anticipated, parameter a_1 results from imposing the convergence speed towards the sliding-mode regime: $a_1 = -1/T_{sm}$, with T_{sm} being the desired time constant. The value of a_2 results from imposing the optimal operating point (OOP) as "target" steady state, corresponding to λ_{opt}. Thus, by constraining the sliding-mode dynamic (3.21) to have the OOP as equilibrium point, a_2 is obtained as $a_2 = -a_1 \cdot \Omega_{h_{opt}}/\Gamma_{G_{opt}}$. A dynamic modification of a_2:

$$a_2 = -a_1 \cdot \frac{\Omega_{h_{opt}}}{\Gamma_{G_{opt}} \cdot \left(1 + k \cdot \dfrac{\Omega_h - \Omega_{h_{opt}}}{\Omega_{h_{opt}}}\right)}, \tag{3.24}$$

with $k \geq 0$, can be adopted in order to reduce the operating point variations around the OOP.

The argument behind (3.24) relies upon some practical reasons, as follows. Because $\left(\Omega_{h_{opt}}, \Gamma_{G_{opt}}\right)$ pair depends on the wind speed, *the sliding surface* (3.22) *is variable with the wind speed*, and so does parameter a_2. Thus, parameter a_2 can take in practice sufficiently large values such that the system leaves the normal operating regime. The larger the value of k is, the more quickly the optimal steady state is reached and therefore the ORC tracking has a better quality – real-time simulation results presented further confirm these expectations. The newly added degree of freedom, k, serves in this way to adjust the ORC tracking accuracy. However, too aggressive ORC tracking may induce significant control input variations, affecting the reliability. The conclusion is that ***parameter k can be used to play a role in the design of a desired energy-reliability trade-off***. Accordingly, as k increases, the slope of sliding surface's image in the rotational speed – power plane also increases, corresponding to a tighter ORC tracking. On the contrary, a more reduced value of k is suitable to diminish mechanical fatique.

The ***on-off*** component of the sliding-mode control law, u_N, results from the quite habitual choice of the Lyapunov (energy) function as being the square of the obtained sliding surface, σ (3.22):

$$u_N = -\alpha \cdot \mathrm{sgn}_h(\sigma), \tag{3.25}$$

where $\mathrm{sgn}_h(\cdot)$ is a hysteretic sign function of width h and α is the amplitude. Finally, the total sliding-mode control law is the sum of the equivalent component (3.23) and the on-off component (3.25): $u = u_{eq} + u_N$.

A ***low-power (6-kW) rigid-drive-train horizontal-axis-turbine-based WECS*** was chosen to implement the above described sliding-mode control approach – results shown next are resumed from [65]. Before presenting some real-time simulation results – illustrative from the viewpoint of *time evolution* of variables of interest – some MATLAB®/SimulinK®results are first presented, which give an intuitive visual representation of the achieved dynamic optimization in the *ORC plane*. Thus, Fig. 3.17 presents simulation results concerning the closed-loop evolution in response to step changes in the wind speed for trade-off parameter $k = 0$ in (3.24). Fig. 3.17a) shows the operating point excursion in the state space, (Ω_h, Γ_G), on a trajectory alternating sliding and non-sliding portions between two optimal steady-state points corresponding to the wind speed of 7 m/s and 8 m/s, respectively. This evolution shows that, once the step in the wind speed takes place, ***the operating point is attracted to the new sliding surface and then evolves in sliding mode to the new optimal point***.

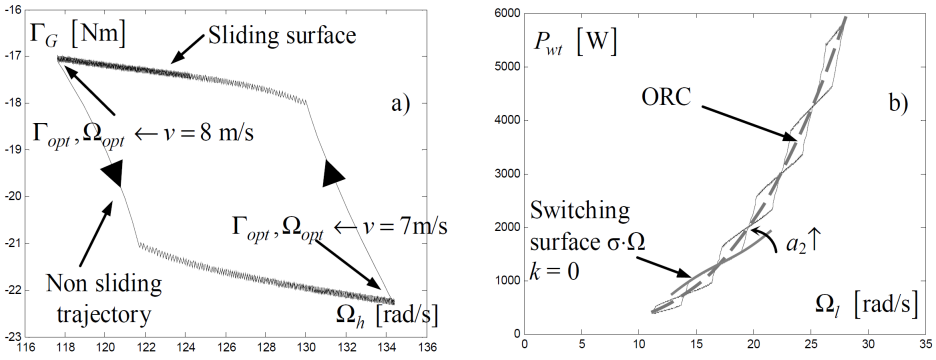

Figure 3.17: WECS optimized by sliding-mode control MATLAB®/SimulinK®results [65]: response to step changes in the wind speed for $k = 0$: a) state space evolution; b) image of the wind-speed-dependent sliding surface in the ORC plane.

Fig. 3.17b) shows the relative position of the ORC *vs.* the sliding surface's image in the ORC plane for different wind speeds, as well as the role of a_2 in tuning the quality of ORC tracking: ***the larger*** a_2 ***is, the closer to the ORC the operating point evolves***.

Validation results obtained on a ***physical simulator*** designed according to HILS methodology (see Section 2.3 in Chapter 2) are presented in the next two figures. For sake of practical compliance with the real-time tests, the initial sliding-mode control law had to suffer some modifications, which are briefly explained below.

- The original form (3.23) of the equivalent control input, u_{eq}, was computed with a modified version of parameter a_2, in order *to compensate for losses*; thus, $a_2 = -a_1 \cdot \eta_{em} \cdot \Omega_{h_{opt}} / \Gamma_{G_{opt}}$, where η_{em} is an estimation of the WECS electromechanical efficiency, having a sigmoid variation with the rotational speed, as established by field measurements.

- The sliding-mode control law uncertainty due to its variability with the constructive parameters – *e.g.*, $A(\lambda, v)$ in (3.23) – can be reduced if increasing the value of parameter α of its on-off component, u_N, with consequent increase of the sliding surface's attractiveness, so of the robustness, but meanwhile of the chattering, potentially responsible for unacceptable generator torque/current variations. A practical manner to alleviate this drawback is to use a *continuous hysteretic sigmoid* (*e.g.*, hyperbolic tangent) function instead of a pure sign (relay) function in (3.25), without significantly affecting the control law robustness.

A set of ControlDesk®captures in Fig. 3.18 illustrate the evolution of the main variables when an energy-reliability optimization by variable speed is implemented in the form of the proposed sliding-mode control.

The trade-off coefficient was set to $k = 12$ and the u_N term is implemented as a sigmoid hysteresis of amplitude $\alpha = 0.3$. The test signal displayed in Fig. 3.18a) is a 2-min pseudorandom wind speed sequence with medium turbulence, computed according to the von Karman spectrum in the IEC standard. The tracking precision of the optimal conversion regime can be estimated from the time evolutions of the tip speed, λ (Fig. 3.18b)) and of the power coefficient, C_p (Fig. 3.18c)). Fig. 3.18d) shows a non-uniform effectiveness of the control law along the concerned operating range, in the (λ, Γ_G) plane. The ORC tracking precision in the rotational speed – power plane can be viewed in Fig. 3.18e). The evolution of the active power fed into the electrical grid, P_{grid}, is plotted in Fig. 3.18f), thus giving indications about the final energy conversion result.

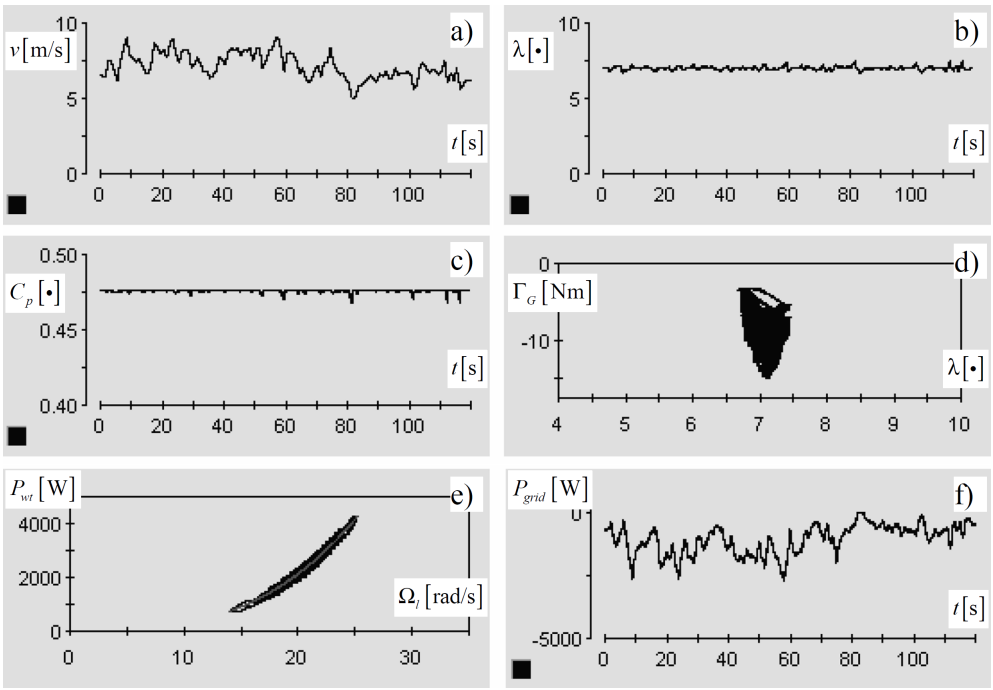

Figure 3.18: WECS optimized by sliding-mode control real-time simulation results [65]: overall behaviour of interest variables.

Finally, Fig. 3.19 shows the influence of the trade-off parameter, k, on accomplishing the control goal.

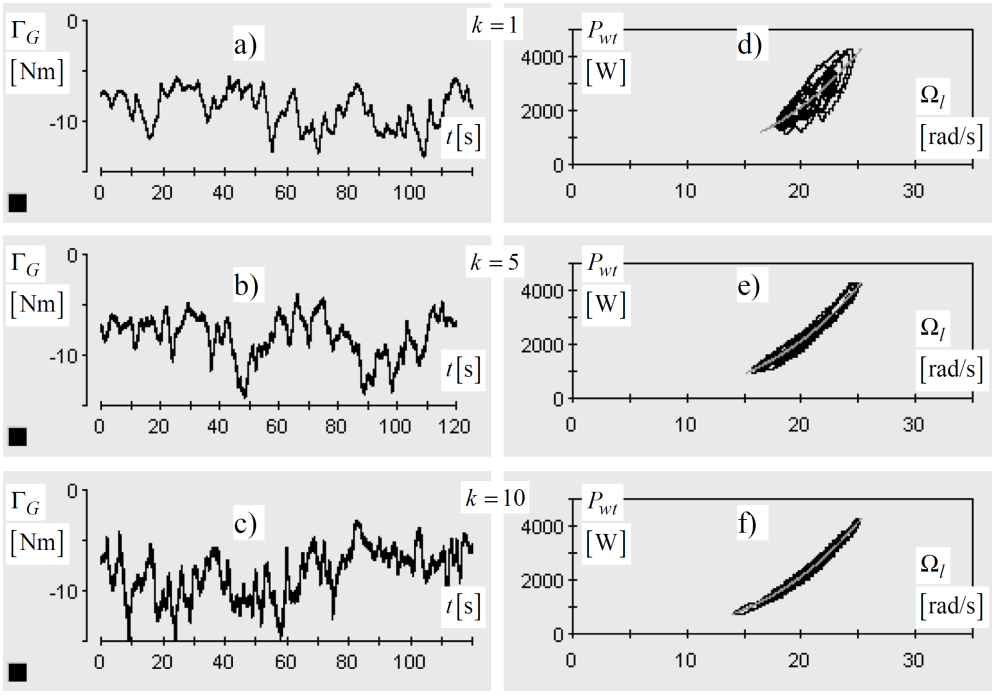

Figure 3.19: WECS optimized by sliding-mode control real-time simulation results [65]: ORC-tracking–control-effort trade-off as k parameter increases (up to bottom).

Indeed, the ORC tracking precision increases as k increases (Figs. 3.19d)–f)), but with the price of increasing the mechanical stress, as control input (electromagnetic torque) variations also increase (Figs. 3.19a)–c)). Therefore, the possibility of adjusting the newly added degree of freedom, k, confers flexibility to the sliding-mode controlled WECS, so that the wind energy conversion efficiency be significantly increased when the particular conditions of the site allow it (*i.e.*, when the mechanical stress induced by the turbulences is not important).

3.2.3 Wind turbulence employed as searching signal in MPPT for WECS

This subsection summarizes the main ideas behind ***using the turbulence component of the wind speed as searching signal in an extremum-seeking-control (ESC)-based MPPT*** for a generic class of variable-speed WECS, irrespective of their aerodynamic, transmission and generation configurations [70].

Without loss of generality, the case of a ***squirrel-cage-induction-generator (SCIG)-based WECS*** (see Fig. 3.8a)) subjected to MPPT control is taken as an example. The approached system presents a higher level control loop superposed on the generator torque control: the high-speed shaft (HSS) rotational speed control, thus allowing the tip speed ratio, λ, direct control, according to the ESC principle presented in Fig. 3.5.

It is assumed that the wind speed signal is described by a fixed-point spectrum, with a seasonal component, v_s, and a turbulence component, $\Delta v = v - v_s \equiv v_t$, whose intensity varies in the usual range, *i.e.*, [0.12;0.18] [44]. It is also assumed that measures of the wind speed, rotational speed and electrical power are available for feedback. Constructive parameters of the whole mechanical-to-electrical conversion chain, as well as its conversion efficiency, η, are supposed known, whereas ***the aerodynamic efficiency curve***, $C_p(\lambda)$, ***is totally unknown***. Under this set of assumptions, the considered model of the variable-speed WECS can be sketched as in Fig. 3.20a). The wind turbulences, together with rotational speed variations around a steady-state value, induce some λ variations around its average value and consequently some nonharmonic, but bounded-spectrum, power coefficient variations, ΔC_p, whose presence is suggested in Fig. 3.20a).

$\lambda(t)$ can be computed by using measures of the wind speed and rotational speed, as to its definition relation (3.1). Under the previously stated assumptions, the instantaneous value of the power coefficient, $C_p(t)$, can be estimated from the measured electrical power, $P(t)$ – related to the wind turbine power, P_{wt}, by means of conversion efficiency η: $P_{wt} = P(t)/\eta$ – and that of the wind speed, $v(t)$, by using P_{wt} definition relation (3.3):

$$C_p(t) = \frac{P(t)}{0.5 \cdot \eta \cdot \rho \cdot \pi R^2 \cdot v(t)^3} \tag{3.26}$$

The main idea of this approach relies upon how the available feedback information is further used. If supposing a Fourier decomposition of $\lambda(t)$ and $C_p(t)$ signals, then each $\lambda(t)$ harmonic component will generate a response

which is a part of $C_p(t)$. Next, by composing/averaging the effects of the respective components of the two Fourier decompositions, the operating point (OP) position on the C_p curve can be obtained by *demodulation*.

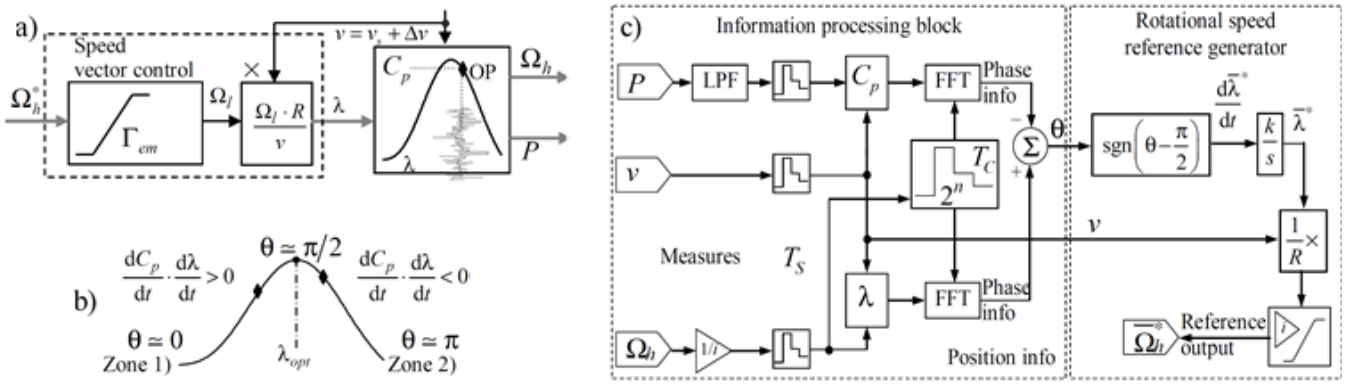

Figure 3.20: Illustration of main ideas and concepts of WECS MPPT control using wind turbulence as searching signal [29], [70]: a) principle of WECS modelling and control; b) feedback processing to deduce the operating point position; c) block diagram of the control structure: feedback information processing and generation of the rotational speed reference.

In particular, demodulation is here implemented by using the *Discrete Fourier Transform* (DFT) on an appropriately chosen time window, in order to extract the phase of each harmonic component of $\lambda(t)$ and $C_p(t)$ and then compute the phase lag between them. An average of these phase lags, further denoted by $\theta(t)$, contains the OP average position information. Values of $\theta(t)$ will get closer to 0 if the OP is on the left (rising) slope of the $C_p(\lambda)$ curve or closer to π if the OP is on the right (falling) one. Hence, Zone 1) from Fig. 3.20b) will be characterized by $\theta < \pi/2$ and Zone 2) by $\theta \geq \pi/2$.

The control law main idea is ***to move slowly*** (as compared to the turbine's dynamics) ***the average OP to the top of the aerodynamic efficiency curve***, C_p, ***by regulating the average value of the tip speed***, λ, computed on a relatively large time window, of width T_C. Thus, the control is implemented using an ***integrator*** fed by the OP position information, which gives the ***search direction*** and whose ***gain***, denoted by k, represents the ***search step***. The control structure, presented in Fig. 3.20c), has two main parts, namely an information processing block and a rotational speed reference generator.

The role of the ***information processing block*** is to output the $C_p(t)$ and $\lambda(t)$ normalized signals – obtained from the electrical power, rotational speed and wind speed measurements – to further feed a FFT algorithm for obtaining their phase spectrum and the corresponding average OP position signal, $\theta(t)$. For information consistency, a sufficiently large window (compared to the turbulence dynamics) must be chosen. The measure information is updated at each sampling period, denoted by T_S, whose choice depends mainly on the turbine dynamics. A time window of width $T_C = 2^n \cdot T_S$ can then be a reasonable choice for FFT computation, where n is a positive integer resulting from a trade-off between suitably tracking the wind speed's variations and complying with the system inertia. It is obvious that a given system will not be ever made to track an unlimitedly turbulent wind.

As the OP position changes smoothly around the optimal one (OOP), the role of the ***rotational speed reference generator*** – at the right of block diagram in Fig. 3.20c) – starts with a preliminary processing of $\theta(t)$ around the OOP. Note first that, when the OP is placed on the positive slope of the C_p curve, the integrator will process a positive value, thus determining the tip speed reference to increase. In contrast, when the OP is on the negative slope of the C_p curve, the tip speed reference must diminish. This can be achieved by integrating a nonlinear function of average phase information, $sgn(\theta - \pi/2)$. As the slope of C_p is continuous, instead of discontinuous feedback information in the form of the sign function a continuous, *e.g.*, a hyperbolic tangent, approximation of the sign function can be used in practice. The result of this operation, applied to the integrator, produces a tip speed reference, renewed every T_C seconds after the computation of the phase shift, θ. The control structure finally outputs the rotational speed reference, computed based upon the tip speed reference.

The integrator gain, k, is a key parameter, whose tuning relies upon both the chosen T_C and the desired search

speed. Some large deviations of the instantaneous tip speed, λ, around its optimal value, λ_{opt}, are possible, whereas its average value should remain close to λ_{opt}. Thus, a good performance of this control structure can be concluded upon a sufficiently small standard deviation of λ around its average value. The value of k can thus be chosen such that the variable-speed turbine compensates λ standard deviation in the computing time T_C.

Some numerical simulation results are shown below, which synthesize the main validation aspects detailed in [70] for ***a low-power (6 kW) variable-speed fixed-pitch rigid-drive-train WECS***, having $\lambda_{opt} \approx 7.2$ and $C_p(\lambda_{opt}) = 0.475$.

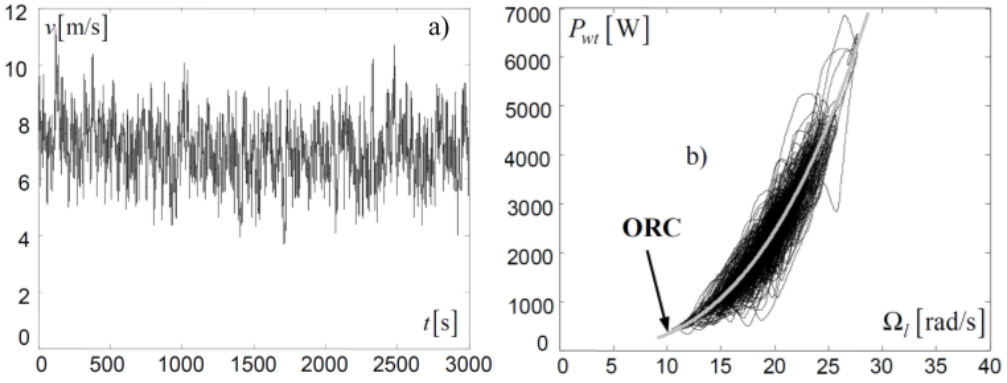

Figure 3.21: Performance of the ESC-based MPPT control with wind turbulence as searching signal [70]: a) the 50-min wind speed sequence used as excitation signal; b) achieving energy optimization by tracking the ORC, with integrator gain $k = 0.02$.

A wind sequence of about 8 m/s of average speed, with a medium turbulence intensity of $I = 0.15$ (Fig. 3.21a)), obtained using the von Karman spectrum in the IEC standard, was chosen to represent a sufficiently rich and challenging excitation signal. Fig. 3.21b) shows the operating point's distribution around ORC (in the speed–power plane), showing a better ORC tracking accuracy of the *wind-turbulence-based* MPPT control law as compared with the *classical* MPPT version (see [70] for details).

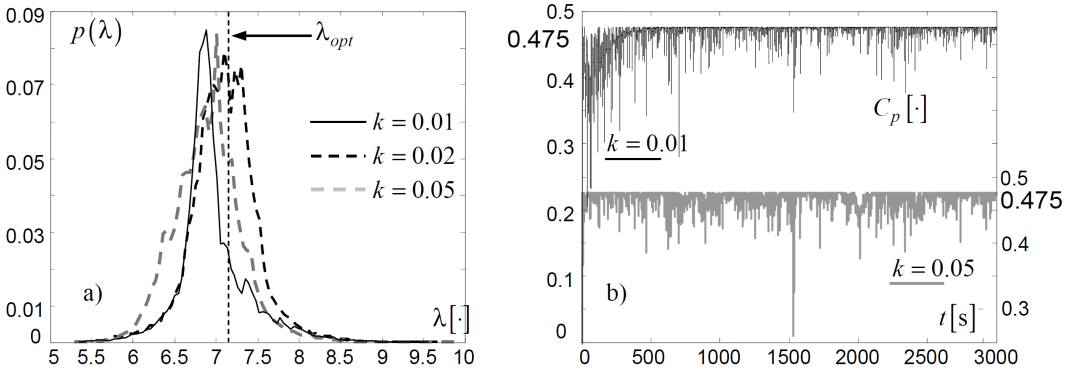

Figure 3.22: Influence of the integration gain, k, on the quality of ESC-based MPPT with wind turbulence as searching signal [70]: a) tip speed's density of probability; b) C_p evolution in relation to $C_p(\lambda_{opt}) = 0.475$.

Different values of the control parameter, k, in the range from 0.005 to 0.5, were tested in simulation for closed-loop performance. Fig. 3.22a) shows how the tip speed's density of probability, $p(\lambda)$, is changing. For small k – corresponding to slow searching – smaller λ standard deviations are obtained, but the average value differs from the optimal one, which denotes poor energy efficiency. For large k – *i.e.*, large searching speed – the standard deviation becomes large despite the mean of the tip speed remaining close to the optimal value, thus also indicating poor efficiency. Fig. 3.22b) suggests that, once the system is in steady-state regime, a small value of k can produce better performance. These remarks suggest the existence of a domain of k values for which optimality close tracking can be successfully designed: a good tracking of the maximum power along with a sufficiently small variance.

3.3 Control of micro-hydro energy conversion systems (miHECS)

Out of the renewable-energy conversion systems (RECS) with demonstrated potential as sustainable alternative to the classical electrical power generation technologies, the ***new hydraulic capturing devices*** aiming at harvesting the energy of ***marine currents and river flows*** represent a distinct class having received significant attention in the energy transition context [71]–[73].

Like in the case of all kind of RECS, and especially of ***wind turbines***, the power generation by the ***water turbines*** should take place with minimal environmental impact, involving the use of limited-span civil engineering structures for conditioning the incoming flows. The water-turbine generated power can be controlled by using pitchable blades or by implementing the concept of *variable-speed operation of the electrical generator*, thanks to the associated power electronic interface. As stated in the RECS-control introductory Section 2.1 in Chapter 2 of this memoir, generator control is important in both *off-grid* mode (stand-alone microgrid) [74] and also in *grid-connected* applications, for providing ancillary services, such as improving power system stability or damping inter-area oscillations [75], [76].

Water-turbine-based generation systems installed in rivers, generally named as **microhydro energy conversion systems (miHECS)**, use various application-dependent capturing devices, of either classical design – such as (semi) Kaplan or Francis water turbines – or more modern trends, such as axial-flow, vertical-axis or cross-flow water turbines (CFWT) [77]–[79]. The free-water-flow operation invariantly requires use of general and already well-established RECS technology concepts, such as generator vector control, variable-speed control, MPPT, *etc.* [72], [80], [81].

The contributions synthesized in this section were obtained for miHECS being based on an original concept of **cross-flow water turbine (CFWT)**, the ***Achard turbine***, developed and patented at the Laboratoire des Écoulements Géophysiques et Industriels (LEGI) in Grenoble, France [82].

CFWTs represent variations of Darrieus turbines [83], with several advantages *vs.* the axial-flow ones (smaller cavitation [84], simpler mechanical structure, more flexible power generation system), as well as several drawbacks (pulsating turbine torque, lower starting torque and lower conversion efficiency). In this context, control contributions briefed here were focused on fully using the advantages of CFWTs, while minimizing their drawbacks.

Fig. 3.23a) presents the three-bladed vertical-axis Achard turbine resulted as an evolution of Darrieus and Gorlov turbines: it has flying-wing-shaped blades fixed on the rotation axis by means of profiled central arms [82], [86]. This basic prime mover was further used within more complex harvesting structures in order to achieve better performance and to overcome the drawbacks inherent to vertical axis turbines; thus, a complex power take-off device was conceived through succesive steps, as follows.

First, *four three-bladed CFWTs* were pilled-up into the same shaft to yield a **CFWT tower**. In order to smooth the mechanical torque, each turbine was installed with angular position shifted with $\pi/2$ with respect to the previous one, thus achieving a spatial filtering of the output power, using the same idea as in [87], [88]. In this way the CFWT tower power coefficient is almost constant irrespective of the tower's position with respect to the water flow direction.

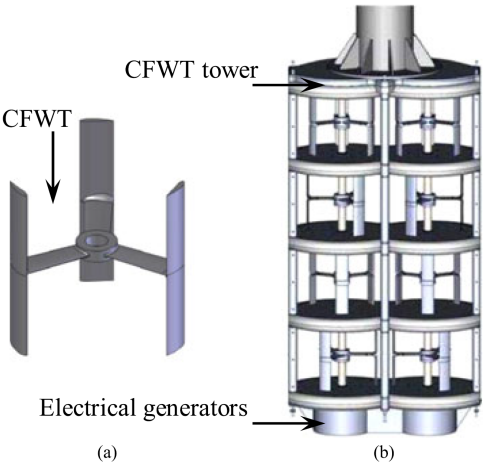

Figure 3.23: Considered CFWT-based hydrokinetic harvesting device: a) basic concept of three-bladed Achard CFWT with straight blades; (b) power take-off structure in the form of two adjacent CFWT towers, each with four piled-up turbines [85].

A CFWT tower directly drives an electrical generator, situated in its lower part, as visible in Fig. 3.23b); the same figure shows that **two CFWT towers rotating in opposite senses** are further placed side by side for purpose of structural loads alleviation in certain operating regimes [86]. Finally, the two CFWT towers are encompassed by fairings to increase the water upstream-*vs.*-downstream differential pressure and, consequently, the captured power under certain water conditions.

It is the ***CFWT tower*** that plays the role of ***prime mover*** for the class of miHECS considered here. Contributions summarized next were obtained during my 2008–2009 post-doctoral internship at G2ELab, within the collaboration with Ph.D. students Ana-Maria ANDREICA-VALLET and Matthieu HAUCK and post-doctoral fellow Iulian MUNTEANU, working under the supervision of Professors Daniel ROYE and Seddik BACHA. It is worthy to note that validation of the different proposed control strategies spanned all the phases, from preliminary checking by MATLAB®/Simulink®numerical simulation, passing through HILS validation on a test bench at G2ELab – with the help of R&D engineer Axel RUMEAU – and finishing with prototype implementation on a pilote site near Grenoble, within the collaboration framework between the two Grenoble research laboratories, LEGI and G2ELab. All these contributions regard electrical generator control exploiting the variable-speed operation capability – they are as follows.

- An original method of ***direct active power control*** of a CFWT-tower-based miHECS in the ***stall region*** – characterized by *unstable* dynamic behaviour – referring to *grid-connected* (otherwise said, ***PQ***) operation, was proposed, investigating the possibility of operating the miHECS as a ***dispatchable*** power generation source ***despite absence of a storage unit***. Main results, synthesized in Subsection 3.3.1, were published in:

  M. Hauck, I. Munteanu, A.I. Bratcu, S. Bacha, D. Roye (2011). Operation of grid-connected cross-flow water turbines in the stall region by direct power control. *IEEE Transactions on Industrial Electronics*, 58(4), 1132–1140.

- As a miHECS – like any other RECS employed within a microgrid (recall the general topology in Fig. 2.1 in Section 2.1 and the control-oriented RECS characterization in the same section) – may be required to switch between the grid-forming (*stand-alone*) and the grid-following (*grid-connected*) modes, systematic design of some ***proper management of "smooth" switching between the two modes*** – ***Vf*** and ***PQ*** – was approached. Subsection 3.3.2 briefs these results, resumed from:

  M. Andreica Vallet, S. Bacha, I. Munteanu, A.I. Bratcu, D. Roye (2011). Management and control of operating regimes of cross-flow water turbines. *IEEE Transactions on Industrial Electronics*, 58(5), 1866–1876.

- ***Synchronization of two CFWT towers*** for some global purpose, *e.g.*, alleviating mechanical efforts inside of a configuration like the one in Fig. 3.23b), was extensively investigated, the towers being also designed as ***twin towers*** in this case. Results concerning this topic – grouped together in Subsection 3.3.3 – made the object of several publications, starting by a patent explaining the main idea of synchronizing two rotating devices, as being ***inspired and adapted from communications technology***:

  A.M. Andreica, S. Bacha, A.I. Bratcu, J. Guiraud, I. Munteanu, D. Roye (Grenoble Institute of Technology, Electricité de France) (2009). *Hydraulic turbomachine for recovering and converting kinetic energy of water currents into electricity, has regulation units electrically regulating power from generator to ensure that shaft rotates at same speed relative to another shaft.* Patent WO2010020735-A1, FR2935159-A1,

  a journal article reporting on some HILS validation results:

  M. Vallet, I. Munteanu, A.I. Bratcu, S. Bacha, D. Roye (2012). Synchronized control of cross-flow-water-turbine-based twin towers. *Renewable Energy*, 48, 382–391

  and the journal article:

  M. Hauck, A. Rumeau, I. Munteanu, A.I. Bratcu, S. Bacha, D. Roye (2018). Identification and control of a river-current-turbine generator – application to a full-scale prototype. *IEEE Transactions on Sustainable Energy*, 9(3), 1365–1374,

  which presents results of ***on-site control validation*** – also including other control methods, like the MPPT – performed on a ***prototype of CFWT-tower-based miHECS*** installed on a headrace canal feeding a hydroelectric plant near Grenoble in France.

3.3.1 Direct active power control of a cross-flow-water-turbine (CFWT)-based miHECS

Despite its obvious interest, RECS power control is a topic that is seldom dealt with because the primary resource intermittence prevent such systems from being fully *dispatchable* – that is, able *to guarantee* a certain imposed level of the provided power when grid connected – unless complemented by storage units.

Control methods ensuring that a low-impedance grid or a load is fed at constant power are reported in the case of hybrid photovoltaic/wind RECS, possibly with energy storage devices [89], [90].

In general, power control of a generation unit concerns its grid-connected – otherwise said, *grid-following* or PQ – operation mode. To fix ideas, a ***grid-connected CFWT-tower-based miHECS*** equipped with a permanent-magnet synchronous generator (***PMSG***) and a ***back-to-back AC–DC–AC power-electronic converter*** interfacing the grid is here considered (Fig. 3.24 [91]). For this topology, control roles are as follows: the grid-side converter ensures the transfer of the entire available DC-link power to the AC grid by regulating the DC-link voltage, V_{DC}, while the machine-side converter is used to control PMSG power by means of its three-phase currents.

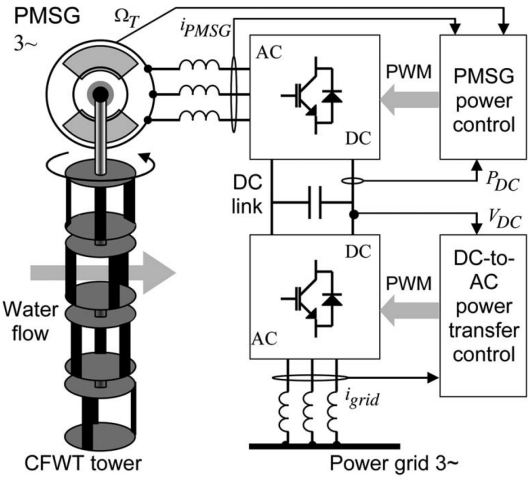

Figure 3.24: Topology of a grid-connected PMSG-based miHECS with Achard CFWT tower [91].

Modeling of water turbines is similar to the one employed for wind turbines. Thus, the hydrodynamic model of a CFWT tower is based on its power coefficient characteristic, $C_p(\lambda)$ in Fig. 3.25a), having the same allure as the one of a single Achard turbine [92].

The extractible power, P_T, depends on the *water* flow speed cubed and on the turbine parameters in a manner similar to *wind* turbines (see also (3.3) in Section 3.1):

$$P_T = 0.5 \cdot \rho \cdot S \cdot w^3 \cdot C_p(\lambda), \tag{3.27}$$

where ρ and w are this time the water density and speed, respectively, S is the surface swept by the turbine blades – $S = 2R_T H_T$, with R_T and H_T being the turbine radius and height, respectively – and the tip speed ratio, λ, preserves the same definition as in the case of wind turbines: $\lambda = R_T \cdot \Omega_T / w$, with Ω_T being the tower's rotational speed.

Fig. 3.25b) shows a tower's mechanical torque, T_T, and power, P_T, curves for a constant water flow speed. It is assumed that all four turbines composing the tower have the same mechanical torque characteristic, so the tower output torque increases proportionally with the number of turbines in the tower. Also, the water flow speed variations are considered very slow in relation to the system dynamics; however, flow turbulences (low-amplitude high-frequency variations) are likely to be present.

For considerations of lower mechanical and hydrodynamic stresses, the system is likely to be operated at ***low rotational speeds***, in the so-called ***hydrodynamic stall region***, *i.e.*, in the $(0, \Omega_{P_{max}}]$ range, identifiable in Fig. 3.25b), where $\Omega_{P_{max}}$ corresponds to the maximum power available for a certain value of water flow speed.

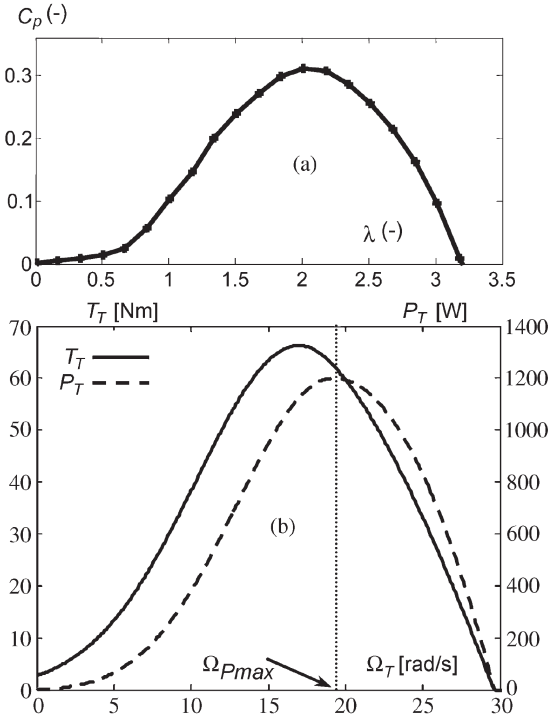

Figure 3.25: Mechanical characteristics of a CFWT tower: a) power coefficient *vs.* tip speed ratio; b) torque and power curves *vs.* rotational speed for a given water flow speed [91].

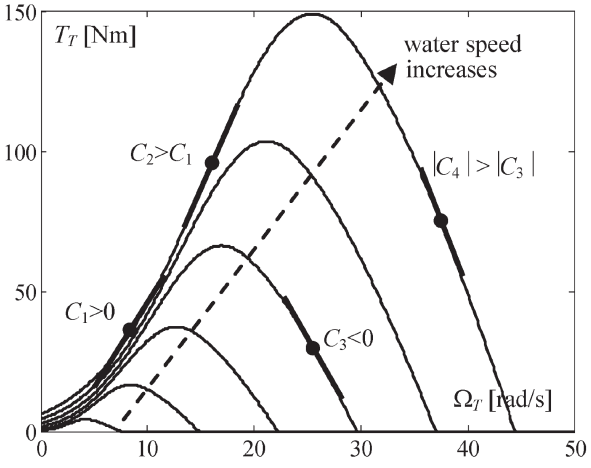

Figure 3.26: CFWT tower torque-*vs.*-rotational-speed curves for various water speed values [91].

Fig. 3.26 depicts the family of torque-*vs.*-rotational-speed curves when the water flow speed varies. $T_T(\Omega_T)$ can be linearized for a given water flow speed value, around a certain operating point, leading to a C-slope linear approximation. C is strongly variant, depending on the water flow speed, being either positive or negative, according to the operating point relative position on the mechanical characteristic with respect to the maximum torque point. Hence, the stall region is characterized by positive values of slope C, as in this case operating points are likely to be placed on the left, ascending branch of T_T curve (see also Fig. 3.25b)).

As the PMSG is directly driven by the CFWT tower, a first-order linear dynamic of rotational speed, Ω_T, results from its swing equation involving the linearized version of mechanical torque, T_T, and PMSG electromagnetic torque, T_G, in the form:

$$\Omega_T(s) = -\frac{1}{Js - C} \cdot T_G(s), \tag{3.28}$$

with J being the inertia of the tower–PMSG coupling. System (3.28) is ***unstable*** over most of the operating range of interest (***stall region***), as C is positive. Whereas employing a rotational speed regulatory control is the usual way to solve this problem, our contribution consists in ***only stabilizing the rotational speed using generator current as the control input***. The argument behind this idea is simple, as follows. The classical dq-frame modelling of the ensemble PMSG-machine-side-converter [67], [68] allows the PMSG torque control by means of the quadrature current, i_q, the direct-current component, i_d, being maintained at zero; thus, $T_G = -K_g \cdot i_q$, where K_g is the torque constant. The current loop dynamic being the fastest within the system, the current value may safely be taken as equal with its reference, $i_{q\_ref} = i_q$. Hence, a first-order transfer from current i_q to Ω_T results:

$$\Omega_T(s) = \frac{K_g}{Js + D} \cdot i_q(s), \tag{3.29}$$

where $D < 0$ is mainly given by the slope C of the $T_T(\Omega_T)$ curve, but may also contain a friction coefficient.

Following the above arguments, the reference of the i_q PMSG current is obtained as the algebraic sum of a ***stabilization*** component, noted by i_{qs}, and a ***regulation*** component, noted by i_{qc}:

$$i_{q\_ref} = -i_{qs} + i_{qc}, \tag{3.30}$$

where the two components, although they have current dimensions, do not represent variables with a physical meaning, but their sum plays the role of reference of the i_q control loop.

Whereas i_{qs} results from suitably selecting a stabilizing feedback gain, computation of i_{qc} is based on having experimentally proved the remarkable property of $P_{DC}(i_{qc})$ static curve of being *unimodal*, *i.e.*, having the same aspect as the power-*vs.*-rotational-speed curve (Fig. 3.25b)). This remark allows envisaging that power control – including the MPPT – can be achieved directly in relation to this current input. Thus, an ***upper-level, slower DC-link power control loop*** can be designed to yield i_{qc} as the output of a PI controller aiming at regulating P_{DC} at an imposed level, P_{DC_ref}. Consequently to having identified a first-order open-loop transfer function $i_{qc} \rightarrow P_{DC}$, penalized by a non-minimum-phase behaviour due to presence of an "unstable" zero, PI controller design results from imposing some desired closed-loop second-order dynamics, where the non-minimum-phase behaviour is still present, but it is strongly attenuated. Open-loop identification and closed-loop design, as well as the global miHECS direct power control block diagram, are detailed in [91].

HILS validation results presented next are also resumed from [91]; they illustrate direct power control of a ***CFWT-tower-based miHECS of*** 1825 W ***rated power at*** 2.3 m/s ***of water flow speed***.

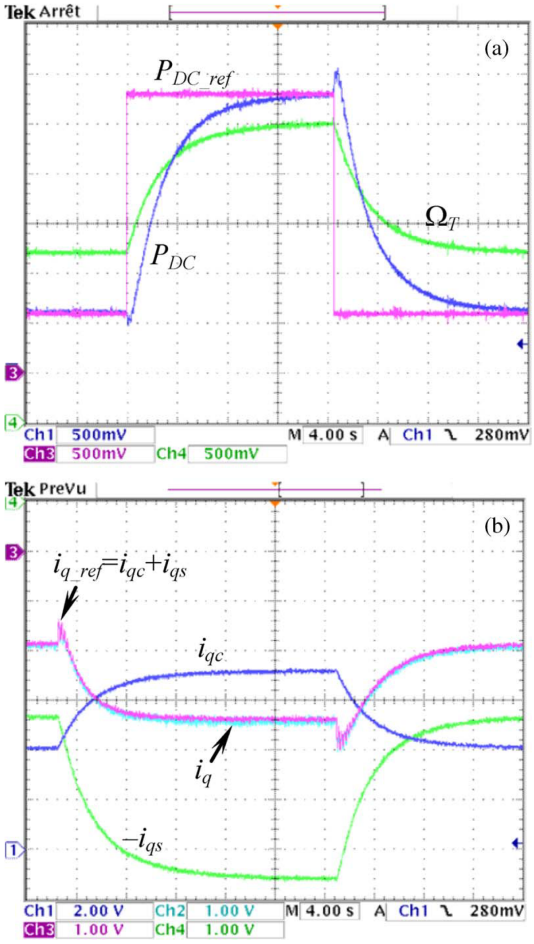

Figure 3.27: CFWT-tower miHECS direct power control closed-loop performance (HILS oscilloscope captures) [91]: a) Ch 1 and Ch3 – DC-link power measure, P_{DC}, and reference, P_{DC_ref}, respectively (250 W/V); Ch 4 – PMSG rotational speed, Ω_T (50 rad/s/V); b) Ch 1 – regulation current, i_{qc} (50 A/V); Ch 2 and Ch3 – generator current measure, i_q, and reference, i_{q_ref}, respectively (5 A/V); Ch 4 – stabilization current, i_{qs} (50 A/V).

Fig. 3.27a) shows the performance of the direct power regulation loop when the power demand steps up from 150 to 700 W and backwards, for a water flow speed of 2 m/s. The about-12-s power transient still keeps a non-minimum-phase behaviour, although much reduced. Note that *the DC-link power controller is here a pure integral gain*; a complete PI controller offering a second degree of freedom can be used if a faster response is aimed at. The rotational speed remains at low values on the left side of the power characteristic (it has the same sense of variation as the captured power).

Fig. 3.27b) shows the variations of the control variables, *i.e.*, the stabilization and regulation currents, i_{qs} and i_{qc}, respectively, their sum, which is the i_q reference, as well as the measured value of i_q. The stabilization current, i_{qs}, evolves synchronously with the rotational speed, its absolute value is much higher than the one of i_{qc}, so the resulting quadrature current, i_q, is always negative (which is coherent with PMSG working as a generator).

To conclude, one of the significant merits of contribution in [91] concerns the broader impact it can have for a larger class of rotating-prime-mover-based RECS. Indeed, experimental validation of the considered miHECS configuration on a HIL simulator allowed an analogy with the operation of WECS, namely by identifying the same operating regions, *i.e.*, partial load, full load and stop at the cut-out water flow speed (see Fig. 3.2 in Section 3.1). This allows the statement of basic control goals for CFWT-based systems in a similar manner as for WECS. Note that water turbines operation is more restrictive than wind turbines operation – as the formers have no pitchable blades and they cannot be put out of the water flow – and even more, one might not expect that the water flow speed could decrease to zero. Therefore, all basic control goals – *i.e.*, power control, rotational speed limitation, MPPT, start and stop – must be entirely achieved by means of the electrical generator control. The direct power control framework in [91] opens the way towards ***implementing all miHECS basic control goals in a simple manner, involving minimal tuning effort, irrespective of the water flow speed value and without measuring it***.

3.3.2 Supervision of smooth switching between operating modes of miHECS

In this subsection, focus is on the ***management of the switching*** between the two main operating modes of a CFWT-tower-based miHECS: the *grid-connected* (*grid-following* or ***PQ***) mode – when the system is required to provide imposed levels of active and reactive power to a "strong" grid – and *islanded* (*stand-alone*, *grid-forming* or ***Vf***) mode, when the system must supply an isolated-load-demanded power and ensure the desired output voltage amplitude and frequency. The same PMSG-based generation configuration is considered. A synthetic control-engineering practical viewpoint of how a miHECS should be controlled across the main operating regimes ***in order to preserve its continuity of service*** is aimed at here.

The CFWT miHECS architecture in Fig. 3.28 shows potential for a large application field, its modularity

allowing adaptation to either river or tidal flows and both PQ and Vf operation.

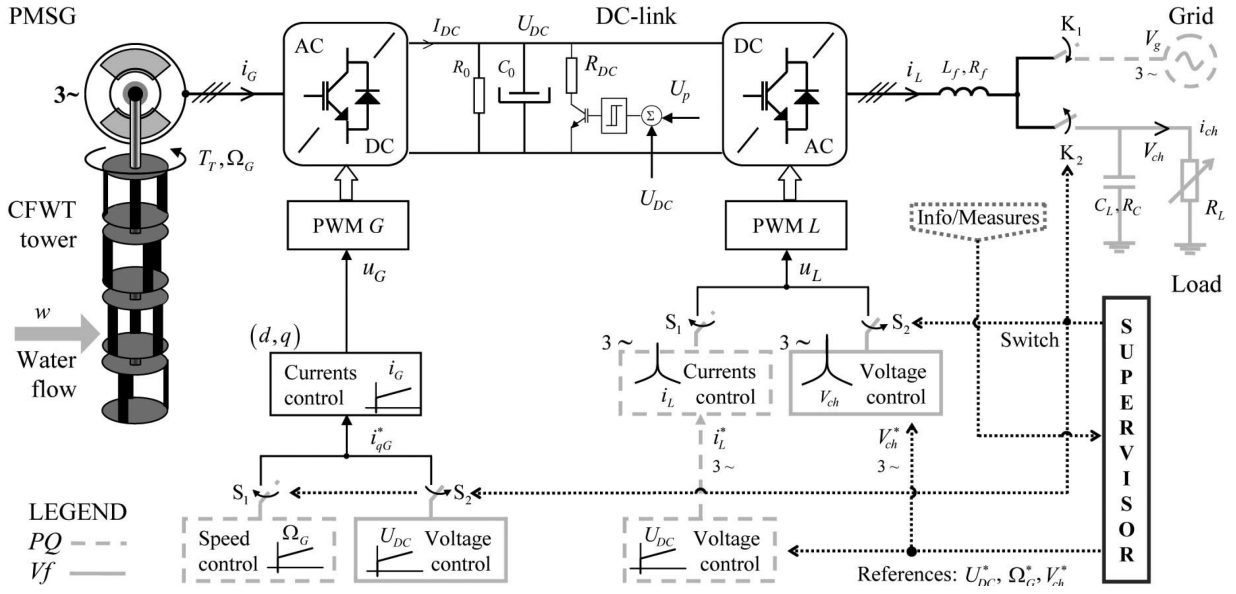

Figure 3.28: CFWT-tower-based miHECS and its control structures for both PQ and Vf modes, emphasizing ***supervisor***'s role in switching between the two [93].

The prime mover is rigidly coupled to the PMSG. A back-to-back three-phase PWM power electronic converter implements the interface between the generator and the grid/load. Free-fluid-flow conditions are assumed, the tower being driven by a river flow. When operating in stand-alone (Vf) mode, the generator feeds a mainly resistive load through an LC filter. The Vf operation may not require storage devices in a first place if, in a preliminary design phase, load supply is guaranteed for the lowest water speed value. Indeed, the storageless operation is possible as discontinuities of the water resource are less probable than, for example, those of the wind, and its relatively slow variations can be reliably predicted.

The control roles assigned to each of the two power electronic converters in Fig. 3.28 are specific to each of the operating modes. The control structure including blocks drawn with a dashed line concerns the PQ mode, while the blocks drawn with a solid line represent controllers enabled within Vf mode – details concerning control goals and design can be found in [94] and [95], respectively.

Thus, in PQ mode, the grid-side converter regulates the DC-link voltage, whereas the generator-side converter controls the turbine's rotational speed (*e.g.*, MPPT in its well-known *hill-climbing* version explained in Fig. 3.4 and Table 3.1). The rotational speed control is preferred to the torque control as it can ensure stable operation of CFWTs at low speeds (see, *e.g.*, details in previous Subsection 3.3.1 and [91]), as well as overspeed regime being avoided [84]. In Vf mode, the load-side converter ensures the load voltage and frequency regulation, while the generator-side converter keeps the DC-link voltage at the required value. Hence, in this mode, the turbine's rotational speed is no longer feedback-controlled.

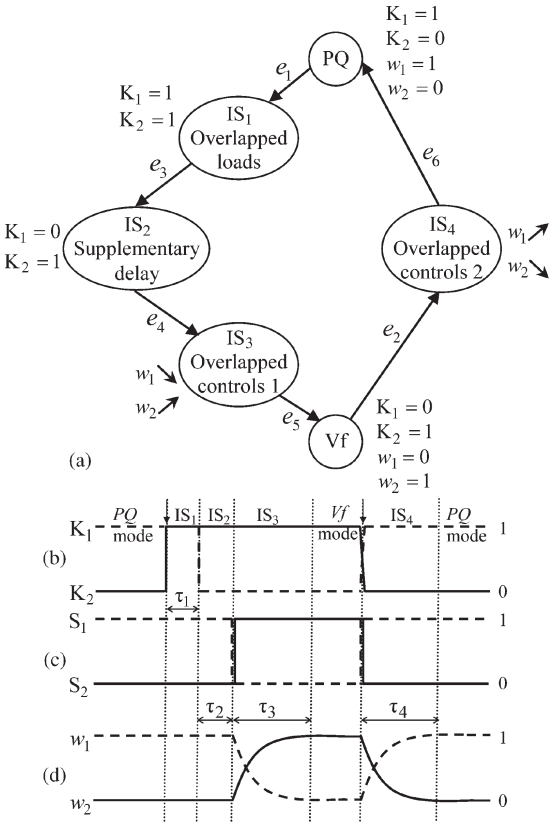

Figure 3.29: Switching between the miHECS operating modes [93]: a) diagram of transition between operating modes; b) contactor signals; c) regulations enabled; d) time evolution of the smooth switching weights.

The ***supervisor*** visible in Fig. 3.28 implements an upper-level control, its role being to ensure the smooth switching between the PQ and Vf control strategies when required, consequently switching the system output between the grid and the load and providing the controlled variables' setpoints to the low-level controllers. Binary-state contactors K_1 and K_2 achieve the connection/disconnection of the grid/load. Signals S_1 and S_2 enable the low-level controllers corresponding to the PQ and Vf operating modes, respectively.

Next, the ***soft switching procedure*** implemented in the supervisor is briefly explained. Transition is smoothed out by allowing certain switching time intervals, instead of instantaneously switching. A quite common control engineering practice to do this is ***to weight references sent to the low-level controllers*** by some signals w_1 and w_2, which are set to vary in opposite senses during a conveniently chosen time interval τ_3 such that $w_1+w_2=1$.

Fig. 3.29a) shows the ***transition diagram*** between the two operating modes, where the intermediary states correspond to the necessary delays introduced for sake of smoothness. Thus, concerning the $PQ \rightarrow Vf$ transition, supplementary delays τ_1 and τ_2 allow overlapping of the electrical loads and hence limitation of the output current decreasing and of the DC-link voltage excessively increasing. The drawback of this choice is a nonnegligible delay when performing this transition (several hundreds of milliseconds).

In Fig. 3.29a), six ***triggering events*** were represented, whose meanings are as follows.

- Events e_1 and e_2 correspond to asynchronous decisions of the upper-level user/operator of passing from PQ mode to Vf mode and *vice versa*, respectively.
- Unlikely, events e_3, e_4, e_5 and e_6 are synchronous with the time.

  Event e_3 marks the end of time interval τ_1 passed since entering in state IS_1; the same holds for event e_4, time interval τ_2 and state IS_2.

  Events e_5 and e_6 correspond to the end of transients of signals w_1 and w_2: the former for w_1 decreasing and w_2 increasing and the latter for w_1 increasing and w_2 decreasing.

The ***time switching sequences*** from PQ mode to Vf mode and backwards can be viewed in Figs. 3.29b)–d). Time intervals that the system has to spend within each of the intermediary states IS_1–IS_4 may result from formulating an optimal control problem under state constraints according to, for example, the formalism developed in [96], which would require in this case both *system stability being preserved and DC-link voltage and output current magnitude constraints being respected during switching.* However, adopting ***some covering values*** for τ_1–τ_4, instead of optimal switching moments – according to some rather *qualitative* guidelines than to precisely quantitative values – can be a sufficiently convenient practical choice in this case.

- Thus, time intervals τ_1 and τ_2 can be chosen such that to allow canceling the load transients when coupling the load into the system ($K_1=1$, $K_2=1$, state IS_1) and respectively decoupling the system from the grid ($K_1=0$, $K_2=1$, state IS_2). In this case, $\tau_1=\tau_2=0.1$ s is considered long enough to ensure load transient cancelling.
- As regards the time intervals τ_3 and τ_4 during which the control laws are switched, their selection is made in relation to the slowest closed-loop dynamic of the electrical variables, *i.e.*, that of the DC-link voltage, U_{DC}. Thus, $\tau_3=\tau_4=0.5$ s is sufficiently long for obtaining quite smooth transients on U_{DC} along with reasonable control effort, that is, maintaining the generator's q current, i_{qG}, and the inverter's current, within reasonable limits.

This subsection ends with some ***HILS validation*** results resumed from [93], which illustrate effective smooth $PQ \rightarrow Vf \rightarrow PQ$ switchings (Fig. 3.30) and their coherence with the different above-selected switching time intervals. The HILS test bench is based on a ***CFWT tower of*** 2.3 kW ***rated power at water speed of*** 2.3 m/s.

In Fig. 3.30a), a global view of the a-phase grid-side variables and the DC-link voltage evolutions are presented, with grid voltage and current zeroing when in Vf mode and their quite soft transients at commutation instants. Zoomed images of the same variables for both ways of switching are shown in Figs. 3.30b) and c), while emphasizing the switching timing.

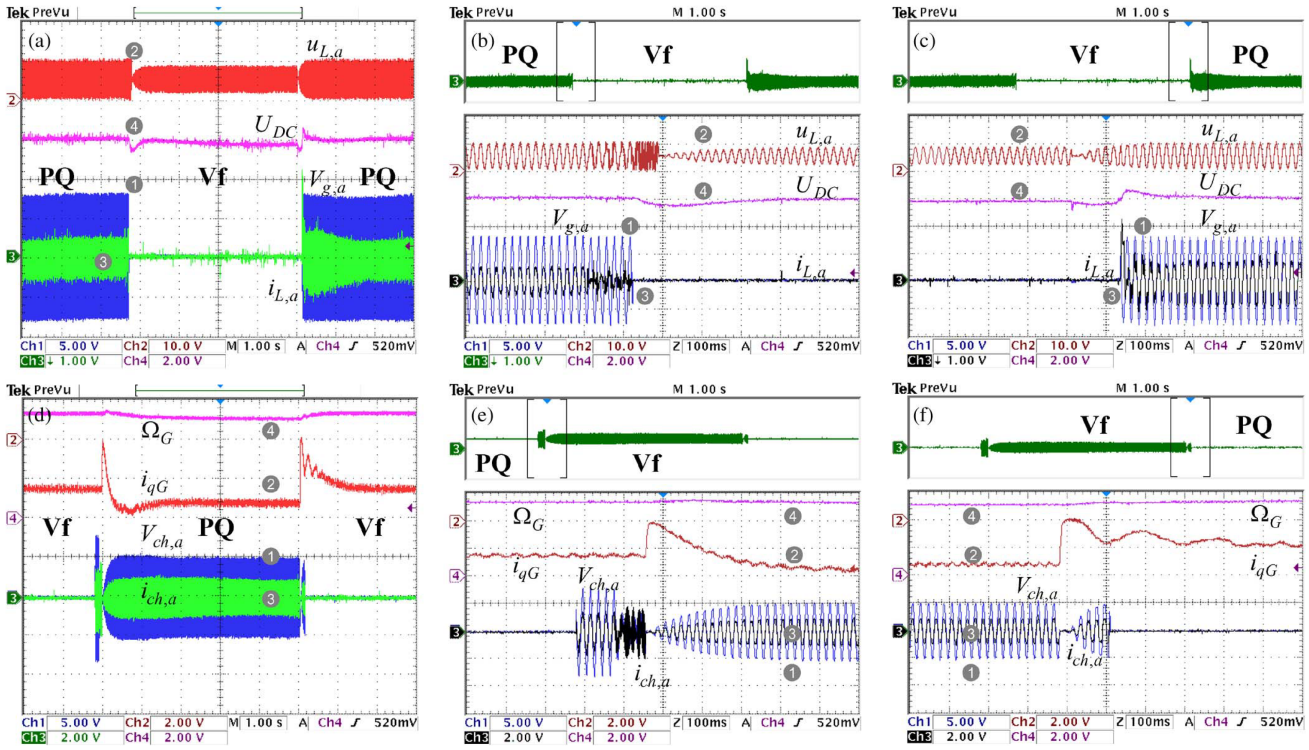

Figure 3.30: Variable evolutions during $PQ \rightarrow Vf$ and $Vf \rightarrow PQ$ switchings (HILS oscilloscope captures) [93]: a)–c) Ch1 – grid voltage, $V_{G,a}$ (25 V/V); Ch2 – inverter duty cycle, $u_{L,a}$ (0.1/V); Ch3 – grid current $i_{L,a}$ (5 A/V); Ch4 – DC-link voltage, U_{DC} (75 V/V); b) and c) are left and right zoom outs of a), respectively; d) – f) Ch1 – load voltage, $V_{ch,a}$ (25 V/V); Ch2 – quadrature PMSG current, i_{qG} (5 A/V); Ch3 – load current $i_{ch,a}$ (5 A/V); Ch4 – PMSG rotational speed, Ω_G (50 rad/s/V); e) and f) are left and right zoom outs of d), respectively.

Evolutions of both PMSG-side (mechanical) and load-side (electrical) variables in response to mode switching are exhibited in Fig. 3.30d). As expected, the system behaves differently when switching as $PQ \rightarrow Vf$ than $Vf \rightarrow PQ$, due to its genuine nonlinearity. Internal variables – such as q-component of generator's current, i_{qG}, rotational speed, load current and voltage – remain within admissible limits during switching. Zoomed images are shown in Figs. 3.30e) and f), where the transient $PQ \rightarrow Vf$ appears to be longer than expected.

3.3.3 Master-slave synchronized operation of miHECS for structural loads alleviation

In this subsection the miHECS under study is based on ***two twin Achard CFWT towers*** as prime movers, operating in a river stream and subject to ***an imposed restriction between their angular positions*** in order to achieve improved hydrodynamic performances, *e.g.*, structural loads alleviation. The need for synchronization can be effectively achieved by a variable-speed-based control approach inspired from ***phase-locked loop*** (**PLL**) ***synchronization techniques*** used in electronics and communications [97], that is, without using any power coupling (mechanical or electrical) between the two towers.

The main idea, detailed in our patent [87], relies upon considering the CFWT tower as a system outputting a rotational position. Being speed-controlled, each tower can consequently be modelled as a frequency-controlled oscillator with a non-negligible dynamic, thus justifying application of PLL principle for synchronization purpose. Oscillators' synchronization is a topic of general interest, with extensive applications in all fields of electrical engineering [98]–[100].

The considered CFWT-twin-tower miHECS architecture is depicted in Fig. 3.31a), where each tower is rigidly coupled to its associated PMSG and individually interfaced to the power grid by means of a back-to-back three-phase converter; hence, the system operates in PQ mode.

Ensuring that the two juxtaposed towers turn at the same speed, but in opposite senses, leads to practically nullifying the global lift force action and increasing the hydrodynamic conversion efficiency [82], [84]. The control goal is thus stated as ***keeping equal the two rotational speeds, meanwhile ensuring the opposite symmetry of the blades***. Fig. 3.31b) shows a schematic upper view of the twin towers, emphasizing their relative angular position lag, noted by α.

As the water speed varies quite slowly, the time response performance is sacrificed for sake of reliability wherever possible, priority being given to guaranteeing the system's continuity of service based upon initial minimal control tuning effort. Within an exclusively-information-coupled ***master-slave*** configuration, the control problem is ***to control the slave tower to track the master tower's rotational speed, while simultaneously regulating their relative angular position lag at a desired constant value***.

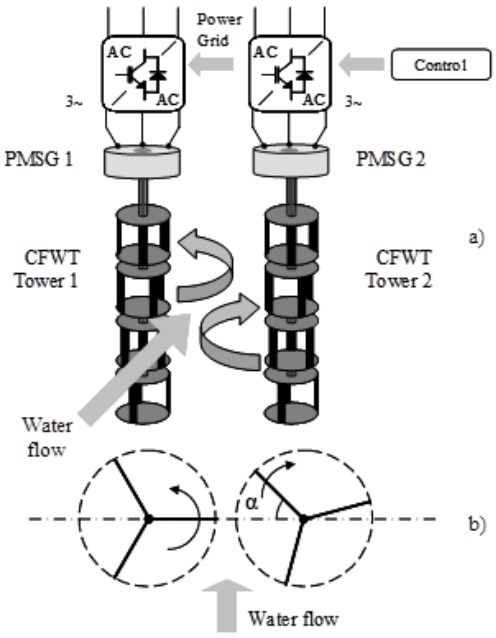

Figure 3.31: CFWT twin towers operation [88]: a) simplified architecture; b) upper view emphasizing the position lag, α.

Modelling and control design are based upon the master-slave cascade control block diagram in Fig. 3.32a), where the master tower is controlled in MPPT – *e.g.*, the conventional *hill-climbing* version recalled in Section 3.1 – both towers being equipped with rotational speed control loops and incremental optical encoders to convey the feedback signals. All "1" indices refer to the master and the "2" indices refer to the slave. The ***phase detector*** senses the occasionally occurring master-slave angular position difference, which is fed to the loop filter. This latter provides the rotational speed difference, $\Delta\Omega$, necessary to adjust the slave rotational speed reference such that to zeroing the difference.

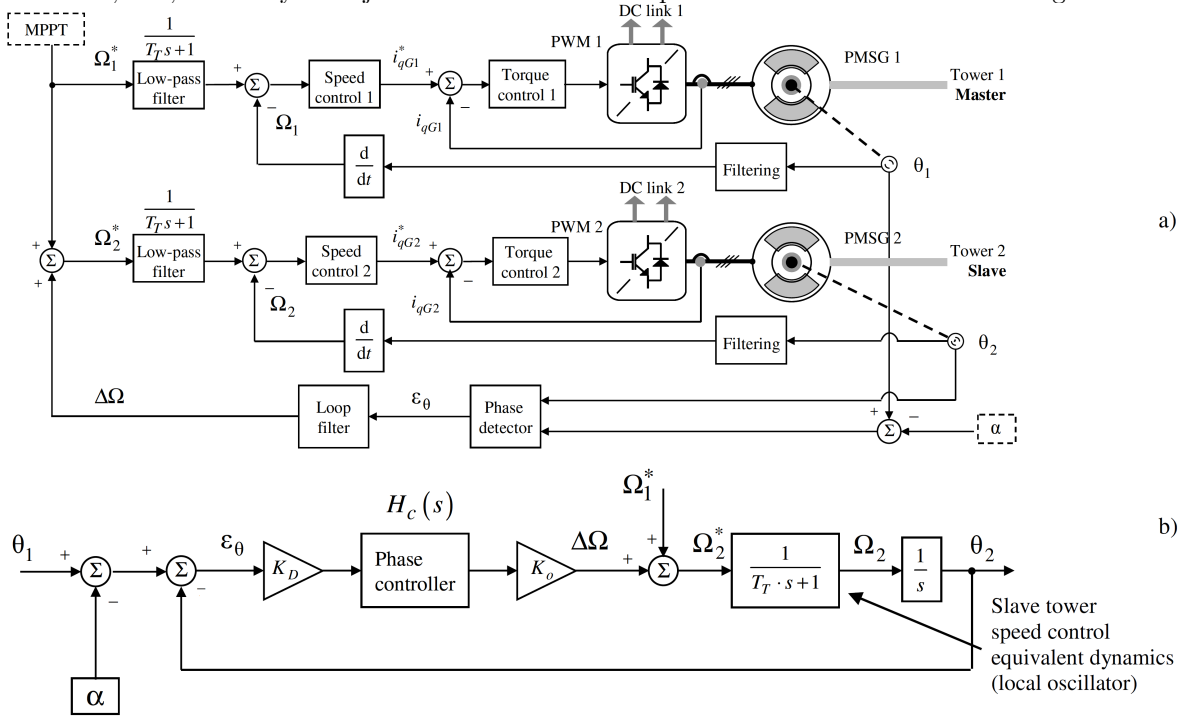

Figure 3.32: Modelling and control structure for purpose of CFWT towers synchronization [88]: a) master and slave towers modelled as two coupled cascade-control systems, emphasizing their respective PMSGs' controls; b) linearized model of the slave tower position control loop.

As the PMSG is torque controlled, the tower-PMSG coupling linearized dynamic is described by a first-order transfer function of form $\frac{1}{Js - C}$ (see also (3.28) in previous Subsection 3.3.1), where J is the tower-PMSG coupling

inertia and $C = \partial T_T \Big/ \partial \Omega$ is the slope of the tower-torque–speed $T_T(\Omega)$ curve for a given value of water speed (see Fig. 3.26 in the current subsection). A rotational speed PI controller can be designed such that to obtain good performance on both the *right* side of $T_T(\Omega)$ (*stable* open-loop behaviour, $C < 0$) and its *left* side (*unstable* open-loop behaviour, $C > 0$), with the particular demand to have a gain large enough to stabilize the behaviour in this latter case. For example, imposing a second-order closed-loop dynamic with about hundred-of-millisecond time constant is a reasonable choice.

In order to obtain reasonable control effort, the master's rotational speed reference, Ω_1^*, is low-pass filtered by $\frac{1}{T_T s + 1}$, as indicated in Fig. 3.32a). For reasons of obtaining the same dynamic for both master and slave, Ω_2^* must also be filtered by the same filter, where T_T can be selected at about seconds, *i.e.*, large enough in relation to the rotational speed closed-loop dynamic. This choice allows the first-order dynamic given by T_T to prevail in the dynamic of $\Omega_2^* \rightarrow \Omega_2$ transfer. Such choice also corresponds to some particular PLLs design of first achieving the superposition of frequencies and then that of phase angles [101].

The ***synchronization loop controller*** is tuned such that a desired closed-loop behaviour from the master's angular position, $\theta_1 + \alpha$ – where α is the imposed angular position lag between the twin towers – to the slave's angular position, θ_2 to be obtained. Fig. 3.32b) contains a block diagram of this transfer.

Some differences due to the nature of the input can be remarked in relation to an analog PLL, namely concerning the information containing the phase angle to be tracked. In the classical linear approach, the sinusoidal waveform containing the phase information is the loop reference and the phase of a local oscillator is adjusted by the output of the loop filter (phase controller) in order to achieve the synchronization with this reference waveform [97]. Here the *phase information* has the genuine form of a *sawtooth signal*, as provided by the master encoder. The slave encoder generates a similar signal representing the output of the local oscillator.

The two sawtooth signals can easily be transformed into harmonic signals (*i.e.*, by applying sinus function), that carry the same phase information. These signals are further applied to a ***phase detector***, just as in the PLL case. The phase detector formula used here is:

$$\varepsilon_\theta = \sin(\theta_1 - \alpha - \theta_2) = \sin(\theta_1 - \alpha) \cdot \cos(\theta_2) - \sin(\theta_2) \cdot \cos(\theta_1 - \alpha), \tag{3.31}$$

thus allowing to ε_θ to be approximated by the sinus argument, $\theta_1 - \alpha - \theta_2$, for sufficiently small values of this latter, hence, to further using a linear PLL design approach. Therefore, a PID controller can be designed to compensate the main dynamic T_T and to ensure tracking of angle lag reference variations, according to imposing the slowest closed-loop dynamic in the system, as placed on the upper-most control level – design details, as well as steady-state and stability analysis of the synchronization closed loop can be found in [88].

Next two figures present some ***HILS experimental results***, resumed from [88], which validate the ***reference-tracking*** and ***disturbance-rejection*** behaviour, respectively. The CFWT tower characteristics are the same as in the test bench used in previous Subsection 3.3.2 – dedicated to management of a miHECS operating modes – that is, each ***CFWT tower has*** 2.3 kW ***of rated power at water speed of*** 2.3 m/s. While the *master*'s dynamic behaviour is *numerically* simulated, the focus is on illustrating the ***slave's physically-simulated behaviour***, while also emphasizing the generation system's electromechanical variables.

Fig. 3.33a) shows the variables' evolutions when a gradient-limited angle lag variation (from 0 to $\pi/2$ rad and backwards) is imposed between the two CFWT towers, for a short time horizon (one minute), the water flow being constant at 2.3 m/s during this time. The master is operated in MPPT; as the slave is synchronized in position, it will find itself at about the same optimal point, as indicated by the power coefficient evolutions, C_{p1} and C_{p2}. The associated control effort is visible on the PMSG currents, i_{qG1} and i_{qG2}, and rotational speed evolutions, Ω_1 and Ω_2, as the slave is either accelerated or decelerated to follow the master angular position; short periods of synchronization loss may thus occur, as Figs. 3.33 a) and b) show. Such intervals are much shorter compared to the slow variations of the water flow speed; therefore, the resulting energy loss is negligible. The tracking dynamic performance can be asssessed by analyzing both the evolution of angle lag response, $\Delta\theta = \theta_1 - \theta_2$, and that of the angle lag error, $\varepsilon_\theta = \Delta\theta - \alpha$.

Fig. 3.33b) displays a six-second zoomed image of the same curves as in Fig. 3.33a). With about-1.5-s transients, the synchronization process is sufficiently fast in order to prevent from long de-synchronization time lags, which are not desired because of hydrodynamic reasons. Oscillations visible on i_{qG2} are due to some unmodelled dynamics and parameter variations, but they are not critical.

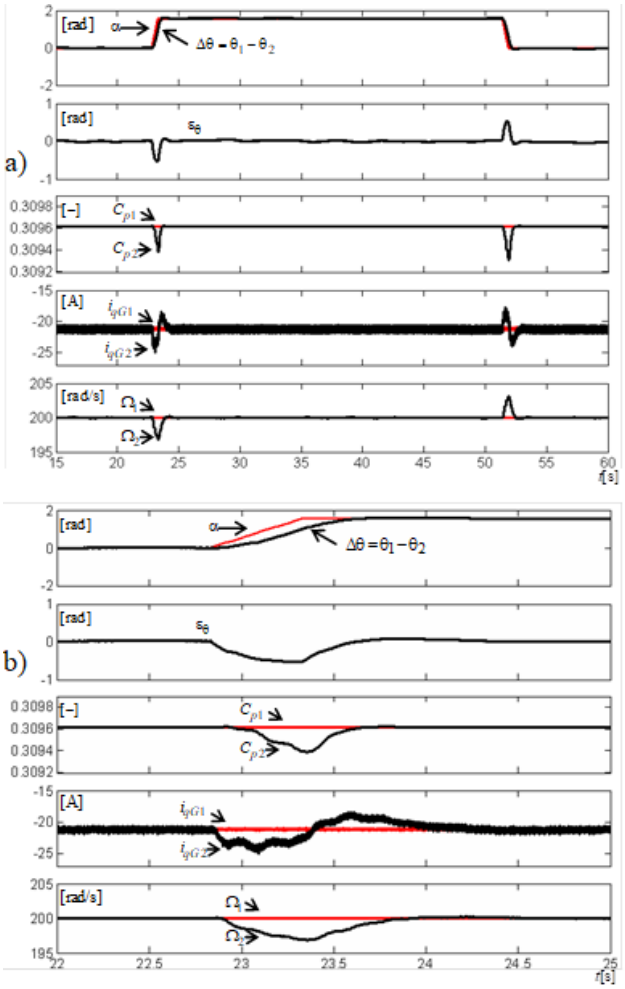

Figure 3.33: HILS validation of miHECS PLL-like synchronized operation – ***reference tracking*** performance (ControlDesk®captures) [88]: a) variables evolution when the imposed angle lag, α, steps like $0 \rightarrow \pi/2 \rightarrow 0$ rad; b) zooms of the same variables.

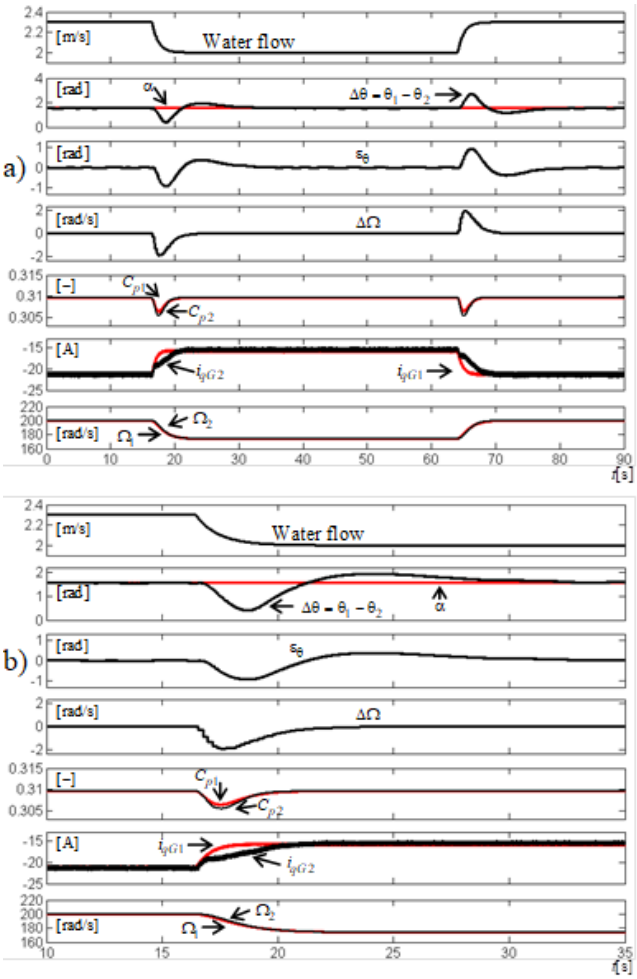

Figure 3.34: HILS validation of miHECS PLL-like synchronized operation – ***disturbance rejection*** performance (ControlDesk®captures) [88]: a) variables evolution under water flow speed filtered step; b) zooms of the same variables.

Figs. 3.34a) and b) show the evolution of the system main variables in response to a filtered-step variation of the water flow speed acting as a disturbance, with, this time, the angle lag α being constant at $\pi/2$ rad. Thus, the water flow speed varies from 2.3 m/s to 2.0 m/s and backwards, while the master generator operates in MPPT. The synchronization controller succeeds in cancelling the angle lag error in about 12 s.

The speed correction imposed to the slave, $\Delta\Omega$, evolves as a glitch, which is either positive or negative. Thus, when the water speed decreases, the slave is advanced in relation to the master, because the *physically*-simulated slave's rotational speed decreases *more slowly* than the *numerically*-simulated master's speed, due to some unmodelled dynamics, *e.g.*, inherent supplementary frictions. Hence, $\Delta\Omega$ must be negative in order to re-cancel the angle lag error. When the water speed increases, the inverse situation happens.

Successful HILS validation of the synchronization control was continued with a ***pilote-site validation*** on a ***prototype of two-twin-CFWT-tower-based miHECS*** installed on a headrace canal feeding a hydroelectric plant near Grenoble in France. Indeed, due to its simplicity and good robustness – as revealed by both formal

analysis and experiments [88] – the above-briefed synchronization method proved to be easily and effectively implementable into practice, with results that confirm theoretical predictions. Some of these results, resumed from [85], are presented next.

The generation system has 16 kW ***of total output rated power at*** 2.8 m/s ***of water flow velocity***, being characterized by maximum power coefficient $C_{p_{max}} = 0.95$ and optimal tip speed ratio $\lambda_{opt} = 2.7$. The PMSG rated rotational speed is 330 rpm.

Fig. 3.35 shows how the position error – above defined as $\Delta\theta = \theta_1 - \theta_2$ – evolves when the angle offset reference, α, is set to zero and master tower's rotational speed increases as a slowly-variable ramp. Evolutions of the two rotational speeds – master's and slave's – are practically superposed, which indicates effective synchronization.

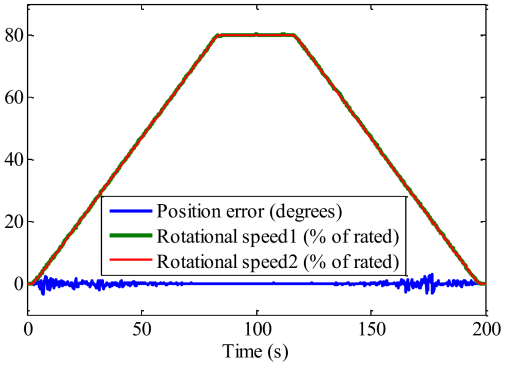

Figure 3.35: Validation of PLL-like master-slave synchronization on a miHECS pilote site [85]: rotational speeds and position error between the two twin towers.

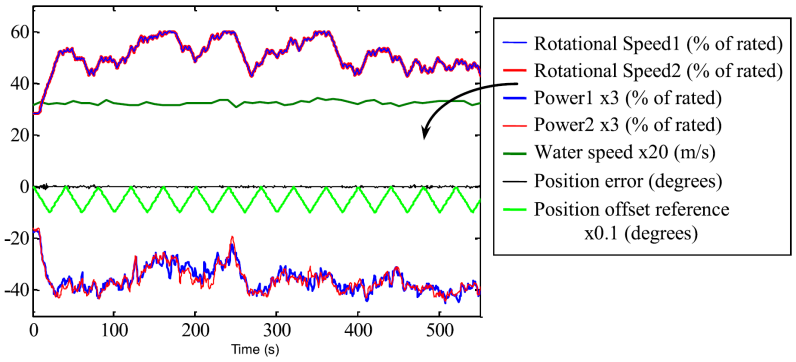

Figure 3.36: Validation of PLL-like master-slave synchronization on a miHECS pilote site [85]: time evolutions of main variables when the two twin towers are synchronized and the master tower operates in MPPT.

Fig. 3.36 synthesizes the results obtained in a more complex scenario, that is, when *the two towers are synchronized and the master tower is operated at MPPT*. When in MPPT mode and under variable water flow speed, the speed reference must be continuously updated, which renders the synchronization more challenging than in other cases. Moreover, a continuous triangle variation of the angle offset reference, α, is also applied to challenge even more the synchronization loop with MPPT. Rotational speed variations show how the system tracks the water velocity changes. Evolutions of the power provided by each of the two twin CFWT towers are also represented in this figure. The position error is effectively corrected to zero despite the continuous variation of α, thus proving a perfect coherence with HILS validation results reported in [88].

As a conclusion to this subsection, some remarks can be made towards generalizing the main merits of the PLL-like synchronization control of rotating prime movers. Indeed, this method is easily applicable for other types of RECS, *e.g.*, for WECS using a similar structure, *i.e.*, employing ***two vertical-axis adjacent wind turbines***. The main idea can also be extended to several synchronized turbines composing a plant. A pertinent example is the synchronization of ***multiple horizontal-axis wind turbines*** in the same wind farm, in order to alleviate the power pulsations due to the tower shadow effect.

3.4 Power optimization control approaches for photovoltaic (PV) systems

Both stand-alone and grid-connected photovoltaic (PV) installations, as well as hybridizations of PV with some other renewable energy sources and/or storage devices, make nowadays part of a familiar landscape [102], [103]. Rendering the PV systems more adequate to the wide use in terms of power, efficiency, grid compliancy and communication capacity for those grid-connected ones, reliability and service time, safety and security, *etc.*, continues to be a topic of great interest. In a larger framework, sizing and operation design of PV systems are usually the result of a *co-design optimization procedure* guided by various and often contradictory criteria, oriented towards

finding the best trade-off within a specific application [104]–[106].

Control approaches are necessary for optimizing the PV systems dynamic performance, in terms of ***reactivity to the variability of*** the primary energy source – *i.e.*, the ***solar irradiance*** – and ***robustness*** to as various as possible kinds of disturbances. A general remark is that, being based upon a very fast physical phenomenon (the *photoelectric effect*) and not supposing any moving mechanical part, PV systems have ***the smallest inertia among all the RECS*** and this comes with the undesirable side effect of a globally reduced robustness.

As in the case of other RECS operating in grid-connected mode, maximization of the captured power is the main goal. Simple, efficient, and minimal-knowledge-demanding MPPT methods aiming at maximizing the extracted energy irrespective of the irradiance conditions were investigated in the literature [107], [108]. In this case, it is about tracking the *Optimal Regimes Characteristic* (ORC) like the one presented in Fig. 3.3 in the introductory Section 3.1 of the current chapter.

Among the various MPPT methods specific to PV systems, the ones relying upon injecting high-frequency small-amplitude (usually harmonic) perturbations in the system in order to detect the sign of the power gradient are mostly known for PV systems as the ***perturb-and-observe (P&O) class of methods*** [109], [110]. Their basic idea is the same as the one used in *Extremum Seeking Control* (ESC), which has been detailed in Section 3.1. It is worthy to note that ESC can also be applied by using ***intrinsic disturbances***, already present in the system, therefore without a need for inducing exogenous excitation signals – such an approach for WECS made the object of one of our contributions briefed in Subsection 3.2.3 in this memoir and its application also proved pertinent in the case of PV systems, as further detailed in Subsection 3.4.3 in the current section.

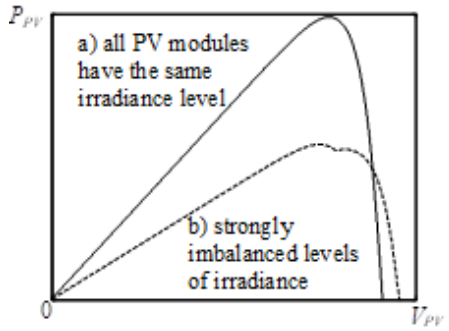

Figure 3.37: Example of a PV array whose $P_{PV}(V_{PV})$ curve exhibits: a) a single maximum; b) multiple maxima under certain irradiance conditions [111].

Whereas MPPT is practically solved in the case of PV systems having unimodal power-*vs.*-voltage, $P_{PV}(V_{PV})$, characteristic, it may not be the case of *large spatially distributed systems*, with high probability of undertaking partial shading, so *strongly imbalanced levels of irradiance*. Indeed, specific configurations of PV modules may have global *multiple-maxima power characteristics* – see, for example, the allure of curves in Fig. 3.37, obtained for the same PV array, but under different irradiance conditions [111]. Adaptations of the general MPPT methods for tracking multiple peaks under rapidly changing irradiance conditions were proposed [112], [113], which also motivated our contribution [114] in this regard.

Having been initiated during my 2008–2009 post-doctoral internship at G2ELab, work on the PV systems control topic also continued during my first years at GIPSA-lab (2012–2014).

Synthetically speaking, our contributions propose some original improvements and adaptations to basic MPPT for grid-connected PV systems.

Thus, contributions summarized next in the two first subsections were developed within the collaboration with Ph.D. student Damien PICAULT, post-doctoral fellow Iulian MUNTEANU and Associate Professor Bertrand RAISON, under the supervision of Professor Seddik BACHA. A short description follows.

- Application of Extremum-Seeking-Control ***(ESC)-based MPPT for grid-connected PV systems*** is systematically considered ***under conditions of strongly variable irradiance***, while emphasizing possible existence of *multiple (local) power maxima* under *partially-shadding* conditions, depending on the PV panels' connection. Main results were published in:

  A.I. Bratcu, I. Munteanu, S. Bacha, B. Raison (2008). Maximum power point tracking of grid-connected photovoltaic arrays by using extremum seeking control. *Control Engineering and Applied Informatics* – Romanian Society of Control Engineering and Technical Informatics (SRAIT), 10(4), 3–12,

  which is among the first publications dealing with systematic application of ESC techniques for achieving the MPPT for PV systems, and makes the object of Subsection 3.4.1.

- Approaching the ***captured power maximization of cascaded*** – or ***series***, instead of the more habitual parallel – ***DC-DC converter architectures of PV modules*** led to an ***MPPT-degraded control strategy***, where simultaneous MPPT of all PV modules needs to be given up whenever safety operating constraints require it. Results concerning this topic – presented next in Subsection 3.4.2 – made the object of an initial conference paper:

  A.I. Bratcu, I. Munteanu, S. Bacha, D. Picault, B. Raison (2009). Power optimization strategy for cascaded DC-DC converter architectures of photovoltaic modules. In: *Procs. of the IEEE International Conference on Industrial Technology – ICIT 2009*, Churchill, VIC, Australia, February 2009, pp. 1–8,

  further extended as a journal publication:

  A.I. Bratcu, I. Munteanu, S. Bacha, D. Picault, B. Raison (2011). Cascaded DC-DC converter photovoltaic systems: power optimization issues. *IEEE Transactions on Industrial Electronics*, 58(2), 403–411,

  which has received ***the largest number of citations among all my journal publications*** (*e.g.*, 225 citations in Web of Science since its publication, in 2011).

The final Subsection 3.4.3 concerns formalization of the ESC-based MPPT and control design guidelines for a class of grid-connected PV systems for which ***the searching signal is already present in the form of the sinusoidal ripple of some variables***. The related main results made the object of a collaboration with post-doctoral fellow Iulian MUNTEANU during 2012–2014 at GIPSA-lab and were published in the journal article:

- I. Munteanu, A.I. Bratcu (2015). MPPT for grid-connected photovoltaic systems using ripple-based extremum seeking control: analysis and control design issues. *Solar Energy*, 111, 30–42.

3.4.1 Extremum-seeking-control (ESC)-based MPPT for photovoltaic (PV) systems

Without loss of generality, a two-conversion-stage topology of a single-phase grid-connected PV energy conversion system is considered in this subsection (Fig. 3.38), which is composed of an array of PV modules whose captured energy is sent to the utility grid after being converted into electrical energy by means of a two-stage power electronic system: a DC-DC converter and a DC-AC converter (inverter) connected through a DC-link. The capturing device consists in a PV array composed of n series connections connected in parallel, each of which is composed of m PV modules. It is supposed that, in general, each module experiences its own irradiance conditions, Irr_{ij}, $i = 1, 2, ...n$, $j = 1, 2, ...m$. The PV array output current is I_{PVa} and its output voltage is V_{PVa}.

Fig. 3.38 also contains the *global control block diagram*, organized on *two levels*. The desired operating regime is decided in the upper level, whereas the low-level control effectively implements the decision taken at the upper level. In the case of grid-connected systems, imposing a certain operating point is equivalent with imposing a certain level of the power provided – in particular, this can be the maximum available in the irradiance. In this latter case, the upper-level control structure from Fig. 1 becomes an optimization control loop, required to track the maximum power operating point – which is in general not precisely known and varies with the irradiance level – instead of tracking an imposed power setpoint.

The ***ESC implementation block diagram*** of this ***upper-level control*** is detailed in the lower part of Fig. 3.38, a PV-adapted version of the general ESC principle illustrated in Fig. 3.5 in Section 3.1. The primary resource, *i.e.*, the solar irradiance, is supposed to be strongly time varying, as well as variable from a module to another. Due to taking into account this double variability, PV-power-*vs.*-voltage curves of the *global PV array* can either be *unimodal* – thus replicating the allure of the power-voltage curve of a *single PV module* – or they can be multimodal. Here the results of applying this method to unimodal PV power curve are only resumed, whereas details of multiple-maxima power curve case can be found in [111].

The role of the DC-DC converter is to boost the voltage level in the DC-link; it is controlled to track either a current or a voltage reference, I^*_{PVa} or V^*_{PVa}, corresponding to the operating point imposed by the upper decision level. The inverter output current, i_{grid}, is controlled such that the DC-link voltage to be maintained at an imposed value, V^*_{DC}.

The ESC block diagram in the lower part of Fig. 3.38 shows that the MPPT is achieved by controlling the DC-DC converter input voltage. As recalled in Section 3.1 of this chapter, the controller performs a modulation/demodulation operation, outputting a harmonic component called the *probing – or searching – signal*. The controller habitually contains a so-called washout filter, a demodulator, a low-pass filter and an integrator for obtaining the average component of the control input, as well as a summation with the probing signal block.

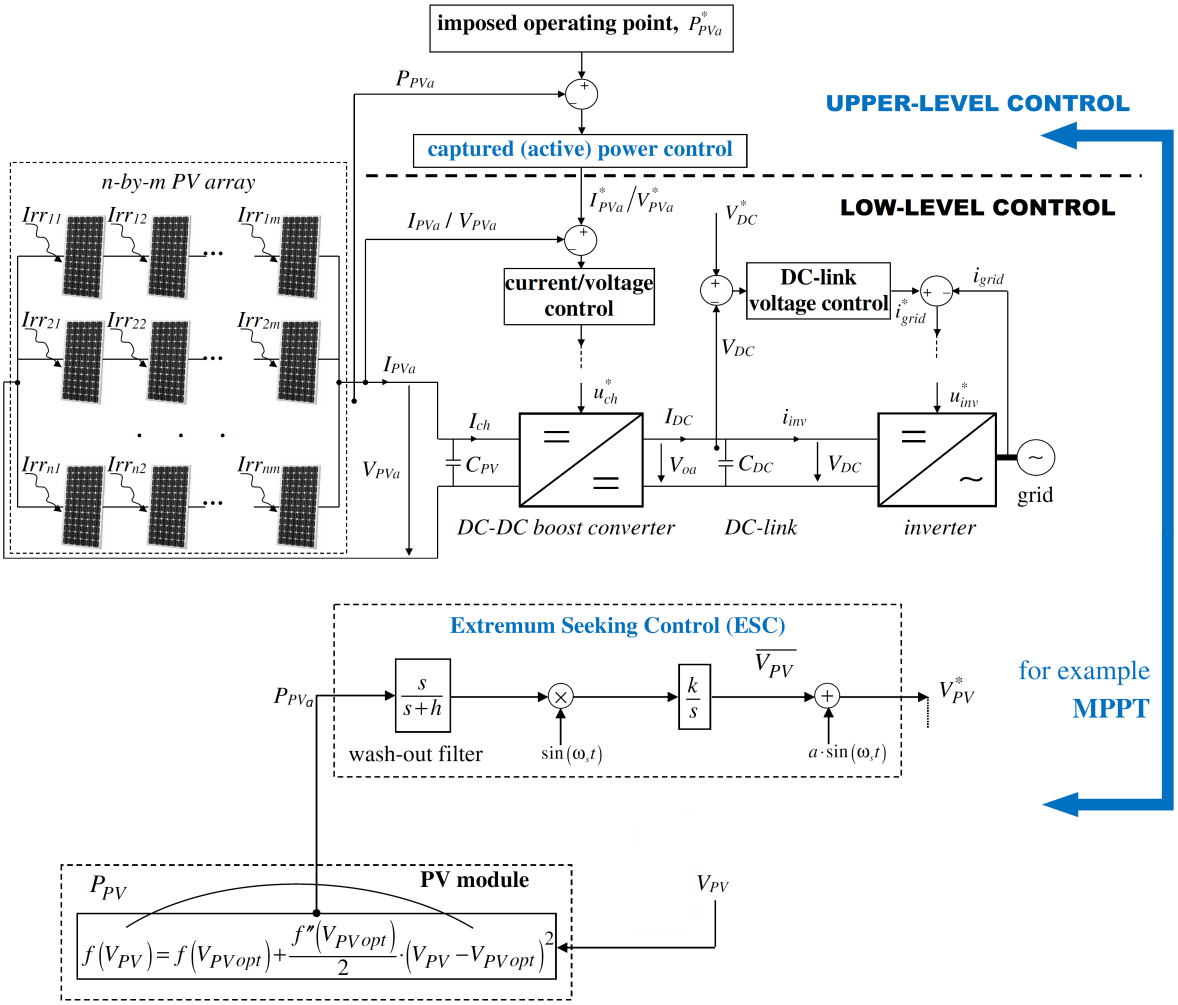

Figure 3.38: Grid-connected PV energy conversion system and the associated *two-level control* structure, where the ***upper-level control*** is particularized as an ***ESC-based MPPT*** with the associated DC-DC converter voltage as control input [111].

To further explain operation of ESC-based MPPT, some modelling details are necessary. A grid-connected PV generator having an unimodal power characteristic is modelled by a generic power function, $P_{PV}\,(V_{PV})$, having a unique maximum at V_{PVopt}, whose argument has two components: an average one, $\overline{V_{PV}}$, and a ***harmonic probing one***, ***artificially induced***, of frequency ω_s and amplitude a (Fig. 3). This function is approximated by its two-term Taylor's series around its maximum, $P_{PV}\,(V_{PVopt})$. The searching error, defined as $\widetilde{V_{PV}} = V_{PV} - \overline{V_{PV}}$, has a negative gradient:

$$\dot{\widetilde{V_{PV}}} = 0.25 \cdot k \cdot a^2 \cdot P''_{PV}\,(V_{PVopt}) \cdot \widetilde{V_{PV}}, \tag{3.32}$$

as constants k and a are positive and $P''_{PV}\,(V_{PVopt})$ is negative, thus achieving a convergent searching process. The closed-loop stability is ensured by a sufficiently large excitation frequency, ω_s, which the washout filter parameter, h, depends on [13] – see also (3.4) in Section 3.1. Input of the integrator in Fig. 3.38, $\mathrm{d}\overline{V_{PV}}/\mathrm{d}t$, will toggle its sign following the excursion of the operating point from a side to the other of the maximum, with a convergence speed depending proportionally on k, a and $1/\omega_s$.

The ***low-level control*** is another cascade control structure itself, namely having an external control loop for controlling the PV array voltage, V_{PVa}, and an internal loop dedicated to chopper current, I_{ch}, control, as suggested in the upper part of Fig. 3.38. Control tuning details can be found in [111].

Some representative ***numerical simulation results*** are next extracted from [111] to illustrate performance of the ESC-based MPPT. They were obtained on a ***PV array with*** $n = 10$ ***modules in parallel*** ($m = 1$), 1100 W ***of maximum global power, global voltage*** of 48 V. A 0.1-V-amplitude sinus MPPT probing signal of frequency $\omega_s = 2\pi \cdot 100$ rad/s was used.

Two aspects were studied about the efectiveness of the ESC-based MPPT: the first one concerns the dynamic performance of tracking *unimodal* power-*vs.*-voltage curves depending on ESC controller integral gain, k (see the lower part of Fig. 3.38), while the second aspect investigates the capability of tracking *multimodal* power curves. In the latter case, as the ESC capability of finding the global extremum is not guaranteed theoretically, simulations showed that performance of tracking the global maximum is affected by the initial state [111]. Next, illustration of the first aspect is only resumed.

If all the modules of the PV array are submitted to the ***same irradiance level***, then ***global unimodal*** power curves are obtained. The evolutions exhibited in Fig. 3.39 correspond respectively to two irradiance scenarios: first, the case a), when the common level of *irradiance* is affected by *step changes* (from 900 W/m^2 to 600 W/m^2, and then back to 900 W/m^2); then b), c) and d), which present the dynamic behaviour under *strongly (stochastically) variable irradiance* conditions.

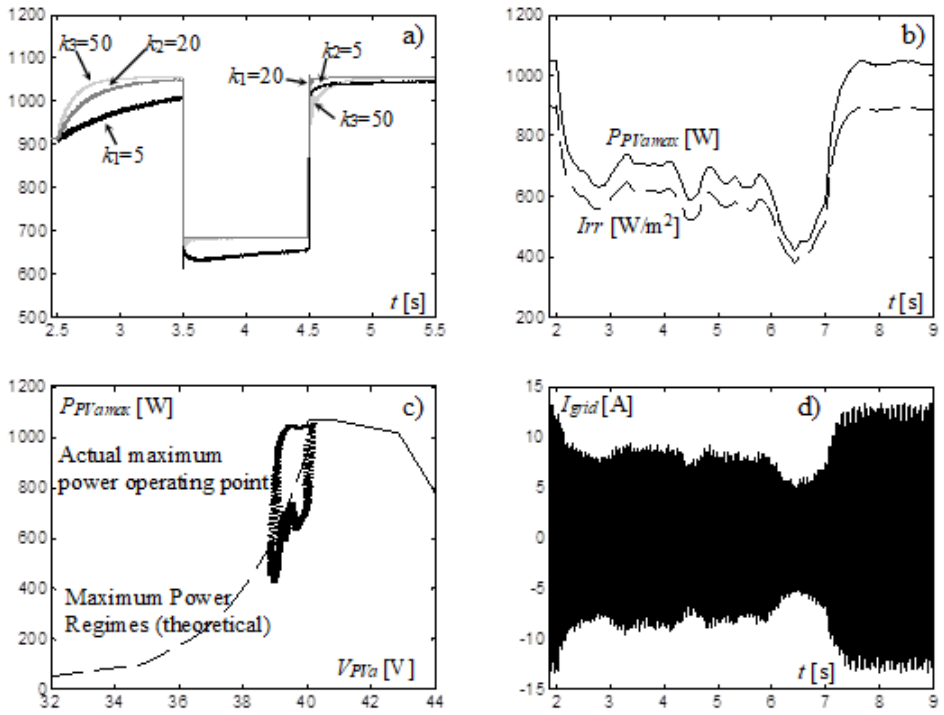

Figure 3.39: ESC performance in tracking the maximum of unimodal PV power curves under strongly variable irradiance – MATLAB®/Simulink®results [111]: a) power responses at step changes of irradiance versus maximum power for different values of the ESC controller gain, k; b) stochastic profile of irradiance and corresponding variation of the maximum power; c) excursion of the operating point in the PV-power–voltage plane; d) grid current under the irradiance profile from b).

The system is set to start from the imposed voltage of V_{PVa}=43 V at 900 W/m^2 irradiance, which does not correspond to the maximum power point. Thus, the first power transient in Fig. 3.39a) shows the MPPT performance in response to the first irradiance step. Three power time evolutions, corresponding to three different values of the ESC controller parameter, k, can be seen. The larger the value of k is, the better the tracking quality, with an effect of performance saturation and even over-tuning for k_3 = 50, as it corresponds to a longer and more turbulent transient.

The *irradiance dynamic model* used for obtaining curves in Fig. 3.39b), c) and d) is set in analogy with the dynamic modelling of another irregular renewable energy source, the wind speed – the wind turbulence modelling has been recalled throughout Section 3.2, dedicated to wind energy conversion systems (WECS) optimal control. Thus, a *two-spectral-component model* – containing an average component and a "turbulence" component – is used here to represent the irradiance dynamic behaviour.

Intuitively, as the light is however more regular than the wind, the frequency of variations would be smaller than in the case of wind. Also, the turbulence component of the irradiance would depend inversely of its average – which would express the assumption that the irradiance turbulence is more significant on cloudy days – unlike the wind, whose turbulence level depends directly on the average wind speed (see (3.13) in Subsection 3.2.1 earlier in this chapter and also Chapter 3 of our Springer monograph [29]). The following irradiance model was used in simulations:

$$Irr(t) = \underbrace{\overline{Irr}}_{\text{average irradiance}} + \underbrace{\left(\frac{Irr_{max}}{\overline{Irr}}\right)^3 \cdot f_t(t)}_{\text{"turbulence" irradiance}}, \tag{3.33}$$

where $f_t(t)$ is a band-limited white noise passed through a suitably chosen low-pass filter with a gain proportional with the desired turbulence variance. The irradiance stochastic signal, shown in Fig. 3.39b) with dashed line, exhibits quite fast variations compared to the usual natural behaviour, but this contributes at challenging even more the robustness of the ESC-based MPPT. The same figure also contains the corresponding variation of the maximum power (with solid line), showing a direct and almost instantaneous relation between the irradiance and the maximum power. The ESC controller integral gain is $k = 30$, with $h = 50$ as washout filter parameter.

Figs. 3.39c) and d) present the ORC tracking performance in the PV-power–voltage plane and the time evolution of the grid-injected current, I_{grid}, respectively. As expected, the PV array voltage around the maximum power point is almost constant. I_{grid} amplitude depends proportionally of the irradiance level.

3.4.2 MPPT-degraded operation of some particular grid-connected PV topologies

This subsection is dedicated to the use of ESC-based MPPT in a more extended framework, which focuses on ***implementing MPPT along with complying with some critical global operating constraints***. Indeed, for some particular PV configurations, it may happen that power optimization to be occasionnaly given up for sake of security, which most of the time means nonviolation of admissible variation limits of some variables. In such cases, MPPT should be integrated within a ***larger supervising structure***, able to detect and manage the different operating modes.

One such particular topology is considered next (Fig. 3.40), where n PV generators, each coupled to its DC-DC boost converter, are **cascaded – instead of paralleled**, which is more commonly used – *on the same DC bus* and interfaced to the grid by means of an inverter. The problem is stated as to find a strategy of operating this architecture at MPPT, given that its different PV generators may undertake supplementary constraints – expressed mainly as ***output-voltage-limitation*** (OVL) ***requirements*** – when exposed to strongly variable irradiance conditions.

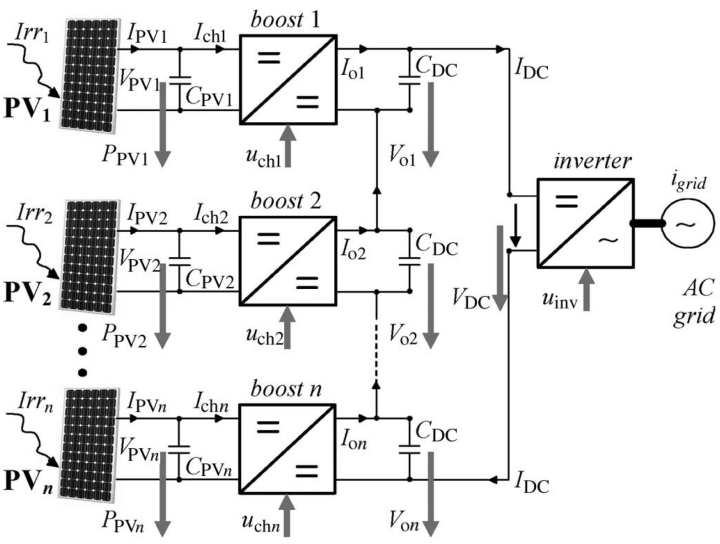

Figure 3.40: Block diagram of the considered cascaded PV architecture [115].

The architecture in Fig. 3.40 features a high-voltage PV string connected to a single inverter, having the advantages of a "converter-per-panel" approach, obviously cheaper, but also more efficient than individual grid-connected inverters [116]. Following the result that the buck and boost converters are the most efficient topologies for a given cost [116], boost DC–DC converters were here employed.

Thus, for a given DC-bus voltage, the individual boost converters can be operated at a relatively small step-up ratio (usually three to four), further resulting in good efficiency along with low cost. On the other hand, the series

connections has somehow ***limited MPPT performance, because the global power is limited by the power given by the worst irradiated panel***. Thus, the total power is susceptible to diminish in the case of, *e.g.*, partial shading on some panels. In this context, our paper [115] provides a numerical-simulation-based comparison between the cascaded case and a parallel case of the same power.

In Fig. 3.40 each converter module i is based on the PV generator PV_i, consisting of either a single panel or a connection of panels, supposed to receive all the same irradiance, such that the power characteristic remains unimodal. Such a PV generator can independently control and thus optimize the power flow from its irradiance Irr_i by means of the duty cycle $u_{\mathrm{ch}i} \in \{0, 1\}$ of its associated chopper i. In grid applications, each chopper performs MPPT for its PV generator, while the grid inverter regulates the DC-bus voltage. At steady state, the same current I_{DC} passes through all the choppers, with the sum of their output voltages being the DC-bus voltage $\sum_{i=1}^{n} V_{\mathrm{o}i} = V_{\mathrm{DC}}$. The chopper output voltages are:

$$V_{\mathrm{o}i} = V_{\mathrm{DC}}^{*} \cdot \underbrace{\frac{I_{\mathrm{PV}i}^{*} \cdot V_{\mathrm{PV}i}^{*}}{\sum_{i=1}^{n} I_{\mathrm{PV}i}^{*} \cdot V_{\mathrm{PV}i}^{*}}}_{w_i}, \quad i = 1, 2, ...n, \tag{3.34}$$

where V_{DC}^{*} is the desired (reference) DC-bus voltage and $(I_{\mathrm{PV}i}^{*}, V_{\mathrm{PV}i}^{*})$, $i = 1, 2, ...n$, are the n operating points. According to (3.34), the DC-bus voltage distribution on the converter modules depends on the weights, w_i, $i = 1, 2, ...n$, of the individual PV power levels in the global provided power.

As long as the irradiance levels are almost the same for all PV generators in the grid-connected cascaded PV topology in Fig. 3.40, one can impose practically the same operating point – in particular, the maximum power one – ensuring that the DC-bus voltage be almost equally supported by the n DC–DC converters and the total power be maximized. Indeed, numerical simulations show that simultaneous MPPT operation of all PV generators is effective only if these ones are almost equally illuminated [115]. Otherwise, if the irradiance levels are sensibly different for some time, then the weights w_i become ***unbalanced*** in (3.34), and some DC–DC converters undergo ***over-voltages*** (possible violation of voltage-limitation-type constraints). Hence, in order to cope with the most unfavourable case, the global power optimization requires ***a supervisor that detects a sufficient degree of degrading the initial optimal strategy such that to allow meeting the constraints***.

Implementation of a supervisor for the above-explained purpose supposes that each PV generator to be equipped with two control laws instead of a single one: the **MPPT** (the main one) and the over-voltage limitation (**OVL**, the secondary one). The supervisor looks at variation trends in a relevant time window, therefore its algorithm runs every T_{sv} s, where T_{sv} is suitably chosen depending on the fastest dynamic of the supervised system.

Assuming that all the generators are in MPPT, the supervisor must be able to detect OVL violations due to unbalance between the power weights of generators and, thus, between their output voltages $V_{\mathrm{o}i}$, $i = 1, 2, ...n$, according to (3.34). The admissible threshold can reasonably be set at $1.2 \cdot V_r$, where V_r is a chopper's *rated* output voltage, whose value results in the initial sizing of the PV system, namely by imposing that the ratio between the DC-bus voltage *ideal* value, $V_{\mathrm{DC}}^{*\mathrm{ideal}}$, and V_r to approach the number of PV generators. Therefore, the following holds:

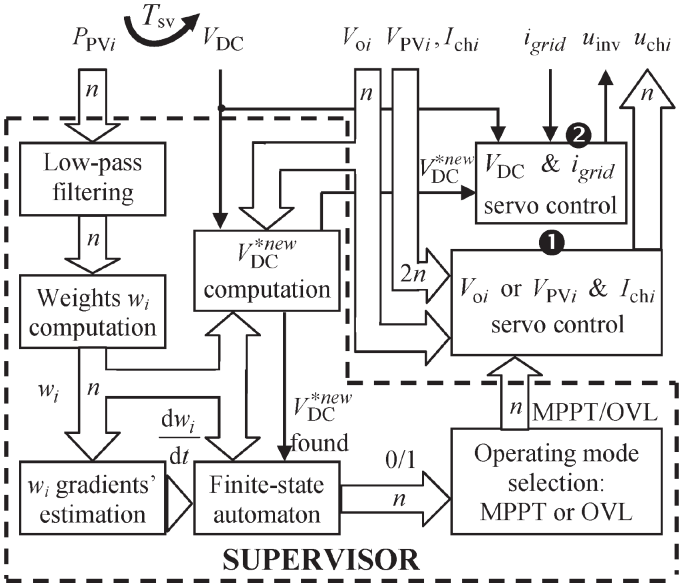

Figure 3.41: Supervisor implementing the global power optimization strategy: block diagram and connections with the choppers' and inverter's control blocks [115].

$$V_r = \frac{V_{\mathrm{DC}}^{*\mathrm{ideal}}}{n} \tag{3.35}$$

When at least one such limitation is detected, then a new possible value of the DC-bus voltage reference is first sought for, in a way such that to reestablish the balance between voltages, meanwhile laying in between ±20% around $V_{\rm DC}^{*\rm ideal}$. If such a value could not be found out, then the supervisor decides switching from MPPT to OVL for the generators having surpassed the admissible threshold voltage, while the other generators remain in MPPT. If the power weight of a generator operating in OVL decreases, this means that the global power has increased. This can only be due to the increasing of the power provided by the generators still operating in MPPT, which indicates that the irradiance balance is going to be reestablished and the MPPT is again possible. The control of the concerned generator can then be switched back to MPPT based on estimating the gradient of the power weight.

The ***supervisor block diagram*** is shown in Fig. 3.41. The formal steps of the supervising algorithm can be found in [115]. Below a description and justifying details of its operation are briefed.

Conveniently designed low-pass filters are used to reflect the trend on the desired time window. Based upon computing the power weights w_i, $i = 1, 2, ...n$, and their gradients, the supervisor outputs n binary decisions referring to the operating modes of the n PV generators: output i is 1 for MPPT and 0 for OVL. Switching between the two controls supposes only changing the voltage reference. These outputs feed block 1 in Fig. 3.41, which generically denotes the n chopper control structures; these latter further provide the duty cycles $u_{{\rm ch}i}$, $i = 1, 2, ...n$, to the choppers.

If the voltage limitation is violated for at least one PV generator, this means that the power available from another generator (or maybe from several others) has decreased. The supervisor should in this case compute a new, reduced, value of the DC-link voltage reference, by using V_r, the chopper *rated* output voltage, given by (3.35):

$$V_{\rm DC}^{*\rm new} = \frac{1.2 \cdot V_r}{\max_{i=1,2,...n}\{w_i\}}, \tag{3.36}$$

which would allow for all the generators to remain in MPPT, meanwhile meeting all the new constraints $V_{oi}^{new} \leq 1.2 \cdot V_r$, $i = 1, 2, ...n$, if the new DC-link voltage (3.36) is declared suitable for the inverter control loop. This takes place if $V_{\rm DC}^{*\rm new} \geq 0.8 \cdot V_{\rm DC}^{*\rm ideal}$ – in this case, it can be provided as a new reference to the inverter control block (block 2 in Fig. 3.41).

A binary variable noted "$V_{\rm DC}^{*\rm new}$ found" is also computed, which, together with w_i and ${\rm d}w_i/{\rm d}t$, $i = 1, 2, ...n$, is used within a finite-state automaton to provide the operating modes of the PV generators. If $V_{\rm DC}^{*\rm new} found = 0$, the supervisor degrades the MPPT of the generators having surpassed the voltage limit by switching their control to OVL at $1.2 \cdot V_r$. *This suboptimal regime corresponds to the less restrictive degradation as it still ensures the constraints to be met at the limit.*

A supervised three-PV-generator cascaded DC–DC converter system having $V_{\rm DC}^{*\rm ideal} = 450$ V was simulated in MATLAB®/Simulink®under the irradiance scenario shown in Fig. 3.42a), with all the PV generators initially operating in ESC-based MPPT – according to control design and implementation details presented in previous Subsection 3.4.1 – under equal irradiance levels at $Irr_1 = Irr_2 = Irr_3 = 900$ W/m^2. Step variations of irradiance, seldom encountered in nature, were used, such as to be most challenging for the power optimization strategy. Supervisor is set to take decisions each $T_{\rm sv}$=0.1 ms.

The considered scenario was built such as to illustrate supervisor's decisions in both the case where a new DC-link voltage reference is possible to be found out, and in the contrary case, as detailed by the results resumed below from [115].

As $n = 3$ for this system, then $V_r = V_{\rm DC}^{*\rm ideal}/n = 150$ V. Fig. 3.42b) indicates that $V_{\rm o2}$ and $V_{\rm o3}$ reach the maximum threshold of $1.2V_r = 180$ V in response at Irr_1 having decreased from 900 to 400 W/m^2. According to (3.36), ***a new acceptable value of the DC-bus voltage reference results*** (Fig. 3.42c)):

$$V_{\rm DC}^{*\rm new} = \frac{1.2 \cdot 150}{\frac{900}{2200}} = 440 \text{ V} > 360 \text{ V} = 0.8 \cdot V_{\rm DC}^{*\rm ideal}$$

Note that (3.36) provides a *theoretical* level of the new DC-bus voltage, as the measured PV power levels and, therefore, their weights w_i are supposed to be in steady state. The abrupt irradiance variations determine that

the optimal power levels change, thus requiring from MPPTs to readjust; moreover, the PV power signals will always exhibit ripples when in MPPT – as it has been shown, for example, in simulation results in Fig. 3.39 in Subsection 3.4.1. It is very probable that this time cannot be waited, so the supervisor must decide the change of V_{DC}^{*} faster than the MPPTs reach their new steady states. Thus, variables appearing in (3.36) have some *transient* values; therefore, actual computation will provide a slightly different value of $V_{\mathrm{DC}}^{*\mathrm{new}}$ compared to the one achieved with *steady-state* values – as suggested by the zoom in Fig. 3.42c) – which must be low-pass filtered before being imposed to the inverter.

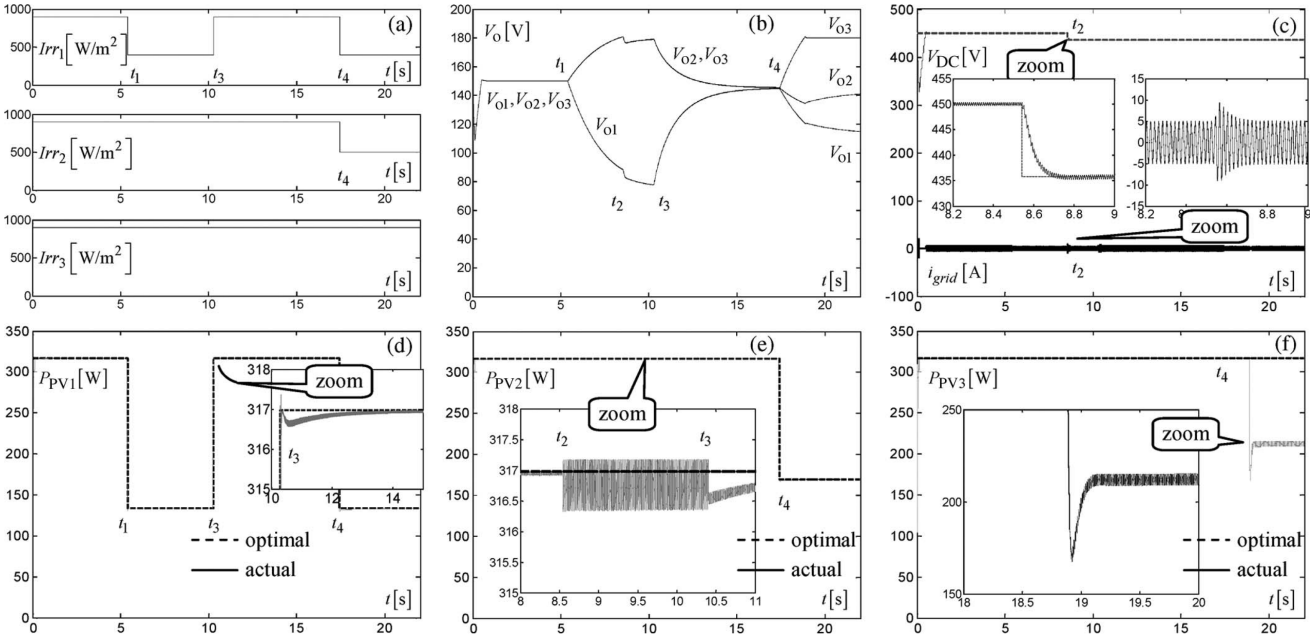

Figure 3.42: Performance of the supervised cascaded PV system under irradiance step variations [115]: a) irradiance scenario; b) output voltages of the three choppers; c) variations of the DC-bus voltage and grid current; d)–f) time evolutions of the power provided by the three PV generators.

Between t_2 and t_3, all the PV generators operate in MPPT (Figs. 3.42d)–f)). At time t_3, Irr_1 comes back to its initial level and the generators remain in MPPT until t_4, when both Irr_1 and Irr_2 decrease abruptly and significantly, from 900 to 400 and to 500 W/m^2, respectively. Shortly after, only V_{o3} reaches the threshold of 180 V, but this time ***a new DC-bus voltage reference cannot be found any longer***. Consequently, the control of the third PV generator is switched from MPPT to OVL (Figs. 3.42b) and f)). The other two generators continue to operate in MPPT, obviously at reduced power levels (Figs. 3.42d) and e)).

Note that this decision is, as the matter of fact, different from the theoretical one the supervisor should have taken. Indeed, the new DC-bus voltage value computed according to (3.36) would be $1.2 \cdot 150/(900/1800) = 360$ V if using the steady-state values of weights w_i. On the other hand, 360 V is exactly the lower admissible threshold for V_{DC}, *i.e.*, 360 V $= 0.8 \cdot V_{DC}^{*\mathrm{ideal}}$.

Therefore, the supervisor should have theoretically allowed the MPPT operation of all PV generators. However, the values of w_i effectively used by the supervisor are smaller than the steady-state ones (Figs. 3.42d) and e)), so finally $V_{DC}^{*\mathrm{new}}$ effectively computed is smaller than 360 V. Thus, the supervisor's actual decision in this particular case is to degrade the MPPT on PV generator 3, thus making sure that voltage constraints are met. Note that slower-than-step variations of irradiance and smaller transients are more probable in nature; in this case, the supervisor is more likely to decide keeping the MPPT operation by reducing the DC-bus voltage reference.

To wrap-up the above-briefed results towards attempting some generalization, the designed ***supervisor*** exemplifies ***a practical way of dealing with different PV-topology-dependent constraints that can act in contradiction with MPPT operation***, as long as the harvested power maximization remains the main purpose.

3.4.3 Intrinsic sinusoidal ripple used as searching signal in ESC-based MPPT for grid-connected PV systems

Taking inspiration on wind-turbulence-based ESC for achieving MPPT of wind energy conversion systems (WECS) – see the approach in [70], described earlier in Subsection 3.2.3 of this chapter – this subsection considers the *ESC-based MPPT* for ***a class of grid-connected PV systems without intermediary DC–DC converter stage***, that is, directly connected to the grid inverter. Thus, different from the classical ESC implementation, the perturbation signal is ***not artificially generated*** by the MPPT algorithm; instead, the method briefed here uses the ***DC-link voltage ripple***, which "naturally" results from the grid inverter operation [117], [118], ***as already present, intrinsic searching (dithering) signal***.

This technique that allows for simplifying the control structure to a certain extent is also known as **ripple correlation control** [119], [120], having been subsequently linked to ESC [118], [121]. Our analysis in [122] emphasized the significant variation of system behaviour with the irradiance and proposed an adaptive control approach for fast-changing irradiance as a possible solution. Here the main ideas are presented.

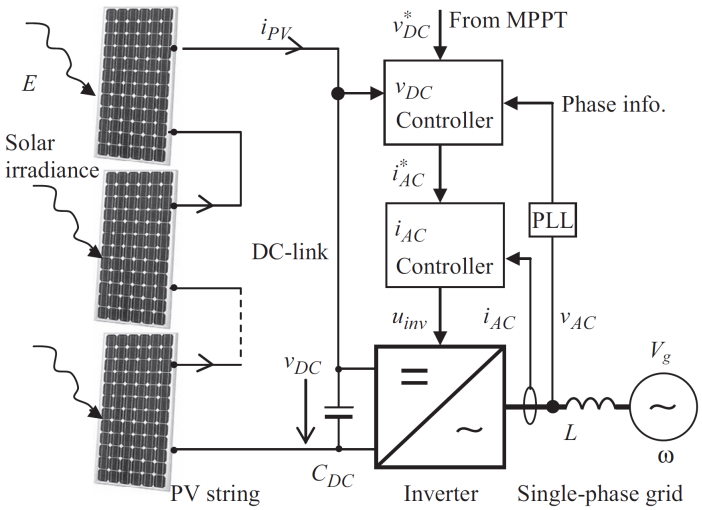

Figure 3.43: Considered PV topology as a string direct connection to AC single-phase grid, where the two-level control system implements classical grid-connected inverter operation [122].

The PV generation system considered here is detailed in Fig. 3.43 and consists in a string of series-connected PV modules, which is in turn connected directly on the inverter DC-link and further to the "strong" grid [123]. Such a topology avoids use of intermediate DC–DC boost converters, with obvious advantages like reduced power losses, simplified overall hardware, instrumentation and control and enhanced reliability.

A single-phase voltage-source inverter is employed in order to transfer the generated DC electrical energy to the grid; to this end, the inverter is classically operated as AC current source, supposing DC-link voltage regulation at a certain value irrespective of the current injected into DC-link by the PV string. Fig. 3.43 shows the considered PV generator structure, where the outer voltage controller imposes the necessary magnitude of AC current, i^*_{AC}, in order to establish the DC-link voltage balance – see also the two-loop control structure presented earlier in Fig. 3.38 in Subsection 3.4.1 [111]. At its turn, the upper-level MPPT control loop must provide to the voltage controller that DC-link voltage reference, v^*_{DC}, corresponding to maintaining the PV string operating point at the MPP, irrespective of irradiance and parameter variations (*e.g.*, panel temperature).

For the PV topology in Fig. 3.43, implementing the MPPT by means of a modified ESC structure which exploits an *already existing high-frequency sinusoidal ripple component in voltage* v_{DC} proved to be a profitable idea. Thus, the MPPT algorithm computes the DC-link voltage reference *by measuring the effect of this high-frequency perturbation on the string output power signal*, p_{PV}. This controlled behaviour supposes relatively ***larger flexibility in DC-link voltage variation***, which hence must be allowed as early as in the initial setup design. Thus, domain of DC-link voltage variations should include the range of MPP PV voltage variations. However, MPPT at low irradiance levels may not be possible, because the inverter cannot operate below a certain v_{DC} value, but power loss is not a critical issue in this case.

The MPPT control structure using ripple-based ESC is given in Fig. 3.44, where acronym CCP stands for current-controlled plant and acronym VVP denotes voltage variation plant. Although in a different form in relation to the habitual one – recalled in Fig. 3.5 in Section 3.1 earlier in this chapter – the ESC structure preserves the ***washout*** (perturbation effect separation) ***filter*** and the ***demodulator***. As the perturbation is intrinsic to the

system itself, it must also be extracted by means of a separation filter. Choice of ***a band-pass filter*** (BPF in Fig. 3.44), ***instead of a high-pass filter*** used in classical ESC, is here motivated to improve closed-loop behaviour under fast variation of irradiance conditions, as justified further.

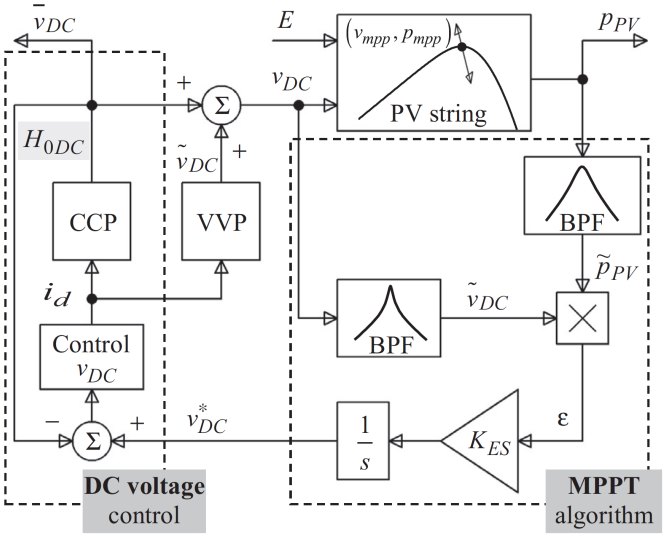

Figure 3.44: PV MPPT by ripple-based ESC: control block diagram [122].

In Fig. 3.44 H_{0DC} represents the *second-order closed-loop DC-link voltage transfer function*, which results by adequately designing a PI controller for the open-loop plant described by the transfer from i_d – the d component of inverter current, i_{AC}, in the dq stationary frame – to the DC-link voltage, v_{DC}; modelling details and choice of closed-loop performance for this low-level control can be found in [122].

Operations performed sequentially within the MPPT algorithm are delimited by dashed line at the right of Fig. 3.44. The MPPT algorithm uses measured signals v_{DC} and p_{PV} as inputs and outputs the DC voltage reference, v^*_{DC}. At each time step, this algorithm performs the following operations: band-pass filtering of signals v_{DC} and p_{PV}, multiplication of these filtered signals, multiplication of the result by the positive gain K_{ES} and finally integration of the result.

Next are resumed the main arguments supporting the ***ripple-based ESC MPPT convergence analysis***.

The PV generator power characteristic, $p_{PV}(v_{PV})$, is supposed unimodal, having its maximum at an *a priori* unknown value, noted as v_{mpp}. As also suggested in Fig. 3.44, notation $p_{mpp} = p_{PV}(v_{mpp})$ is adopted. Note that irradiance variations are almost instantaneously experienced by both v_{mpp} and p_{mpp}. The argument of this function has two main components: an average one, $\overline{v_{PV}} \equiv \overline{v_{DC}}$, and the a-magnitude 2ω-sinusoidal perturbation, with ω being the grid pulsation:

$$\widetilde{v_{DC}} = a \cdot \sin(2\omega t), \tag{3.37}$$

which plays here the role of probing signal. The three-term truncation of Taylor's series of the power function around its maximum, p_{mpp}:

$$p_{PV}(v_{DC}) \approx p_{mpp} + p'_{PV}(v_{mpp}) \cdot (v_{DC} - v_{mpp}) + \frac{1}{2} p''_{PV}(v_{mpp}) \cdot (v_{DC} - v_{mpp})^2, \tag{3.38}$$

makes appear the first-order and the second-order derivative of PV power curve with respect to voltage, p'_{PV} and p''_{PV}, respectively. Both $f_1 = p'_{PV}(v_{mpp})$ and $f_2 = p''_{PV}(v_{mpp})$ vary with the irradiance.

According to (3.38), system dynamics while tracking the MPP is different depending on whether the operating point is near to the MPP or it is far from it. The two regions can respectively be identified on the $P-V$ curve in Fig. 3.45, along with a parabola useful for estimating the second-order derivative at MPP, which is a value characterizing the behaviour "close to MPP".

Notation $\varepsilon = \widetilde{v_{DC}} \cdot \widetilde{p_{PV}}$ is already implicitly introduced in Fig. 3.44, whereas notation:

$$\varepsilon_v = \overline{v_{DC}} - v_{mpp} \tag{3.39}$$

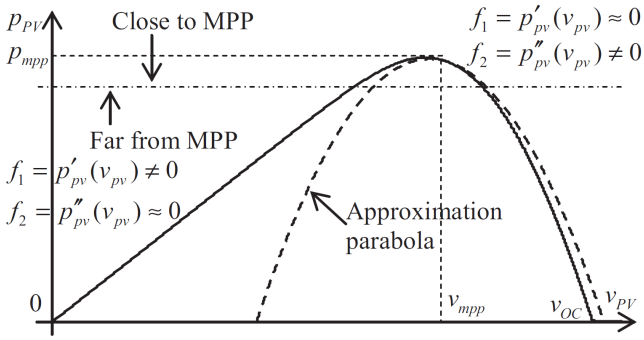

Figure 3.45: Typical PV-power–voltage curve for constant irradiance, where the two regions – "far from MPP" and "close to MPP", respectively – are identified for convergence analysis purpose [122].

is introduced to denote ***the voltage searching error***. As indicated in Fig. 3.44, reference v_{DC}^* applied to the PV voltage control loop is finally computed by integrating signal ε with gain K_{ES}. Thus, ***convergence analysis*** results obtained in [122] can be synthesized as follows.

- When in operation "***close to MPP***":

$$v_{DC}^* = \frac{1}{2}a^2 f_2 K_{ES} \int \varepsilon_v \mathrm{d}t \tag{3.40}$$

  The integrator input, ε_v, toggles its sign as the operating point moves from a side to the other of the P_{PV} curve's maximum. As constant K_{ES} is positive and value f_2 is negative in this region (see Fig. 3.45), (3.40) defines a process convergent to v_{mpp} – as the voltage searching error, ε_v, diminishes – whose convergence speed depends proportionally on K_{ES} and a^2 [13].

  Choice of the washout filter's parameters depends on the excitation frequency, 2ω, but here this frequency is fixed, as imposed by the grid, so it is not a tuning parameter. Therefore, the other parameters make the object of a suitable design. Oscillations magnitude, a, depends on the irradiance value corroborated with the operating point position on the PV power characteristic, thus yielding variability of dynamic response. Rendering the value of K_{ES} adaptive with a can be a pertinent solution for obtaining more uniform dynamic behaviour.

- When in operation "***far from MPP***":

$$v_{DC}^* = \frac{1}{2}a^2 f_1 K_{ES} \int \mathrm{d}t, \tag{3.41}$$

  which also defines a process convergent to abscissa of maximum, as constant K_{ES} is positive and value f_1 is either positive or negative, depending on whether the current voltage is smaller or larger than that of maximum, respectively (see Fig. 3.45). It results that convergence speed does not depend on error ε_v in this case, indicating an approximately linear decreasing of maximum searching speed on a constant-irradiance P–V curve.

Coming now back to use of a band-pass filter (**BPF**) rather than a high-pass one (HPF) as washout filter (see ESC ripple-based MPPT control diagram in Fig. 3.44), justification of such a choice appears pertinent especially ***when irradiance variations are strong enough to produce some side effects on maximum searching dynamic performance***. To this end, Taylor-series-truncation modelling of signal p_{PV} in the region "close to MPP" is resumed:

$$p_{PV} \approx p_{mpp} + \frac{1}{4}f_2 a^2 + f_2 \varepsilon_v a \sin(2\omega t) - \frac{1}{4}f_2 a^2 \cos(4\omega t) \tag{3.42}$$

Because irradiance variations are practically instantaneously repercuted in PV power variations, variables such as p_{mpp}, f_2 and voltage oscillations magnitude a (which depends on PV power) also vary strongly. Term $p_{mpp} + f_2 a^2/4$ is not constant any longer, but represents a signal of the same bandwidth f_E as the irradiance, whose spectrum is presented in Fig. 3.46a). This figure also presents spectrum of term $f_2 \varepsilon_v a \sin(2\omega t)$, which is approximately $\pm f_E$ centred around frequency 2ω, taking account of variations of a and f_2. Higher-frequency components are not presented here.

Supposing that an HPF is used to select the 2ω-sinusoidal component, as represented with dashed-dotted line in Fig. 3.46a), HPF folding frequency must ideally be chosen larger than f_E and smaller than $2\omega - f_E$. As grid frequency ω cannot be modified, such choice may prove restrictive, even more as bandwidth f_E is larger, *i.e.*, it represents fast irradiance variations. Therefore, one cannot guarantee that the two spectra are not superposed. It is thus very probable that, whatever choice of HPF frequency is, a part of irradiance spectrum be further replicated by modulation in high frequency, around 2ω (triangle-shaped spectrum with dashed line in Fig. 3.46b) [124]. It may also be the case of higher-frequency components (at 4ω in (3.42)) to be replicated by demodulation around frequency 2ω (trapezoidal spectrum with dashed line in Fig. 3.46b)).

It results that possible alterations of expected dynamic performance to be experienced because of intrusion of undesired and uncontrollable dynamics like those of irradiance, suggesting that HPF to be replaced by a more precise filtering like, *e.g.*, band-pass filtering – also suggested by dashed-dotted line in Fig. 3.46a) – for sake of preserving accuracy of imposed performance. Moreover, use of HPF as washout filter possibly shortens convergence time to MPP. Trading off advantages and drawbacks of different types of washout filters may further make the object of a more-in-depth analysis.

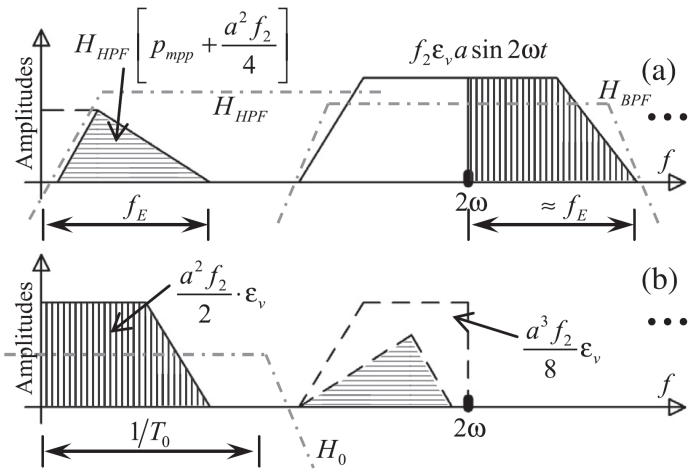

Figure 3.46: Symbolic representation of filtering and modulation process that precedes integration in ESC ripple-based MPPT control diagram in Fig. 3.44, to justify choice of a band-pass filter as wash-out filter [122], where spectra of interest are: a) before filtering; b) after modulation.

As a conclusion of the above analysis, abrupt, large-spectrum irradiance variations are likely to be not accurately tracked and may potentially induce instability. These results are coherent with the theoretical analysis of ESC performance and limitations in [12], while their more intuitive presentation form contribute at formulating clearer guidelines for control design. On the other hand, assumption of stepwise irradiance variations corresponds to the most unfavourable case, quite improbable to occur in the nature.

Concerning ***control design*** of this specific MPPT method for PV systems, it is based upon average, low-frequency, modelling of *ESC around the MPP*, leading to a *parameter-varying* third-order closed-loop transfer function, whose parameters depend on both gain K_{ES}, as a tuning parameter, and on irradiance level. ***Root locus method*** can be a solution for imposing suitable closed-loop dynamic performance, along with an ***adaptive formula of*** K_{ES}.

Thus, based on relatively easy measuring voltage oscillation magnitude, a, and supposing that desired dynamic performance is calibrated at the rated operating point – usually, the one under reference irradiance of 1000 W/m^2 – with K_{ES_rated}, then for a given operating point different from rated the gain is rendered adaptive as:

$$K_{ES} = \frac{a_{rated}^2}{a} \cdot K_{ES\_rated}, \tag{3.43}$$

where a_{rated} and a are voltage oscillation magnitudes at rated and at the current operating point, respectively. The *continuous gain scheduling* in (3.43) only compensates a part of plant variation by reasonably exploiting the limited knowledge about the system. Closed-loop performance is consequently expected to alter along the operating domain, but less than without any adaptation.

This subsection will end with ***some numerical simulation results*** reported in [122], which were performed for validation purpose on a PV system of class described in Fig. 3.43, ***having*** 2020 W ***of rated power and MPP voltage*** V_{mpp} = 462 V, both at reference irradiance E = 1000 W/m^2. For this system, a_{rated} = 11 V and K_{ES_rated}=2.4. Strongly-variable irradiance scenarios were used, as considered relevant for challenging the ***adaptive-gain MPPT performance***.

Irradiance scenario in Fig. 3.47 consists in a ***ramp-wise*** positive and then negative variation occurring when system operated initially at 1000 W/m^2 of irradiance, its reference value. PV power evolution copies practically instantaneously irradiance variation (Fig. 3.47a)). Fig. 3.47b) shows how voltage oscillation magnitude, a, varies, as well as evolution of gain K_{ES}, rendered adaptive according to (3.43). Fig. 3.47c) shows comparatively evolution of PV voltage with and without adaptation, indicating a response time significantly improved in the case of an adaptive gain. Fast tracking is necessary to avoid that error between v_{mpp} and $\overline{v_{DC}}$ to become larger than oscillation magnitude, a; otherwise, tracking would not be any longer effective.

Last simulation scenario aims at illustrating system dynamic behaviour under strongly variable irradiance

conditions, close to those encountered in the nature. To this end, the same ***stochastic*** two-component dynamic model of ***irradiance*** as in [115] – explicited in (3.33) in Subsection 3.4.1, earlier in this section – was used, to reflect realistic irradiance variation. Irradiance variation according to this model is shown in Fig. 3.48a); the corresponding PV maximum power variation is shown in Fig. 3.48b).

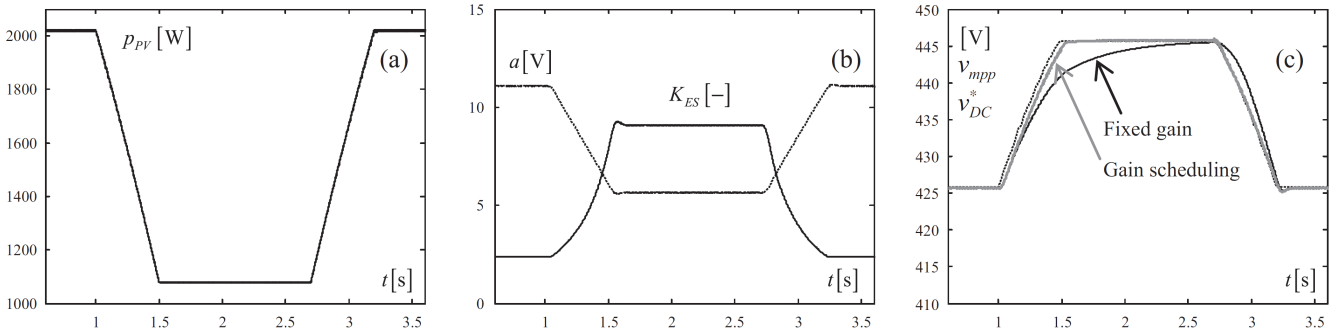

Figure 3.47: Closed-loop performance of ESC ripple-based MPPT in response to ***irradiance* ramp *variations*** of -1000 W/m^2/s starting from 1000 W/m^2 during 0.5 s and backwards – time evolution of interest variables [122]: a) PV power; b) voltage oscillation magnitude and adaptive ESC gain; c) PV voltage evolution comparatively with and without K_{ES} adaptation.

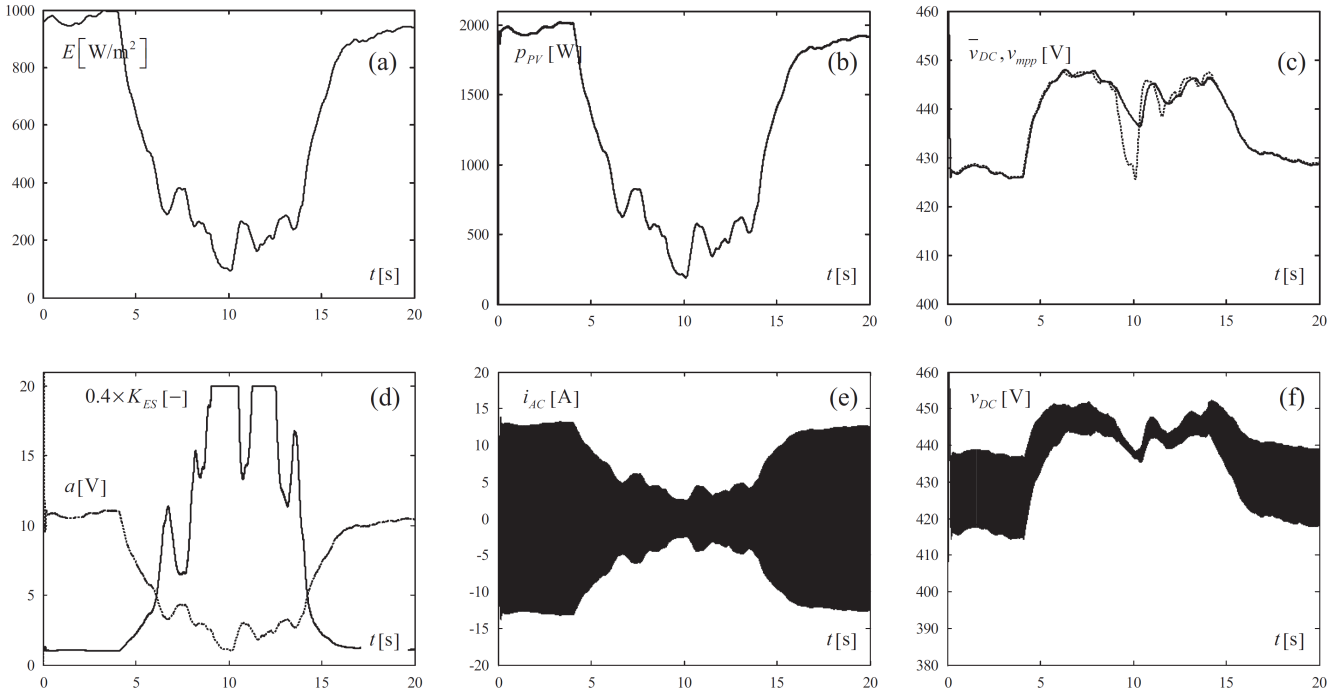

Figure 3.48: ESC ripple-based MPPT performance in response to **stochastic *variation of irradiance*** [122]: a) irradiance variation; b) corresponding variation of maximum PV power; c) PV voltage tracking performance; d) variation of ESC perturbation signal magnitude, a, and limited variation of adaptive gain K_{ES}; e) grid current variation; f) PV voltage evolution.

Fig. 3.48c) presents performance of tracking voltage at maximum power, v_{mpp}, by the average value of PV voltage, $\overline{v_{DC}}$, emphasizing significant alteration of the voltage tracking performance when irradiance goes abruptly too low (smaller than 300 W/m^2). This happens because perturbation signal's magnitude a also decreases and, consequently, according to adaptation formula (3.43), value of ESC gain, K_{ES}, increases rapidly with potentially negative effects on the global stability. Gain limitation was here the preferred solution for preserving stability (Fig. 3.48d)), at the price of temporarily sacrificing voltage tracking quality. This compromise is, however, quite affordable since power loss due to MPPT degradation at too low irradiance values represents in general a rather insignificant percentage of rated power (less than 5 W in this case), due to flatness of P–V curve around maximum.

Fig. 3.48e) gives information about the grid-injected current, whereas Fig. 3.48f) presents the time evolution of total voltage signal v_{DC} (that is, including the ripple component whose magnitude ultimately depends on irradiance).

3.5 Summary of contributions and conclusion

This final section aims at summarizing the contributions that we chose to detail throughout this chapter, with respect to ***control*** of some types of renewable energy conversion systems (***RECS***). Althought not exhaustive, Fig. 3.49 attempts to offer ***an unitary vision*** of the main features and strong points of our contributions.

As ***grid-connected*** RECS applications were the ones mainly dealt with, it appears somehow obvious that ***maximization of captured power irrespecive of the primary resource variations*** to be of ***focal interest***. Thus, Maximum Power Point Tracking (***MPPT***) proved to be the main control objective having been identified as common to all three types of approached RECS: wind energy conversion systems (WECS), micro-hydro energy conversion systems (miHECS) and photovoltaic energy conversion systems (PV).

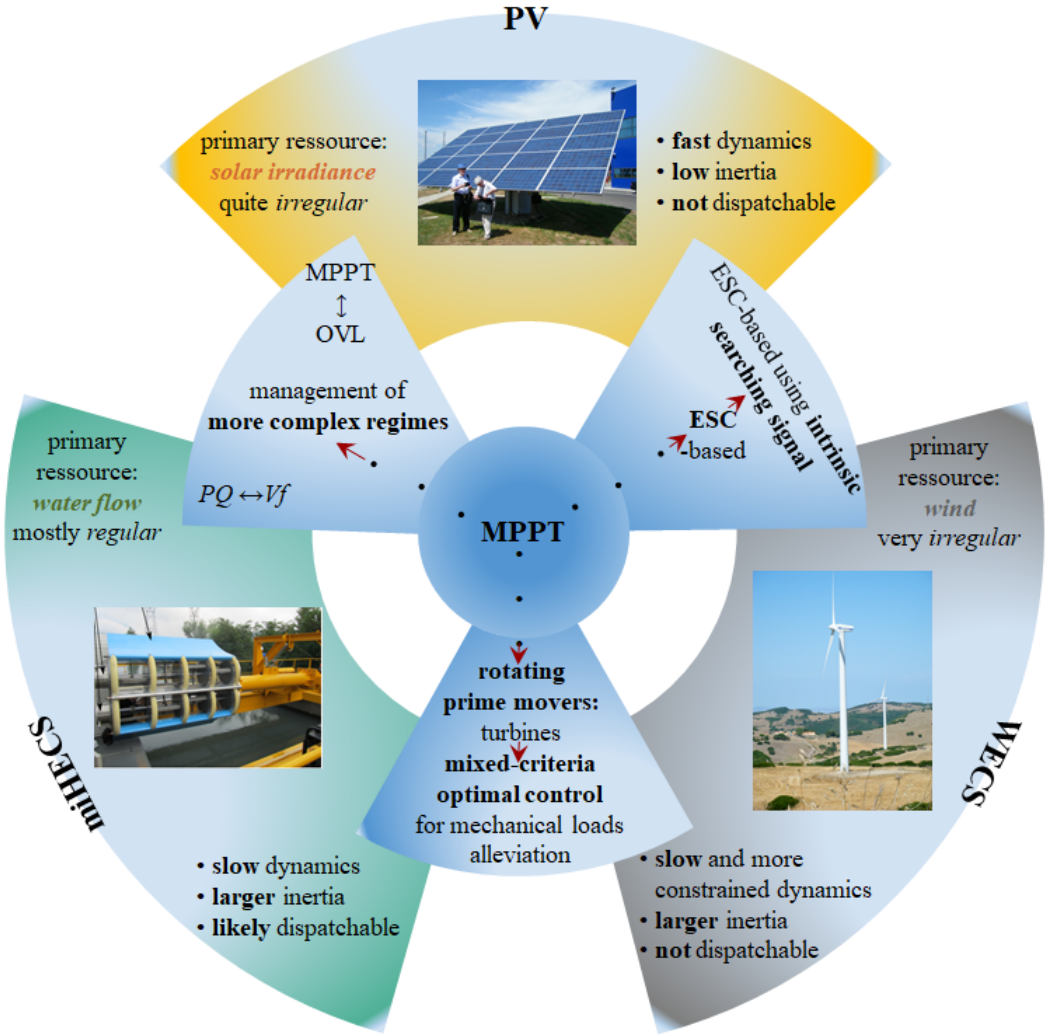

Figure 3.49: Suggested axes towards an unitary vision of the RECS control approaches presented in Chapter 3.

Some comments must specifically be made in relation to grid-connected RECS applications and microgrids, in particular, because having put the focus on this topic equally impacted on ***control*** problem ***statement***, control-oriented ***modelling*** and control ***design***.

Thus, the grid-connected – or, otherwise called, PQ operation – is different, including from a control viewpoint,

from the Vf operation, when the microgrid is islanded from a "strong" grid (or stand-alone). The two operating modes have been recalled in Section 2.1 in Chapter 2 earlier in this memoir. As its name shows, when in PQ operation, a microgrid is required to provide a certain amount of active (P) and reactive (Q) power to the main grid; this objective is achievable only if the respective power amounts can be *guaranteed*, otherwise said, if the power source (microgrid) is *dispatchable*. Or, taking account of the *irregularity of their primary resources* and also of their *relatively small inertia* (quite fast dynamics), ***RECS*** are *a priori* ***not dispatchable***. A possibility to increase their regularity and predictability, so their dispatchability, is to complement (hybridize) them with ***storage units***.

There are, however, ***different degrees of dispatchability***, as synthetically indicated in Fig. 3.49 for each RECS type. Thus, in view of the combination between the primary source regularity and the inertia, miHECS appear as being the most dispatchable. Indeed, this was an aspect emphasized when proposing a direct power control for such systems. Regarding the other two RECS types, PV systems look rather more dispatchable than WECS. Thus, the two are submitted to quite variable primary resource – with slightly more significant irregularity for the wind, in view of its high-frequency, turbulence component, compared to the solar irradiance – whereas PV systems are clearly characterized by the smallest inertia (fastest dynamics) among the three types of RECS considered here. However, the lack of PV inertia may look easier to handle and compensate than mechanical loads and high-frequency excitation of moving parts in WECS. Hence, PV systems would be rather superior to WECS from the dispatchability viewpoint, althought this remains arguable.

As a partial conclusion of the above arguments, since RECS are unlikely dispatchable by themselves when grid connected, then they can be required to provide the maximum – instead of a certain amount – of power available in the resource. Hence, our interest for MPPT methods, which came as a quite complex control challenge, as it has previously been detailed within this chapter.

Instead of being exhaustive and uselessly analytical by attempting conclusions on all the previously briefed approaches, a concluding discussion around the schematic guidelines suggested in Fig. 3.49 is here preferred. This figure suggests how ***different formal control approaches*** were employed in order ***to implement the MPPT***, some of which are common to two of the three RECS types, obviously depending on some identified common features, as above argued.

Thus, MPPT had to be integrated within mixed-criteria dynamic optimization when control efforts had to be taken into account – it is the case of rotating-prime-mover-based RECS, like WECS and miHECS, for which MPPT well performance may be paid back by important mechanical loads. Application of ***frequency-separation principle for WECS*** led to an ***LQG optimal control problem*** being formulated, whereas more practical – less formal, but more intuitive – control solutions were proposed for ***miHECS***, like ***phase-locked-loop (PLL)-based synchronization***, taking inspiration from communications engineering.

An extremely profitable role in acheieving ***MPPT*** based on ***minimal knowldege*** about the system was played by the Extremum Seeking Control (***ESC***) techniques, guaranteeing convergence and a certain implicit robustness against the only approximate *a priori* knowledge. Belonging, from a principle viewpoint, to the larger class of so-called *Perturb and Observe* (P&0) methods, application of ESC in its "conventional" form proved beneficial, especially in the case of PV systems. Then, idea of integrating the ***already existing turbulence wind speed as a high-frequency searching signal*** within an ESC-based strategy for WECS MPPT was an original adaptation and, meanwhile, improvement. That allowed, instead of adding exogenous perturbation, using the already present one: the primary resource turbulence component, thus also implicitly alleviating mechanical efforts.

This new idea of "adapted ESC" further turned out to be again fruitful in the PV case, namely for the class of directly-grid-inverter-connected PV systems. In this case, inverter operation determines ***ripple – proportional with the solar irradiance level – of intermediary DC-link voltage***, which in turn can be used as "intrinsic", endogenous searching signal in ESC.

Last, but not least, MPPT as global control method found its place into ***more complex management and control strategies*** – and this was the case especially for miHECS, as well as for PV systems. In both cases, some ***event-driven supervisors*** had to be designed in the form of state automata in order to suitably handle switchings between different operating modes. In this context, PQ-to-Vf-to-PQ switchings were particularly studied for a

miHECS-based microgrid. As regards PV case, such an approach was necessary for a common-DC-link *cascaded* – instead of a *paralleled* – topology that needed giving up MPPT from time to time, to prevent from safety (over-voltage) limits' violation.

Before the end, it is appropriate to mention the role of validation, which is of great importance for any control design. Thourough numerical simulation validations were conducted for all the proposed control methods, most of which have subsequently also been validated on real-time test benches, according to hardware-in-the-loop simulation (***HILS***) principles. Validation on a real-world prototype was also possible in the case of miHECS, thus marking the successful passage from preliminary checking and rapid prototyping towards effective, on-site implementation.

Chapter 4

Exploiting heterogeneity of multi-source energy systems (MSES) in a robust control approach

In this chapter a summary of our main research contributions concerning the ***multi-source energy systems*** (**MSES**) is presented. It is here about ***electrical*** energy sources, including storage technologies that provide electrical energy as output. Focal ideas turn around taking advantage of the ***heterogeneity*** and ***complementarity*** of the various sources towards ***harmoniously "orchestrate"*** them, such that to effectively guarantee the best exploitation of each one of them.

Indeed, the promised benefits of complementarity-based hybridization of sources within MSES-based microgrids can only be ensured by control action, as it has been recalled in Section 2.2 in Chapter 2 earlier in this memoir. The control structure or algorithm able to achieve coordination of power flows according to some imposed specifications is called a ***Power Management System*** (**PMS**). In this case, the PMS should result by ***taking systematically into account the reliability requirements*** related to each of the sources, in order to maximize their respective life and service times.

The **robust control paradigm** was chosen to serve the above-expressed goal. Thus, the $\mathcal{H}_\infty$ ***framework***, possibly in combination with linear-paramater-varying (***LPV***) polytopic methods, allows for a controller to be found, able to fulfill multi-criteria optimization. Performance of this control solution is paid by its relatively significant complexity. However, our technology transfer experience in this regard proved that embedding an $\mathcal{H}_\infty$ controller into a numerical device for a microgrid use case is perfectly affordable in terms of both costs and resource consuming.

The formal foundations and main mathematical tools are overviewed in the introductory Section 4.1.

The reporting envisaged next globally concerns a research direction explored during the last ten years, **2011–2021**, that is, since I have joined GIPSA-lab. Thus, Sections 4.2 and 4.3 are each dedicated to ***robust PMS systematic design*** for an ***MSES-based stand-alone microgrid application***, namely, a *three-storage-unit power supply on board of electric vehicles* and hybridization used for *frequency and voltage regulation in AC microgrids*, respectively.

The final Section 4.4 is intended to summarize some pertinent insights.

4.1 Formal foundations and mathematical tools

This section aims at overviewing some basic concepts of $\mathcal{H}_\infty$ and ***LPV*** control frameworks, as well as the main associated mathematical tools. Indeed, this mixture of control approaches appears pertinent as justfied by the analysis and modelling of the considered MSES, revealing their definitory ***parameter-varying nature***, as well as the fact that they are ***disturbance-driven***, having to supply the (*a priori* uncontrollable) load power demand. In particular, LPV framework is employed in Section 4.2 for a multi-storage instance of MSES. Principles of ***genetic-algoritm*** (GA)***-based multi-objective optimization*** are also re-called, as GA were used within the two mentioned frameworks.

Consider in a first place a *linear time-invariant* (LTI) dynamical system Σ of the form:

$$\Sigma : \begin{bmatrix} \dot{\mathbf{x}} \\ \mathbf{z} \\ \mathbf{y} \end{bmatrix} = \begin{bmatrix} \mathbf{A} & \mathbf{B}_1 & \mathbf{B}_2 \\ \mathbf{C}_1 & \mathbf{D}_{11} & \mathbf{D}_{12} \\ \mathbf{C}_2 & \mathbf{D}_{21} & \mathbf{D}_{22} \end{bmatrix} \cdot \begin{bmatrix} \mathbf{x} \\ \boldsymbol{\omega} \\ \mathbf{u} \end{bmatrix}, \tag{4.1}$$

where $\mathbf{x}(t) \in \mathbb{R}^n$ is the system's state vector, $\mathbf{u}(t) \in \mathbb{R}^{n_u}$ is the control input vector, $\boldsymbol{\omega}(t) \in \mathbb{R}^{n_\omega}$ is the exogenous (disturbance) input vector, $\mathbf{z}(t) \in \mathbb{R}^{n_z}$ is the controlled output vector and $\mathbf{y}(t) \in \mathbb{R}^{n_y}$ is the measured output vector, with state ($\mathbf{A}$), input ($\mathbf{B}_1$, $\mathbf{B}_2$), output ($\mathbf{C}_1$, $\mathbf{C}_2$) and direct transfer ($\mathbf{D}_{11}$, $\mathbf{D}_{12}$, $\mathbf{D}_{21}$, $\mathbf{D}_{22}$) matrices of appropriate dimensions.

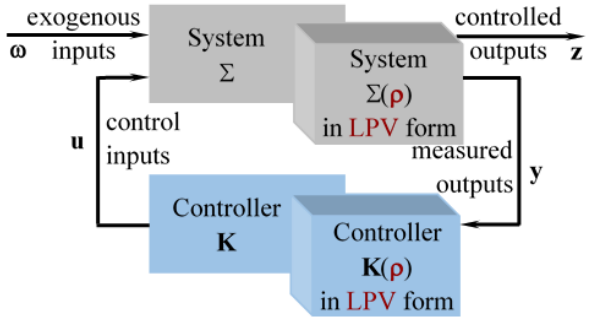

Figure 4.1: Closed-loop block diagram supporting $\mathcal{H}_\infty$ control problem formulation, including within the LPV framework.

The $\mathcal{H}_\infty$ control problem is a ***disturbance-attenuation problem***, which consists in finding a dynamical output feedback controller $\mathbf{K}$ of the form:

$$\mathbf{K} : \begin{bmatrix} \dot{\mathbf{x}_c} \\ \mathbf{u} \end{bmatrix} = \begin{bmatrix} \mathbf{A}_c & \mathbf{B}_c \\ \mathbf{C}_c & \mathbf{D}_c \end{bmatrix} \cdot \begin{bmatrix} \mathbf{x}_c \\ \mathbf{y} \end{bmatrix}, \tag{4.2}$$

having $\mathbf{x}_c \in \mathbb{R}^{n_c}$ as internal state, which ensures the closed-loop minimization of the impact of the exogenous input vector $\boldsymbol{\omega}(t)$ on the controlled output vector $\mathbf{z}(t)$ (see block diagram in Fig. 4.1). Mathematically, with notation $\| \cdot \|_2$ standing for $\mathcal{L}_2$ signal norm, controller $\mathbf{K}$ ensures that, for a given real positive number γ:

$$\sup_{\omega(t) \neq 0} \frac{\| \mathbf{z} \|_2}{\| \boldsymbol{\omega} \|_2} \leq \gamma, \tag{4.3}$$

or, equivalently:

$$\| T_{z\omega}(s) \|_\infty = \| \mathcal{C} (s\mathbf{I} - \mathcal{A})^{-1} \cdot \mathcal{B} + \mathcal{D} \|_2 \leq \gamma, \tag{4.4}$$

where $\mathbf{I}$ is the identity matrix and $\mathcal{A}$, $\mathcal{B}$, $\mathcal{C}$ and $\mathcal{D}$ are the closed-loop state-space matrices, computed respectively as:

$$\begin{cases} \mathcal{A} = \begin{bmatrix} \mathbf{A} + \mathbf{B}_2 (\mathbf{I} - \mathbf{D}_c\mathbf{D}_{22})^{-1} \mathbf{D}_c\mathbf{C}_2 & \mathbf{B}_2 (\mathbf{I} - \mathbf{D}_c\mathbf{D}_{22})^{-1} \mathbf{C}_c \\ \mathbf{B}_c (\mathbf{I} - \mathbf{D}_c\mathbf{D}_{22})^{-1} \mathbf{C}_2 & \mathbf{A}_c + \mathbf{B}_c (\mathbf{I} - \mathbf{D}_c\mathbf{D}_{22})^{-1} \mathbf{D}_{22}\mathbf{C}_c \end{bmatrix} \\ \mathcal{B} = \begin{bmatrix} \mathbf{B}_1 + \mathbf{B}_2 (\mathbf{I} - \mathbf{D}_c\mathbf{D}_{22})^{-1} \mathbf{D}_c\mathbf{D}_{21} \\ \mathbf{B}_c (\mathbf{I} - \mathbf{D}_c\mathbf{D}_{22})^{-1} \mathbf{D}_{21} \end{bmatrix} \\ \mathcal{C} = \begin{bmatrix} \mathbf{C}_1 + \mathbf{D}_{12} (\mathbf{I} - \mathbf{D}_c\mathbf{D}_{22})^{-1} \mathbf{D}_c\mathbf{C}_2 & \mathbf{D}_{12} (\mathbf{I} - \mathbf{D}_c\mathbf{D}_{22})^{-1} \mathbf{C}_c \end{bmatrix} \\ \mathcal{D} = \mathbf{D}_{11} + \mathbf{D}_{12} (\mathbf{I} - \mathbf{D}_c\mathbf{D}_{22})^{-1} \mathbf{D}_c\mathbf{D}_{21} \end{cases} \tag{4.5}$$

In order to take into account the parameter-varying nature of most of dynamical systems, while still keeping linearity assumptions, the more complex framework of *linear parameter-varying* (LPV) systems was elaborated. LPV systems appear as a bridge between the nonlinear and the well-known LTI systems [125]. The theory of LPV systems offers systematic design methods for guaranteeing robust stability and performance, compared to classical gain-scheduled control [126].

An ***LPV system*** is described by the same state-space representation as in (4.1), where at least one of the matrices depends on an N-dimensional ***parameter vector*** $\boldsymbol{\rho}(t) = \begin{bmatrix} \rho_1(t) & \rho_2(t) & ... & \rho_N(t) \end{bmatrix}^T \in \mathbb{R}^N$, assumed to be ***measurable*** (or ***observable***) and ***bounded*** ($\boldsymbol{\rho}(t) \in \mathcal{P}$) for all time instants. Next, for sake of simplicity, $\boldsymbol{\rho}(t)$ is simply noted as $\boldsymbol{\rho}$; it is also called ***scheduling*** parameter vector. Hence, an LPV system can be described as:

$$\Sigma(\boldsymbol{\rho}) : \begin{bmatrix} \dot{\mathbf{x}} \\ \mathbf{z} \\ \mathbf{y} \end{bmatrix} = \begin{bmatrix} \mathbf{A}(\boldsymbol{\rho}) & \mathbf{B}_1(\boldsymbol{\rho}) & \mathbf{B}_2(\boldsymbol{\rho}) \\ \mathbf{C}_1(\boldsymbol{\rho}) & \mathbf{D}_{11}(\boldsymbol{\rho}) & \mathbf{D}_{12}(\boldsymbol{\rho}) \\ \mathbf{C}_2(\boldsymbol{\rho}) & \mathbf{D}_{21}(\boldsymbol{\rho}) & \mathbf{D}_{22}(\boldsymbol{\rho}) \end{bmatrix} \cdot \begin{bmatrix} \mathbf{x} \\ \boldsymbol{\omega} \\ \mathbf{u} \end{bmatrix}, \tag{4.6}$$

where notation meanings are preserved. Depending on the nature of parameter vector $\boldsymbol{\rho}$ variation, different classes of systems result by particularizing (4.6); thus:

- LTI systems are obtained if $\boldsymbol{\rho}$ does not vary with time;
- if $\boldsymbol{\rho}$'s dependence with time is explicit, then it is about *linear time-variant* (LTV) systems;
- *quasi-linear parameter-varying* (qLPV) systems result if $\boldsymbol{\rho}$ depends on the state vector – *i.e.*, $\boldsymbol{\rho}(t) \equiv \boldsymbol{\rho}(\mathbf{x}(t))$;
- finally, genuine LPV systems are obtained if $\boldsymbol{\rho}$ is external (independent) to the system.

If the system's matrices are affine with respect to the parameter vector $\boldsymbol{\rho}$, then the system is called an *affine* LPV system. ***Polytopic*** LPV systems are a special class of affine LPV systems, whose matrices are convex combinations of some constant matrices:

$$\mathbf{A}(\boldsymbol{\rho}) = \sum_{i=1}^{2^N} \alpha_i(\boldsymbol{\rho}) \cdot \mathbf{A}_i \quad \mathbf{B}(\boldsymbol{\rho}) = \sum_{i=1}^{2^N} \alpha_i(\boldsymbol{\rho}) \cdot \mathbf{B}_i \quad \mathbf{C}(\boldsymbol{\rho}) = \sum_{i=1}^{2^N} \alpha_i(\boldsymbol{\rho}) \cdot \mathbf{C}_i \quad \mathbf{D}(\boldsymbol{\rho}) = \sum_{i=1}^{2^N} \alpha_i(\boldsymbol{\rho}) \cdot \mathbf{D}_i, \tag{4.7}$$

where 2^N is the number of vertices of the polytope corresponding to the extreme values of the N-dimensional parameter vector $\boldsymbol{\rho}$, $\sum_{i=1}^{2^N} \alpha_i(\boldsymbol{\rho}) = 1$ and all $\mathbf{A}_i$, $\mathbf{B}_i$, $\mathbf{C}_i$ and $\mathbf{D}_i$ matrices are constant. Hence, a polytopic LPV system is a ***convex hull of a finite number of LTI systems***, each of which is "placed" at a vertex of the polytope. This feature turns out to be of great interest in control design and implementation, as shown next.

Now, the $\mathcal{H}_\infty$ framework is extended to LPV systems. Thus, for the LPV system (4.6) the LPV/$\mathcal{H}_\infty$ control problem consists this time in finding a dynamical output feedback controller that is also parameter varying:

$$\mathbf{K}(\boldsymbol{\rho}) : \begin{bmatrix} \dot{\mathbf{x}}_c \\ \mathbf{u} \end{bmatrix} = \begin{bmatrix} \mathbf{A}_c(\boldsymbol{\rho}) & \mathbf{B}_c(\boldsymbol{\rho}) \\ \mathbf{C}_c(\boldsymbol{\rho}) & \mathbf{D}_c(\boldsymbol{\rho}) \end{bmatrix} \cdot \begin{bmatrix} \mathbf{x}_c \\ \mathbf{y} \end{bmatrix}, \tag{4.8}$$

that guarantees not only the closed-loop stability, but also satisfies the performance (4.3) for all values of parameter vector $\boldsymbol{\rho}$. Fig. 4.1 suggests that such a framework extension can take place somehow naturally. In this case, the optimal $\mathcal{H}_\infty$ gain, noted as γ^*, is the smallest gain for all existent controllers $\mathbf{K}(\boldsymbol{\rho})$:

$$\gamma^* = \min_{\mathbf{K}(\boldsymbol{\rho})} \| T_{z\omega}(s) \|_\infty \tag{4.9}$$

As regards the ***solution*** of the stated ***LPV/$\mathcal{H}_\infty$ control problem***, a parameter-varying controller of form (4.8), having the same order as the LPV system ($n_c = n$), is obtained by solving a theoretically *infinite* number of linear matrix inequalities (LMIs) – as parameter vector $\boldsymbol{\rho}$ varies continuously – while minimizing γ [150], [128]. Different approaches can be used in order to relax this problem and reduce it to solving a *finite* number of LMIs:

- by suitably defining a grid of the parameter space and selecting basis functions [129];
- by transforming the parameter-dependent system into an uncertain system using the Linear Fractional Transformation (LFT) [130];
- by adopting a ***polytopic*** approach, consisting in solving 2^N LMIs only, that is, for each vertex of the polytope corresponding to the extreme values of the N-dimensional parameter vector $\boldsymbol{\rho}$ [150] – this is the method having led to the results summarized next in Section 4.2.

Let us resume the definition (4.7) of a polytopic LPV system as a convex combination of multiple LTI systems $(\mathbf{A}_i, \mathbf{B}_i, \mathbf{C}_i, \mathbf{D}_i)$ evaluated at each vertex i of the polytope, $i = 1, 2, ...2^N$. For each scheduling parameter ρ_j

its miniumum and maximum values are noted as $\underline{\rho_j}$ and $\overline{\rho_j}$, respectively. To each vertex i is associated an N-dimensional vector ζ_i, whose j-th element is defined as:

$$\zeta_{i_j} = \begin{cases} \overline{\rho_j}, & \text{if parameter } \rho_j \text{ at vertex } i \text{ is } \underline{\rho_j} \\ \underline{\rho_j}, & \text{otherwise} \end{cases} \tag{4.10}$$

The LPV system in (4.7) can be written under the equivalent form:

$$\begin{bmatrix} \mathbf{A}(\boldsymbol{\rho}) & \mathbf{B}(\boldsymbol{\rho}) \\ \mathbf{C}(\boldsymbol{\rho}) & \mathbf{D}(\boldsymbol{\rho}) \end{bmatrix} = \sum_{i=1}^{2^N} \alpha_i(\boldsymbol{\rho}) \cdot \begin{bmatrix} \mathbf{A}_i & \mathbf{B}_i \\ \mathbf{C}_i & \mathbf{D}_i \end{bmatrix}, \tag{4.11}$$

where weights $\alpha_i(\boldsymbol{\rho})$ are defined as:

$$\alpha_i(\boldsymbol{\rho}) = \frac{\prod_{j=1}^{N} |\rho_j - \zeta_{i_j}|}{\prod_{j=1}^{N} |\overline{\rho_j} - \underline{\rho_j}|} \geq 0, \quad \sum_{i=1}^{2^N} \alpha_i(\boldsymbol{\rho}) = 1 \ , \tag{4.12}$$

with ζ_{i_j} given by (4.10). At each vertex i of the polytope the associated LMI set is solved *off line* to yield a controller $\mathbf{K}_i : \begin{bmatrix} \mathbf{A}_{c_i} & \mathbf{B}_{c_i} \\ \mathbf{C}_{c_i} & \mathbf{D}_{c_i} \end{bmatrix}$. The global LPV/$\mathcal{H}_\infty$ controller, $\mathbf{K}(\boldsymbol{\rho})$, is finally computed *on line* as the convex combination of the *off-line* computed local (vertex) controllers, $\mathbf{K}_i$, in analogy with (4.11):

$$\mathbf{K}(\boldsymbol{\rho}) : \begin{bmatrix} \mathbf{A}_c(\boldsymbol{\rho}) & \mathbf{B}_c(\boldsymbol{\rho}) \\ \mathbf{C}_c(\boldsymbol{\rho}) & \mathbf{D}_c(\boldsymbol{\rho}) \end{bmatrix} = \sum_{i=1}^{2^N} \alpha_i(\boldsymbol{\rho}) \cdot \begin{bmatrix} \mathbf{A}_{c_i} & \mathbf{B}_{c_i} \\ \mathbf{C}_{c_i} & \mathbf{D}_{c_i} \end{bmatrix}, \tag{4.13}$$

thus resulting in a gain-scheduled form. A comprehensive review concerning this approach can be found in [131].

Genetic algorithms (GAs) represent one of the most popular ***multi-objective optimization methods***, being inspired from the natural mechanism of adaptation and evolution. Thus, basic principles of GAs are employed towards developing generations of members (parameters) in a way such as to extremize multi-objective functions [132], [133]. Members in the decision space are classified regarding some suitably defined ***fitness (objective) functions*** into the decision space (see Fig. 4.2 [134]).

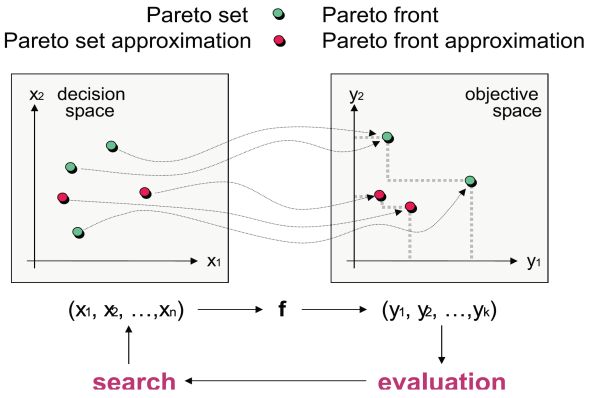

Figure 4.2: Multi-objective optimization process as performed by GAs [134].

GAs are very effective in finding a convenient solution where the problem to solve involves large sets of parameters to be determined – ***evolutionary process*** principles are formalized and employed to this end. The idea is to use probabilistic, multi-point search, random operations – such as ***mutation*** and ***crossover*** – and data from the previous generation in order to improve the evaluation of current population.

Some GA basic concepts are:

- *individual* or *member*: it refers to any possible solution in the decision space where any acceptable combination of the parameters can form an individual;
- *population* or *generation*: it refers to a group of individuals;
- *chromosome*: it refers to one *parameter* among the individual parameters;
- *genome*: it refers to a group of chromosomes in an individual.

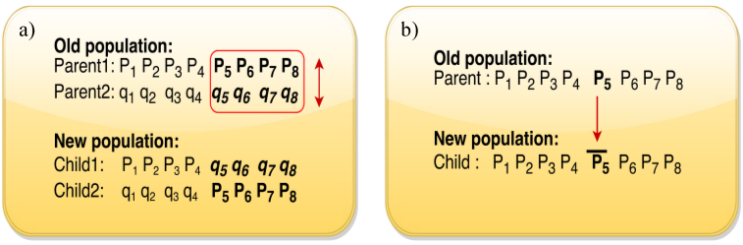

Figure 4.3: Illustration of two important GA operations: a) cross-over; b) mutation.

A GA-based optimization process consists of ***several steps***, starting by randomly choosing the first generation; the generations are further developed through four main steps that are ***evaluated sequentially in a continuous loop***. The process is terminated when the desired number of generations is achieved. The main four steps are as follows.

- The ***individual fitness functions*** are computed; individuals better "fitted" are more probable to be selected for the next steps.
- ***Selection*** is performed at this step, *i.e.*, individuals are sorted and copied in descending order of their fitness function values. The most widely used selection methods are *proportionate* selection [132] and *tournament* selection [135].
- The main operation acting on the population of parents is the ***cross-over***, suggested in Fig. 4.3a). It is based on exchanging parts between two selected individuals (parents) to form two new individuals (children). This exchange process is applied either to a single or to multiple chromosomes.
- At this step ***mutation*** is applied by changing randomly either a chromosome or a genome in the individual (child), as suggested in Fig. 4.3b). Mutation is an important operation since it allows creating new members, different from all developed generations.

4.2 Design of robust Power Management Systems (PMSs) for *multi-storage* systems

This section focuses on a certain class of MSES, namely the multi-storage MSES, where several (two or more) technologically complementary storage units are coordinated in order to effectively operate complementarily. To fix ideas, a ***multi-storage power supply on board on an electric vehicle*** (EV) was considered. The approach and results briefed next continue and generalize our work reported in this regard in [18]–[21], previously introduced in Section 2.2 in the motivation Chapter 2 of this memoir.

Since it is mainly about *storage* units, then it is about *DC* microgrids, which appear to have gained popularity in the last years *vs.* AC ones, due to their more simplified operation (*e.g.*, no need for synchronization). Stand-alone applications in avionic, automotive and marine industries, but also power supply of remote areas may benefit from this advantage, among others [136], [137].

In MSES, the roles of Energy Management System (EMS) and Power Management System (**PMS**) mainly concern sources' coordination towards ensuring a ***desired power sharing*** between sources to satisfy the load demand, while ***preserving reliability of all sources*** and extending their remaining useful life [138].

Efficient PMS can be designed using a variety of control approaches. Model Predictive Control (MPC) – with its nonlinear and/or stochastic versions – may be applied at coordinated multivariable control strategies for stand-alone microgrids and/or MSES, with or without renewable sources, as it successfully deals with multiple constraints [139], [14], [140]. However, need of an adequate plant mathematical model and of *a priori* knowledge of load variation to predict the behaviour may be regarded as drawbacks when employing this framework. Indeed, in the particular case of EVs, this results in driving-cycle-dependent PMS solutions. Nonlinear methods [15], [16] or even more sophisticated approaches, like multi-agent-based and games theory [141], proved to be of interest to explore.

PMS design reported here is related to taking into account the ***requirements of reliable operation characteristic of each source***, under a suitable form, for example, "translated" and/or adapted from its data sheet specifications. Such an approach leads to considering complex techno-economical criteria in the MSES PMS design. In particular, ***reliability-aware design*** habitually relies on complex degradation and ageing models of storage units, along with optimization methods [142]. The multi-time-scale character of MSES justify hierarchical control structures [143], with dynamically separated layers for enabling operation of sources in their "specialization" range of variations – according to Ragone's taxonomy, recalled in Fig. 2.3 in Chapter 2 – to improve their reliability [144]. In this way, high-power-density sources (like ultracapacitors), specialized in providing high-amplitude fast-varying currents, are able to protect high-energy-density sources (like fuel cells or batteries), whose current variations must be smoother. As already stated previously in the motivation Section 2.2, filtering is the most straightforward way

of dynamic separation, where variations of current of each source are confined in a predefined frequency interval [18], [145], [19], whereas LQG approach may also be applied, but restricted to only two sources [20], [21].

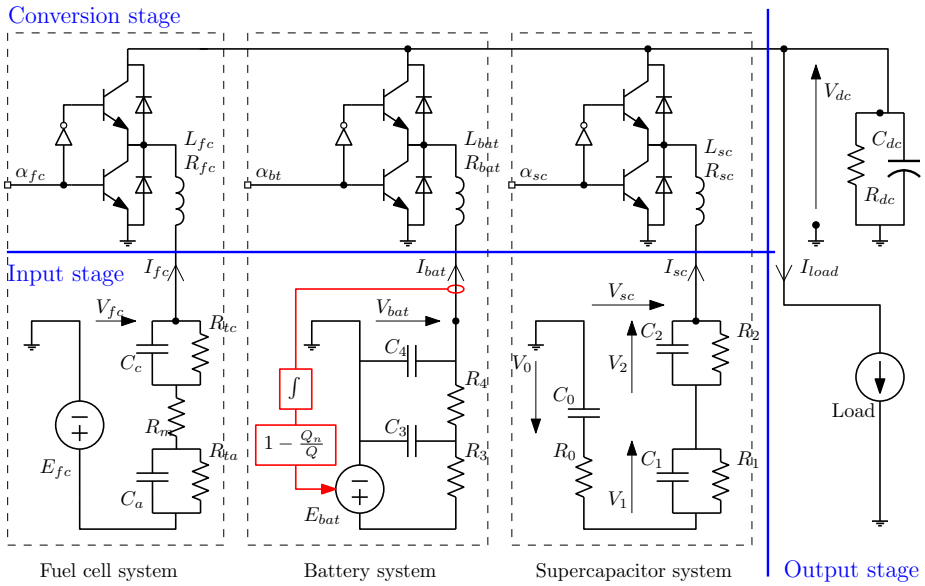

Figure 4.4: Electrical schematic of a three-storage – ***fuel cell / battery / ultracapacitor*** – power supply system, detailing the equivalent electrical models of the storage units [146].

To further fix ideas, a ***three***-storage – ***fuel cell, battery and supercapacitor*** – MSES in an electromobility use case, *i.e.*, as a power supply on board of an electric vehicle is here considered. The number of storage units was chosen such as to illustrate the generality of the employed approach – whereas having considered only two sources would have appeared like a particular case. Thus, the multi-storage parallel configuration in Fig. 4.4 is considered, having the advantage of flexibility (sources' independent operation, facility to replace/add power sources, *etc.*)

The *fuel cell* acts here as the *main* source, it is *unidirectional*, being thus connected to a one-quadrant DC-DC converter. The two *auxiliary* sources – the *battery* and the *supercapacitor*, both *bidirectional* – have the role of responding to relatively fast power demand variations and to collect the reversed power (during braking phase). To this end, each auxiliary source is connected to a two-quadrant converter allowing charging/discharging. The electrical motor together with its converter plays the role of load for this DC supply system.

Among the tasks of the PMS is ***to guarantee that each source***, independently controlled by means of its DC-DC converter, ***operates in its dynamic specialization range***, thus ensuring its most rational exploitation.

The results presented next were obtained within collaboration with Ph.D. student Jean-Marc Waleed NWESATY, working under the supervision of Professor Olivier SENAME and myself, and made the object of the following main publications:

- W. Nwesaty, A.I. Bratcu, O. Sename (2016). Power sources coordination through multivariable LPV/$\mathcal{H}_\infty$ control with application to multi-source electric vehicles. *IET Control Theory and Applications*, 10(16), 2049–2059

  – summarized in Subsection 4.2.1 – in which the approach of casting the PMS design into the LPV/$\mathcal{H}_\infty$ framework methodology is briefed, leading to a ***generic PMS solution*** for multi-storage systems with potentially ***any number of sources***, that guarantees closed-loop robust stability;

- J.-M.W. Nwesaty, A.I. Bratcu, A. Ravey, D. Bouquain, O. Sename (2020). Robust energy management system for multi-source DC energy systems – real-time setup and validation. *IEEE Transactions on Control Systems Technology*, 28(6), 2591–2599

  – briefed in Subsection 4.2.2 – which reports about the ***PMS preliminary proof of concept*** achieved in collaboration with colleagues (Associate Professors David BOUQUAIN and Alexandre RAVEY) from FEMTO-ST Laboratory in Belfort, France, by hardware-in-the-loop-simulation (***HILS***) validation on a test bench comprising real battery and supercapacitor, as well as an entirely emulated fuel cell system. A dSPACE™ MicroAutoBox®II device was chosen to embed the designed control, due to its flexibility and ease of programming with MATLAB®.

Taking into account the significant potential of the results obtained during J.-M. W. Nwesaty's Ph.D. thesis of being transferred to the industry, between 2017 and 2018 we pursued activities related to the designed robust PMS ***proof of concept*** in an EV use case. Funding received from the Institut Carnot *Logiciels et Systèmes Intelligents* (LSI) within the ***technology pre-transfer project***

- ***K-INF****: Embedded real-time PMS for multi-source electrical energy systems*

allowed ***PMS embedding on a general-purpose*** Texas Instruments ***microcontroller*** and closed-loop real-time demonstrations on a test bench built around a rapid-prototyping system dSPACE™ MicroAutoBox®II, thus advancing the technology readiness level (TRL) of our PMS solution. This made the object of an APP (*Agence pour la Protection des Programmes – Software Protection Agency*) software application deposit (alphabetical order of authors):

- A.I. Bratcu, I. Munteanu, J.-M.W. Nwesaty, O. Sename (2018). *K-INF Multi-source management system robust design.* Grenoble Institute of Technology, Grenoble Alpes University. RT2018013, version 1.1 May 2018.

Some relevant results and conclusions of *K-INF* technology pre-transfer project are summarized in Subsection 4.2.3, to offer an overall glimpse of practical feasibility of a well-performing, yet quite complex, control solution.

4.2.1 Robust PMS design for a three-storage DC power supply microgrid on board of an electric vehicle

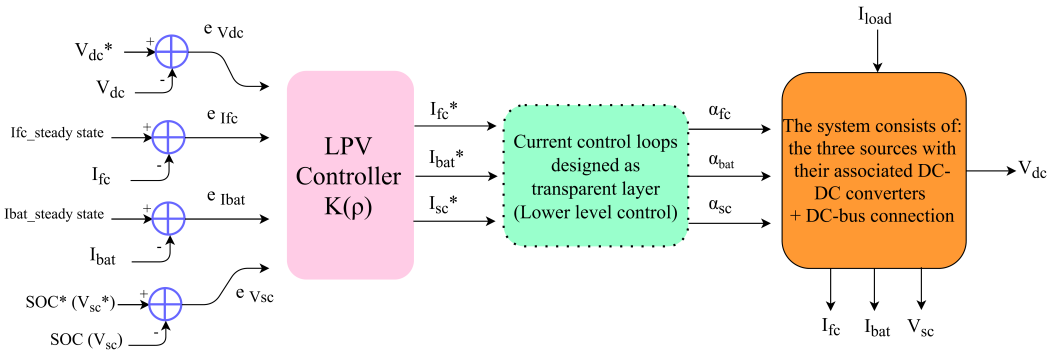

Figure 4.5: Global two-level control block diagram with the LPV/$\mathcal{H}_\infty$ controller on the upper level [147].

The PMS design for the above-described on-board EV MSES-based power supply begins with adopting a classical global two-level control structure, as shown in Fig. 4.5: the DC-DC converters' current control loops on a lower level and the LPV/$\mathcal{H}_\infty$ -based PMS on an upper level, in charge with providing the references to the lower level. The dynamic (frequency)-separation operation of the three storages should take place while meeting some other constraints, leading to the following control objectives being formulated:

- maintain the DC-link voltage constant, around V_{dc}^* setpoint within an error of $\pm 10\%$ regardless of the load current variations. This requirement is very general in the sense that it applies to all configurations where different sources are paralleled on a common DC link. It is this requirement that allows the control problem being stated as a disturbance-attenuation problem and cast into the $\mathcal{H}_\infty$ framework;
- ensure frequency separation of storages, *i.e.*, each storage supplies power with respect to its characteristic frequency according to Ragone's plot – see (2.1) and Fig. 2.3 in Section 2.2. To this end, ***suitable shaping of weighting functions associated to $\mathcal{H}_\infty$ control design*** plays a key role;
- maintain the supercapacitor state of charge (SoC) slowly around 50%, which allows continuity in absorbing/providing power to fulfill instantaneous load power demand;
- impose a desired steady-state behaviour for the fuel cell and the battery, that corresponds to some desired power sharing between sources in steady state. This allows to operate the fuel cell at a desired working point, *e.g.*, the one corresponding to maximum efficiency. Steady-state behaviour could be used to determine battery long-term charging cycle, depending on its technology – in particular, battery charging could be achieved by using the main power source, the fuel cell.

Concerning the ***low-level control design***, by supposing that the DC-link voltage V_{dc} is maintained constant at its reference value V_{dc}^* by the PMS, converters' currents have linear dynamics, which justifies their control by classical PI controllers. Being a ***tracking*** control level, it is designed to be fast enough to be neglected at the slower-dynamic upper level. Hence, the following equalities hold in the sequel: $I_{fc}{}^*=I_{fc}$, $I_{bat}{}^*=I_{bat}$ and $I_{sc}{}^*=I_{sc}$.

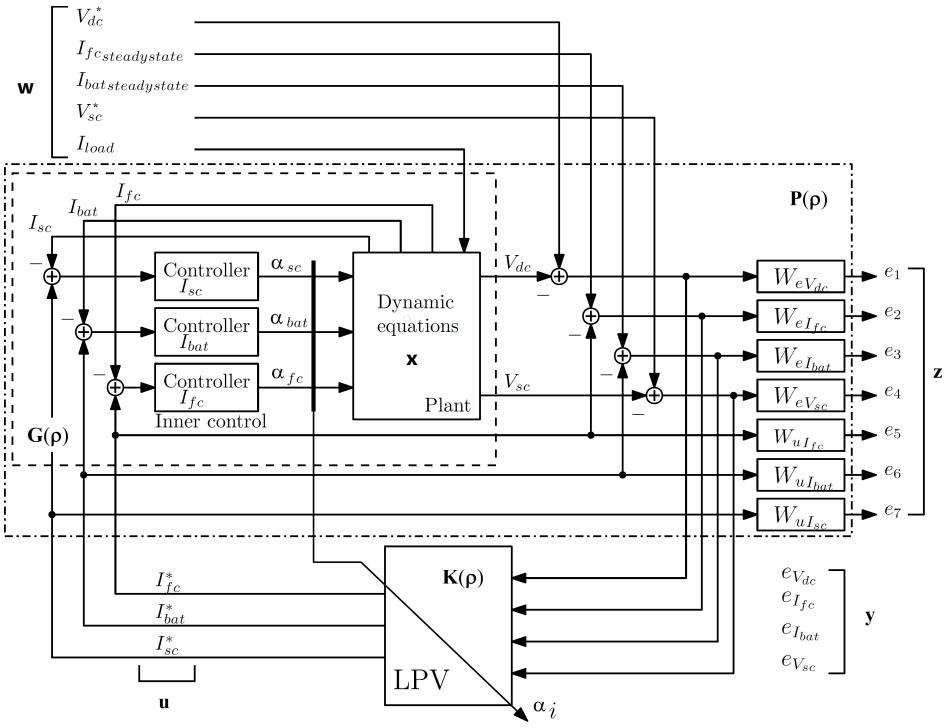

Figure 4.6: Closed-loop **P**–**K** form used in the LPV/$\mathcal{H}_\infty$ design, where the plant is extended by adding the weighting functions [146].

The three tracking low-level loops have the converters' duty cycles, α_{fc}, α_{bat} and α_{sc}, as control inputs. It is thus reasonable to identify the ***varying parameter vector as being composed of the three duty cycles***: $\boldsymbol{\rho} = [\rho_1 \quad \rho_2 \quad \rho_3]^T \equiv [\alpha_{fc} \quad \alpha_{bat} \quad \alpha_{sc}]^T$.

The sought-for LPV controller $\mathbf{K}(\boldsymbol{\rho})$ in Fig. 4.5 must therefore ensure closed-loop stability, meanwhile minimizing the effect of load current, I_{load}, acting as a disturbance, namely on the DC-link voltage. Control design is thus tackled in the $\mathcal{H}_\infty$ framework applied to LPV systems. The control design diagram is given in Fig. 4.6 under the so-called **P**–**K** form, where the plant $\mathbf{G}(\boldsymbol{\rho})$ is extended with the ***weighting functions*** – denoted by W – suitably selected such as to represent the above-listed performance requirements.

Whereas $\mathbf{G}(\boldsymbol{\rho})$ plant's state vector is $\mathbf{x} = [V_{dc} \quad V_1 \quad V_2 \quad V_0]^T$ – see Fig. 4.4 – composition of the other different vectors involved in the design is suggested in Fig. 4.6: the exogenous vector, $\mathbf{w}$, contains the disturbance signal I_{load}, all the other being reference signals; $\mathbf{u}$ is the control vector; $\mathbf{y}$ is the output vector containing the errors in relation to references and, finally, $\mathbf{z}$ is the controlled output vector, composed of the "conditioned"-by-weighting-function errors and control inputs.

The following choices of weighting functions proved to be appropriate in this case, as explained below.

- A first-order $W_{eV_{dc}}$ function is suitable to ensure both desired time response and acceptable DC-link voltage, V_{dc}, tracking error range.
- A first-order $W_{eV_{sc}}$ function is used to maintain supercapacitor SoC slowly around about 50%, that is, in the middle of its variation range, where the supercapacitor's voltage, V_{sc}, is a direct image of its SoC;
- First-order $W_{uI_{fc}}$, fourth-order $W_{uI_{bat}}$ and fourth-order $W_{uI_{sc}}$ shape the dynamic behaviour of current references of the fuel cell, the battery and the supercapacitor, respectively, according to some prespecified frequency ranges, thus implementing dynamic-specialization-based separation of power sources, *i.e.*, with respect to their respective characteristic frequencies.
- Fuel cell and battery steady-state behaviours are conditioned by means of $W_{eI_{fc}}$ and $W_{eI_{bat}}$, respectively, both constant; a desired steady-state power sharing can further be imposed by using $I_{fc_{steadystate}}$ and $I_{bat_{steadystate}}$ exogenous inputs.

Since the parameter vector $\boldsymbol{\rho}$ has the three converters' duty cycles as elements, bounded within [0.1;0.9] for practical reasons of avoiding the extreme values, the generalized LPV MIMO system is represented under a polytopic form with $2^{N=3} = 8$ vertices:

$$\begin{bmatrix} \dot{\mathbf{x}} \\ \mathbf{z} \\ \mathbf{y} \end{bmatrix} = \begin{bmatrix} \mathbf{A} & \mathbf{B}_1 & \mathbf{B}_2(\boldsymbol{\rho}) \\ \mathbf{C}_1 & \mathbf{D}_{11} & \mathbf{D}_{12} \\ \mathbf{C}_2 & \mathbf{D}_{21} & \mathbf{D}_{22} \end{bmatrix} \cdot \begin{bmatrix} \mathbf{x} \\ \mathbf{w} \\ \mathbf{u} \end{bmatrix}, \tag{4.14}$$

where, using circuit element notations in Fig. 4.4 and block diagram in Fig. 4.6, the different matrices are:

$$\mathbf{A} = \begin{bmatrix} -\frac{1}{C_{dc}R_{dc}} & 0 & 0 & 0 \\ 0 & -\frac{1}{C_1R_1} & 0 & 0 \\ 0 & 0 & -\frac{1}{C_2R_2} & 0 \\ 0 & 0 & 0 & 0 \end{bmatrix} \quad \mathbf{B}_1 = \begin{bmatrix} 0 & 0 & 0 & 0 & -\frac{1}{C_{dc}} \\ 0 & 0 & 0 & 0 & 0 \\ 0 & 0 & 0 & 0 & 0 \\ 0 & 0 & 0 & 0 & 0 \end{bmatrix} \quad \mathbf{B}_2(\boldsymbol{\rho}) = \begin{bmatrix} \frac{1-\rho_1}{C_{dc}} & \frac{\rho_2}{C_{dc}} & \frac{\rho_3}{C_{dc}} \\ 0 & 0 & -\frac{1}{C_1} \\ 0 & 0 & -\frac{1}{C_2} \\ 0 & 0 & -\frac{1}{C_0} \end{bmatrix}$$

$$\mathbf{C}_2 = \begin{bmatrix} -1 & 0 & 0 & 0 \\ 0 & 0 & 0 & 0 \\ 0 & 0 & 0 & 0 \\ 0 & 0 & 0 & -1 \end{bmatrix} \quad \mathbf{D}_{21} = \begin{bmatrix} 1 & 0 & 0 & 0 & 0 \\ 0 & 1 & 0 & 0 & 0 \\ 0 & 0 & 1 & 0 & 0 \\ 0 & 0 & 0 & 1 & 0 \end{bmatrix} \quad \mathbf{D}_{22} = \begin{bmatrix} 0 & 0 & 0 \\ -1 & 0 & 0 \\ 0 & -1 & 0 \\ 0 & 0 & 0 \end{bmatrix}$$

with the other matrices – $\mathbf{C}_1$, $\mathbf{D}_{11}$ and $\mathbf{D}_{12}$ – depending on parameters of the seven weighting functions in Fig. 4.6. In this case it is about finding *nineteen* such parameters, which is not a trivial task from a practical viewpoint. As heuristic methods appeared as a pertinent solution, **GAs** as evolutionary-inspired optimization method were preferred to facilitate selection of these parameters. Since convergence to optimality is guaranteed, optimization progress can be stopped when an arbitrarily chosen maximum number of iterations is reached, the solution being considered sufficiently good in relation to some predefined objective functions.

The ***two GA objective functions*** were originally proposed in our conference paper [148], as follows:

- ensuring ***sufficient closed-loop stability*** by imposing the real parts of closed-loop eigenvalues to be smaller than a certain desired value δ:

$$\min\left\{ f_1 = \max_i \left\{ \mathrm{Re}\left(\lambda_i\right) \right\} < -\delta, \delta > 0 \right\}, \tag{4.15}$$

where $\mathrm{Re}\left(\lambda_i\right)$ is the real part of the eigenvalue λ_i;

- ensuring the ***frequency-splitting "ability"*** of the weighting functions by minimizing the $\mathcal{H}_\infty$ norm corresponding to the transfer from disturbance I_{load} for each power source *outside* the desired – *i.e.*, its specialization – working frequency interval; this goal can be expressed mathematically as:

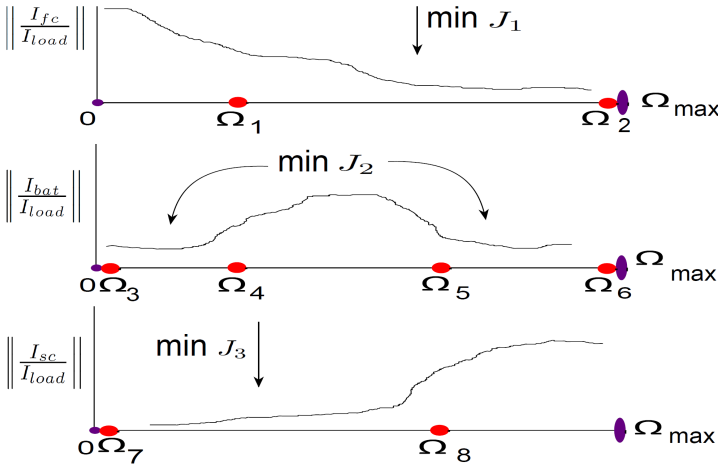

Figure 4.7: Illustrative representation of objective function f_2 of the GA with frequency intervals corresponding to configurable dynamic separation of sources [149].

$$\min\left\{ f_2 = \left(J_1 + J_2 + J_3\right)/3 \right\}, \tag{4.16}$$

with:

$$J_1 = \frac{\left\| \frac{I_{fc}}{I_{load}} \right\|_{\infty,(\omega_1,\omega_2)}}{\left\| \frac{I_{fc}}{I_{load}} \right\|_{\infty}}, \quad J_2 = \frac{1}{2} \cdot \frac{\left\| \frac{I_{bat}}{I_{load}} \right\|_{\infty,(\omega_3,\omega_4)}}{\left\| \frac{I_{bat}}{I_{load}} \right\|_{\infty}} + \frac{1}{2} \cdot \frac{\left\| \frac{I_{bat}}{I_{load}} \right\|_{\infty,(\omega_5,\omega_6)}}{\left\| \frac{I_{bat}}{I_{load}} \right\|_{\infty}}, \quad J_3 = \frac{\left\| \frac{I_{sc}}{I_{load}} \right\|_{\infty,(\omega_7,\omega_8)}}{\left\| \frac{I_{sc}}{I_{load}} \right\|_{\infty}},$$

where $\|\cdot\|_{\infty,(\omega_i,\omega_j)}$ is the $\mathcal{H}_\infty$ norm computed within the (ω_i, ω_j) frequency interval and the involved ω_i's are frequency values ordered like roughly suggested in Fig. 4.7 to correspond to the user-imposed relative frequency separation between power sources.

The LPV/$\mathcal{H}_\infty$ controller is found in the polytopic approach [128], according to the *quadratic-stabilization* framework [150], [151]. Thus, a set of LMIs are solved *off line* at each vertex of the polytope as a convex-optimization problem using *a single Lyapunov function*, which leads to $2^3 = 8$ vertex controllers of the form $\mathbf{K}_i : \begin{bmatrix} \mathbf{A}_{c_i} & \mathbf{B}_{c_i} \\ \mathbf{C}_{c_i} & \mathbf{D}_{c_i} \end{bmatrix}$, $i = 1, 2, ...8$. The methodology re-called in the previous Section 4.1 is further applied: a unique, global LPV controller $\mathbf{K}(\boldsymbol{\rho})$ is computed *on line* as a convex combination of the vertex controllers $\mathbf{K}_i$, according to (4.13), where expressions (4.12) of $\alpha_i(\boldsymbol{\rho})$ are here particularized by taking into account that:

$$\begin{aligned} \overline{\rho_j} &= \max \rho_j = 0.9, \\ \underline{\rho_j} &= \min \rho_j = 0.1, \\ j &= 1, 2, 3 \end{aligned}$$

Each of the eight vertex controllers is an *eighteenth*-order LTI system, thus suggesting potential difficulties with the practical implementation. Indeed, HILS validation of the developed PMS – as a step towards proving its practical feasibility – pointed out the need for a possibly more "alleviated" version of

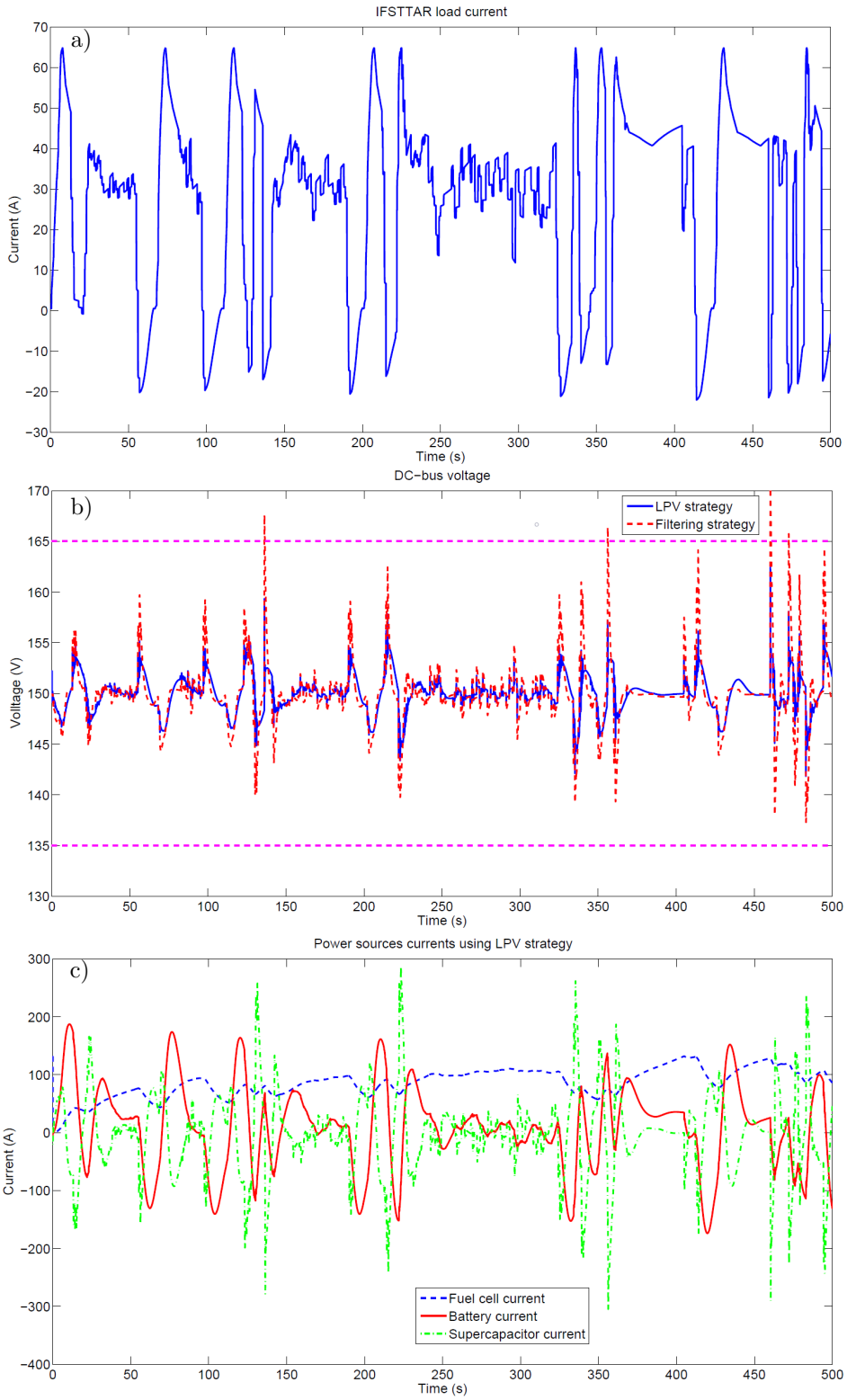

Figure 4.8: MATLAB®/Simulink®closed-loop performance assessement of LPV/$\mathcal{H}_\infty$ -based PMS for a three-storage MSES on board of an electric vehicle [147]: a) I_{load} variation corresponding to IFSTTAR driving cycle; b) DC-link voltage variation ensured by the LPV/$\mathcal{H}_\infty$ PMS against the one obtained by classical filtering; c) dynamically-separated time variations of currents of the three sources.

the controller, thus motivating the results briefed in the next Subsection 4.2.2. ***LPV/$\mathcal{H}_\infty$ controller order reduction*** was originally investigated in our conference paper [152], in order to reduce the controller complexity. To this end, MORE toolbox [153] was used to find a reduced-order model that fits the original controller for a certain bounded frequency range. More precisely, the iterative singular value decomposition tangential Krylov algorithm was applied on each vertex controller for the whole closed-loop bandwidth, to finally yield *tenth*-order vertex controllers. Values of both $\mathcal{H}_2$ and $\mathcal{H}_\infty$ norms of full-order and reduced-order closed-loop systems are close in view of the chosen criterion, even though the complexity is highly reduced [147], thus suggesting realistic feasibility of embedding the obtained controller into a numerical device.

This subsection ends with some representative numerical simulation results resumed from [147]. The ***IFSTTAR*** *(Institut Français des Sciences et Technologies des Transports, de l'Aménagement et des Réseaux – French Institute of Science and Technology for Transport, Development and Networks)* ***driving cycle*** profile (Fig. 4.8a)), representing the ***urban*** driving conditions – comprising acceleration, deceleration, fixed speed and full brake – was chosen for being rich in frequency content, thus sufficiently challenging to allow assessing performance of DC-bus voltage regulation and the way the three sources are coordinated to satisfy the power demand.

The DC-link voltage well regulation at its reference value, 150 V, within accepted tracking error of ±10%, is a prioritary goal, adequately achieved as Fig. 4.8b) shows. Time evolutions in Fig. 4.8c) confirm the desired suitable dynamic separation of the three power sources: their currents are provided to the system in the manner of fuel cell supplying average current and supercapacitor handling peak variations, while the battery provides the midrange current variations.

The *PI-based filtering PMS* was also run in simulation for benchmarking purposes; results are skipped here, they can be found in [147]. Being characterized by a set of parameters to be tuned manually and different design constraints that prevent control objectives from being independently achieved, this baseline PMS strategy is difficult to handle. The comparison with the baseline PMS solution suggests a broader conclusion: the LPV/$\mathcal{H}_\infty$ PMS can be viewed as a ***generalized filtering strategy*** in a ***MIMO*** context, *i.e.*, completed with certain degrees of freedom to meet a multitude of control goals and ***optimized*** according to some user-defined criteria.

4.2.2 HILS-assessed PMS real-time performance

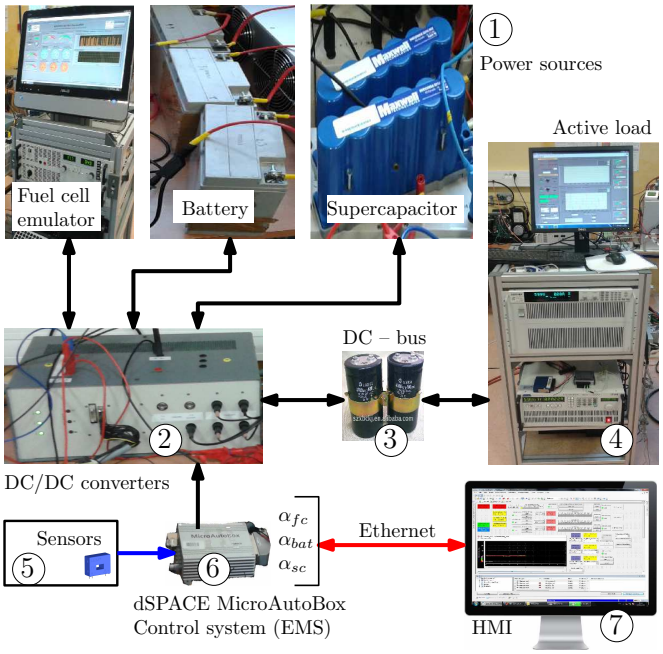

Figure 4.9: Schematics of the rapid-prototyping test bench built at FEMTO-ST Laboratory in Belfort, France, used to validate the LPV/$\mathcal{H}_\infty$ PMS [146].

This section refers to some further validation results, namely those obtained on a dedicated test-bench designed in collaboration with FEMTO-ST Laboratory in Belfort, France. Real battery and supercapacitor are used in the test bench, whereas a complete real-time emulator developed at FEMTO-ST Laboratory represents the fuel cell [154]. A reduced-order version of the controller is employed in real time. Fig. 4.9 shows an expanded view of the interconnections between the different parts used in the assembled test bench. The active load variation is controlled to represent the desired driving cycle scenario by means of a rapid-prototyping platform based on the dSPACE™ MicroAutoBox®II device.

Running hardware-in-the-loop simulations required some *adaptations* having been made. Thus, application of the proposed methodology was resumed, this time on the test bench model, and yielded a reduced-order controller suitable for real-time implementation. Saturations of sources' currents were taken into account in the design. Comparison between real-time and numerical simulation results was performed

under the same scenario. Thus, samples of the measured load current were used to reperform numerical simulation.

Adaptations regarding selection of control references and weighting functions were also necessary, as detailed in [146]. As a global result, some differences between numerical simulation and real-time results were obtained, which are normal since they confirm reasonable expectations. Fig. 4.10 offers a view of real-time evolutions of the three currents of interest, where dynamic separation can again be confirmed and qualitatively compared with homologue numerical simulation results in Fig. 4.8c).

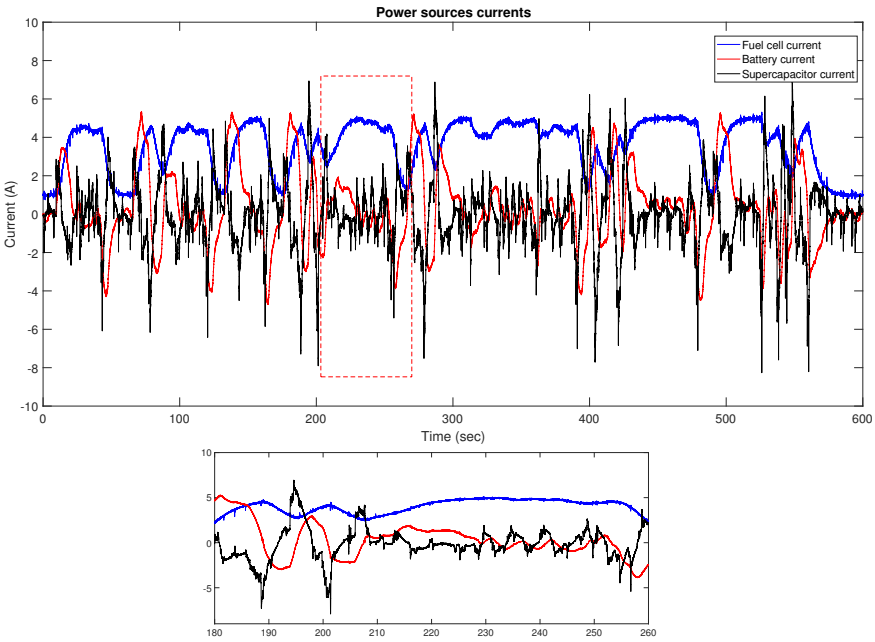

Figure 4.10: Real-time results obtained on the test bench in Fig. 4.9 [146]: the three power sources' currents corresponding to IFSTTAR driving cycle and zoom.

The modeling uncertainty of sources was expected to be the main source of differences here, that is, differences between nominal and real values of parameters characterizing each of the three sources. While datasheet values of parameters were used in numerically-implemented models and simulations, real values of these parameters – resistances, inductances, capacities – vary in time and may not any longer be equal to the datasheet ones. Therefore, currents of sources had slightly different time evolutions in real time compared to numerical simulation. Meanwhile, as expected, the proposed control strategy performed robustly against these parameter variations.

4.2.3 Some results of embedding robust PMSs in general-purpose microcontrollers

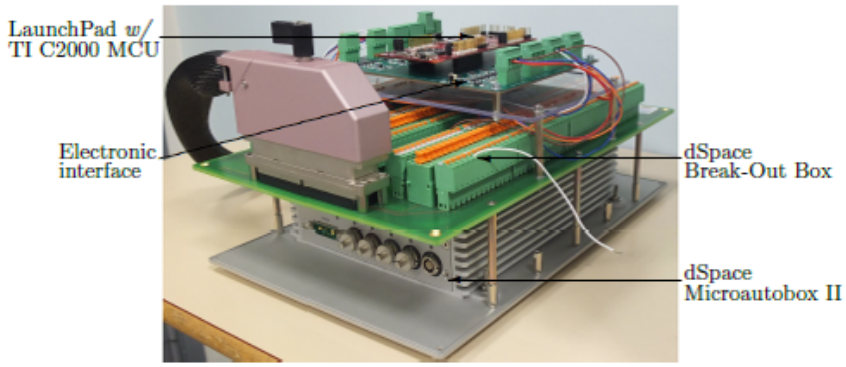

Figure 4.11: Photo of the K-INF demonstrator at GIPSA-lab, built within the technology pre-transfer project funded by Institut Carnot LSI.

Funding obtained between 2017 and 2018 from Institut Carnot *Logiciels et Systèmes Intelligents* (LSI) in the framework of the ***K-INF: Embedded real-time PMS for multi-source electrical energy systems*** technology pre-transfer project allowed further advancing the technology readiness level (TRL) of our PMS solution. Efforts were oriented towards achieving a ***laboratory proof of concept***.

To this end, the K-INF PMS design code, written in MATLAB® for the electric vehicle application described in the previous two sections, was translated into executable code, then effectively embedded into the ***general-purpose Texas Instruments (TI) C2000 microcontroller*** – chosen as target real-time computing device – by using dedicated libraries of MATLAB®.

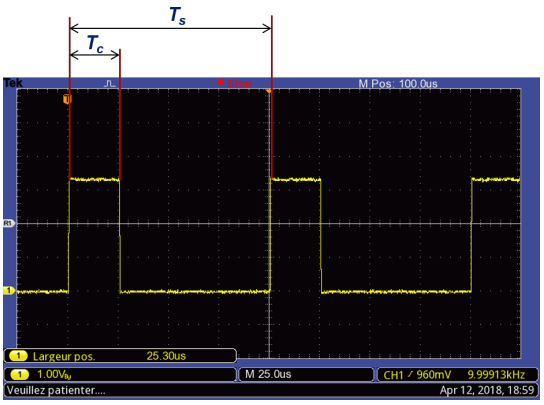

Figure 4.12: K-INF technology pre-transfer project results: oscilloscope capture of the total time the TI C2000 microcontroller spends with K-INF PMS computations, T_c, against sampling time, T_s.

The mathematical model of the three-source power supply on board of EV was embedded into dSPACE^{TM} rapid-prototyping system, which was further coupled in closed loop with the microcontroller, in order to support real-time tests. In this way, the ***K-INF demonstrator*** in Fig. 4.11 – whose functional design is mainly due to Iulian MUNTEANU, who assumed the role of technical expert in this project – was built and put into service at GIPSA-lab, with the help of R&D engineers Gelu IONESCU and Christophe SAVARIAUX, heads of GIPSA-lab Technical Service, and R&D engineers Sophie MIN-PICAULT and Julien MINET.

One of the objectives of this project was ***to check practical implementation feasibility of the new PMS***, from the viewpoint of necessary computation resources (computation time and allocated memory). Indeed, given its complexity, the new control structure appeared to challenge computation performance of some supporting device. Fig. 4.12 allows concluding that the total computation time $T_c \approx 25$ µs, that is, 25% of the sampling time, $T_s = 100$ µs, programmed in the TI C2000 microcontroller. Also, the total memory used is approximately 20 kB, that is, only 10% of the available memory. These evaluations indicate that there is still sufficient room for possibly accommodating an even more complex PMS, if needed – conversely, a less powerfull (also cheaper) microcontroller can be employed instead.

The demonstrator allowed extensive tests having been performed, under a plethora of driving cycle scenarios, including some standard driving cycles, all of which were user-configured by means of a monitoring console under ControlDesk®(software tool provided by dSPACE^{TM}). Rapid-prototyping code allowed suitable replication of real-environment phenomena, like noises, pure delays, filtering, *etc.* Another monitoring console, this time under MATLAB®, allowed completing visualization of results (time evolutions and frequency analysis).

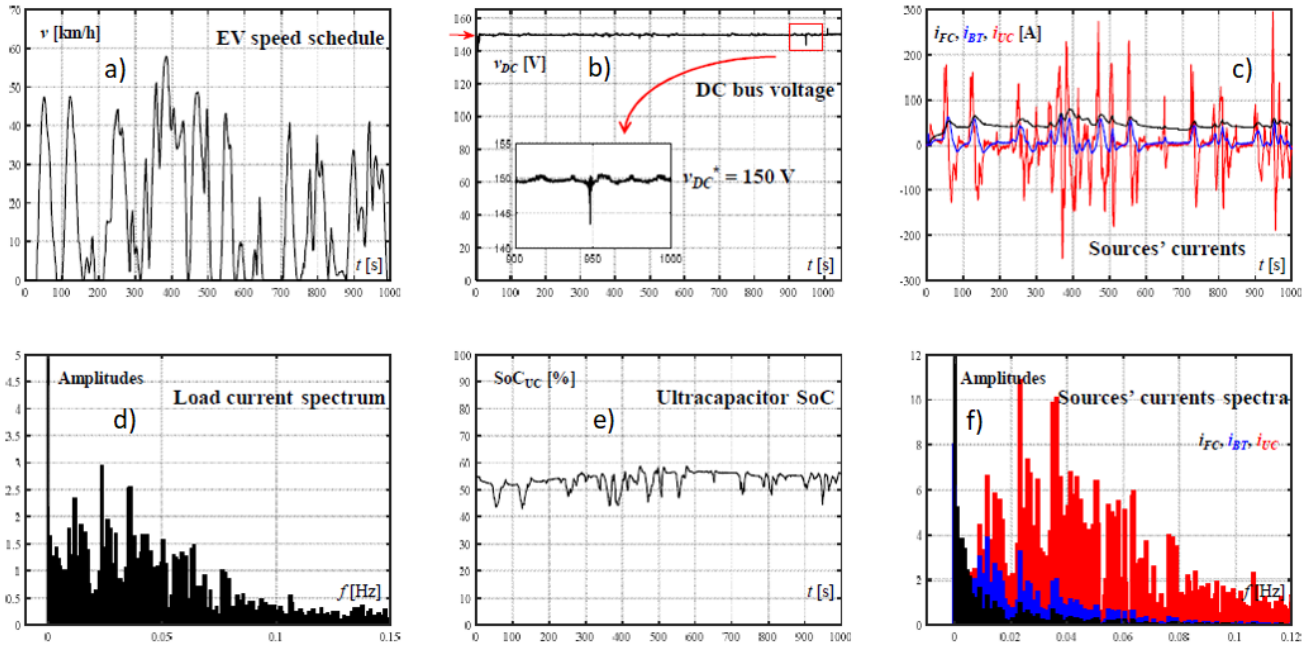

Figure 4.13: K-INF technology pre-transfer project results: time evolutions of variables of interest for Artemis Urban standard driving cycle.

Effectiveness of K-INF PMS was concluded under the whole set of scenarios. Fig. 4.13 gives a synthetic image of some relevant results, where *Artemis Urban driving cycle* was chosen as excitation scenario. The corresponding

electric vehicle speed profile can be seen in Fig. 4.13a), whereas the associated amplitude spectrum of the load current demand is shown in Fig. 4.13d). Performance of DC-bus voltage regulation and time variation of the unltracapacitor state of charge are exhibited in Figs. 4.13 b) and e), respectively. Figs. 4.13 c) and f) illustrate convenient dynamic separation of sources in time and frequency domain, respectively.

4.3 Robust PMS design for frequency and voltage regulation in *multi-source AC microgrids*

While remaining in the nowadays "fashionable" domain of microgrids (MGs), the focus is in this section shifts to ***AC MGs***, more precisely, to those having a high penetration rate of renewables. In this context, to ensure MG stability and suitable overall performance is a challenge of crucial importance, especially during ***islanded*** – otherwise said, ***isolated*** or ***autonomous***, or again ***off-grid*** or ***stand-alone*** – mode, where low inertia, uncertainties, and intermittent nature of distributed energy resources play an even more constraining role [2], [3].

Thus, **compelling frequency and voltage deviations** to stay within some maximally admissible ranges as imposed by stiff **grid codes** is of focal importance in stand-alone operation mode. Finding pertinent technological solutions to this problem has determined a large research effort being deployed lastly, out of which ***use of short- and medium-term storage systems*** – *e.g.*, batteries, flywheels, or supercapacitors – has proved to open a promising way towards feasible implementations. The resulted new grid configurations have again emphasized the need for advanced control structures to deal with unexpected disturbances and model uncertainties. Results briefed in this section remain thus focused on how to ensure a judicious management of storage units, in order to enhance the mixture of classical and renewable sources. They are coherent with those in the literature, where it is shown that, if suitable dynamical coordination of storages with other generation sources is achieved and saturations are avoided, then relatively small storages can significantly reduce both frequency [155] and voltage [156] variations.

To fix ideas, the chosen storage system is a ***supercapacitor***, which is further inserted into a ***Diesel-PV hybrid MG*** rated at MW and operating in stand-alone mode, as depicted in Fig. 4.14. The different power sources are connected in parallel to a point of common coupling (PCC) and feed a common load.

The $\mathcal{H}_\infty$ robust control design formalism was proposed as solution to both frequency and voltage regulation problems, in a coherent systematic approach based on a suitable control-oriented modelling and rigourous formal translation of various engineering specifications, among which the (micro)grid codes.

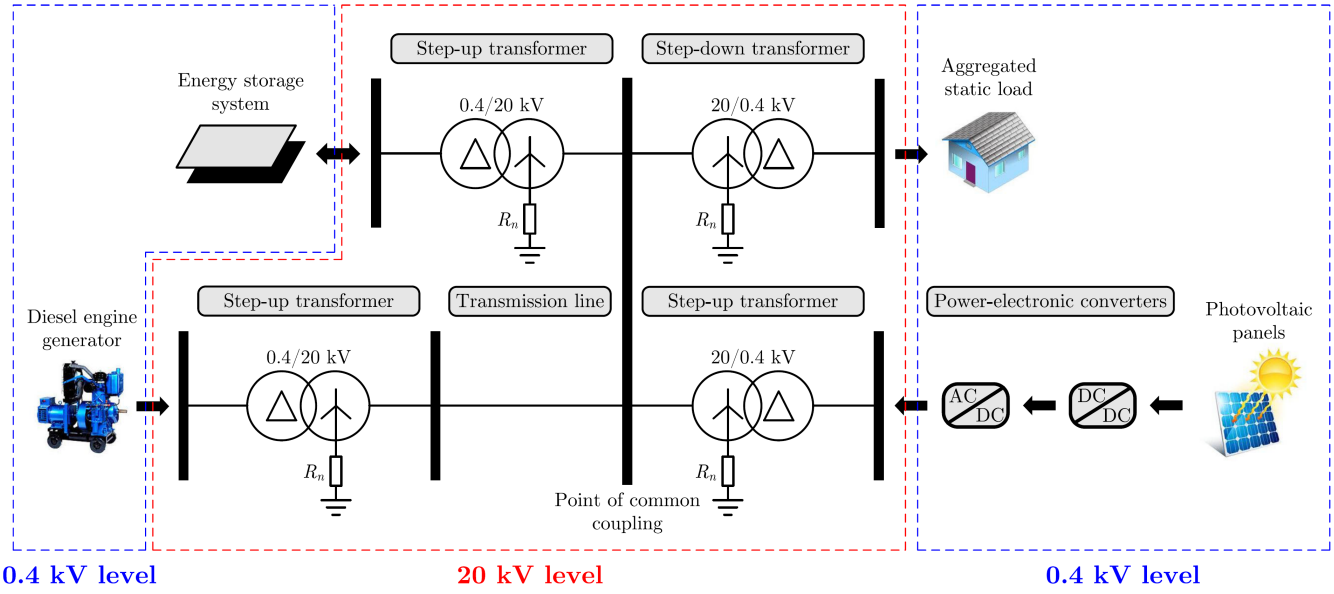

Figure 4.14: Functional schematics of the stand-alone AC MG considered for $\mathcal{H}_\infty$ robust frequency and voltage regulation purposes [157].

The results presented next were obtained within collaboration with Ph.D. student Quang-Linh LAM, working under the supervision of Professor Delphine RIU and myself, and made the object of the following main publications:

- Q.L. Lam, A.I. Bratcu, C. Boudinet, M. Thomas, A. Labonne, D. Riu (2020). Primary frequency $\mathcal{H}_\infty$ control in stand-alone microgrids with storage units: a robustness analysis confirmed by real-time experiments. *International Journal of Electrical Power and Energy Systems*, 115, art. no. 105507

  – summarized in Subsection 4.3.1 – in which the primary ***frequency*** regulation problem is first solved within a robust $\mathcal{H}_\infty$ approach, then uncertainty in the steady-state value of the supercapacitor SoC is taken into account in a μ–analysis to determine its maximum variation range for which the imposed closed-loop performances are still respected for the considered operating point. With the help of R&D engineers Cédric BOUDINET, Martin THOMAS and Antoine LABONNE from Grenoble Electrical Engineering Laboratory (G2ELab), a rapid-prototyping test bench was configured to support power hardware-in-the-loop simulations under meaningful scenarios;

- Q-L. Lam, A.I. Bratcu, D. Riu (2021). Multi-variable $\mathcal{H}_\infty$ control approach for voltage ancillary service in autonomous microgrids : design and sensitivity analysis. *IEEE Access*, 9, 140212–140234

  – presented in Subsection 4.3.2 – which deals with an $\mathcal{H}_\infty$ –based ***voltage*** controller that robustly forces the voltage magnitude of a PCC, such as to satisfy design requirements.

TRL advancing of K-INF PMS solution developed in the ***technology* pre-*transfer*** project – presented previously in Subsection 4.2.3 – was pursued, but this time by changing the use case. Thus:

- ***technology transfer*** project *K-INF: Robust PMS for multi-source electrical energy systems* (*Gestionnaire d'énergie robuste embarqué des systèmes multi-sources*),

  funded by Linksium Grenoble Alpes Technology Transfer Office (TTO) between 2018 and 2020, adapted K-INF PMS design methodology – including microcontroller embedding – to the use case of ***frequency regulation in MGs with renewable energy sources and* hybrid storage *units***; more precisely, a **battery-supercapacitor** storage tandem was considered. This made the object of an APP software application deposit, accompanied by a know-how documentation, as follows (alphabetical order of authors):

  – A.I. Bratcu, I. Munteanu (2019). *K-INF Multi-storage energy management system robust design for frequency regulation in AC microgrids.* Grenoble Institute of Technology, CNRS, Grenoble Alpes University. *APP software application*;
  – A.I. Bratcu, I. Munteanu (2020). *Design procedure of a robust multi-storage energy management for frequency regulation in AC microgrids.* Grenoble Institute of Technology, CNRS, Grenoble Alpes University. *Know-how patent application.*

Some interesting results and conclusions of *K-INF* technology transfer project are summarized in Subsection 4.3.3 – among them, *quantitative assessment of hybridization benefit* in terms of sources' lifetime savings. Website `http://www.k-inf.fr` was created for presenting details about this project's history and K-INF PMS technical outcomes and economical benefits in the MG primary frequency regulation use case.

4.3.1 *Frequency*-regulation PMS for an *ultracapacitor*-based AC microgrid: robust control design and PHILS validation

When high penetration of renewables is aimed at, especially in stand-alone operation, frequency variations can lead to global instabilities [158]. In the MG in Fig. 4.14, primary frequency regulation relies upon participation of both the energy storage system (ESS – the supercapacitor in this case) and the classical source (the Diesel generator), where the task assigned to the former is a faster recovery of the MG frequency, f_{grid}, in response to either load or production power variation.

Thus, ***dynamic performance*** of the frequency response – overshoot, response time, steady-state error – is imposed by the ***grid codes***, whose requirements may slightly vary in different countries or regions. These grid

codes can be pertinently "translated" based on the time-domain response in the case where only the classical source participates in primary control – in this way, a template of the MG small-signal frequency deviation can result, like shown in Fig. 4.15. Another dynamic specification concerns the DC-bus voltage regulation (here, the reference value is chosen at V_{dc}^{ref}=150 V). Note that in this case it is not about some stiff grid codes to be met, but just to define some suitable performance specification like, for example, indicated in Fig. 4.16 [159], [160].

Time-domain templates in Figs. 4.15 and 4.16 are important, as they further help at deducing the corresponding templates in the ***frequency*** domain – namely, in the form and parameters of the ***weighting functions*** – coherently with the $\mathcal{H}_\infty$ control design.

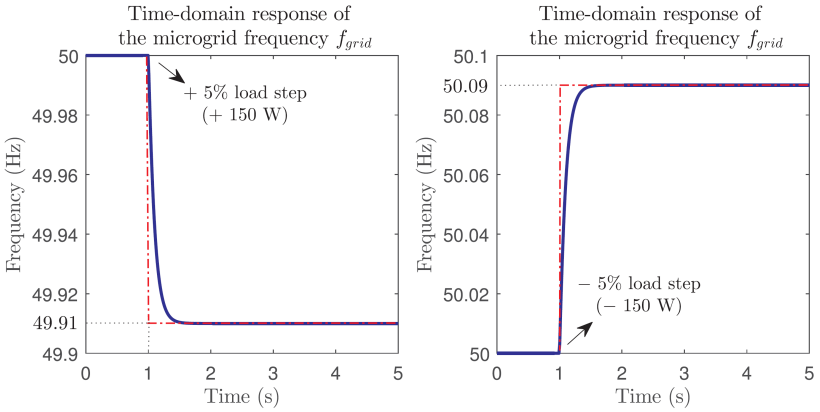

Figure 4.15: *Translation of* ***frequency*** *grid codes*: time-domain performance specification on the MG frequency variation in response to a step disturbance of ±5% of the load rated active power [161].

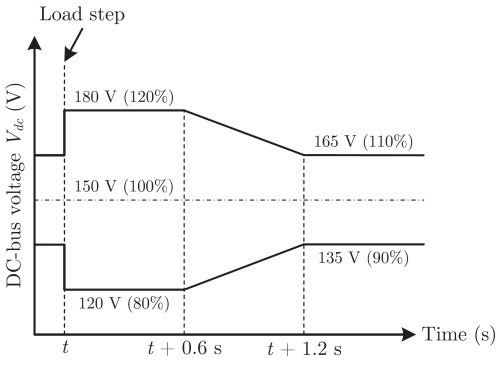

Figure 4.16: Some suitable time-domain performance specification on the DC-bus voltage variation in response to a load step disturbance [161].

Fig. 4.17 depicting the MG electrical circuit diagram serve at further obtaining the MG ***linearized per-unit model*** around a typical steady-state operating point. Indeed, per-unit modelling was here preferred for its generally better numerical conditioning, thus improved numerical computation stability, especially when it is about high-order, possibly multi-scale systems [162], [163].

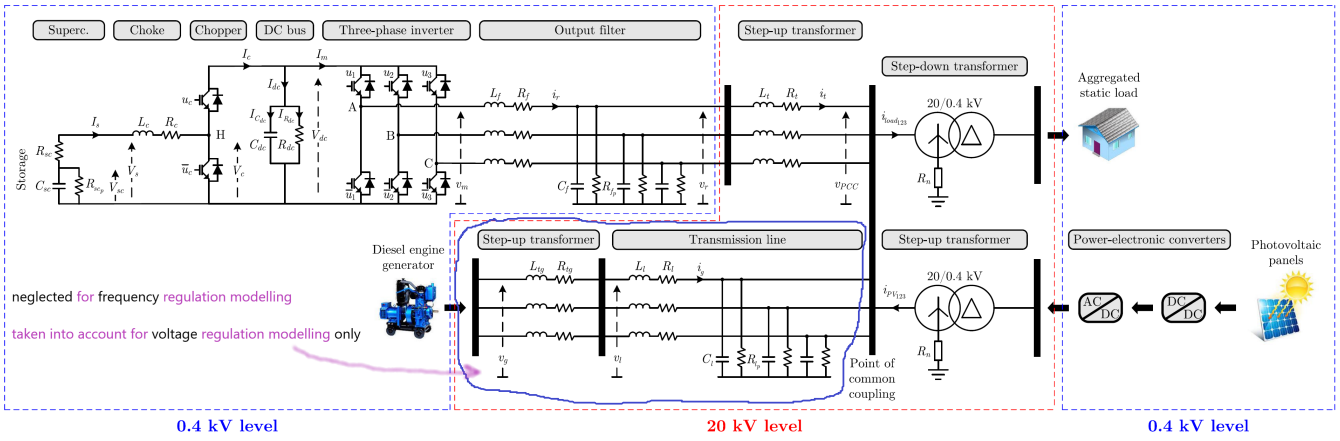

Figure 4.17: Electrical circuit diagram of the studied MG for modelling purposes, where notations of interest variables for both frequency and voltage regulation are introduced [157].

Some simplifying, still realistic, assumptions are first adopted. Thus, since frequency control is at this time aimed at, it is sufficient to only consider the *mechanical dynamic* of the Diesel generator – of T_{diesel} time constant – whereas, for example, its local voltage regulation is much faster and not intervening in the frequency control. As such, the circled part of the diagram in the figure is neglected for frequency-regulation modelling purposes, being taken into account for voltage-regulation modelling only (as briefed in the next Subsection 4.3.2). Also, supposing that active power variations – responsible for the MG frequency variations – do not significantly influence the PCC voltage, then PCC voltage direct and quadrature components remain constant (*i.e.*, ΔV_{rd}=0 and ΔV_{rq}=0).

For sake of brevity, detailed state-space modelling is skipped here – it can be found in [161] and [164] – whereas allowing to drive a conclusion for control purposes, that is, adoption of a ***two-level hierarchical control strategy***.

Thus, by adopting the underline notation "$\underline{\Delta x}$" for denoting linearized per-unit variations of variable x and following the same justification and guidelines as in the case of multi-storage (DC) MGs considered in previous Section 4.2, the outer (upper) control level deals with output regulation imposing low-frequency dynamics (*e.g.*, supercapacitor and DC-link voltage per-unit variations, $\underline{\Delta V_{sc}}$ and $\underline{\Delta V_{dc}}$, respectively, Diesel power per-unit variations, $\underline{\Delta P_{diesel}}$, and MG frequency per-unit variations, $\underline{\Delta f_{grid}}$) and the inner (lower) level concerns current reference tracking of high-frequency dynamics (*e.g.*, supercapacitor current per-unit variations, $\underline{\Delta I_s}$, and inverter current d- and q-component per-unit variations, $\underline{\Delta I_{rd}}$ and $\underline{\Delta I_{rq}}$, respectively) .

In this way, the classical principle of cascade control is here illustrated: the ***outer loop*** results from demanding to reject disturbances coming from the aggregated load power per-unit variations, $\underline{\Delta P_{load}} - \underline{\Delta P_{PV}}$ – this ***disturbance-rejection*** problem is cast into the $\mathcal{H}_\infty$ formalism to yield an $\mathcal{H}_\infty$ controller that further provides references $\underline{\Delta I_s^{ref}}$, $\underline{\Delta I_{rd}^{ref}}$ and $\underline{\Delta I_{rq}^{ref}}$ to the ***inner tracking loops***. In particular, as the quadrature current I_{rq} does not participate to frequency control, its variation is set to 0 ($\underline{\Delta I_{rq}}$=0), hence only two control inputs are effectively used: $\underline{\Delta I_s}$ and $\underline{\Delta I_{rd}}$. Moreover, this strategy is coherent with considering the power sources as current sources – whose currents are explicitly controlled by lower-level PI controllers – thus being preferable from an application viewpoint. Fig. 4.18 shows the proposed global control structure, with some newly introduced notations: $\underline{s_{diesel}}$ is the speed regulator droop value, $\underline{H}$ is the MG equivalent inertia constant and $\underline{D_{load}}$ is the load damping constant.

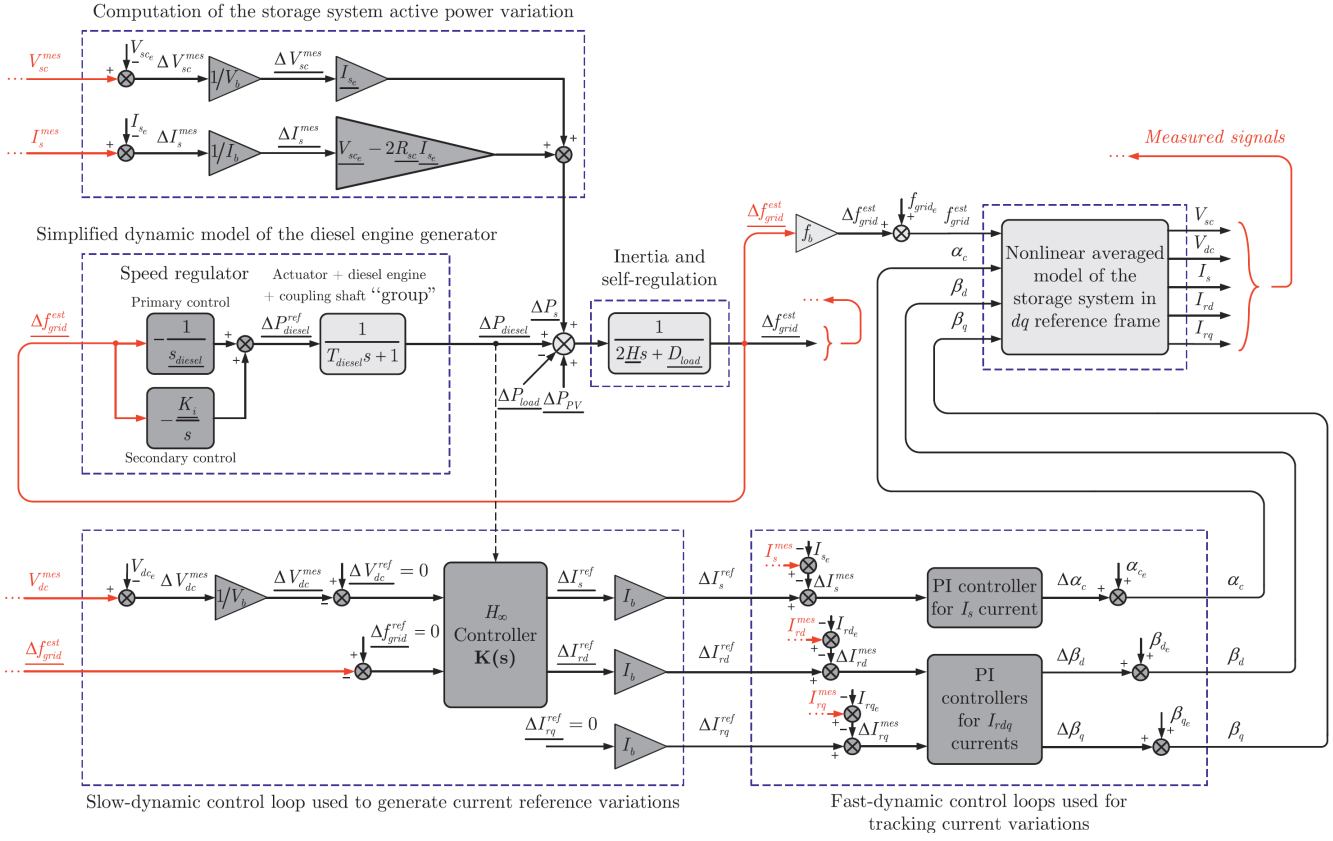

Figure 4.18: Block diagram of the $\mathcal{H}_\infty$ -based two-level control structure dedicated to stand-alone MG primary frequency regulation [164].

Based on the general control configuration in [165], the primary frequency regulation problem can now be classically cast into an $\mathcal{H}_\infty$ formalism, as depicted in Fig. 4.19, where the so-called **P**–**K** form can be identified, making appear vector $\underline{\Delta \mathbf{z}}$ of ***performance outputs***, which must be suitably "conditioned" by the ***weighting functions***, W, such as to comply with the performance specifications. For purpose of brevity, this form appears in this figure already completed with the uncertainty $\mathbf{\Delta}$ blocks, further required by the robustness μ-analysis, as explained later.

Because disturbance rejection is here aimed at and tracking is not an issue, the S/KS ***mixed-sensitivity optimization in the standard regulation form*** must typically be solved [165], with sensitivity functions being defined as

$$S_1(s) = \frac{\underline{\Delta V_{dc}}(s)}{\underline{\Delta P_{load}}(s) - \underline{\Delta P_{PV}}(s)} \quad S_2(s) = \frac{\underline{\Delta f_{grid}}(s)}{\underline{\Delta P_{load}}(s) - \underline{\Delta P_{PV}}(s)} \tag{4.17}$$

and complementary sensitivity functions

$$KS_1(s) = \frac{\underline{\Delta I_s^{ref}}}{\underline{\Delta P_{load}}(s) - \underline{\Delta P_{PV}}(s)} \quad KS_2(s) = \frac{\underline{\Delta I_{rd}^{ref}}}{\underline{\Delta P_{load}}(s) - \underline{\Delta P_{PV}}(s)} \tag{4.18}$$

allowing limitation of the $\mathcal{H}_\infty$ controller size and bandwidth, with direct impact on the control energy used. This design method requires an appropriate choice of weighting functions $W_{perf}(s)$ to formalize the disturbance rejection performance specifications and weighting functions $W_u(s)$ to translate the constraints imposed to the control inputs. Thus, first-order weighting functions W_{perf}, band-pass weighting function W_{u_1} and first-order weighting function W_{u_2} are used, as detailed in [161].

The optimization problem aiming at minimizing the norm $\left\| \begin{matrix} W_{perf}S \\ W_uKS \end{matrix} \right\|_\infty$ is numerically solved based upon the model directly instantiated with the test bench parameter values, resulting in a multi-variable eight-order $\mathcal{H}_\infty$ controller, with an optimal value γ of 2.1 and an $\mathcal{H}_\infty$ norm of 0.47.

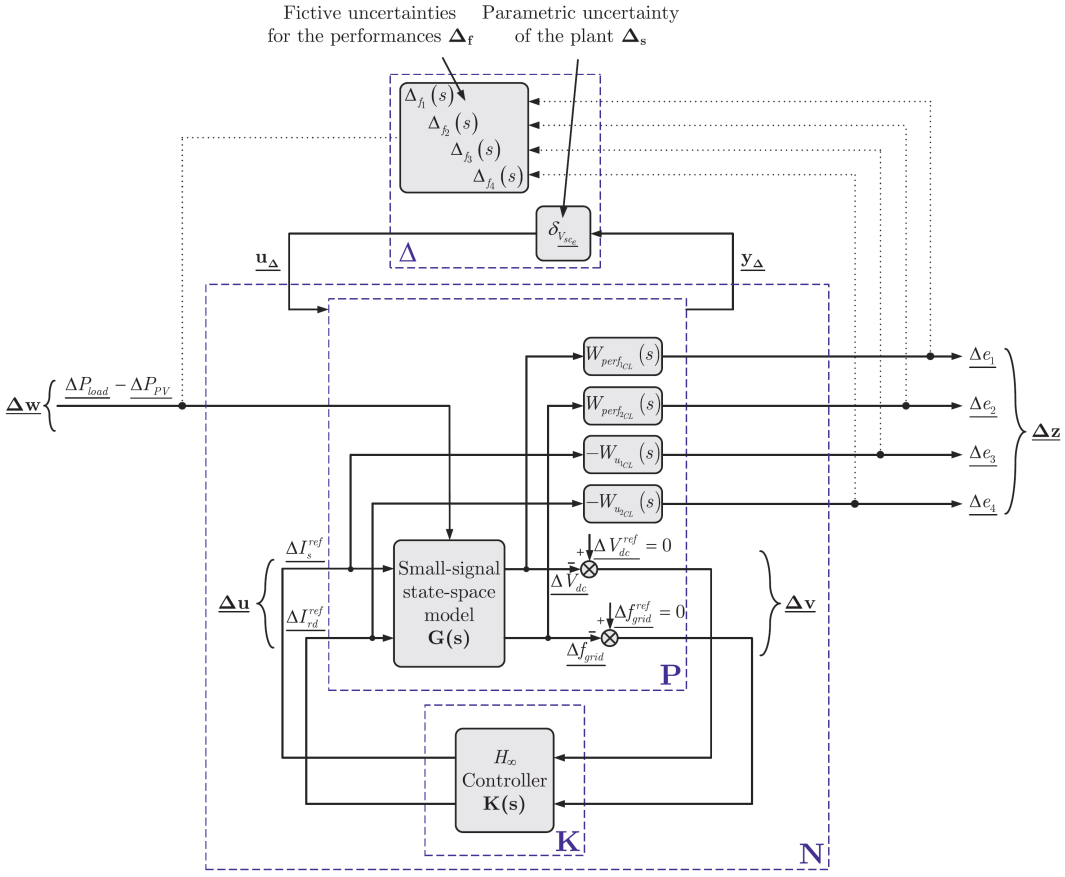

Figure 4.19: **P**–**K** block diagram for $\mathcal{H}_\infty$ primary frequency control design, completed with the **N**–$\mathbf{\Delta}$ form for robust performance analysis [160], [161].

Next, the robustness analysis in the presence of modelled parameter uncertainties is carried out using the μ–analysis. Here, the parameter chosen to answer the robust performance test is the steady-state value of the supercapacitor voltage, V_{sc_e}, as it is directly representative of its state of charge (SoC). The $\mathcal{H}_\infty$ design initially considers this value as being constant, *i.e.*, in the middle of its variation range (36 V in this case, corresponding to the real supercapacitor used in the test bench).

To this end, the extended general control configuration in the so-called **N**–$\mathbf{\Delta}$ form [165] is included in Fig. 4.19, where **N**(s) is defined as the connection of the plant together with the weighting functions and the previously designed $\mathcal{H}_\infty$ controller. The linear time-invariant uncertain matrix $\Delta(s) = \text{diag}\{\Delta_\mathbf{f}(s)\ \Delta_\mathbf{s}(s)\}$, where $\Delta_\mathbf{f}(s)$ is the fictive full-block complex uncertain matrix representing the $\mathcal{H}_\infty$ norm specifications and $\Delta_\mathbf{s}(s)$ is the block-diagonal real uncertain matrix representing the parametric uncertainty in V_{sc_e}.

Note that the weighting functions used for the robust performance analysis and appearing in Fig. 4.19 bear subscript "*CL*", as they are different from the ones used for the nominal design in the sense of "normalization" by the previously obtained value of γ: $W_{perf_{CL}}(s) = W_{perf}(s)/\gamma$ and $W_{u_{CL}}(s) = W_u(s)/\gamma$.

Finally, results of computing an upper bound and a lower bound of the structured singular value μ for the considered controlled MG led to the conclusion that the closed-loop system remains robust in performance up to 37% uncertainty in V_{sc_e} around its design value, which indicates a "robust" variation range theoretically covering the whole supercapacitor's SoC variation domain [161]. This result confirms that the chosen supercapacitor can effectively be employed for robust primary frequency control, as its ***SoC can vary from empty to full without resulting in closed-loop stability or performance degradation***.

This subsection ends with some representative ***power*** hardware-in-the-loop simulation (***P***HILS) results resumed from [161]. This kind of validation technique supposes using a *power amplifier* in addition to a basic HILS structure, in order to get even closer to the real-world system.

The test bench built for PHIL validation (see Fig. 4.20) – configured in the framework of collaboration with G2ELab – is composed of two main subsystems: the real supercapacitor-based ESS including a PWM-controlled two-quadrant chopper and a PWM-controlled three-phase voltage-source inverter, and a second subsystem aiming at emulating the remainder of the studied MG – that is, the Diesel engine generator, the PV system and the aggregated static load – by means of a real-time digital simulator and a power amplifier.

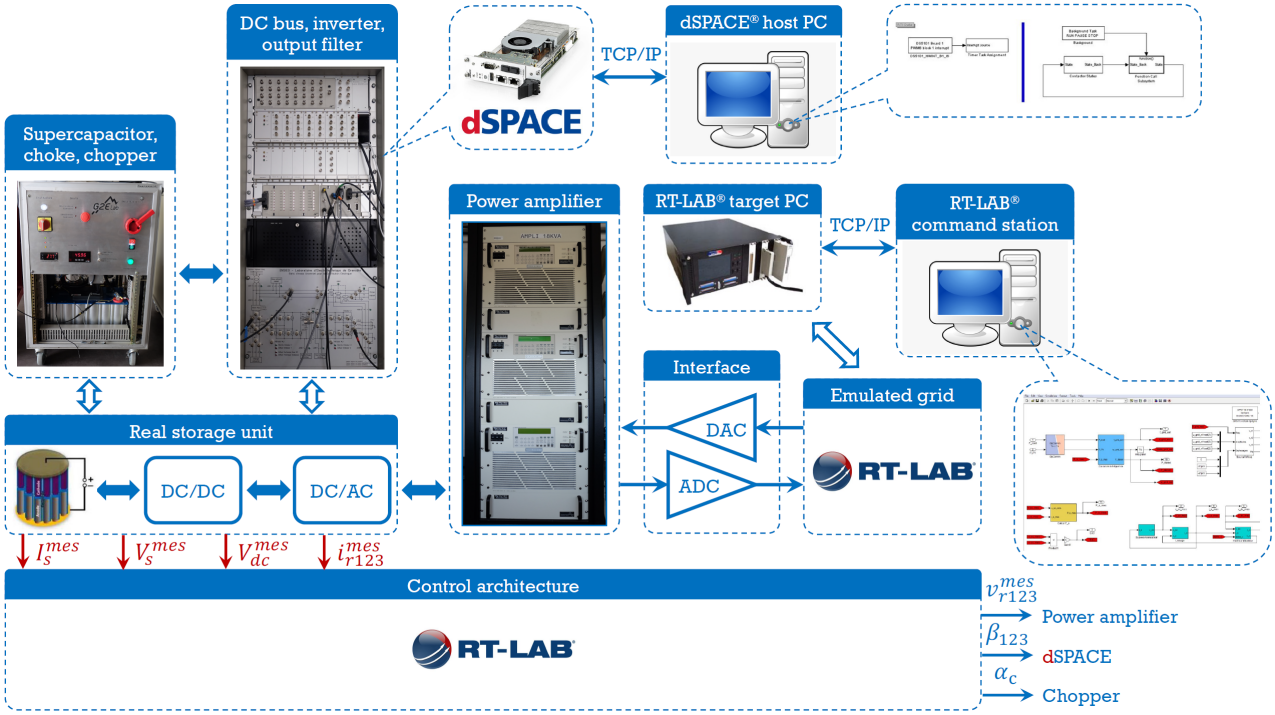

Figure 4.20: PHIL test bench for validation of the stand-alone MG robust control [164].

Two real-time digital simulators, RT-LAB®and dSPACE™, are used in parallel for controlling the hardware parts of the test bench. As regards the software layer of the emulated subsystem, it is composed of MATLAB®/Simulink®models of the Diesel generator, the PV system and the aggregated load, as well as the RT-LAB®-supported control architecture. The real supercapacitor-based ESS is rated at kW-level, a power level much lower than that of the considered MG; therefore, the analogous scaling law was used for dynamic replication [161].

Results in Fig. 4.21 confirm predictions of the robustness analysis: the imposed closed-loop overshoot performance of the DC-bus voltage, V_{dc} (*i.e.*, maximum overshoot of 7.5 V) is preserved regardless of the initial value of supercapacitor SoC, SoC_{sc}, meanwhile employing a reasonable control effort (the supercapacitor current, I_s, remains below its maximum admissible value – here, 32 A).

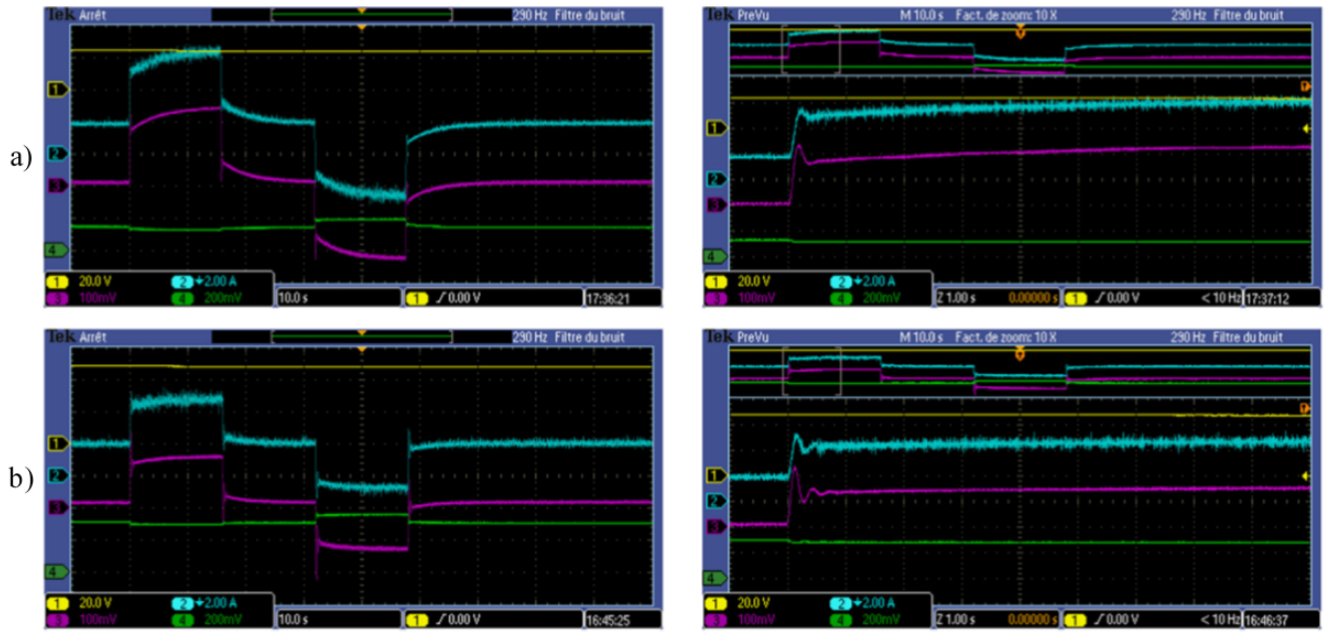

Figure 4.21: Closed-loop PHIL results for the MG in Fig. 4.17, suggesting robust performance for the two extreme values of the supercapacitor SoC [161]: time-domain responses of supercapacitor voltage V_{sc} (channel 1, 20 V/div), supercapacitor output current I_s (channel 2, 2 A/div), DC-bus voltage variation ΔV_{dc} (channel 3, 2.5 V/div) and chopper PWM duty cycle α_c (channel 4, 0.2/div) under small load step disturbances of ±5% of load rated active power (± 150 W), where: a) SoC_{sc_e}=25%; b) SoC_{sc_e}=100% – at the right, zooms in a time interval.

4.3.2 *Voltage*-regulation PMS for an *ultracapacitor*-based AC microgrid: robust control design and numerical simulation validation

Recalling the stand-alone MG topology case study in Fig. 4.14 in the previous Subsection 4.3.1, the interest moves now to MG robust *voltage* control. Whereas the majority of works in the literature usually neglect MG interaction dynamics or assume them as lump-sum external disturbance, explicitly including accurate modelling of overall MG dynamics obviously lead to designing a control robustified to interaction dynamics. To this end, in contrast with *frequency*-control-oriented modelling in the previous subsection, *voltage*-control-oriented model will now include the circled part in Fig. 4.17, *i.e.*, the detailed model of the Diesel generator together with its primary voltage control.

The ***supercapacitor*** is again assigned the role of ***complementing the Diesel generator in the high-frequency domain***, but this time for guaranteeing faster recovery of the line-to-line ***voltage*** *magnitude* at the point of common coupling (PCC), U_{PCC}, consequent to a load or PV output ***reactive*** *power variation*. Thus, a template for the PCC line-to-line voltage magnitude deviation in response to a load reactive power step disturbance can be defined as in Fig. 4.22 to formalize grid code requirements in terms of dynamic performance (overshoot, response time, steady-state error). This template, together with the one for the DC-bus voltage, V_{dc}, already defined in Fig. 4.16 in relation to the frequency control, further serve as input data for the robust control design procedure.

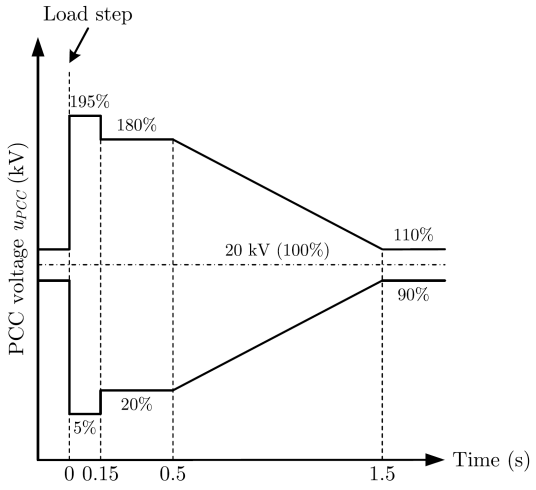

Figure 4.22: *Translation of* ***voltage*** *grid codes*: time-domain performance specification of PCC voltage magnitude in response to a load step disturbance [157].

A ***thirteen-order per-unitized state-space model*** results in this case – with three-phase variables repre-

sented by their d and q components – which is submitted to $\Delta I_{loadd} - \Delta I_{PVd}$ and $\Delta I_{loadq} - \Delta I_{PVq}$ as disturbances corresponding to aggregated-load-PV reactive power variations. The PCC line-to-line voltage magnitude variation, ΔU_{PCC}, exhibits ***non-minimum-phase behaviour and oscillations*** of its d and q components due to presence of right-half-plane complex-conjugate zero pairs. For sake of brevity, modelling details are skipped here, they can be found in [157] and [164].

Following the same idea as for the frequency control design, a ***hierarchical two-level control architecture*** can be again put in place, as shown in Fig. 4.23, where notations of interest variables are visible.

This cascade system is composed of a regulation outer level and a tracking inner level. Being in charge with rejecting disturbances coming from $\Delta I_{loadd} - \Delta I_{PVd}$ and $\Delta I_{loadq} - \Delta I_{PVq}$ and imposing low-frequency dynamics (*e.g.*, ΔV_{dc}, ΔV_{PCCd}, ΔV_{PCCq}), the outer loop is based on an $\mathcal{H}_\infty$ controller and provides ΔI_s^{ref}, ΔI_{rd}^{ref} and ΔI_{rq}^{ref} as references to the high-frequency inner PI-based control loops.

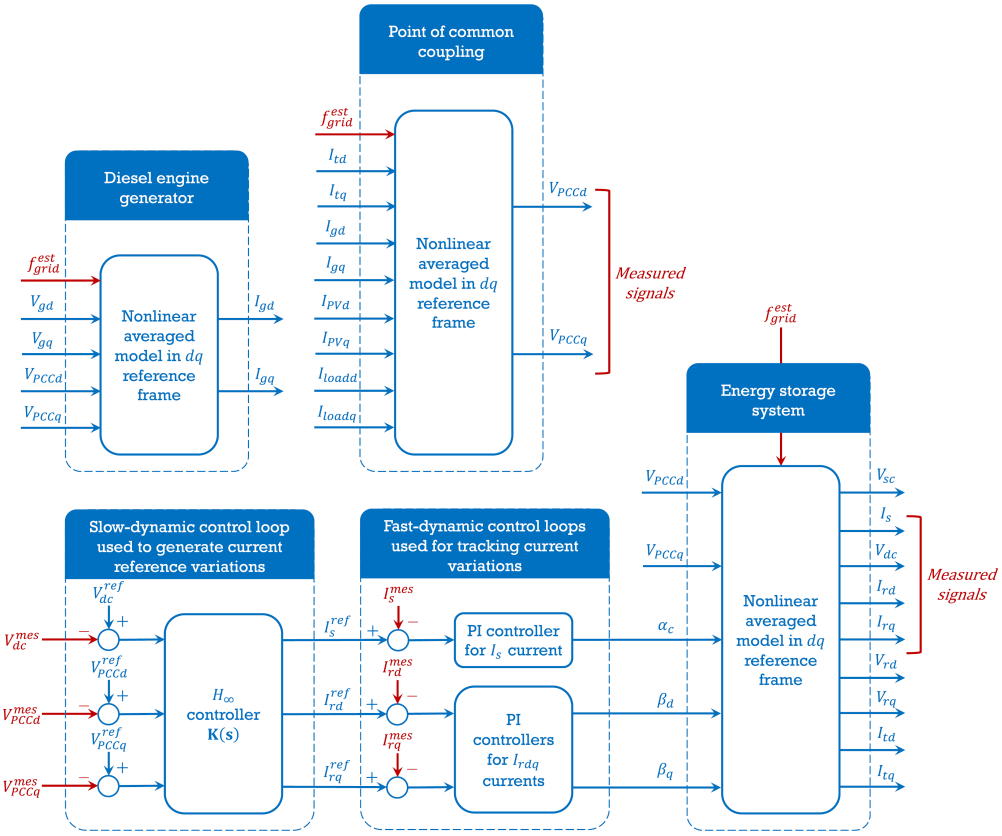

Figure 4.23: $\mathcal{H}_\infty$ -based two-level control block diagram dedicated to stand-alone MG primary voltage regulation [157], [164].

ω_{grid} is considered a time-invariant parameter in voltage regulation, *i.e.*, $\Delta\omega_{grid} = 0$ and thus $\omega_{grid} = \omega_{grid_e} = 2\pi \cdot 50$ rad/s. As in the previously discussed $\mathcal{H}_\infty$ -based two-level frequency regulation case, the outer $\mathcal{H}_\infty$ plant "sees" $\Delta I_s \equiv \Delta I_s^{ref}$, $\Delta I_{rd} \equiv \Delta I_{rd}^{ref}$ and $\Delta I_{rq} \equiv \Delta I_{rq}^{ref}$, because inner control loops ensures much faster dynamics. Also, the supercapacitor voltage V_{sc} is considered time invariant in the $\mathcal{H}_\infty$ controller design, hence $\Delta V_{sc} = 0$. It is also assumed that the Diesel engine generator output voltage is well regulated at its setpoint value, so $\Delta V_{gd} = 0$ and $\Delta V_{gq} = 0$.

Under the above assumptions, the **P**–**K** form in Fig. 4.24 is obtained to further guide the $\mathcal{H}_\infty$ primary voltage control design as an S/KS ***mixed-sensitivity optimization problem*** [165].

The generalized plant **P** has five inputs, namely: the d- and q-component of the aggregated-load-PV current variations, $\Delta I_{loadd} - \Delta I_{PVd}$ and $\Delta I_{loadq} - \Delta I_{PVq}$, respectively, acting as disturbance inputs, $\Delta\mathbf{w}$, and the current reference variations ΔI_s^{ref}, ΔI_{rd}^{ref} and ΔI_{rq}^{ref}, composing the control input vector, $\Delta\mathbf{u}$. The measured output vector $\Delta\mathbf{y}$ is composed of the DC-bus voltage variation, ΔV_{dc}, and the d- and q-component of the PCC voltage variation, ΔV_{PCCd} and ΔV_{PCCq}, respectively. Finally, ΔV_{dc}, ΔV_{PCCd} and ΔV_{PCCq}, as well as ΔI_s^{ref}, ΔI_{rd}^{ref} and ΔI_{rq}^{ref}, are chosen as performance outputs, thus making the object of further conditioning by means of some suitable weighting functions, such as to express the performance requirements. Their vector is noted $\Delta\mathbf{z}$.

Again, the key of this design method is the appropriate definition of weighting functions "applied" to the performance output vector, $\Delta\mathbf{z}$: $W_{perf}(s)$ to guarantee the performance specifications and $W_u(s)$ to formalize the control input constraints.

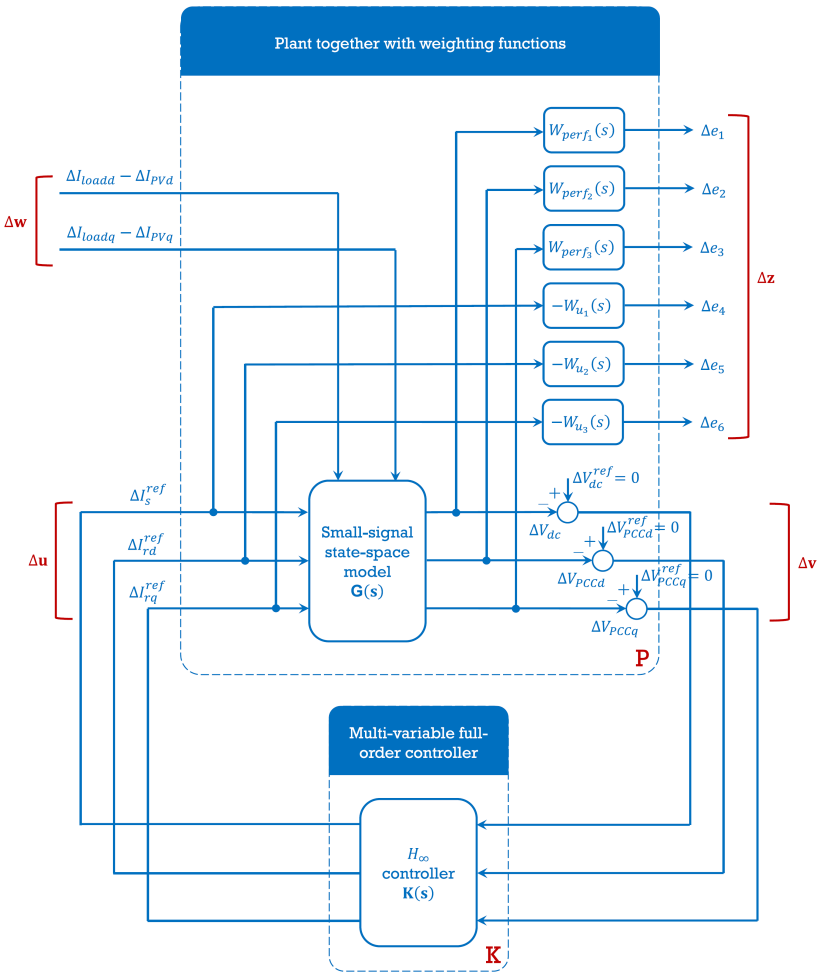

Figure 4.24: **P**–**K** block diagram for $\mathcal{H}_\infty$ primary voltage control design [157], [164].

The performance template corresponding to grid requirements imposed in Fig. 4.22 for ΔU_{PCC} is identically transferred to its d-component, ΔV_{PCCd}, because its q-component is much smaller than its d-component. First-order forms were chosen for both $W_{perf}(s)$ and $W_u(s)$, as detailed in [157].

After having computed a fifteen-state $\mathcal{H}_\infty$ controller as a solution of the S/KS mixed-sensitivity optimization problem, numerical-simulation validations were performed under small-signal-disturbance scenarios. Further, a MATLAB®/Simulink®-***based sensitivity analysis*** was performed to give an idea about the obtained closed-loop robustness. To this end, uncertainties in the steady-state value of the supercapacitor SoC, SoC_{sc_e} (or, equivalently, supercapacitor voltage, V_{sc_e}) and the length l of the transmission line connecting the Diesel engine generator to the PCC were chosen as varying parameters.

Fig. 4.25 and Fig. 4.26 present time evolutions of voltages of interest, when taking into account the uncertainty in supercapacitor SoC and in the transmission line length, respectively.

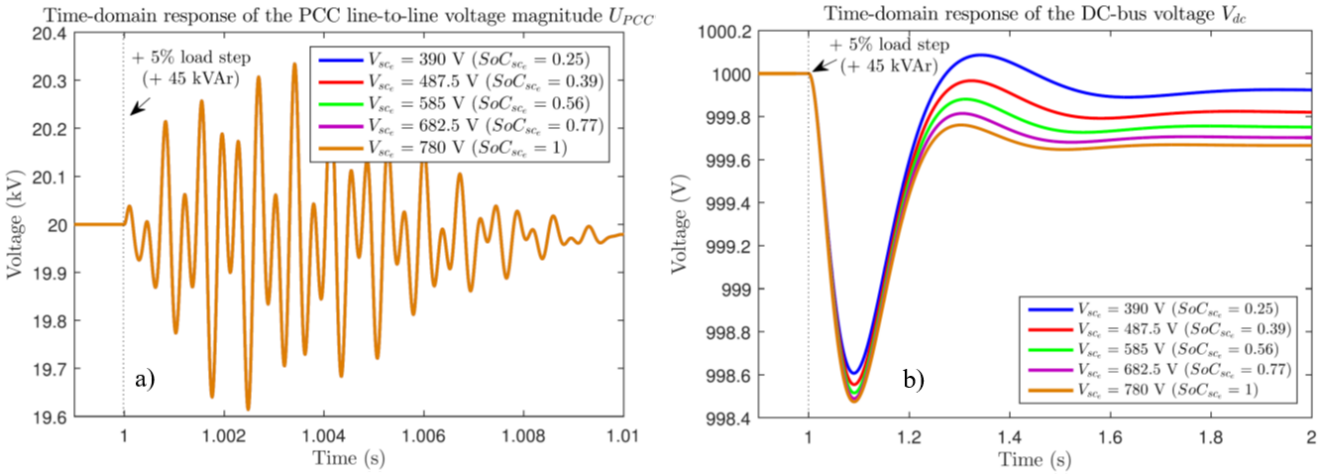

Figure 4.25: Time-domain responses to a small (5%) load step disturbance of the load rated reactive power (45 kVAr for the considered MG), when taking into account the uncertainty in supercapacitor SoC, the transmission line length being fixed at l=1 km [157]: a) PCC line-to-line voltage magnitude, U_{PCC}; b) DC-bus voltage, V_{dc}.

Fig. 4.25a) shows that the five curves of the PCC line-to-line voltage magnitude – corresponding to different SoC levels between empty (here taken as 25%) and full (100%) – are practically superposed, which suggests

that performance is unaltered irrespective of the supercapacitor SoC value varying within the considered domain. Fig. 4.25b) exhibits some slight variations of the DC-bus voltage with the SoC value, however still complying with the performance template proposed in Fig. 4.16. These results allow concluding that the designed $\mathcal{H}_\infty$ controller is robust in performance for the whole considered domain of supercapacitor SoC variation, *i.e.*, [25; 100]%.

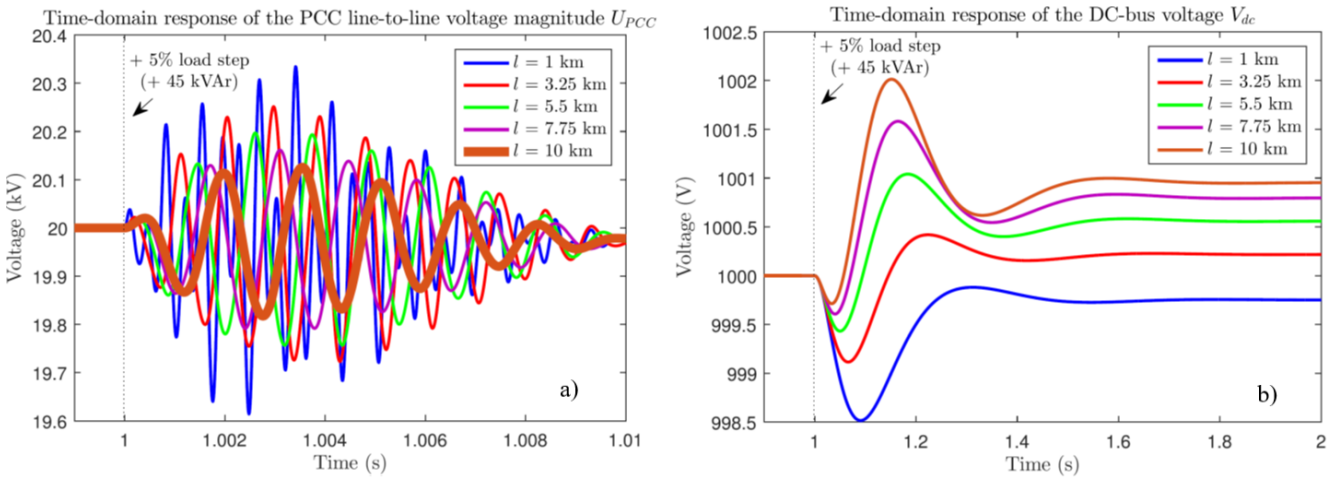

Figure 4.26: Time-domain responses to a small (5%) load step disturbance of the load rated reactive power (45 kVAr for the studied MG), when taking account of the uncertainty in the transmission line length, l, the supercapacitor SoC being fixed at SoC_{sc_e}=56% (V_{sc_e}=585 V) [157]: a) PCC line-to-line voltage magnitude, U_{PCC}; b) DC-bus voltage, V_{dc}.

At their turn, results synthesized in Fig. 4.26 also suggest the closed-loop robustness in performance, this time when l varies between 1 and 10 km. Both sets of results, a) and b), emphasize that the larger l is, the more damped the oscillations of U_{PCC} and V_{dc} are, respectively, because the line resistance increases, determining the system damping coefficient increasing.

The above-reported results of the numerical-simulation-based sensitivity analysis confirm that the chosen supercapacitor can effectively fulfill its role in the robust primary voltage control – as it was also the case for the frequency control, discussed in the previous Subsection 4.3.1 – because its ***SoC can vary from empty to full all by maintaining the closed-loop stability and imposed performance***. These results also suggest relatively good flexibility in sizing the transmission line length without trespassing the primary voltage regulation grid codes.

4.3.3 *Frequency*-regulation PMS for a *battery-ultracapacitor* AC microgrid: some results of microcontroller embedding

Results reported within this subsection were obtained in the framework of a technology transfer project funded between 2018 and 2020, whose aim was ***to prove the practical feasibility of an $\mathcal{H}_\infty$ -based PMS solution and quantify its economical benefits***, in order to advance its technology readiness level (TRL) as close as possible to market commercialization. The use case considered to this end was that of the ***primary frequency regulation*** in a stand-alone MG equipped with both classical and renewable (PV) sources and with a ***hybrid*** *energy storage system* (HESS) consisting of a ***battery*** and a ***supercapacitor***.

The important penetration rate of the renewables justifies in the first place the need of ***hybridizing*** the storage, that is, to consider two ***complementary storage technologies***. Here, this complementarity is represented by the battery for supplying the load slow, long-term, low-frequency variations and the supercapacitor able to supply fast, instantaneous, high-frequency (and possibly high-magnitude) load variations, respectively. Thus, the supercapacitor preserves its obvious role of "fast" backup storage – as in MG considered in the previous subsections – moreover, it protects the "slow" storage, the battery, from being sollicited by abrupt load variations. In this ***reliability-aware*** context, battery lifetime saving results in some quantifiable economical benefits, like, for example, reduction of initial investment costs.

MG configuration in Fig. 4.27 was considered to fix the ideas. Contribution of **K-INF PMS** is to optimally manage this complementarity, such as to result in a "*fusion*" of the two storages. The used methodology is generalizable to any number of storages/sources, applying the same principle as described in the electric-vehicle use case reviewed in Section 4.2. Some design and implementation details are purposely ommited here, for reasons of intellectual property protection.

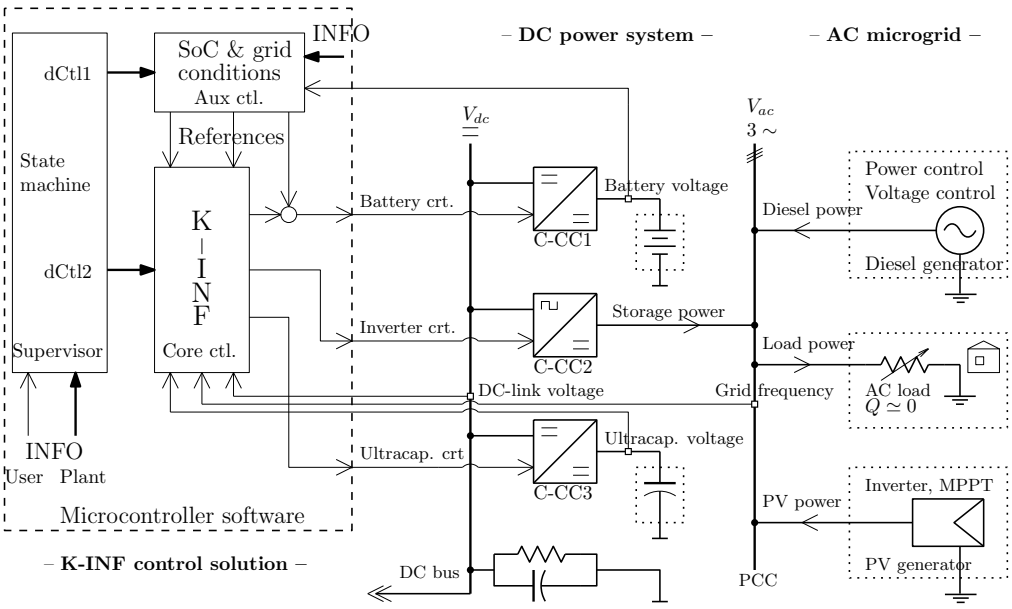

Figure 4.27: Block diagram of a stand-alone MG with large penetration of renewable energy (PV) and hybrid (battery-supercapacitor) storage, controlled by K-INF PMS.

Funding obtained to pursue K-INF TRL advancing allowed employing the demonstrator built in the technology pre-transfer phase – whose photo has been presented in Fig. 4.11 in Subsection 4.2.3 – within a more complex test bench presented in Fig. 4.28, where a ***real*** – instead of only simulated – ***battery pack*** together with its ***boost DC-DC converter*** were used.

Such a setup enabled real-time tests aimed at submitting the real battery pack to cycles relevant to the frequency-regulation use case, in order to further assess its aging parameters, in particular, the *residual capacity of discharge*.

To this end, the K-INF PMS version adapted to the frequency-regulation use case was embedded on the same TI C2000 microcontroller. In the end, ***more than 50% increase of battery lifetime*** was predicted based on post-cycling measurements, which suggests significant economical benefits of hybridization combined with K-INF PMS – more details can be found on the project website, `http://www.k-inf.fr`.

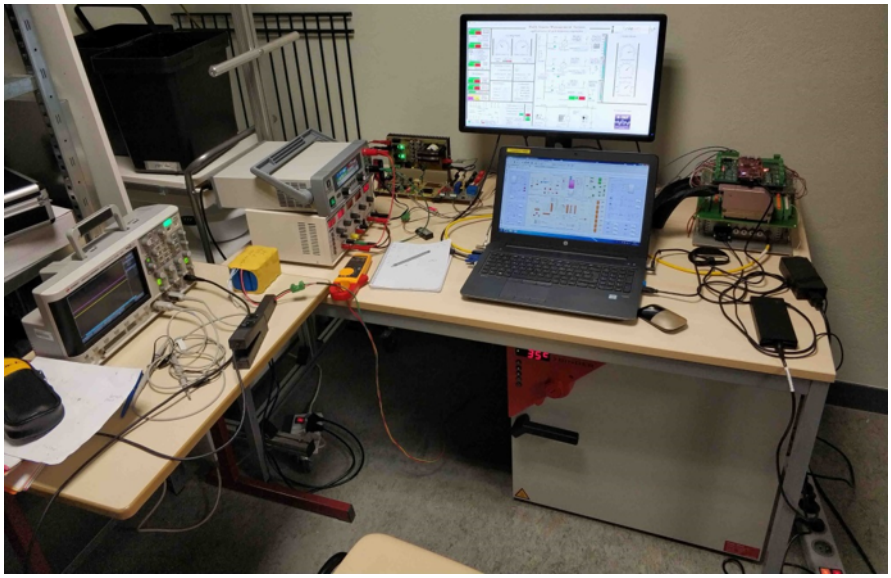

Figure 4.28: Photo of the HILS test bench at GIPSA-lab, replicating configuration of K-INF-controlled MG in Fig. 4.27 – here the test bench is used for ***battery cycling*** in the primary-frequency-regulation use case.

Fig. 4.29 gives an idea about K-INF closed-loop dynamic performance under most unfavourable load power scenario, *i.e.*, consisting of a series of step variations. Fig. 4.29a) presents the time evolutions of load power, P_{LD}, Diesel generator power, P_{GD}, and supercapacitor power, P_{SK}, with the corresponding time evolutions of d-component of inverter current, i_{rd}, battery current, i_{bt}, and supercapacitor current, i_{uc}, shown in Fig. 4.29b).

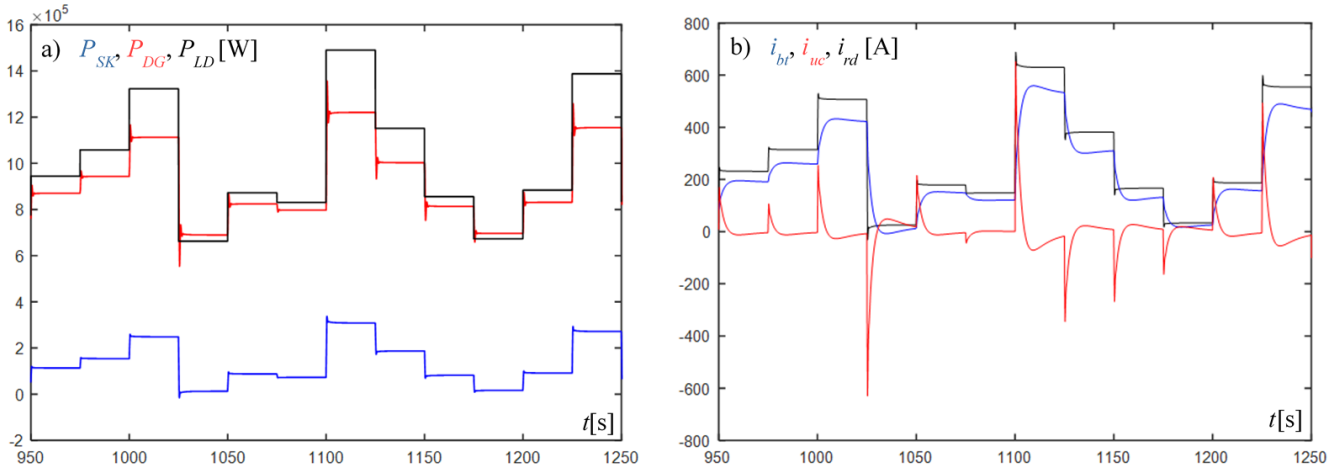

Figure 4.29: Time-domain illustration of the two storage technologies' dynamic complementarity in the MG primary-frequency-regulation case: a) step-variation load power scenario; b) evolutions of concerned currents.

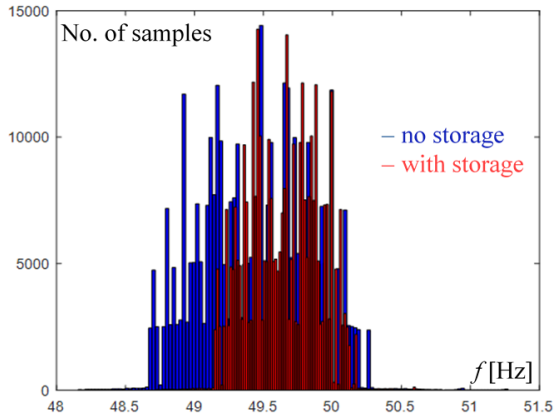

Figure 4.30: Histogram of MG primary-regulated frequency values, with and without storage.

Dynamic separation of battery and supercapacitor currents can be concluded based on time evolutions of the concerned curents in Fig. 4.29b), where battery usage is "smoothed" due to presence of supercapacitor, able to supply high-amplitude high-frequency power variations. Hence, promises of ***storage hybridization*** resulting in more reasonable, less extreme sollicitation of sources can be effectively kept. This further implies ***aging phenomena being slowed down***, with positive economical effects, like both initial investment cost (CAPital EXpenditure – CAPEX) and operation cost (OPerational EXpenditure – OPEX) reduction.

Finally, a more general viewpoint – namely, concerning the storage beneficial role in renewable-based MG control – is expressed in Fig. 4.30 visualizing a histogram-based comparison of no-storage- *vs.* storage-based PMS: average of the MG frequency values appear to be closer to the rated one (here 50 Hz) if the storage is present.

4.4 Summary of contributions and conclusion

At the end of this chapter a concluding regard is aimed at, with focus on main features and strengths of our contributions.

The research effort reported here concerns the microgrids (MGs) operating in ***grid-forming*** (stand-alone) mode, namely by considering – without loss of generality – two main use cases: the so-called "mobile" and "stationary" applications, respectively. The feature of disposing of ***large penetration of renewables*** adds further precision to the studied MG characterization, as well as consequent use of ***storage units*** as a mean of "taming" the resulting stochasticity and unpredictability.

From a control viewpoint, ***heterogeneity*** of the plant – that is, the MG to control – is in a first place expressed by the classical-*vs.*-renewable-source taxonomy, which can further be extended to storage units too, that is, by employing at least two different storage technologies. It is precisely at this point where our contributions come in, namely by proposing ***to transform an initial drawback*** – the heterogeneity, mainly expressed by ***co-existence of different dynamic natures*** – into an advantage: the ***complementarity***. A systematic manner of dealing with this is proposed in the ***robust $\mathcal{H}_\infty$ control framework*** and applied to Power Management Systems (**PMSs**) design, mainly focused on optimally exploiting MG's sources complementarity.

Indeed, it is its ***dynamic*** substrate that enables complementarity to justify and meanwhile be exploited for control and coordination purposes.

More precisely, our proposed PMS design procedures are fed with input data characterizing the ***dynamic specialization*** of sources, as extracted from their datasheets and according to their placement on the energy-density-*vs.*-power-density Ragone plot – recalled earlier in Fig. 2.3 in Section 2.2 of motivation Chapter 2 – enabling definition of ***own frequencies*** (see (2.1) in the same section) as a precise quantification of their dynamic properties. Such an approach proved to be coherent in a broader sense with a ***reliability-aware***, thus ***sustainable*** design.

$\mathcal{H}_\infty$ formal framework allowed the PMS design being cast as an S/KS ***mixed-sensitivity problem***, with further possibility of performing ***systematic robustness analysis***. The use of "fast" storages – like supercapacitors in our case – was proven as beneficial and robustly well-performing in both improving closed-loop dynamic behaviour – in primary regulation of frequency, as well as of voltage – and also in protecting other "slower" storages – like batteries – from being over-sollicited outside their "specialization" operation range, with significant gains of service time extension.

The role of hardware-in-the-loop simulation (HILS) validation was again focal, allowing experiments on dedicated test benches and hence going deeper within the proof of concept. Results of the two technology pre-transfer and transfer projects practically *demythized the fear of a "too complex and computationally heavy" control algorithm, difficult to run with good performance on an ordinary numerical device.*

Thus, ***practical feasibility of embedding $\mathcal{H}_\infty$ -based PMS solutions on general-purpose microcontrollers was largely confirmed***. Moreover, our PMS solution, called K-INF, employs a MATLAB®/Simulink®-based automatic design procedure, easily adaptable to specific use cases and their various needs of multiple design iterations.

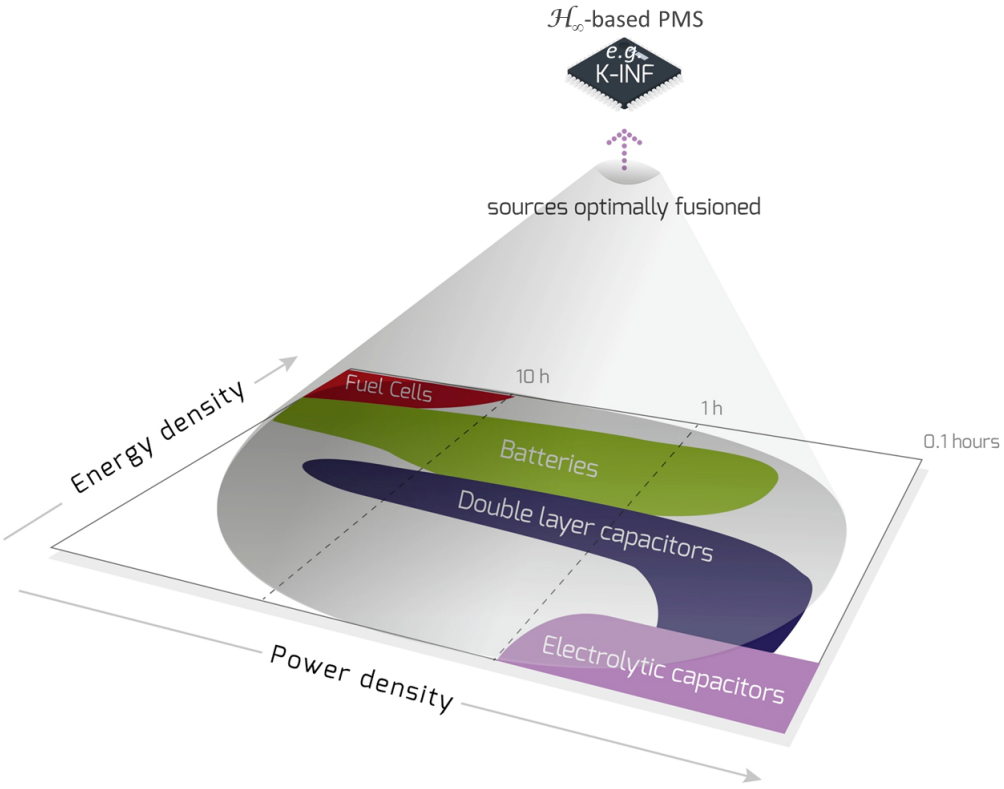

Figure 4.31: Intuitive representation of PMS design, handling heterogeneity and complementarity towards optimal coordination in multi-source/multi-storage MGs.

As a corollary projection on a more philosophical plane, a suggestive representation of ***our PMS control design vision*** is given in Fig. 4.31, where the idea of ***harmonious fusion*** between different power sources naturally emerges as an instance of a more general consensus principle.

Chapter 5

Perspectives and scientific project

This concluding chapter aims at proposing ***a road map of what I believe being of interest for my research activity from a medium- and long-term perspective***.

Generally speaking, I envisage to pursue the main directory lines of my present research by going deeper in certain directions. Being application-oriented, my research aims at finding its motivations in the actual scientific challenges and societal needs, always taking into account real-world constraints, as well as pertinence and feasibility of the corresponding proposed solutions and implementations. Some identified perspectives are detailed next.

5.1 Towards a comprehensive co-design approach for modern microgrids

The term "***co-design***" is presently at the core of rich debates, especially around economical and ecological issues. This term globally denotes complex interactions between heterogeneous subsystems composing the environment of a given engineering solution or product, including its initial sizing, investment, operational and maintenance costs, as well as quantification of its environmental effect and possibly recycling and/or dismantling costs. Recent works in the literature having approached MGs from a broader, techno-economical viewpoint, suggest that ***suitable formalization of a co-design problem corresponds to a multi-criteria optimization problem*** [166], [167].

To fix ideas and place co-design within the microgrids (MGs) topic, the MG Power Management System (PMS) design will be regarded from a larger perspective, where different economical elements are also considered, namely related to MG configuration and initial sizing, including number of sources and storages, their technologies, power levels and costs. Intuitively speaking, a "good" PMS design would have to explicitly suppose ***a certain economical and ecological awareness*** – reliability requirements are an example, as explained before – further implying that, with the promise of such a PMS, a more rational and sustainable MG overall operation will emerge in a long term.

5.1.1 Generic robust PMS design for multi-source microgrids

The term "***generic***" added to the design of robust and LPV optimal control methods for coordination inside of multi-source MGs regards the generalization of the PMS design procedures already proposed for three-source systems – and summarized in Section 4.2 in Chapter 4 – to ***any number of sources***, while also taking into account the parameter-varying nature of all sources.

The LPV approach is nowadays increasingly used – possibly coupled with some other powerful control design techniques – because, being derived from classical linear control techniques, it allows representing relatively-general

classes of nonlinear systems, while taking account of time-varying objectives and effectively coordinating the various actuators of a multi-variable system. This flexibility renders LPV approaches quite easily acceptable in the industry, despite their relative complexity.

As renewable-based MGs are becoming ubiquitous in the future electrical energy distribution landscape, ***storage units*** are becoming at their turn ubiquitous within these MGs, representing technical means used in the first place for taming variations and uncertainties. Thus, taking into account constraints of maintaining the state of charge of the different storage units within some imposed limits is of great interest. Integrated into the MGs control, this objective can lead to a complex optimization problem as the number of sources/storages increases, as ***scalability of the $\mathcal{H}_\infty$ –LPV design for this case*** appears in a first place to be affordable, but still needs to be studied. This complexity – possibly alleviated by order reduction methods – is further repercuted onto the real-time embedding of the resulted controllers by challenging the computing performance of the numerical devices.

The experience we had with embedding an $\mathcal{H}_\infty$ –solution on a *general-purpose microcontroller* (of C2000 family of Texas Instruments), in the framework of the technology pre-transfer and transfer projects between 2017 and 2020, revealed that an *eight-order $\mathcal{H}_\infty$ controller* requires *less than 25% of computation resources* (memory and run time), while preserving some suitable sampling time. Obviously, application to a more complex system would require more computation resources being mobilized. As a medium-term goal, systematic analysis and order-reduction methods are required to confort the real-world application acceptability.

From a different viewpoint, pursuing funding opportunities allowing TRL advancing of our PMS, K-INF, by validation on MG pilote sites remains a priority. At the present, the aim is to reach a concertation in an European context. Thus, our efforts are focused on joining an European consortium in order to apply for 2022 fall call of **EIC** (European Innovation Council) **Pathfinder Challenges**, a funding instrument specifically tailored for ***boosting laboratory proof of concepts towards market and commercialization***. Within this call, our targeted theme is "*Mid- to long-term and systems integrated energy storage*".

5.1.2 Effective estimation methods of storage state of health

Also related to management of storage units in various MG applications, I have very recently been given the opportunity to begin exploration of estimation methods of state of health (SoH) parameters of batteries, namely in the framework of a research project funded in the context of national IDEX (*Investissements d'avenir*) programme through local IRGA (*Initiatives de Recherche à Grenoble Alpes*) funding scheme. The goal of this eighteen-month 2022–2024 project is that, starting from the partial-derivative-equation (PDE)-based (Enhanced) Single Particle Model [168]–[170] – which provides exhaustive description of battery internal governing phenomena, such as diffusion, intercalation and electrochemical kinetics, like suggested in Fig. 5.1 [171] – to explore the ***systematic design, feasibility and effectiveness of battery SoH PDE-based estimators***.

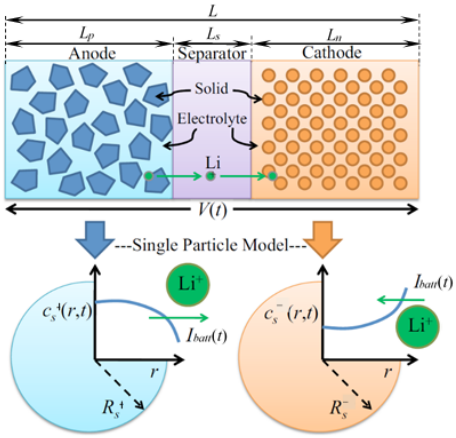

Figure 5.1: Illustration of Single Particle Model for batteries [171].

For sake of accurate capturing of physical substrate, an as generic as possible approach is aimed at, in the sense of exploiting as deep as possible PDE features before applying different approximation methods needed for numerically solving them [172]. Thus, a ***semigroup approach with infinite-dimensional Kalman filters*** is chosen to solve the estimation problem. Collaboration with collegues at LEPMI (Laboratoire d'Électrochimie et de Physicochimie des Matériaux et des Interfaces) in Grenoble will further enable *benchmarkig against objective SoH mesures* issued from real batteries cycling tests.

Such a goal is obviously subsumed to a control and/or optimization one, being ***coherent with the MG PMS reliability-aware consensus design*** summarized in Chapter 4. At a longer term, predictions of such an SoH estimator may also be used for *benchmarking against artificial-intelligence-based estimation methods*, as a substitute

of objective mesures, which may be long and difficult to obtain. Extensions towards a more general, data-driven paradigm can further be envisageable.

5.1.3 Towards formalizing microgrids co-design

Quantification of storage hybridization benefits performed for our PMS solution, K-INF, has allowed to conclude that the service time of the low-frequency (long-term) storage – a battery in the considered case – is prolonged if accompanied by a high-frequency (short-term) storage, like a supercapacitor.

This conclusion can be used in an N-source MG co-design context, as it can be extended to any complementary storage pair and further to a set of N sources – not necessarily only storages – whose own (characteristic) frequencies, f_i can be put in relation with the pair (technology, power)$_i$, according to power sources taxonomy and Ragone's plot. Thus, if ***the length of dynamic interval where the source i is exploited*** is further denoted by Δf_i, then the above result indicates that Δf_i ***is in inverse relation with the source i's life and service time***.

Hence, reliability of long-term storages can be preserved if narrowing their respective exploitation dynamic ranges by hybridization with one (or more) relatively shorter-term storage(s).

On the other hand, a preliminary analysis of MG load variation spectrum allows to determine the maximal frequency f_{load}. Therefore, union of all intervals Δf_i must cover the entire load spectrum, f_{load}, whereas the intersection between all pairs of adjacent intervals Δf_i should be minimized because these intervals should be as disjoint as possible, in order to reflect complementary usage of sources.

Finally, the co-design problem can be stated as finding the minimum number of sources out of the N available, such as to minimize the total investment cost and the cost-per-service-time ratio for each source i. The optimally configured multi-source MG will operate in closed loop with the PMS ensuring "tuning" of each source i on its "specialization" dynamic interval, Δf_i, around its own frequency, f_i.

5.2 Control of particular topologies of power electronic converters

Remaining in the domain of electrical energy conversion, it is worthy to look closer to the involved ***actuators***, the ***power electronic converters***, which are themselves dynamic systems quite challenging from a control viewpoint. International and industrial collaborations I have recently started have offered me an excelent opportunity to go deeper into the modelling and control of some particular power electronic topologies, each of which presents technical and operational gains, but also requires customized control approaches.

Katium is a specific patented DC-DC power converter topology [173], particularly well suited for railway applications, being an isolated, current-input, high-frequency soft-switching system.

Katium converter modelling and control has been approached in 2020 in the context of its use as a battery charger for railway applications, according to terms of collaboration with Faiveley Transport – WABTEC in Tours, France. An ***LPV state-space model subject to step, as well as periodic disturbances***, has been proposed in our conference paper [174] and further exploited within a ***resonant-integrator-based state-feedback control*** in the conference paper [175]. Preliminary validation tests on Faiveley plant in Tours have started during 2020 fall.

The idea of including resonant integrators within a classical state-feedback control design – with the aim of rejecting periodic (sinusoidal) disturbances – originated in the conference paper [176] I co-authored together with Professor Remus TEODORESCU from Aalborg University, dealing with another particular conversion topology, that of ***modular multi-level converters*** (MMCs).

MMCs represent a shift in the power electronic converters technology, that consists in multiplying the number of layers containing switching devices, which thus operate at a *lower switching frequency*. Lower losses and higher operating efficiency are thus obtained. Multilevel topology also ensures improved harmonic performance at a given switching frequency. MMCs are a promising solution to high-voltage direct-current (HVDC) transmission systems over long distances, to facilitate grid integration of renewable energy systems, thus being coherent with long-term European sustainability strategies.

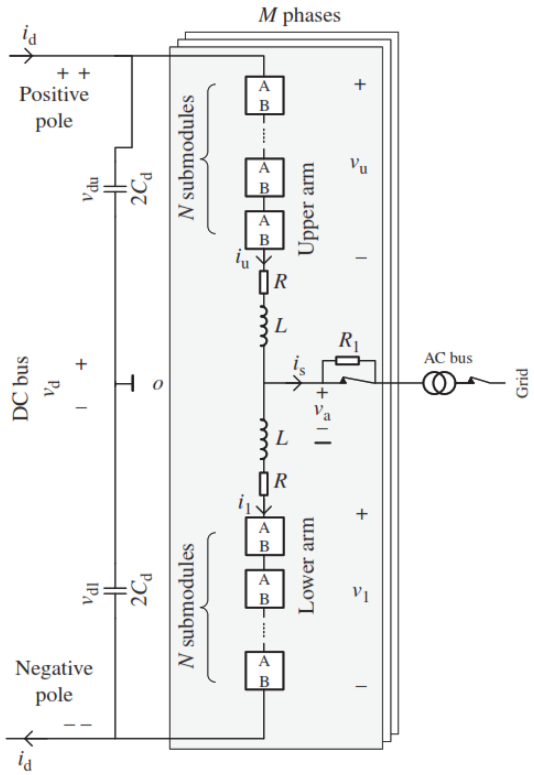

Figure 5.2: Topology of a typical M-phase MMC, showing all the important variables, including DC and AC bus [177].

Pertinent solutions to control problems of MMCs are still required, so this research direction is envisaged at long term. Actual solutions make extensive use of several-level hierarchical, highly-imbricated, generally linear, controls, which suffer of lack of robustness. Instead of a large DC-side capacitor, MMCs have many lower-capacity capacitors, behaving as a spatially-distributed energy storing capacity. The ***dynamic energy balancing between submodule capacitors*** over time has been identified as one of crucial problems to solve by control actions; its solution defines in general the lower limit for the switching frequency. Fig. 5.2 is introduced here for terminology clarification purposes.

Control of circulating current of each leg is necessary to ensure the energy balance between submodules. In our conference paper [176] a change of control viewpoint is proposed against the classical, hierarchical one, presently widely used in industry [177]: a ***state-feedback control of both grid and circulating current*** – ensuring that the input-coupled dynamics of the two currents to be MIMO controlled – proved to outperform the two-loop conventional control under unbalanced grid conditions. A genetic-algorithm-based selection of gains of such a state feedback has been subsequently investigated in our conference paper [178].

Formal modelling of MMCs is not trivial, because their original bilinear dynamics are complexified by presence of binary variables, like the ones indicating if a submodule is inserted or bypassed at a given time. Hybrid dynamics can thus be emphasized.

Like for the other converter types, MMC *averaged* and *switched* (exact) models exist; several types of averaged models are available, depending on which physical level average is made at (leg level, arm level, submodule level – see Fig. 5.2). Averaged models are suitable for most applications; however, switched models may be needed when binary variables are explicitly taken into account. Thus, it is pertinent to explore relevance of considering ***modulation process modelling*** within the control design for submodule energy balancing, as they are intimately linked by the switch instants of individual submodules. Such an approach would lead to an ***optimization problem***, whose solution may require some pertinent relaxations corresponding to acceptable levels of sub-optimality in the solution. Similar points of view have been proposed in [179] – where the optimal-switching-sequence-based control (OSBC) is applied to matrix converters – and in [180], where convex optimization is combined with LMIs for robustly designing switching surfaces for multilevel inverters modelled as bilinear systems with binary inputs.

Another challenging modelling issue consists in deriving ***an explicit MMC model under faulty and/or unbalanced conditions***, suitable to further use for fault-tolerant control design.

Last, but not least, interest may be oriented to some light topology variations in the MMCs, namely the case when ***batteries – instead of capacitors*** – are used in the submodules. In this case, because the energy balancing between submodules relies upon disposing of accurate and reliable ***battery state of charge estimations***, solution may be found out in the above-mentioned investigation of PDE-based estimation of ***state of health***, *e.g.*, by means of Kalman filters.

5.3 Control-purpose modelling of energy–communication interaction in smart grids

It is of significant importance to obtain a reliable model of the communication traffic present within a smart grid, because a bad-quality communication negatively influences the grid global performance, leading even to

blackouts as catastrophic expression of loss of stability. Moreover, at the present ***none of the most-commonly used communication protocols is accepted as a unique standard***, thus rendering even more complex the modelling and control tasks. This topic is perceived as quite a challenge and has been identified as a priority of the European research on smart grids [181].

In France a multitude of research and proof-of-concept projects – among which AMI-ADEME GREENLYS, SOGRID, NICEGRID – showed a clear interest of both scientific and industrial communities, as well as of public authorities, to demonstrate the practical necessity and effectiveness of transition to smart grids. However, such projects aim at rather short-term technological advances, which must be accompanied by a formalization effort towards representative, accurate and flexible models of the energy–communication interaction.

In this context, the already obtained results concerning the traffic modelling – based on ARIMA time-series models, as summarized in Section 5.3 in Chapter 2 earlier in this memoir – have shown that *processing of the information provided by a network analyzer* needs a systematic method, in order to extract that traffic information which is relevant for the communication delay estimation.

These results have great potential of being used in an ***interoperability context***, that is, when two or several smart grids – based on possibly different communication protocols – are required to ***cooperate for a common goal***. In this context, I am already involved in 2020–2022 ADAGIO (*Analyse des retarDs dans les smArt Grids InterOpérables – Analysis of Delays in Interoperable Smart Grids*), project funded by Institut Carnot *Énergies du Futur* and led by G2ELab (*Grenoble Electrical Engineering Laboratory*) and CEA (*Commissariat à l'Énergie Atomique et aux Énergies Alternatives*). A possible test setup is suggested in Fig. 5.3, where estimation of a delay propagated over a transmission line needs in a first place synchronization between the two concerned remote grid sectors.

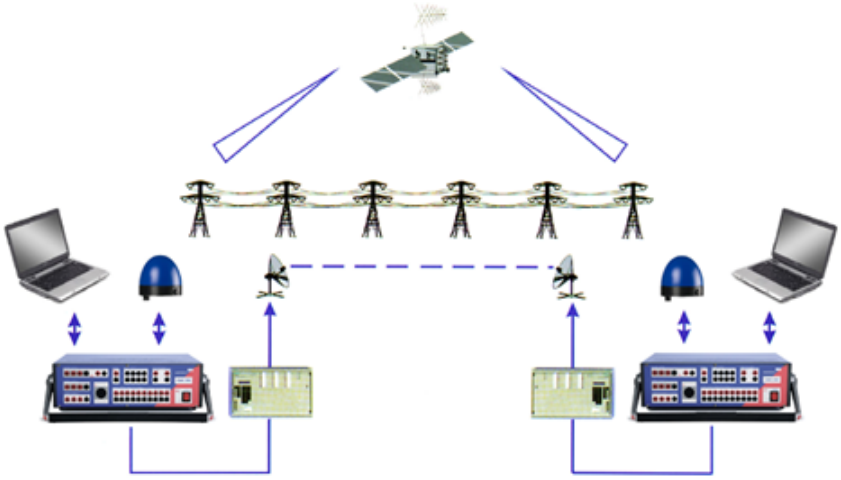

Figure 5.3: Synchronization of two remote smart grids for estimation of delays in a transmission-line-protection scenario.

Necessity of confining maximum delays within admissible limits is here of crucial importance. The already obtained models must first be adapted and extended to the case when the communication network architecture is *a priori* not known (*e.g.*, Internet instead of proprietary communication network).

Pertinence of models used in the literature to characterize and analyze the communication (*e.g.*, Internet) traffic must be evaluated. Stochasticity and complexity of involved phenomena suggest the opportunity of combining more classical models – such as, *e.g.*, time-series-based or long short-term memory (LSTM)-based – with ***black-box, data-driven, possibly machine-learning-based models***. Some preliminary, yet only simulation-based results have recently been reported in our conference paper [182]. At this stage of research development, necessity of defining and putting in place relevant scenarios, representative of smart grid operation, is a key factor in advancing comprehension. Real-time tests on interoperable platforms are on progress for model validation and maximum delay estimation. This latter delay is habitually variable in the time, depending on the observation time window – adaptive sliding windows will thus be necessary to compensate for it.

On a longer term, modelling should help at identifying ***relevant classes of smart grids***, depending on the type of their communication networks and/or types of their energy–communication interactions. Their ***global structural properties as variable-time-delay systems*** – among which the stability – can further be assessed on this basis.

Bibliography

[1] N. Hatziargyriou, H. Asano, R. Iravani, C. Marnay (2007). Microgrids. *IEEE Power Energy Magazine*, 5(4), 78–94.

[2] B. Kroposki, R. Lasseter, T. Ise, S. Morozumi, S. Papathanassiou, N. Hatziargyriou (2008). Making microgrids work. *IEEE Power Energy Magazine*, 6(3), 40–53.

[3] D.E. Olivares, A. Mehrizi-Sani, A.H. Etemadi, C.A. Caizares, R. Iravani, M. Kazerani, *et al.* 2014. Trends in microgrid control. *IEEE Transactions on Smart Grid*, 5(4), 1905–1919.

[4] M. S. Mahmoud, N. M. Alyazidi, M. I. Abouheaf (2017). Adaptive intelligent techniques for microgrid control systems: A survey. *International Journal of Electrical Power & Energy Systems*, 90, 292–305.

[5] J.A.P. Lopes, C.L. Moreira CL, A.G. Madureira (2006). Defining control strategies for microgrids islanded operation. *IEEE Transactions on Power Systems*, 21(2), 916–924.

[6] H. Gaztañaga Arantzamendi, I. Etxeberria-Otadui, S. Bacha, D. Roye (2006). Real-time analysis of the control structure and management functions of a hybrid microgrid system. In: *Procs. of 2006 Annual Conference on IEEE Industrial Electronics – IECON 2006*, Paris, France, pp. 5137–5142.

[7] A. Bertani, C. Bossi, F. Fornari, S. Massucco, S. Spelta, F. Tivegna (2004). A microturbine generation system for grid connected and islanding operation. In: *Procs. of IEEE PES Power Systems Conference and Exposition – PSCE 2004*, New-York, NY, U.S.A., vol. 1, pp. 360–365.

[8] R. Teodorescu, F. Iov, F. Blaabjerg (2004). Flexible control of small wind turbines with grid failure detection operating in stand-alone and grid-connected mode. *IEEE Transactions on Energy Conversion*, 19(5), 1323–1332.

[9] I. Schiemenz, M. Stiebler (2000). Maximum power point tracker of a wind energy system with a permanent-magnet synchronous generator. In: *Procs. of 2000 IEEE International Conference on Electrical Machines – ICEM 2000*, Helsinki, Finland, August 2000, pp. 1083–1086.

[10] R. Datta, V.T. Ranganathan (2003). A method of tracking the peak power points for a variable speed wind energy conversion system. *IEEE Transactions on Energy Conversion*, 18(1), 163–168.

[11] B. Connor, W.E. Leithead (1993). Investigation of fundamental trade-off in tracking the Cpmax curve of a variable speed wind turbine. In: *Procs. of the 12th British Wind Energy Conference*, Norwich, U.K., pp 313–319.

[12] M. Krstič, H.-H. Wang (2000). Stability of extremum seeking feedback for general nonlinear dynamic systems. *Automatica*, 36, 595–601.

[13] K.B. Ariyur, M. Krstič (2003). *Real-time optimisation by extremum seeking control.* Wiley-Interscience. ISBN 978-0471468592.

[14] A.M. Dizqah, A. Maheri, K. Busawon, P. Fritzson (2015). Standalone DC microgrids as complementarity dynamical systems: Modeling and applications. *Control Engineering Practice*, 35, 102–112.

[15] T. Alnejaili, S. Drid, D. Mehdi, L. Chrifi-Alaoui, H. Sahraoui (2015). Sliding mode control of a multi-source renewable power system. In: *Procs. of the 3rd International Conference on Control Engineering and Information Technology – CEIT 2015*, Tlemcen, Algeria, May 2015, pp. 1–6.

[16] M. Rajabzadeh, S.M.T. Bathaee, M.A. Golkar (2016). Dynamic modeling and nonlinear control of fuel cell vehicles with different hybrid power sources. *International Journal of Hydrogen Energy*, 41(4), 3185–3198.

[17] A. Kuperman, I. Aharon (2011). Battery/ultracapacitor hybrids for pulsed current loads: a review. *Renewable and Sustainable Energy Reviews*, 15, 981–992.

[18] A. Florescu, S. Bacha, I. Munteanu, A.I. Bratcu (2012). Frequency-separation-based energy management control strategy of power flows within electric vehicles using ultracapacitors. In: *Procs. of the 38th Annual Conference of IEEE Industrial Electronics Society – IECON 2012*, Montreal, Canada, October 2012.

[19] A. Florescu, S. Bacha, I. Munteanu, A.I. Bratcu, A. Rumeau (2015). Adaptive frequency-separation-based energy management system for electric vehicles. *Journal of Power Sources*, 280, 410–421.

[20] A. Florescu, A.I. Bratcu, I. Munteanu, S. Bacha (2012). Energy management system within electric vehicles using ultracapacitors: an LQG-optimal-control-based solution. In: *Procs. of the 15th IFAC Workshop on Control Applications of Optimization – CAO 2012*, Rimini, Italy, September 2012, pp. 229–234.

[21] A. Florescu, A.I. Bratcu, I. Munteanu, A. Rumeau, S. Bacha (2015). LQG optimal control applied to on-board energy management system of all-electric vehicles. *IEEE Transactions on Control Systems Technology*, 23(4), 1427–1439.

[22] C. Nichita, E. Ceangă, A. Piel, J.J. Belhache, L. Protin (1994). Real time servo system for wind turbine simulator. In: *Procs. of the 3rd International Workshop on Advanced Motion Control*, Berkeley, CA, U.S.A., March 1994, pp. 1039–1048.

[23] C. Nichita, E. Ceangă, I. Bivol, I. Munteanu (1998). Hardware-in-the-loop techniques for the real time simulation. *Annals of "Dunărea de Jos" University of Galaţi*, III, 83-87. http://www.ann.ugal.ro/eeai/index.html.

[24] A.D. Diop, C. Nichita, J.J. Belhache, B. Dakyo, E. Ceangă (1999). Modelling variable pitch HAWT characteristics for a real time wind turbine simulator. *Wind Engineering*, 23(4), 225–243.

[25] H. Hanselmann (1993). Hardware-in-the loop simulation as a standard qpproach for development, customization, and production test of ECU's. In: *Procs. of International Pacific Conference On Automotive Engineering*, SAE Technical Paper 931953.

[26] H. Hanselmann (1996). Hardware-in-the-loop simulation testing and its integration into a CACSD toolset. In: *Procs. of the Joint Conference on Control Applications Intelligent Control and Computer Aided Control System Design*, Dearborn, MI, U.S.A., September 1996, pp. 152–156.

[27] U. Kiffmeier (1996). A hardware-in-the-loop testbench for ABS controllers. In: *Procs. of the 1st International Conference on Control and Diagnostics in Automotive Applications*, Genova, Italy, October 1996.

[28] C. Nichita, M. El Mokadem, B. Dakyo (2006). Wind turbine simulation procedures. *Wind Engineering*, 30(3), 187-200.

[29] I. Munteanu, A.I. Bratcu, N.A. Cutululis, E. Ceangă (2008). *Optimal control of wind energy systems – Towards a global approach*. Advances in Industrial Control Series, Springer, London, U.K. ISBN 978-1-84800-079-7.

[30] I. Munteanu, A.I. Bratcu, S. Bacha, D. Roye (2010). Real-time physical simulation of wind energy conversion systems. In: *Wind Power* (Ed. S.M. Muyeen), pp. 233–258. IN-TECH. ISBN 978-953-7619-81-7.

[31] I. Munteanu, A.I. Bratcu, S. Bacha, D. Roye, J. Guiraud (2010). Hardware-in-the-loop-based simulator for a class of variable-speed wind energy conversion systems: design and performance assessment. *IEEE Transactions on Energy Conversion*, 25(2), 564–576.

[32] C. Vlad, A.I. Bratcu, I. Munteanu, S. Epure (2014). Real-time replication of a stand-alone wind energy conversion system: Error analysis. *International Journal of Electrical Power and Energy Systems*, 55, 562–571.

[33] I. Al-Anbagi, M. Erol-Kantarci, H.T. Mouftah (2013). Priority- and delay-aware Medium Access for wireless sensor networks in the smart grid. *IEEE Systems Journal*, 1–11.

[34] M. Manbachi, M. Nasri, B. Shahabi, H. Farhangi, A. Palizban, S. Arzanpour, M. Moallem, D.C. Lee (2014). Real-time adaptive VVO/CVR topology using multi-agent system and IEC 61850-based communication protocol. *IEEE Transactions on Sustainable Energy*, 5(2), 587–597.

[35] E. Padilla, K. Agbossou, A. Cardenas (2014). Towards smart integration of distributed energy resources using distributed network protocol over Ethernet. *IEEE Transactions on Smart Grid*, 5(4), 1686–1694.

[36] Y. Susuki, T.J. Koo, H. Ebina, T. Yamazaki, T. Ochi, T. Uemura, T. Hikihara (2012). A hybrid system approach to the analysis and design of power grid dynamic performance. *Proceedings of the IEEE*, 100(1), 225–239.

[37] S. Al-Areqi, D. Görges, S. Liu (2014). Stochastic event-based control and scheduling of large-scale networked control systems. In: *Procs. of 2014 European Control Conference – ECC 2014*, Strasbourg, France, June 2014, pp. 2316–2321.

[38] R. Feizimirkhani, A.I. Bratcu, Y. Bésanger, A. Labonne, T. Braconnier (2021). A methodology for the evaluation of the message transmission delay over IEC 61850 communication network – a real-time HV/MV substation case study. *Sustainable Energy, Grids and Networks*, 28, art. no. 100555.

[39] J.P. Georges, N. Krommenacker, T. Divoux, E. Rondeau (2006). A design process of switched Ethernet architectures according to real-time application constraints. *Engineering Applications of Artificial Intelligence*, 19(3), 335–344.

[40] J.Y. Le Boudec, P. Thiran (2004). *Network Calculus – a theory of deterministic queuing systems for the Internet*. Lecture Notes in Computer Science Series, vol. 2050, pp. 83–157. Springer, London, U.K. ISBN 978-3540421849.

[41] R.L. Cruz (1991). A calculus for network delay, part II: Network analysis. *IEEE Transactions on Information Theory*, 37(1), 132–141.

[42] Y. Zhang, Z. Cai, X. Li, R. He (2015). Analytical Modeling of Traffic Flow in the Substation Communication Network. *IEEE Transactions on Power Delivery*, 30(5), 2119–2127.

[43] R.L. Cruz (1991). A calculus for network delay, part I: Network elements in isolation. *IEEE Transactions on Information Theory*, 37(1), 114–131.

[44] T. Burton, D. Sharpe, N. Jenkins, E. Bossányi (2001). *Wind energy handbook* – First Edition. John Wiley & Sons, New-York, U.S.A. ISBN 9780471489979.

[45] P. Sharma, V. Agarwal (2014). Exact maximum power point tracking of grid-connected partially shaded pv source using current compensation concept. *IEEE Transactions on Power Electronics*, 29(9), 4684–4692.

[46] K.S. Tey, S. Mekhilef (2014). Modified incremental conductance algorithm for photovoltaic system under partial shading conditions and load variation. *IEEE Transactions on Industrial Electronins*, 61(10), 5384–5392.

[47] J.D. Bastidas-Rodriguez, E. Franco, G. Petrone, C.A. Ramos-Paja, G. Spagnuolo (2014). Maximum power point tracking architectures for photovoltaic systems in mismatching conditions: a review. *IET Power Electronics*, 7(6), 1396–1413.

[48] K.J. Åström, B. Wittenmark (1995). *Adaptive control* – Second Edition. Addison-Wesley. ISBN 978-0201558661.

[49] I. Munteanu, N.A. Cutululis, A.I. Bratcu, E. Ceangă (2005). Optimization of variable speed wind power systems based on a LQG approach. *Control Engineering Practice*, 13(7), 903–912.

[50] K. Pierce (1999). *Control method for improved energy capture below rated power*. Technical Report NREL/CP-500-26322, National Renewable Energy Laboratory, Colorado, U.S.A.

[51] E. Muljadi, K. Pierce, P. Migliore (2000). *A conservative control strategy for variable-speed stall-regulated wind turbines*. Technical Report NREL/CP-500-24791, National Renewable Energy Laboratory, Colorado, U.S.A.

[52] I. Munteanu, A.I. Bratcu, L. Frangu (2004). Nonlinear control for stationary optimization of wind power systems. In: *Procs. of the 4th IFAC Workshop Automatic systems for building the infrastructure in the developing countries – DECOM-TT 2004*, Bansko, Bulgaria, November 2004, pp. 195–200.

[53] I. Munteanu, N.A. Cutululis, A. Bratcu, E. Ceangă (2006). Using a nonlinear controller to optimize a variable speed wind power system. *Journal of Electrical Engineering*, 6(4), on-line: http://www.jee.ro/index.php/jee/article/view/WW1151314467W449faa23f2738.

[54] T. Ekelund (1997). *Modeling and linear quadratic optimal control of wind turbines.* Ph.D. Thesis, Chalmers University, Göteborg, Sweden.

[55] I. Munteanu, A.I. Bratcu, N.A. Cutululis, E. Ceangă (2005). A two loop optimal control of flexible drive train variable speed wind power systems. In: *IFAC Proceedings Volumes – Procs. of the 16th Triennial IFAC World Congress*, 38(1), 344–349.

[56] J.-P. Hautier, J.-P. Caron (1997). *Automatic systems. Tome 2: Control systems* (in French: *Systèmes automatiques. Tome 2 : Commande des processus*). Ellipses, Paris. ISBN 2729897208.

[57] E. Welfonder, R. Neifer, M. Spanner (1997). Development and experimental identification of dynamic models for wind turbines. *Control Engineering Practice*, 5(1), 63–73.

[58] L. Lublin, M. Athans (1996). Linear quadratic regulator control. In: *The control handbook* (Ed. W.S. Levine), pp. 635–650. CRC Press, IEEE Press. ISBN 9780849385704.

[59] A.W. Pike, M.J. Grimble, M.A. Johnson, A.W. Ordys, S. Shakoor (1996). Predictive control. In: *The control handbook* (Ed. W.S. Levine), pp. 805–814. CRC Press, IEEE Press. ISBN 9780849385704.

[60] Y. Long, S. Hanba, K. Yamashita, H. Miyagi (1999). Sliding mode controller design via $\mathcal{H}_\infty$,theory for windmill power systems. In: *Procs. of the IEEE International Conference on Systems, Man and Cybernetics*, Tokyo, Japan, October 1999, vol. I, pp. 56–61.

[61] H. De Battista, P.F. Puleston, R.J. Mantz, C.F. Christiansen (2000). Sliding mode control of wind systems with DOIG – Power efficiency and torsional dynamics optimization. *IEEE Transactions on Power Systems*, 15(2), 728–734.

[62] H. De Battista, R.J. Mantz (2004). Dynamical variable structure controller for power regulation of wind energy conversion systems. *IEEE Transactions on Energy Conversion*, 19(4), 756–763.

[63] R.A. DeCarlo, S.H. Zak, S.V. Drakunov (1996). Variable structure, sliding-mode controller design. In: *The control handbook* (Ed. W.S. Levine), pp. 941–951. CRC Press, IEEE Press. ISBN 9780849385704.

[64] K.D. Young, V.I. Utkin, U. Ozgüner (1999). A control engineer's guide to sliding mode control. *IEEE Transactions on Control System Technology*, 7(3), 328–342.

[65] I. Munteanu, S. Bacha, A.I. Bratcu, J. Guiraud, D. Roye (2008). Energy-reliability optimization of wind energy conversion systems by sliding mode control. *IEEE Transactions on Energy Conversion*, 23(3), 975–985.

[66] R.S. Peña, R.J. Cardenas, G.M. Asher, J.C. Clare (2000). Vector controlled induction machines for stand-alone wind energy applications. In: *Procs. of the 35th IAS Annual Meeting and World Conference on Industrial Applications of Electrical Energy – IAS 2000*, Rome, Italy, October 2000, vol. 3, pp. 1409–1415.

[67] B.K. Bose (2001). *Modern power electronics and AC drives.* Prentice–Hall, Englewood Cliffs, NJ, U.S.A. ISBN 978-0130167439.

[68] W. Leonhard (2001). *Control of electrical drives* – Third Edition. Springer, Berlin – Heidelberg – New-York. ISBN 978-3-642-56649-3.

[69] J. Wilkie, W.E. Leithead, C. Anderson (1990). Modelling of wind turbines by simple models. *Wind Engineering*, 14(4), 247–274.

[70] I. Munteanu, A.I. Bratcu, E. Ceangă (2009). Wind turbulence used as searching signal for MPPT in variable-speed wind energy conversion systems. *Renewable Energy*, 34(1), 322–327.

[71] M.J. Khan, G. Bhuyan, M.T. Iqbal, J.E. Quaicoe (2009). Hydrokinetic energy conversion systems and assessment of horizontal and vertical axis turbines for river and tidal applications: A technology status review. *Applied Energy*, 86(10), 1823–1835.

[72] M. Benbouzid *et al.* (2013). Concepts, modeling and control of tidal turbines. In: *Marine renewable energy handbook*, ch. 8, pp. 217–278. John Wiley & Sons, New-York, U.S.A.

[73] Z. Zhou, M. Benbouzid, J. F. Charpentier, F. Scuiller, T. Tang (2017). Developments in large marine current turbine technologies – A review. *Renewable and Sustainable Energy Reviews*, 71, 852–858.

[74] F. Hernández, L. E. Chiang, P. Corbalán (2017). A general architecture for electric power management of small scale NCRE converters: Design methodology and validation. *Energy for Sustainable Development*, 41, 128–138.

[75] H.H.H. Aly (2016). Dynamic modeling and control of the tidal current turbine using DFIG and DDPMSG for power system stability analysis. *International Journal of Electrical Power and Energy Systems*, 83, 525–540.

[76] S. Mehri, M. Shafie-khah, P. Siano, M. Moallem, M. Mokhtari, J.P.S. Catal˜ao (2017). Contribution of tidal power generation system for damping inter-area oscillation. *Energy Conversion and Management*, 132, 136–146.

[77] I. Loots, M. van Dijk, B. Barta, S.J. van Vuuren, J.N. Bhagwan (2015). A review of low head hydropower technologies and applications in a South African context. *Renewable and Sustainable Energy Reviews*, 50, 1254–1268.

[78] D. Kumar, S. Sarkar (2016). A review on the technology, performance, design optimization, reliability, techno-economics and environmental impacts of hydrokinetic energy conversion systems. *Renewable and Sustainable Energy Reviews*, 58, 796–813.

[79] F. Behrouzi, M. Nakisa, A. Maimun, Y.M. Ahmed (2016). Global renewable energy and its potential in Malaysia: A review of hydrokinetic turbine technology.*Renewable and Sustainable Energy Reviews*, 62, 1270–1281.

[80] Z. Zhou, F. Scuiller, J.F. Charpentier, M.E.H. Benbouzid T. Tang (2013). Power smoothing control in a grid-connected marine current turbine system for compensating swell effect. *IEEE Transactions on Sustainable Energy*, 4(3), 816–826.

[81] S.B. Elghali, M.E.H. Benbouzid, J.F. Charpentier (2010). Modelling and control of a marine current turbine-driven doubly fed induction generator. *IET Renewable Power Generation*, 4(1), 1–11.

[82] J.-L. Achard, T.Maître (Grenoble Institute of Technology) (2008). *Hydraulic turbomachine*. European Patent EP 1718863.

[83] A.N. Gorban, A.M. Gorlov, V.M. Silantyev (2001). Limits of the turbine efficiency for free fluid flow. *Journal of Energy Resources Technology*, 123(4), 311–317.

[84] S. Antheaume, T. Maître, J.-L. Achard (2008). Hydraulic Darrieus turbines efficiency for free fluid flow conditions versus power farms conditions. *Renewable Energy*, 33(10), 2186–2198.

[85] M. Hauck, A. Rumeau, I. Munteanu, A.I. Bratcu, S. Bacha, D. Roye (2018). Identification and control of a river-current-turbine generator – application to a full-scale prototype. *IEEE Transactions on Sustainable Energy*, 9(3), 1365–1374.

[86] T. Jaquier (2011). *Cross-flow water turbines: development of a prototype in river canal* (in French: *Hydroliennes à flux transverse : développement d'un prototype HARVEST en canal*). Ph.D. Thesis, Grenoble Institute of Technology, Grenoble, France.

[87] A.M. Andreica, S. Bacha, A.I. Bratcu, J. Guiraud, I. Munteanu, D. Roye (Grenoble Institute of Technology, Electricité de France) (2009). *Hydraulic turbomachine for recovering and converting kinetic energy of water currents into electricity, has regulation units electrically regulating power from generator to ensure that shaft rotates at same speed relative to another shaft*. Patent WO2010020735-A1, FR2935159-A1.

[88] M. Vallet, I. Munteanu, A.I. Bratcu, S. Bacha, D. Roye (2012). Synchronized control of cross-flow-water-turbine-based twin towers. *Renewable Energy*, 48, 382–391.

[89] F. Valenciaga, P.F. Puleston, P.E. Battaiotto (2003). Power control of a solar/wind generation system without wind measurement: A passivity/sliding mode approach. *IEEE Transactions on Energy Conversion*, 18(4), 501–507.

[90] J. Jeon, S. Kim, C. Cho, J. Ahn, J. Kim (2007). Power control of a grid-connected hybrid generation system with photovoltaic/wind turbine/battery sources. In: *Procs. of the 7th IEEE International Conference on Power Electronics*, Daegu, South Korea, October 2007, pp. 506–510.

[91] M. Hauck, I. Munteanu, A.I. Bratcu, S. Bacha, D. Roye (2011). Operation of grid-connected cross-flow water turbines in the stall region by direct power control. *IEEE Transactions on Industrial Electronics*, 58(4), 1132–1140.

[92] M. Andreica (2009). *Energy optimization of water energy conversion systems – Modeling, control and experimental achievement* (in French: *Optimisation énergétique de chaînes de conversion hydroliennes – modélisation, commandes et réalisations expérimentales*). Ph.D. Thesis, Grenoble Institute of Technology, Grenoble, France.

[93] M. Andreica Vallet, S. Bacha, I. Munteanu, A.I. Bratcu, D. Roye (2011). Management and control of operating regimes of cross-flow water turbines. *IEEE Transactions on Industrial Electronics*, 58(5), 1866–1876.

[94] M. Andreica, S. Bacha, D. Roye, I. Exteberria-Otadui, I. Munteanu (2008). Micro-hydro water current turbine control for grid-connected or islanding operation. In: *Procs. of the 39th IEEE Power Electronics Specialists Conference – PESC 2008*, Rhodes Island, Greece, June 2008, pp. 957–962.

[95] M. Andreica, S. Bacha, D. Roye, I. Munteanu, A. I. Bratcu, J. Guiraud (2009). Stand-alone operation of cross-flow water turbines. In: *Procs. of IEEE International Conference on Industrial Technology – ICIT 2009*, Churchill, VIC, Australia, February 2009, pp. 1–6.

[96] P. Mhaskar, N.H. El-Farra, P.D. Christofides (2005). Predictive control of switched nonlinear systems with scheduled mode transitions. *IEEE Transactions on Automatic Control*, 50(11), 1670–1680.

[97] G.-C. Hsieh, J.C. Hung (1996). Phase-locked loop techniques – A Survey. *IEEE Transactions on Industrial Electronics*, 43(6), 609–615.

[98] A. Takano (1996). Quick-response torque-controlled induction motor drives using phase-locked loop speed sontrol with disturbance compensation. *IEEE Transactions on Industrial Electronics*, 43(6), 640–646.

[99] V.D. Shalfeev, V.V. Matrosov, M.V. Korzinova (1998). Chaos synchronization in coupled phase systems. In: Procs. of the 1998 IEEE International Symposium on Circuits and Systems – ISCAS 1998, Monterey, CA, U.S.A., vol. 4, pp. 580–582.

[100] A. Pikovsky, M. Rosenblum, J. Kurths (2000). Phase synchronization in regular and chaotic system. *International Journal of Bifurcation and Chaos*, 10(10), 2291–2305.

[101] S. Haykin (2000). *Communication systems* – Fourth Edition. John Wiley & Sons, New-York, U.S.A. ISBN 9780471178699.

[102] S. Jemeï, D. Hissel, A.-S. Coince, B. Al-Nasrawi (2006). Optimization and economic analysis of an hybrid fuel cell, photovoltaic and battery electric power generation system. *Journal of Fuel Cell Science and Technology*, 3(4), 410–414.

[103] L. Wang, C. Singh (2009). Multicriteria design of hybrid power generation systems based on a modified particle swarm optimization algorithm. *IEEE Transactions on Energy Conversion*, 24(1), 163–172.

[104] A. Fernández-Infantes, J. Contreras, J.L. Bernal-Agustín (2006). Design of grid connected PV systems considering electrical, economical and environmental aspects: a practical case. *Renewable Energy*, 31(13), 2042–2062.

[105] J.-H. Shi, X.-J. Zhu, G.-Y. Cao (2007). Design and techno-economical optimization for stand-alone hybrid power systems with multi-objective evolutionary algorithms. *International Journal of Energy Research*, 31(3), 315–328.

[106] M. Kolhe (2009). Techno-economic optimum sizing of a stand-alone solar photovoltaic system. *IEEE Transactions on Energy Conversion*, 24(2), 511–519.

[107] V. Salas, E. Olıás, A. Barrado, A. Lázaro (2006). Review of the maximum power point tracking algorithms for stand-alone photovoltaic systems. *Solar Energy Materials and Solar Cells*, 90(11), 1555–1578.

[108] V.V.R. Scarpa, S. Buso, G. Spiazzi (2009). Low-complexity MPPT technique exploiting the PV module MPP locus characterization. *IEEE Transactions on Industrial Electronics*, 56(5), 1531–1538.

[109] N. Femia, G. Petrone, G. Spagnuolo, M. Vitelli (2005). Optimization of perturb and observe maximum power point tracking method. *IEEE Transactions on Power Electronics*, 20(4), 963–973.

[110] D. Sera, R. Teodorescu, J. Hantschel, M. Knoll (2008). Optimized maximum power point tracker for fast-changing environmental conditions. *IEEE Transactions on Industrial Electronics*, 55(7), 2629–2637.

[111] A.I. Bratcu, I. Munteanu, S. Bacha, B. Raison (2008). Maximum power point tracking of grid-connected photovoltaic arrays by using extremum seeking control. *Control Engineering and Applied Informatics* – Romanian Society of Control Engineering and Technical Informatics (SRAIT), 10(4), 3–12.

[112] H. Patel, V. Agarwal (2008). Maximum power point tracking scheme for PV systems operating under partially shaded conditions. *IEEE Transactions on Industrial Electronics*, 55(4), 1689–1698.

[113] L. Gao, R.A. Dougal, S. Liu, and A.P. Iotova (2009). Parallel-connected solar PV system to address partial and rapidly fluctuating shadow conditions. *IEEE Transactions on Industrial Electronics*, 56(5), 1548–1556.

[114] W. Nwesaty, A.I. Bratcu, A. Hably (2013). Extremum seeking control techniques applied to photovoltaic systems with multimodal power curves. *Procs. of IEEE International Conference on Renewable Energy Research and Applications – ICRERA 2013*, Madrid, Spain, October 2013, pp. 1–6.

[115] A.I. Bratcu, I. Munteanu, S. Bacha, D. Picault, B. Raison (2011). Cascaded DC-DC converter photovoltaic systems: power optimization issues. *IEEE Transactions on Industrial Electronics*, 58(2), 403–411.

[116] G.R. Walker, P.C. Sernia (2004). Cascaded DC–DC converter connection of photovoltaic modules. *IEEE Transactions on Power Electronics*, 19(4), 1130–1139.

[117] A. Cocconi, S. Ćuk, R.D. Middlebrook (1983). High-frequency isolated 4 kW inverter for utility interface. In: *Procs. of the 7th International PCI 1983 Conference*, Geneva, Switzerland, September 1983, pp. 325–345.

[118] S.L. Brunton, C.W. Rowley, S.R. Kulkarni, C. Clarkson (2010). Maximum power point tracking for photovoltaic optimization using ripple-based extremum seeking control. *IEEE Transactions on Power Electronics*, 25(10), 2531–2540.

[119] T. Esram, J.W. Kimball, Ph.T. Krein, P.L. Chapman, P. Midya (2006). Dynamic maximum power point tracking of photovoltaic arrays using ripple correlation control. *IEEE Transactions on Power Electronics*, 21(5), 1282–1291.

[120] J.W. Kimball, Ph.T. Krein (2008). Discrete-time ripple correlation control for maximum power point tracking. *IEEE Transactions on Power Electronics*, 23(5), 2353–2362.

[121] A.M. Bazzi, Ph.T. Krein (2014). Ripple correlation control: an extremum seeking control perspective for real-time optimization. *IEEE Transactions on Power Electronics*, 29(2), 988–995.

[122] I. Munteanu, A.I. Bratcu (2015). MPPT for grid-connected photovoltaic systems using ripple-based extremum seeking control: analysis and control design issues. *Solar Energy*, 111, 30–42.

[123] S.B. Kjaer, J.K. Pedersen, F. Blaabjerg (2005). A review of single-phase grid-connected inverters for photovoltaic modules. *IEEE Transactions on Industry Applications*, 41(5), 1292–1306.

[124] L.W. Couch II (1997). *Digital and analog communication systems* – Fifth Edition, ch. 4 and 5. Prentice-Hall, One Lake Street, Upper Saddle River, NJ, U.S.A. ISBN 978-7302029458.

[125] J.C. Doyle, B.A. Francis, A. Tannenbaum (1992). *Feedback control theory*. Macmillan Publishing Company, New York, U.S.A. ISBN 9780029464083.

[126] F. Wu. A generalized LPV system analysis and control synthesis framework (2001). *International Journal of Control*, 74(7), 745–759.

[127] P. Apkarian, P. Gahinet, G. Becker (1995). Self-scheduled $\mathcal{H}_\infty$ control of linear parameter-varying systems: a design example. *Automatica*, 31(9), 1251–1261.

[128] C. Scherer, P. Gahinet, M. Chilali (1997). Multiobjective output-feedback control via LMI optimization. *IEEE Transactions on Automatic Control*, 42(7), 896–911.

[129] P. Apkarian, R.J. Adams (1998). Advanced gain-scheduling techniques for uncertain systems. *IEEE Transactions on Control Systems Technology*, 6(1), pp. 21–32.

[130] P. Apkarian, P. Gahinet (1995). A convex characterization of gain-scheduled $\mathcal{H}_\infty$ controllers. *IEEE Transactions on Automatic Control*, 40(5), 853–864.

[131] C. Poussot-Vassal (2008). *Multi-variable LPV robust control for vehicle chassis* (in French: *Commande robuste LPV multivariable de chassis automobile*). Ph.D. Thesis, Grenoble Institute of Technology, Grenoble, France.

[132] J.H. Holland (1975). *Adaptation in natural and artificial systems: an introductory analysis with applications to biology, control, and artificial intelligence* (1975). The University of Michigan Press, Ann Arbor, Michigan, U.S.A. ISBN 978-0472084609.

[133] D.E. Goldberg, J.H. Holland (1988). Genetic Algorithms and Machine Learning. *Machine Learning*, 3(2–3), 95–99.

[134] E. Zitzler, M. Laumanns, S. Bleuler (2004). A tutorial on evolutionary multiobjective optimization. In: *Metaheuristics for multiobjective optimisation*, pp. 3–37. Springer, London, U.K.

[135] B.L. Miller, D.E. Goldberg (1995). Genetic algorithms, tournament selection, and the effects of noise. *Complex Systems*, 9(3), 193–212.

[136] J.M. Guerrero, M. Chandorkar, V. Lee, P.C. Loh (2013). Advanced control architectures for intelligent microgrids – Part I: Decentralized and hierarchical control. *IEEE Transactions on Industrial Electronics*, 60(4), 1254–1262.

[137] J.J. Justo, F. Mwasilu, J. Lee, J.W. Jung (2013). AC-microgrids versus DC-microgrids with distributed energy resources: a review. *Renewable and Sustainable Energy Reviews*, 24, 387–405.

[138] D. Iannuzzi (2007). Use of supercapacitors, fuel cells and electrochemical batteries for electric road vehicles: a control strategy. In: *Procs. of the 33rd Annual Conference of the IEEE Industrial Electronics Society – IECON 2007*, Taipei, Taiwan, November 2007, pp. 539–544.

[139] S. Schuler, D. Schlipf, P.W. Cheng, F. Allgöwer (2013). $\mathcal{L}_1$-optimal control of large wind turbines. *IEEE Transactions on Control Systems Technology*, 21(4), 1079–1089.

[140] S. Xie, H. He, J. Peng (2017). An energy management strategy based on stochastic model predictive control for plug-in hybrid electric buses. *Applied Energy*, 196, 279–288.

[141] M.R.B. Khan, R. Jidin, J. Pasupuleti (2016). Multi-agent based distributed control architecture for microgrid energy management and optimization. *Energy Conversion and Management*, 112, 288–307.

[142] F. Martel, S. Kelouwani, Y. Dubé, K. Agbossou (2015). Optimal economy-based battery degradation management dynamics for fuel-cell plug-in hybrid electric vehicles. *Journal of Power Sources*, 274, 367–381.

[143] X. Xiandong, H. Jia, D. Wang, D.C. Yu, H.-D. Chiang (2015). Hierarchical energy management system for multi-source multi-product microgrids. *Renewable Energy*, 78, 621–630.

[144] A. Castaings, W. Lhomme, R. Trigui, A. Bouscayrol (2016). Decomposed Energy Management of a Multi-Source Fuel Cell Vehicle using Energetic Macroscopic Representation. In: *Procs. of 2016 IEEE Vehicle Power and Propulsion Conference – VPPC 2016*, Hangzhou, China, October 2016, pp. 1–6.

[145] M.A. Silva, J.P. Trovao, P.G. Pereirinha, H.M. Jorge (2013). Application of a decoupling method based on online filtering technique for multi-source electric vehicles. In: *Procs. of 2013 15th European Conference on Power Electronics and Applications – EPE 2013*, Lille, France, September 2013, pp. 1–10.

[146] J.-M.W. Nwesaty, A.I. Bratcu, A. Ravey, D. Bouquain, O. Sename (2020). Robust energy management system for multi-source DC energy systems – real-time setup and validation. *IEEE Transactions on Control Systems Technology*, 28(6), 2591–2599.

[147] W. Nwesaty, A.I. Bratcu, O. Sename (2016). Power sources coordination through multivariable LPV/$\mathcal{H}_\infty$ control with application to multi-source electric vehicles. *IET Control Theory and Applications*, 10(16), 2049–2059.

[148] W. Nwesaty, A.I. Bratcu, O. Sename (2014). Optimal frequency separation of power sources by multivariable LPV/$\mathcal{H}_\infty$ control: application to on-board energy management systems of electric vehicles. In: *Procs. of 2014 IEEE 53rd Annual Conference on Decision and Control – CDC 2014*, Los Angeles, California, U.S.A., December 15–17 2014, pp. 5636–5641.

[149] W. Nwesaty (2015). *LPV/$\mathcal{H}_\infty$ control employed for designing electric vehicle on-board power management system* (in French: *LPV/$\mathcal{H}_\infty$ contrôle utilisé à concevoir de gestion énergétique à bord des véhicules électriques*). Ph.D. Thesis, Grenoble Institute of Technology, Grenoble, France.

[150] P. Apkarian, P. Gahinet, G. Becker (1995). Self-scheduled $\mathcal{H}_\infty$ control of linear parameter-varying systems: a design example. *Automatica*, 31, 1251–1261.

[151] A.-L. Do, O. Sename, L. Dugard (2012). LPV modeling and control of semiactive dampers in automotive systems. In: *Control of Linear Parameter Varying Systems with Applications* (Eds. J. Mohammadpour, C.W. Scherer), pp. 381–411. Springer U.S.A. ISBN 978-1-4614-1833-7.

[152] W. Nwesaty, A.I. Bratcu, O. Sename (2015). Reduced-order LPV controller for coordination of power sources within multi-source energy systems. In: *Procs. of the 8th IFAC Symposium on Robust Control Design – ROCOND 2015*, Bratislava, Slovakia, July 8–11 2015. IFAC-PapersOnLine, 48(14), 132–137.

[153] C. Poussot-Vassal, P. Vuillemin (2012). Introduction to MORE: A MOdel REduction toolbox. In: *Procs. of the 2012 IEEE International Conference on Control Applications – CCA 2012*, Dubrovnik, Croatia, October 2012, pp. 776–781.

[154] F. Gao, B. Blunier, M.G. Simoes, A. Miraoui (2011). PEM fuel cell stack modeling for real-time emulation in hardware-in-the-loop applications. *IEEE Transactions on Energy Conversion*, 26(1), 184–194.

[155] Y. Han, P.M. Young, A. Jain, D. Zimmerle (2015). Robust control for microgrid frequency deviation reduction with attached storage system. *IEEE Transactions on Smart Grid*, 6(2), 557–565.

[156] C. Wang, P. Yang, C. Ye, Y. Wang, Z. Xu (2016). Voltage control strategy for three/single phase hybrid multimicrogrid. *IEEE Transactions on Energy Conversion*, 31(4), 1498–1509.

[157] Q-L. Lam, A.I. Bratcu, D. Riu (2021). Multi-variable $\mathcal{H}_\infty$ control approach for voltage ancillary service in autonomous microgrids : design and sensitivity analysis. *IEEE Access*, 9, 140212–140234.

[158] G. Delille, B. François, G. Malarange (2012). Dynamic frequency control support by energy storage to reduce the impact of wind and solar generation on isolated power system's inertia. *IEEE Transactions on Sustainable Energy*, 3(4), 931–939.

[159] D. Hernández-Torres (2011). *Robust control of hybrid electrochemical generators* (in French: *Commande robuste de générateurs électrochimiques hybrides*). Ph.D. Thesis, Grenoble University, Grenoble, France.

[160] Q.L. Lam, A.I. Bratcu, D. Riu (2016). Robustness analysis of primary frequency H-inf control in stand-alone microgrids with storage units. In: *Procs. of the 2016 IFAC Workshop on Control of Transmission and Distribution Smart Grids – CTDSG 2016*, Prague, Czech Republic, October 11–13 2016. IFAC-PapersOnLine, 49(27), 123–128.

[161] Q.L. Lam, A.I. Bratcu, C. Boudinet, M. Thomas, A. Labonne, D. Riu (2020). Primary frequency $\mathcal{H}_\infty$ control in stand-alone microgrids with storage units: a robustness analysis confirmed by real-time experiments. *International Journal of Electrical Power and Energy Systems*, 115, art. no. 105507.

[162] P. Kundur (1994). *Power system stability and control*. McGraw Hill, New York, U.S.A.

[163] A. Yazdani, R. Iravani (2010). *Voltage-sourced converters in power systems*. John Wiley & Sons, New York, U.S.A.

[164] Q.L. Lam (2018). *Advanced control of microgrids for frequency and voltage stability: robust control co-design and real-time validation*. Ph.D. Thesis, Grenoble Alpes University, Grenoble, France.

[165] S. Skogestad, I. Postlethwaite (2005). *Multivariable feedback control: analysis and design*. John Wiley & Sons, New York, U.S.A.

[166] J. Nömm, S.K. Rönnberg, M.H.J. Bollen (2021). Techno-economic analysis with energy flow modeling for investigating the investment risks related to consumption changes within a standalone microgrid in Sweden. *Energy*, 225, art. no. 120156.

[167] P. Mathiesen, M. Stadler, J. Kleissl, Z. Pecenak (2021). Techno-economic optimization of islanded microgrids considering intra-hour variability. *Applied Energy*, 304, art. no. 117777.

[168] M. Doyle, T.F. Fuller, J. Newman (1993). Modeling of galvanostatic charge and discharge of the lithium/polymer/insertion cell. *Journal of Electrochemical Society*, 140, 1526–1533.

[169] N. Dufour, M. Chandesris, S. Geniès, M. Cugnet, Y. Bultel (2018). Lithiation heterogeneities of graphite according to C-rate and mass-loading: A model study. *Electrochimica Acta*, 272, 97–107.

[170] A. Allam, S. Onori (2021). Online capacity estimation for lithium-ion battery cells via an electrochemical model-based adaptive interconnected observer. *IEEE Transactions on Control Systems Technology*, 29(4), 1636–1651.

[171] S.J. Moura, N.A. Chaturvedi, M. Krstič (2014). Adaptive partial differential equation observer for battery state-of-charge/state-of-health estimation via an electrochemical model. *Journal of Dynamic Systems Measurement and Control*, 136(1), art. no. 011015.

[172] R.F. Curtain, H. Zwart (1995). An Introduction to Infinite-Dimensional Linear Systems Theory. In: *Texts in Applied Mathematics*, vol. 21. Springer-Verlag, New York, U.S.A.

[173] M. Coyaud (2019). *Switch mode power converter structure*. European Patent ES2727286.

[174] A.I. Bratcu, F. Ihuel, A. Contrepois (2021). Katium-power-converter-based Li-ion battery charger for railway applications: control-oriented modelling. In: *Procs. of the 2021 IEEE Conference on Control Technology and Applications – IEEE CCTA 2021*, San Diego, California, U.S.A., August 9–11 2021, pp. 583–588.

[175] A.I. Bratcu, F. Ihuel, A. Contrepois (2021). Two-level state-space-based control strategy of Katium-power-converter-based Li-ion battery charger for railway applications. In: *Procs. of the 23rd European Conference on Power Electronics and Applications – EPE ECCE 2021*, Ghent, Belgium, September 6–10 2021, pp. 1–9.

[176] A.I. Bratcu, R. Teodorescu (2020). State-feedback control of grid and circulating current in modular multilevel converters. In: *Procs. of the 21st IFAC World Congress*, Berlin, Germany, July 12–17 2020. IFAC-PapersOnLine, 53(2), 12396–12401.

[177] K. Sharifabadi, L. Harnefors, H.-P. Nee, S. Norrga, R. Teodorescu (2016). *Design control and application of modular multilevel converters for HVDC transmission systems*. John Wiley & Sons.

[178] R. Ghassani, A.I. Bratcu, R. Teodorescu (2022). Genetic algorithm applied to state-feedback control design of grid and circulating current in modular multilevel converters. In: *Procs. of the 11th IFAC Symposium on Control of Power and Energy Systems – CPES 2022*, virtual, June 21–23 2022.

[179] A. Tajfar, S.K. Mazumder (2016). Sequence-based control of an isolated DC/AC matrix converter. *IEEE Transactions on Power Electronics*, 31(2), 1757–1773.

[180] L. Hetel, M. Defoort, M. Djemaï (2015). Binary control design for a class of bilinear systems: application to a multilevel power converter. *IEEE Transactions on Control Systems Technology*, 24(2), 719–726.

[181] *** (2012). SmartGrids SRA 2035 – SmartGrids Strategic Research Agenda (SRA) for research, development and demonstration needs towards 2035 on line: https://www.etip-snet.eu/wp-content/uploads/2017/04/sra2035.pdf, May 2022.

[182] R. Feizimirkhani, V.H. Nguyen, Y. Bésanger, Q.T. Tran, A.I. Bratcu, A. Labonne, T. Braconnier (2021). Application of Long Short-Term Memory (LSTM) neural network for the estimation of communication network delay in smart grid applications. In: *Procs. of 2021 IEEE International Conference on Environment and Electrical Engineering and 2021 IEEE Industrial and Commercial Power Systems Europe – EEEIC/I&CPS Europe 2021*, Bari, Italy, September 7–10 2021, pp. 1–6.